ISBN 978-82-326-2346-4 (printed ver.)
ISBN 978-82-326-2347-1 (electronic ver.)
ISSN 1503-8181

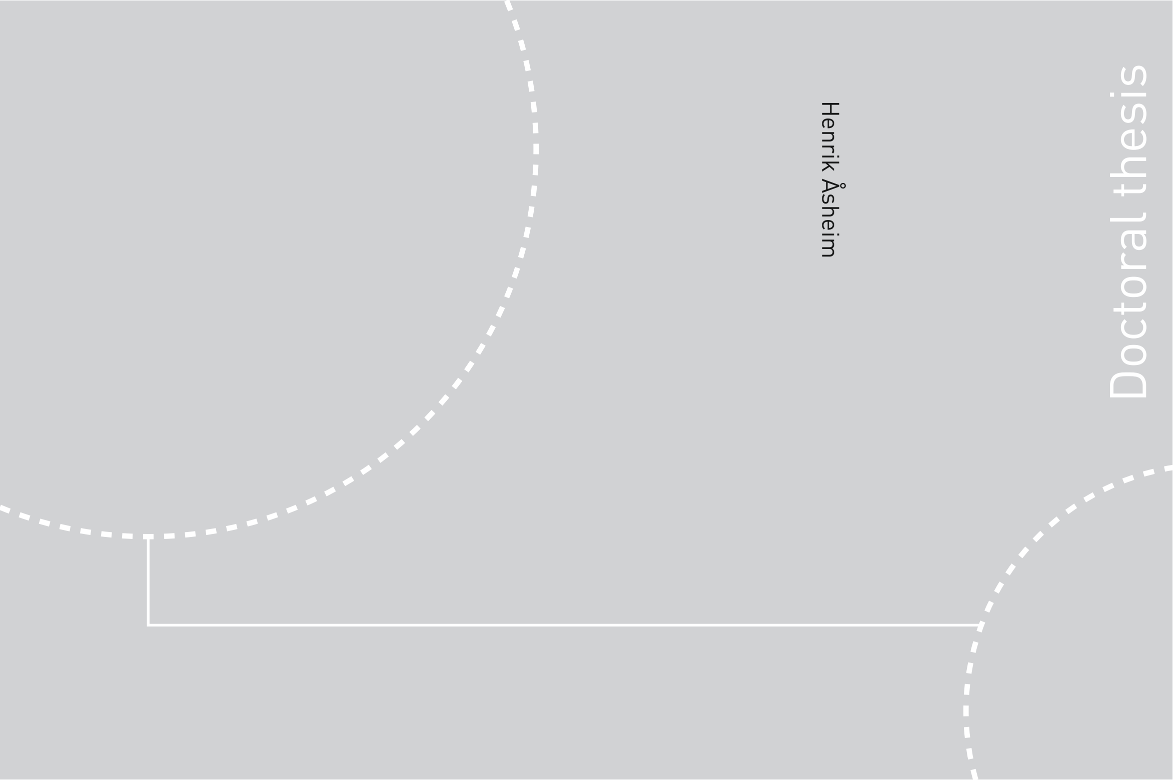

Henrik Åsheim

Doctoral thesis

Doctoral theses at NTNU, 2017:137

NTNU
Norwegian University of Science and Technology
Thesis for the Degree of
Philosophiae Doctor
Faculty of Natural Sciences
Department of Materials Science and
Engineering

NTNU
Norwegian University of
Science and Technology

NTNU

Doctoral theses at NTNU, 2017:137

Henrik Åsheim

PFC Evolution in the Aluminium Production Process

NTNU
Norwegian University of
Science and Technology

Henrik Åsheim

PFC Evolution in the Aluminium Production Process

Thesis for the Degree of Philosophiae Doctor

Trondheim, May 2017

Norwegian University of Science and Technology
Faculty of Natural Sciences
Department of Materials Science and Engineering

NTNU
Norwegian University of
Science and Technology

NTNU
Norwegian University of Science and Technology

Thesis for the Degree of Philosophiae Doctor

Faculty of Natural Sciences
Department of Materials Science and Engineering

© Henrik Åsheim

ISBN 978-82-326-2346-4 (printed ver.)
ISBN 978-82-326-2347-1 (electronic ver.)
ISSN 1503-8181

Doctoral theses at NTNU, 2017:137

Printed by NTNU Grafisk senter

Preface

This thesis is submitted to the Norwegian University of Science and Technology (NTNU) in partial fulfilment of the requirements for the degree of philosophiae doctor. The thesis is the result of research performed during the years 2012 to 2016. Most of the work was conducted at the Department of Materials Science and Engineering, NTNU, with one industrial measurement campaign taking place at Hydro Årdal during a week in 2013.

The thesis is written as a collection of articles, with some already published, while others are intended for publication at a later stage. Additionally there is an introductory chapter presenting a short overview of the aluminium production process and its history, together with a short description of the motivation for this work. A second introductory chapter also briefly presents the methodology used in this work, in addition to some gas analysis and electrochemical measurement techniques.

All the experimental work is presented in Chapters 3 to 8. Chapters 3, 4, 5 and 6 are published according to the following list:

[1] H. Åsheim, T. A. Aarhaug, A. Ferber, O. S. Kjos, and G. M. Haarberg. "Monitoring of Continuous PFC Formation in Small to Moderate Size Aluminium Electrolysis Cells." In: *Light Metals 2014*. John Wiley & Sons, Inc., 2014. 535–539. doi: `10.1002/9781118888438.ch91`

[2] H. Åsheim, T. Aarhaug, E. Sandnes, O. S. Kjos, A. Solheim, and G. M. Haarberg. A Laboratory Study of Partial Anode Effects during Aluminium Electrowinning. *ECS Transactions* **69**(15): 1–12, 2015. doi: `10.1149/06915.0001ecst`

[3] H. Åsheim, T. A. Aarhaug, E. Sandnes, O. S. Kjos, A. Solheim, S. Kolås, and G. M. Haarberg. "Anode Effect Initiation During Aluminium Electrolysis in A Two Compartment Laboratory Cell." In: *Light Metals 2016*. John Wiley & Sons, Inc., 2016. 551–556. doi: `10.1002/9781119274780.ch92`

[4] H. Åsheim, T. A. Aarhaug, W. Gębarowski, E. Sandnes, A. Solheim, and G. M. Haarberg. Partial Anode Effect in a Two-Compartment Laboratory Alumina Reduction Cell. In: *Light Metals 2017*. Ed. by A. P. Ratvik. Springer International Publishing, 2017, 525–532. doi: 10.1007/978-3-319-51541-0_66

Chapters 7 and 8 are presently not published, but may be published at a later stage. The content of the published work and the mentioned chapters is almost the same, although formatting has been changed to better fit the layout of the thesis and some minor corrections have been made for spelling, typos and clarity.

All the individual chapters present the people who has been involved in the authorlist. Generally all writing has been done by me with input from the co-authors. All experimental work was conducted by myself except for the operation of the high sensitity FT-IR used in Chapter 3, which was controlled by Alain and Thor. Additionally, all the wetting experiments of Chapter 8 were conducted in collaboration with Ingrid.

A list of nomenclature used in the thesis is presented in the back matter from page 163.

I believe there is some useful information in the following pages, at least I have learned quite a bit over the past four years, and in many ways that does not show itself in the written text.

Henrik Åsheim

Henrik Åsheim
Halden, February 26, 2017

Acknowledgements

I would like to thank my supervisor, Prof. Geir Martin Haarberg, for providing me with the opportunity of a Ph.D. study. I also very much enjoyed our trips, discussions and the open office policy where one could just pop in for questions.

I would like to thank my co-supervisor Asbjørn Solheim for sharing his vast and long-time knowledge and experience of all the ins and outs of the alumina reduction process.

I also greatly appreciate my co-supervisor Thor Anders Aarhaugs input on gas analysis and equipment and his work in making some apparatus available for my research. Additionally I enjoy our gadget discussions – be it cameras, bikes or other gear.

I wish to thank Ingrid A. Eidsvaag for the extensive work performed with the wetting apparatus.

I would like to thank Espen Sandnes for being the main contact with the industry, i.e. Hydro Primary Metal Technology, and helping the project unfold in its early stages. Additionally I am grateful for feedback on the work, especially on the wetting work with Ingrid.

I wish to thank my room-mate and fellow Ph.D. candidate Jørgen Svendby. It was for the most part off-topic discussions although I consider many of them necessary to the study.

I would like to thank Wojciech Gębarowski for discussions both on topics related to alumina reduction, as well as stuff like computer equipment and electronics. Thanks to you I have a thin wallet from all the electronics equipment I was tricked into buying.

Thanks are also due to all the colleagues and friends at the department of Materials Science and Engineering, NTNU, both former and present. Especially my “Chemistry Hall G” colleagues Camilla Sommerseth and Rebecca Thorne, and the Guitar Hero “gang”.

I also wish to thank Jomar Thonstad for interesting discussions and comments.

I am also grateful to SINTEF Materials an Chemistry and I would notably mention Ole S. Kjos, Henrik Gudbrandsen and Ana Maria Martinez.

I would like to thank Hydro Primary Metal Technology and the Norwegian Research Council for financial support!

A big thank you is sent to Aksel Alstad at the workshop for manufacturing and assembling most of the samples in addition to interesting discussions about “the good ol’ days”.

Finally I would like to thank Hanna and our little daughter Ines – you two are the best! Thanks for having patience with me during this time with some odd and long work-hours. Thanks Ines for always smiling when I get home, making me smile too. I look forward to spending more time with the both of you!

Summary

Improvements in the Hall–Héroult process for electrowinning of aluminium have drastically reduced the anode effect duration, frequency and its associated perfluorocarbon (PFC) evolution, especially over the past 50 years. Not too long ago it was desirable to have at least one anode effect (AE) per cell day to be sure no sludge had formed under the metal pad, however, with the advent of modern process control this became unnecessary and the frequency is today less than 0.1 AE per cell day for modern cells. With improved process control and better analysis equipment PFCs were also found be evolved outside of the traditional AE phenomena, and at normal electrolysis potentials. Albeit small in magnitude, the cumulative emissions could be substantial.

To be able to visualise the phenomena in the laboratory a system with more than one anode was created. It was found that low cell-voltage PFC evolution is not specific to any cell size or technology, but can develop all the way from the large industrial cell with 40 plus anodes and down to the smallest laboratory cell with a single anode. The probability and recurrence are, however, very much related to cell properties such as the number of parallel anodes and electrolyte/alumina mixing. With a smaller cell there is less room for redistribution of current between the parallel segments without an abrupt increase in voltage, and at the extremity of one anode, redistribution can only occur by introducing a current gradient within that segment. Similarly, sheer cell size and electrolyte mixing may further enhance such a redistribution of current. With a lower possibility of redistribution it is less likely with small bursts of PFC from one or a few anodes, and the cell will instead enter the conventional anode effect accompanied by high voltage.

The initiation of the low cell-voltage anode effect looks to develop in the same manner as that of the conventional anode effect with the aforementioned properties of the cell dictating if it will be a passing evolution of PFC, or if it will propagate into a full conventional anode effect.

Anodic passivation potential was found to increase with alumina content in the electrolyte. PFC was in some cases found to be evolved before full passivation, and at the earliest from 2.8 V against the aluminium pseudo-reference electrode. With the increased electrolyte convection observed on a purely vertical sample PFC was not observed until the potential reached 5.2 V. The incipience potential of PFC is in all likelihood somewhat lower as it has been identified that some PFC gets decomposed by the electrolyte, temperature and surrounding materials. This is arguably also why PFC is often not detected until the transition to full passivation develops.

Wetting of graphite under different polarisation regimes were investigated by the immersion/emersion technique. The results show the graphite/electrolyte wetting to improve with polarisation potential, even well past the potential where PFCs could thermodynamically be produced. De-wetting was observed only upon passivation. De-wetting is thus arguably not the cause of an anode effect, although it helps to maintain passivation by making less anode area available for reaction.

Sammendrag

Hall–Héroult prosessen for elektrolytisk produksjon av aluminium har gjennomgått mange forbedringer som har senket både blussvarighet og blussfrekvens, og dets tilhørende utslipp av perfluorokarboner (PFC). Dette gjelder spesielt de siste 50 år med inntoget av billig datakraft for kontinuerlig prosessovervåkning av elektrolysecellene. Tidligere var det ikke uvanlig med bluss på hver celle hver dag – faktisk var det ønsket ettersom dette antydet at det ikke hadde blitt dannet slam av alumina og kryolitt under metallspeilet. I dag er blussfrekvensen under 0.1 anodeeffekter per dag for moderne celler takket være prosessoptimaliseringer og prosesskontroll. Med moderne måleutstyr har en den siste tiden også funnet PFC gasser unnslippe fra cellene selv utenfor det vanlige anodeeffekt fenomenet. Utslippene er små i absolutt størrelse, men det kumulative omfanget kan være stort.

For å undersøke fenomenet i laboratoriet var det nødvendig å lage et oppsett med mer enn en anode. Det ble funnet at lavvolts PFC utvikling ikke er koblet til en spesifikk cellestørrelse eller teknologi. PFC utvikling kan forekomme i store industrielle celler med 40 eller flere anoder, så vel som i den minste laboratoriecelle med en enkel anode. Sannsynligheten for forekomst er strengt koblet til celleutforming og teknologi, slik som antall anoder og aluminadistribusjon i elektrolytten. En liten celle med få anoder vil gi lite rom for en omdistribuering av strøm mellom de parallelle segmentene uten at det oppstår en kraftig økning i cellespenning. I det ekstreme tilfellet med kun en anode, slik det ofte er i laboratorieforsøk, vil omdistribuering av strøm kun være mulig innenfor samme segment. Cellestørrelsen og elektrolyttmiksingen vil kunne forsterke denne omdistribueringen av strøm. Ved lav mulighet for omdistribuering er det mindre trolig med små PFC utslipp fra en eller noen få anoder, i stedet vil kritisk strøm på enkeltelementer overskrides og et konvensjonelt bluss med høy cellespenning vil inntreffe.

Lav cellespennings anode effekt og konvensjonell anode effekt ser ut til å være samme fenomen og begynne på samme måte. Det er utforming og egenskaper ved cellen, samt prosessprosedyrer, som dikterer om det skal bli et forbigående utslipp av PFC, eller om det vil utvikle seg til et konvensjonelt bluss med høy cellespenning.

Anodisk passiveringspotensial ble funnet til å øke med konsentrasjonen av alumina i elektrolytten. PFC ble i noen tilfeller funnet til å bli utviklet før full passivering inntraff, tidligst ved 2.8 V målt mot aluminium pseudo-referanselelektroden. Ved økt elektrolyttkonveksjon på en vertikal anodeprøve ble det ikke sett noen utvikling av PFC før potensialet hadde nådd 5.2 V. Siden PFC kan dekomponere i elektrolytten, av høy temperatur og en del ildfaste materialer er det trolig at utviklingen startet ved et noe lavere potensial. Dette er også formodentlig grunnen til at en ofte ikke ser PFC før full passivering inntreffer.

Fukting av grafitt ved ulike polariseringsbetingelser ble undersøkt ved å senke/heve prøver i elektrolytt mens vekt ble registrert. Resultatene viser at fuktingen grafitt/elektrolytt øker med polariseringspotensial, selv ved potensialer godt over der hvor PFC termodynamisk sett kan produseres. Negativ fukting ble kun observert ved passivering av anoden og det er derfor ikke trolig at denne negative fuktingen er opphavet til anode effekt, selv om den utvilsomt bidrar til å vedlikeholde en passivering, ettersom et mindre areal blir gjort tilgjengelig for kjemisk reaksjon.

Contents

1 Introduction 1

1.1 A brief history of aluminium production 1
1.2 The Hall-Héroult process 2
1.3 Anode effect 6
1.4 Aim and outline of the thesis 11

2 Methodology 15

2.1 Types of experimental work 15
2.2 The electrochemical cell 18
2.3 Gas analysis 19
  2.3.1 Fourier transform infrared spectroscopy 19
  2.3.2 Mass spectrometry 22
2.4 Electrochemical measurement techniques 26
2.5 Thermodynamics 32

3 Monitoring of Continuous PFC Formation in Small to Moderate Size Aluminium Electrolysis Cells 35

3.1 Introduction and theory 36
  3.1.1 Introduction 36
  3.1.2 Background and principle 37
3.2 Experimental 38
3.3 Results and discussion 38
3.4 Conclusions 47

4 A Laboratory Study of Partial Anode Effects During Aluminium Electrowinning 49

4.1 Introduction 50
  4.1.1 Cell and anode voltage 50
  4.1.2 Energy flux at electrodes 52
  4.1.3 Aim 53

4.2 Experimental 53
4.3 Results and discussion 55
  4.3.1 Onset of partial PFC production 55
  4.3.2 Self-termination of partial PFC production 58
  4.3.3 On and off partial anode effect 61
4.4 Conclusions 63

5 Anode Effect Initiation During Aluminium Electrolysis in a Two-Compartment Laboratory Cell 65
5.1 Introduction 66
  5.1.1 Cell and anode voltage 66
5.2 Parallel circuitry 67
  5.2.1 Properties of parallel anodes 67
  5.2.2 Virtual anodes 69
5.3 Methods and equipment 71
  5.3.1 Experimental cell and electrodes 71
  5.3.2 Electrical equipment and data loggers 73
  5.3.3 Gas analysis 74
5.4 Results and discussion 74
5.5 Conclusions 77

6 Partial Anode Effect in a Two-Compartment Laboratory Alumina Reduction Cell 79
6.1 Introduction 80
  6.1.1 Components of the cell voltage 81
6.2 Methods and equipment 82
  6.2.1 Cell and electrodes 82
  6.2.2 Electrical equipment and data loggers 83
  6.2.3 Gas analysis 84
6.3 Results and discussion 85
6.4 Conclusions 91

7 Anodic Passivation of Carbon Materials in Cryolite-Alumina Melts 93
7.1 Introduction 94
7.2 Experimental 95
  7.2.1 Electrical equipment 96
  7.2.2 Gas analysis 98
  7.2.3 Experimental procedures 98
7.3 Results and discussion 99
  7.3.1 Cyclic voltammetry and passivating potentials 99
  7.3.2 Voltammetry and gas analysis 106

7.4 Conclusions 111

8 The Influence of Polarisation on the Wetting of Graphite in Cryolite-Alumina Melts 113

8.1 Introduction 114
8.2 Theory 115
  8.2.1 Surface tension and wetting angles 115
  8.2.2 The immersion-emersion technique 116
8.3 Experimental 117
  8.3.1 Apparatus and equipment 117
  8.3.2 Materials 118
  8.3.3 Measuring sequence 119
8.4 Results and discussion 123
  8.4.1 Wetting behaviour of polarised carbon samples 123
  8.4.2 Wetting during polarisation 128
  8.4.3 Increased passivation time 131
  8.4.4 Increased alumina content 132
  8.4.5 Equilibrium wetting angle 134
8.5 Conclusions 136

9 Discussion 137

10 Conclusions 143

11 Suggestions for Further Work 145

Bibliography 147

Nomenclature 163

List of Figures 167

List of Tables 171

List of Publications 173

Appendices

A FTIR Reference Spectra A-1

B Mass Spectrometer Fragmentation Data B-1

C Thermodynamic Data C-1

Chapter 1

Introduction

1.1 A brief history of aluminium production

Aluminium is one of the most chemically reactive metals, and as a consequence of this it is never found in elemental form in nature, but in an oxidised state in compounds. It is the third most abundant element in the earth's crust (only beaten by oxygen and silicon) and the most abundant metal with a concentration of about 8 wt% [5]. It is found combined in over 270 different minerals, most notably are the different silicates, but other important compounds are oxide hydrates like bauxite [6]. The latter compound, bauxite, is at present the dominating raw material for the industrial production of aluminium.

The first person to be partially successful in separating the metal was H. Davy whom in 1808 used an electrothermic-electrochemical method to isolate small amounts of an Al−Fe alloy which he called aluminium.

An impure form of the metal was obtained by H. C. Ørsted in 1825. He reacted anhydrous aluminium chloride with potassium amalgam subsequently distilling mercury from the product. The metal was reported to have the colour and lustre of tin.

Two years later F. Wöhler produced small amounts of aluminium by heating anhydrous aluminium chloride with metallic potassium, a process which he improved in 1845 by passing vapours of $AlCl_3$ over molten potassium.

The next stage was initiated in 1854 H. E. Sainte-Claire Deville. Sodium was introduced as a reductant instead of the more expensive potassium. The world production of aluminium was 0.96 Mt in 1859 [6].

In 1882 the production of aluminium had reached 2 Mt per annum. It was regarded as a semiprecious metal and for the most part produced by Deville's chemical reduction method [7]. Aluminium was at the time priced to about $12 per pound, while silver was only $15 per pound. In 1886, Charles M. Hall in the US and Paul L. T. Héroult in France independantly discover and patent a nearly identical process for electrochemical reduction of alumina to aluminium metal. Hall's first cell used 8 anodes, had a current throughput of 1800 A and operated at 4 V with external heating [8]. It lasted only six days and produced a total of 13.5 kg of aluminium, giving it an energy consumption of 75 kWh/kg Al with a current efficiency (CE) of 16 %. Subsequent attempts raised the cell voltage to 8 V for heat generation and made changes to the electrolyte to improve alumina solubility. In January of 1889 this cell had an energy consumption of 30 kWh/kg Al and a current efficiency of 78 % [8]. Héroult started with production of aluminium-bronze as it was estimated the market for pure aluminium was too small. The first cell had a single anode that was kept stationary while the surroundings revolved to induce stirring of the melt. The cell was operated at 8 – 10 V and 4000 A, with a very high current density of 6.2 $\mathrm{A\,cm^{-2}}$. The rotating equipment failed in 1890, whereas the cells functioned as before so rotation was henceforth abandoned. Aluminium-bronze was produced with a current efficiency of 75 % and total energy consumption of 37.5 kWh/kg Al. Energy efficiency was improved by increasing the number of anodes to 4 and then eight, simultaneously decreasing current density. Eventually the aluminium-bronze was substituted with production of pure aluminium [8].

Further improvements to energy efficiency was introduced by enlarging the cells, improving the surface to volume ratio, thus reducing the heat loss per unit of cavity volume. Over the years improvements to bath chemistry, heat balance, magnetic field compensation and automatic alumina feeding have all contributed in lowering the energy consumption and increasing the current efficiency. The biggest shift can perhaps be assigned the invention of the computer with continuous monitoring and process control. In modern cells the energy efficiency is around 13 – 14 kWh/kg Al with some smelters even lower. The current efficiency of the best performing cells is around 94 – 96 %, although many smelters, even fairly modern prebake ones, operate down to about 90 % CE due to factors like alumina impurities, phosphorous content and operational practices.

Attempts have been made to replace the process, e.g. direct carbothermic reduction and oxygen evolution on inert anodes. It has successfully withstood any attacks and will likely not be threatened in the foreseeable future.

1.2 The Hall-Héroult process

The process is named after its discoverers whom independently in 1886 developed and patented an electrolytic process where alumina (Al_2O_3), dissolved in an electrolyte of mainly cryolite (Na_3AlF_6), is reduced to liquid aluminium at about 960 °C. In a cell one to several carbon anodes are dipped into the electrolyte and carbon dioxide (CO_2) is discharged from the anodes. Below the electrolyte there is a pool of liquid aluminium contained by a preformed carbon lining and sideledge (frozen cryolite). Aluminium is formed from aluminium-containing ions that get reduced at the electrolyte/metal interface. The overall reaction producing aluminium from dissolved alumina and carbon can then be written:

$$\frac{1}{2}\,\mathrm{Al_2O_3(diss)} + \frac{3}{4}\,\mathrm{C\,(s)} = \mathrm{Al\,(l)} + \frac{3}{4}\,\mathrm{CO_2(g)} \tag{1.1}$$

A sketch of an industrial cell for prebaked carbon anodes is given in Figure 1.1. In addition to the components already mentioned important features are the steel shell and insulating refractories used to ensure proper heat balance, the crust breaker and alumina feeding mechanism and the anode beam of the superstructure that ensures a proper distance between the anodes and metal pad (anode to cathode distance, ACD) [9].

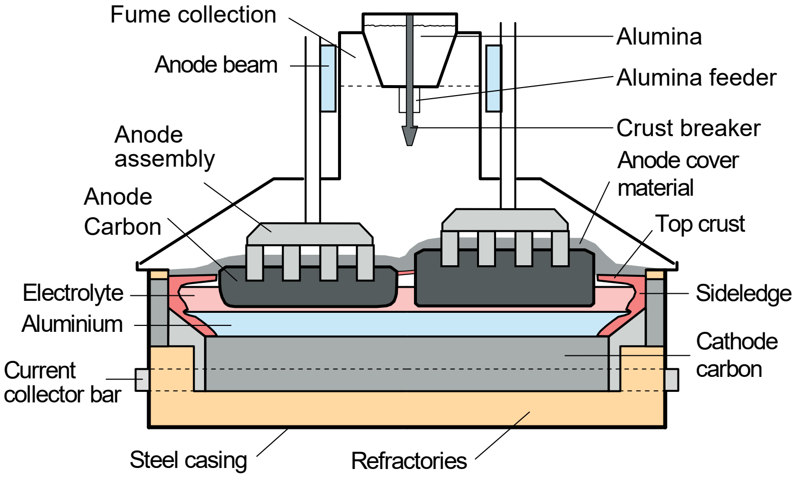
Fume collection
Anode beam
Anode assembly
Anode Carbon
Electrolyte
Aluminium
Current collector bar
Steel casing
Refractories
Alumina
Alumina feeder
Crust breaker
Anode cover material
Top crust
Sideledge
Cathode carbon

Figure 1.1: Schematic illustration of the Hall-Héroult alumina reduction cell for prebaked anodes.

The electrolyte

Cryolite (Na_3AlF_6) is the dominant bath constituent and mainly used for its unparalleled capacity as an alumina solvent. The electrolyte is not consumed during normal electrolysis, but can be partially consumed during anode effect (AE). Losses will still occur from cathode penetration, work processes like anode change, hydrolysis with evolution of HF and vaporisation ($NaAlF_4$) [10, 11]. Most of the evaporation losses will be picked up by alumina in the gas treatment centre (GTC) and fed back to the cell with the secondary alumina. Perfluorocarbon gases does not get captured.

In addition to cryolite modern industrial baths contain about 6 – 10 wt% excess ALF_3, 4 – 6 wt% CaF_2 and 2 – 5 wt% Al_2O_3. Some smelters may also include LiF and MgF_2. Some smelters get bath modifiers like LiF, MgF_2 and KF to their cells from impurities in the alumina. The main purpose of additives is to improve the physico-chemical properties like lower melting point, reduced metal solubility and higher electrical conductivity, lower density and reduced vapour pressure. Additives reduce the melting point and thereby the operating temperature; regrettably they also decrease the alumina solubility [9]. Although with today's automation and modern feeding techniques this is not critical and modern cells are normally far from saturated in alumina.

The modern cell has an interpolar distance of 3 – 5 cm separating the bottom of the anode from the top surface of the molten aluminium cathode. This distance, in addition to passing the current between the electrodes, acts as a heat-generating resistor that is the main component of the self-heating of the cell. The ACD additionally physically separates the anodically produced carbon dioxide from the cathodically produced aluminium metal. Carbon dioxide in the melt will react with dissolved aluminium metal at the cathode/electrolyte boundary layer according to Equation (1.2), denoted the back reaction. The reaction decreases current efficiency as it consumes aluminium, and it also increases anode consumption and accounts for a large part of the carbon monoxide released from smelters.

$$\mathrm{Al(diss)} + \frac{3}{2}\,\mathrm{CO_2(g)} = \frac{1}{2}\,\mathrm{Al_2O_3(diss)} + \frac{3}{2}\,\mathrm{CO\,(g)} \qquad (1.2)$$

Another very important task of the electrolyte, or more specifically cryolite, is to act as container for the cell. Due to the extreme corrosiveness of molten cryolite very few materials can withstand it. Cells are therefore designed to have a certain heat-loss through the sides that assures some cryolite will freeze out and act as a container for the system – the sideledge.

Alumina

Alumina is the raw material for the process and is usually extracted from bauxite through the Bayer process, invented by K. J. Bayer in 1988 [12, 13]. In modern prebake cell cells a crust breaker pierces a hole into the bath and an above alumina hopper doses a specific amount of alumina. This is done on a regular basis often with underfeeding and overfeeding periods. Small additions enhance the ability of alumina to mix with the electrolyte, whereas large additions more easily agglomerate to sludge formations that sink through the metal and down to the carbon cathode blocks. This is also partly why the total alumina content in the electrolyte is kept far below saturation. Low alumina can also be problematic as it risks a change of the anode process that can lead to a full anode effect with high voltages and irregular current distribution. The gas evolved during an anode effect is enriched in the perfluorocarbons (PFCs) CF_4 and C_2F_6 which are unwanted for their high global warming potentials (GWP).

Alumina, often mixed with crushed bath, is furthermore used as a thermal insulator on top of the cryolite crust formed between the anodes to conserve heat. Covering the anodes yields additional heat conservation as well as reduced carbon air burn.

Lastly alumina is used as a dry scrubbing agent for cleaning the anode gas. It absorbs hydrogen fluoride and entraps many fluoride containing particulates like $NaAlF_4$. The chemically inert PFCs are not picked up by the GTC and pass on to the environment along with CO_2. The resulting secondary alumina feeds the captured fluorides and other impurities back to the cell.

The anodes

A feature of the Hall-Héroult process is that the anodes as are consumable and take part in the reaction. Over the years there has been two largely different designs, one where the anodes are baked continuously – the Søderberg anode, and one which employs pre-baked anodes – the prebake technology (see Figure 1.1). Prebake has the advantage of lower carbon consumption per tonne Al and gives a better quality product [5]. Consequently more and more Søderberg plants are closed down and all new smelters employ prebake technology. Prebaked anodes are consumed down to roughly a quarter of their initial size, which usually is an interval of about 22 – 30 days [9]. Prebake anodes are made from fractioned petroleum coke aggregate mixed together with 12 – 15 wt% coal tar pitch binder and baked at around 1200 °E, where °E is the equivalent temperature, which is a measure of baking level frequently used within the industry [14, 15].

The cathode

The cathode consists of prebaked carbonaceous blocks made of anthracite and pitch, blends of anthracite and graphite or of semi-graphitized carbon often connected by carbon glue or ramming paste [16]. Steel bars are placed in slots in the cathode block to extract the passing current. One of the most important tasks for the cathode is to ensure good electrical contact with the aluminium metal pad. Even though the metal pad protects the underlying carbon during operation, the blocks still swell due to sodium and electrolyte penetration. The cathode will ultimately fail, but is nowadays usually exchanged well prior to its expiry date. Relining of the cathode is one of the more costly parts of aluminium production.

1.3 Anode effect

The anode effect can be described as a blockage of the anode that greatly hinders transport of current through the cell, or more specifically between the anode and the electrolyte. The main governor for the occurence of the anode effect is the alumina content in the melt, i.e. the oxide content at the anode/electrolyte interface. Under galvanostatic conditions the conventional anode effect manifests itself as a rapid increase in cell voltage. The increase is usually in the range of 8 to 20 V, but can sometimes reach more than 100 V [9]. Sparks can be seen at high voltages and from about 130 V a continous arc has been observed [17, 18]. Under potentiostatic conditions, the conventional anode effect is observed as an abrupt and massive drop in current density.

The phenomena is not restricted to anodic polarisation of carbon in cryolite melts, but is also present in the electrowinning of neodymium from NdF_3-LiF [19] and can occur in all molten halides [9]. “Anode effect” has also been observed in aqueous electrolysis at very high current densities, however, it was likely caused by the Leidenfrost effect as the electrode became much hotter than the boiling point of the electrolyte, creating a gaseous envelope [20].

Perfluorocarbon generation

During anode effect perfluorocarbon (PFC) gases are evolved in addition to CO and CO_2. The most commonly observed gases are CF_4 and C_2F_6 which can be formed according to the following reactions,

$$Na_3AlF_6(l) + \frac{3}{4}\,C\,(s) = 3\,NaF\,(l) + Al\,(l) + \frac{3}{4}\,CF_4(g) \tag{1.3}$$

$$Na_3AlF_6(l) + C\,(s) = 3\,NaF\,(l) + Al\,(l) + \frac{1}{2}\,C_2F_6(g) \tag{1.4}$$

with a standard potential, E^0, of –2.57 and -2.79 V at 960 °C, respectively. Voltammetric studies performed by Calandra et al. [21] and Qiu et al. [22] show an additional peak between that of CO_2 and the one ascribed to CF_4, which has been attributed to the formation of COF_2. It is seldom reported in the literature, likely because it readily decomposes in the presence of carbon to produce CF_4/C_2F_6 and CO or moisture to produce HF and CO_2. However, it has been observed by Dorreen et al. [23] in the laboratory and by Aarhaug et al. [24] at a smelter plant. The formation of COF_2 can be associated with the following reaction,

$$\frac{1}{2}\,\mathrm{Na_3AlF_6(l)} + \frac{1}{4}\,\mathrm{Al_2O_3(diss)} + \frac{3}{4}\,\mathrm{C\,(s)} = \frac{3}{2}\,\mathrm{NaF\,(l)} + \mathrm{Al\,(l)} + \frac{3}{4}\,\mathrm{COF_2(g)} \quad (1.5)$$

with a standard potential of $E^0 = -1.92\,\mathrm{V}$ at 960 °C. Considering regular production (1.1) has a standard potential of $E^0 = -1.19\,\mathrm{V}$ and an overpotential of about 0.5 V is usually associated with the anode [25, 26], no large potential elevation is needed for PFC generation to become thermodynamically possible. Nordmo et al. [27] has shown that the CF_4 content during AE in pure cryolite reached 90 %, quickly decreasing to 10 % in melts with 1 wt% Al_2O_3. The content of C_2F_6 has industrially been found to often be about 1/10 that of CF_4 on a weight basis [28–31].

For a long time PFC generation was believed to only take place during the conventional anode effect with high potentials and an erratic current distribution. However it is not the whole story. Recently there has been several reports documenting the evolution of PFC gases during aluminium production at normal cell voltages [1, 32–36]. PFC emissions during normal cell voltages are usually small in magnitude, when compared to the traditional anode effect, nevertheless they can be difficult to detect without individually monitoring the current through each and every anode. Thereby the instantaneous emission may pass undetected, possibly making the time-cumulative total very large. In a survey by Marks et al. [35] the median contribution of low cell-voltage PFC emissions was found to be 70 % from 13 smelters in China and 22 % from the 17 smelters outside China. PFC evolution during normal cell voltages are usually localised to just one or a few anodes, likely due to concentration gradients of alumina in the electrolyte, and depending on the circumstances the anode effect may turn back to regular production, or possibly propagate to the rest of the cell, creating a conventional anode effect [37].

Environmental aspects of PFC gases

Appreciable amounts of PFC gases were discovered in the atmosphere in the 1980s. The compounds were found to be powerful greenhouse gases, which exhibited very long lifetimes (10^4 to 10^5 years) [38]. The compounds were also associated with high global warming potentials (GWPs) compared to that of the CO_2 reference, showing values over a hundred year period (GWP_{100}) of 6630 and 11 000 for CF_4 and C_2F_6, respectively [39]. The atmospheric concentration of CF_4 is about 60 ppt to 80 ppt with C_2F_6 1/20 of that, a ratio that has approximately halved over the past thirty or so years [40, 41]. Up until the 1970-80's the aluminium industry was the main anthropogenic source of PFCs [40]. Today this is shared with the emissions from the semiconductor industry which has become a significant contributor, almost on par with the aluminium industry [31]. Emissions from production of rare earth metals are also very large on a per product basis, and the off-gas with today's production technology can contain up to several percent of PFC gases [42]. The annual production of rare earth metals is currently not that large, which limits its total influence.

PFCs have gone from mainly being of academic interest to becoming a large environmental and political issue over the past few decades. Great efforts has been made to reduce both the duration and frequency of anode effects, thus decreasing the magnitude of emissions as evidenced by Figure 1.2.

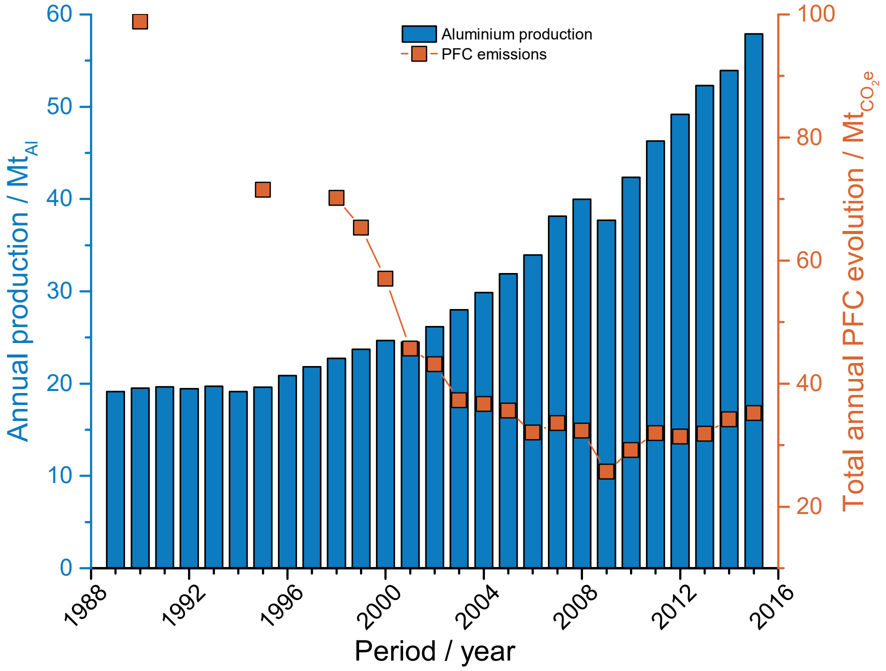

Figure 1.2: PFC emissions from the aluminium smelters together with annual aluminium metal production. Data sourced from [43, 44].

Decomposition of PFC gases

PFCs like CF_4 are often very inert compounds. However, in the presence of certain catalysts it may decompose, even at fairly low temperatures.

Modica et al. [45] observed that CF_4 and also CF_4 diluted with argon decomposed to CF_3, CF_2 and F at temperatures above 1900 °C in the pure gas state. Rogers et al. [46] observed a reaction between CF_4 and steel and tungsten at 1000 °C and White et al. [47] demonstrated the reaction of C_2F_6 with silica even down to 600 °C, producing CO, CO_2 and SiF_4. Thonstad et al. [48] has shown that the conversion of CF_4 over activated alumina begins at about 500 °C and Castellano et al. [49] found that 26 % of CF_4 was transformed into CO_2 when passing through a cryolite melt enriched with 2 wt% Al_2O_3. The latter two works likely by the following reaction,

$$\mathrm{CF_4(g)} + \frac{2}{3}\,\mathrm{Al_2O_3(diss)} = \mathrm{CO_2(g)} + \frac{4}{3}\,\mathrm{AlF_3(diss)} \tag{1.6}$$

which is strongly displaced to the right ($\Delta G^0_{960\,^\circ\mathrm{C}} = -379\,\mathrm{kJ\,mol^{-1}}$) [50]. CF_4 may also hydrolyse in a similar manner to that of COF_2 as shown by the following reaction,

$$\mathrm{CF_4(g)} + 2\,\mathrm{H_2O\,(g)} = \mathrm{CO_2(g)} + 4\,\mathrm{HF\,(g)} \tag{1.7}$$

which is again strongly shifted to the right ($\Delta G^0_{960\,^\circ\mathrm{C}} = -411\,\mathrm{kJ\,mol^{-1}}$). Conversion of CF_4 through this mechanism was shown by El-Bahy et al. [51] to approach completion on several metal–aluminium-oxides with a H_2O/CF_4 ratio of 51/1 and 680 °C.

Anode effect terminology

Before the discovery that PFCs could be produced under seemingly normal cell conditions one needed just relate to the term *anode effect*, and this was the condition where a large elevation of potential was observed, in addition to erratic current distribution between the anodes of the industrial cell. Guidelines were put up by the industry that the voltage had to pass a certain voltage threshold for a specific amount of time before an anode effect was declared and countermeasures were implemented to terminate it. Two common thresholds used are that the voltage needs to be above 8 V or 10 V for more than 3 s before it is declared as an anode effect, the latter likely to keep the automated termination system from acting on voltage noise or a very short spike.

From an industrial point of view this is probably a reasonable way to log the performance of a cell and keep track of emissions. However, scientifically, the difference between cell events of i.e. 9 V for 2 s and 9 V for 4 s can be disputed. With thresholds of 8 V and 3 s only the last would be registered as an anode effect and with thresholds of 10 V and 3 s none would be registered.

In the following an *anode effect* will be treated as a condition where the anode undergoes a different reaction than the regular one, possibly an undesired reaction, and not necessarily a passing of a voltage/time trigger. As long as a fraction of the passing current is used to produce PFC the author considers the term warranted, although usually described as *partial anode effect* when it just amounts to a small part of the total reaction. The term *local anode effect* can be considered a synonym, as an anode effect can be local to a certain part of an anode, although more used when talking about anode effects in an industrial cell local to one or a few anodes. The terms *conventional anode effect* and *traditional anode effect* are here used interchangeably to cover the phenomena where most of the anodes, if not all, are on anode effect accompanied by high cell voltage and erratic current distribution. The term *Full anode effect* is used to describe the same phenomena, but most often used when just talking about one anode that has a high current, often oscillating and accompanied by a high production of PFC gas(es).

The terms *background PFC* and *continuous PFC* is at the time of writing considered unwise to use as they imply that some PFC is always produced and evolved from a cell. While this might be the case and tiny concentrations of PFC are evolved from the cells all the time there is little evidence to support such an assumption.

Low cell-voltage PFC (LCV–PFC) or *low cell-voltage AE* (LCV–AE) is the term that has been settled on to describe PFC emissions that occur outside the main anode effect phenomena (conventional/traditional/full AE). The term is long and heavy and we can all just hope it will be improved upon in the future. This anode effect and PFC evolution takes place at seemingly normal cell voltages. Having the word “cell” in the term is important because otherwise it would imply the anode to be at low voltage. The anode potential is in fact elevated and this is one of the reasons why production of PFC can occur.

When an anode becomes *passivated* or *blocked* it means that it almost does not pass any current relative to initial conditions because of increased resistance towards reaction. The wording is most relevant under conditions where there is a cap on the voltage a system can supply. *Partial passivation* refers to degrees of passivation where current throughput is something in between that of regular production and full passivation.

It must be said that terminology has been a thought process and there has been a change of wording, and hopefully also precision, over time from one chapter to the next. As an example the term “non-anode effect PFC” (NAE–PFC), much used in Chapter 3, would not have been used now as the reasoning above requires an anode effect to produce PFC. Many of these terms have not been updated because it is the author’s belief that the educated reader will understand what is meant from the context and presented figures, as well as to try and keep the chapters consistent with the published articles.

Anode effect termination

When an anode effect has been declared most modern smelters act by automatically introducing quite a bit of alumina to the bath. Too little alumina is one of the main causes of an anode effect. To facilitate stirring the bath is agitated by moving the anodes further down in the bath. Shorting the anodes with the metal helps to "clean" the anode base and prepare it for normal electrolysis. The procedure in which the busbar and attached anodes is lowered is something that can vary from smelter to smelter.

Sometimes the automated procedure has trouble extinguishing the anode effect. It is then common to manually stir the bath under the anodes using wooden poles or compressed air.

An anode effect, especially a low cell voltage AE, can also self terminate without any help from either an automatic procedure or manual labour. Reasons can be anything from improved convection, improved alumina distribution, work practices, etc.

1.4 Aim and outline of the thesis

Aim and motivation

One of the areas of improvement in the alumina reduction process is the anode effect phenomena and the related emission of PFC gases. In later years these emissions have become of political interest, and at about the same time the industry discovered that the evolution of perfluorocarbons were not just a property of the conventional anode effect, but could also take place outside this phenomena. For quite some time it was by many believed that the low cell-voltage anode effect was only a property of large cells with high amperage (>300 kA). A partial goal of this work was to investigate and discuss if this was a sound differentiation.

The main motivation of this work was to investigate if the low cell-voltage anode effect could be reproduced in a laboratory setting and try to discover the mechanism behind this phenomena, and if/how it differed from that of the conventional anode effect.

To broaden our understanding of the anode effect it was also decided to conduct a series of experiments that affected or were affected by an anode effect and record the results. In the present case this comprised voltammetry with and without gas analysis on carbon samples in a cryolite melt, as well as electrolyte/anode wetting by moving carbon samples in and out of the electrolyte while recording the forces acting on the samples with a load cell.

Outline

In Chapter 3 the occurrence of PFC evolution not related to the conventional anode effect is presented for a small industrial smelter with an amperage of about 200 kA. A few cells were perturbed to better facilitate the PFC production, but not in a way that could not have occurred naturally. Production gas from a train of 28 cells were measured with a high sensitive FTIR.

Chapter 4 presents the two-compartment cell with two anodes connected in parallel. The chapter treats partial anode effects with a small redistribution of current as well as the different heats produced at the anode by regular and anode effect electrolysis.

Chapter 5 treats the onset and self-termination of partial PFC in both an industrial cell and a laboratory cell, and discusses why the likelihood of seeing this behaviour in a regular laboratory set-up with one anode is so low. Additionally the chapter provides suggestions on how to better observe the phenomena. It is meant as a theoretical document describing the concept of virtual anodes as electrical load elements in parallel with real anodes that in some way can be used to simulate the large multi-anode industrial cell. No results with the new set-up had at the time been produced and are thus not present, however discussions of results from related set-ups are provided.

Chapter 6 uses the two-compartment cell with two real anodes and a series of electric resistive elements connected in parallel to produce both partial anode effects with little PFC production as well as full conventional anode effect (if only on one anode) with a high fraction of PFC produced. This was accomplished by varying the number of virtual anodes, and by extension the drive to push current through the real anodes.

In Chapter 7 voltammetric techniques are used together with gas analysis to investigate when passivation of an anode occur and what affects it, as well as recovery from a passivated condition. Additionally, single anode experiments treat the evolution of PFCs from partial passivation, before an anode is fully passivated.

Chapter 8 treats the effect polarisation has on the wetting properties of graphite anodes towards the electrolyte. The immersion/emersion technique was employed, making it possible to detect the full wetting hysteresis of the samples. Wetting was performed on samples that was treated to regular electrolysis as well as passivation to investigate its relation to the anode effect and PFC production.

Chapter 2

Methodology

The true mechanism behind the anode effect has troubled the aluminium business for about 130 years and is still not fully understood. Most agree that the alumina content in the electrolyte is one of the major constituents, if not the governing one, although the true initiating factor is disputed.

With the discovery of PFC gases being evolved outside the traditional anode effect phenomena in industrial cells it was questioned if this was a completely different phenomena entirely, as nothing similar had been discovered in controlled laboratory experiments, save for a PFC shoulder sometimes discovered a few minutes before the conventional anode effect initiated – a feature quite common to industrial anode effects as well.

2.1 Types of experimental work

Low voltage PFC emissions from low amperage industrial cells

An industrial measurement campaign was undertaken at a plant with cells running at about 200 kA. Measurements were performed on a train of 28 cells with an FTIR that is able to detect CF_4 down to the some ppb (even to about 100 ppt under ideal laboratory conditions). To increase likelihood of observing PFC emissions at normal cell voltages some cells were disturbed, e.g. by having one alumina feeder turned off. One of the resulting figures also compare it to PFC release from a laboratory experiment with one anode before the full anode effect eventually initiates.

Simulating low cell voltage PFC evolution

When comparing a circuit diagram of a large industrial cell with many anodes, with the same diagram of a typical single-anode laboratory set-up several realisations were made. Industrial anodes vary their current pull over their lifetime, often low when newly inserted before attaining an average current and slightly increasing towards their “end of life” after the anode slots have been burned off [37]. This is opposite what one would expect from higher bubble resistance, nevertheless, the effect is attributed to the increased surface area that appears and the decreased linear wear rate, lowering the ACD. With such a current profile the individual anode potential will also vary as ohmic potential drops within an anode circuit-segment vary with current. This phenomena is difficultly realised with just one anode under constant current conditions, which is the case for most laboratory set-ups, as there are no other anodes to divert current to. Some redistribution of current may take place within an anode block, however, this too is mostly applicable to the large industrial anodes. There is little room for large alumina concentration gradients within the electrolyte of most laboratory set-ups with a single anode. Additionally the cell voltage of an industrial and a laboratory cell is often plus/minus 4 V and plus/minus 2 V, respectively; meaning the anodes, or areas of an anode, are able to approach the same potential values with current redistribution. This is far past PFC producing potentials for the industrial case, while still being below direct PFC production for the laboratory cell.

Another important parameter is how the electrical energy being introduced to the system is controlled. Industrial cells are provided a constant flow of current, although the anodes can likely best be described to be under pseudo constant voltage control, as all the different anode circuit-segments observe the same potential. The individual anode potential will however vary with parameters like anode age, interpolar distance, local electrolyte composition, etc. Such changes will distribute the current unevenly over the anodes and elevate the potential, the extent to which is proportional to the aforementioned parameters and inversely proportional to the number of anodes. This mode of power delivery cannot easily be realised in a laboratory cell with a single anode. When approaching alumina depletion under constant current conditions the voltage will rise to very high values to account for the increased resistance towards reaction. Under constant voltage conditions the same approach to alumina depletion will be met with reduced current throughput, possibly no throughput depending on the voltage set-point.

To investigate the low cell potential PFC evolution in the laboratory a set-up with two anodes connected in parallel were constructed. The anodes shared the same cathode and had the ability to employ dissimilar electrolyte compositions.

The anode potentials were elevated to industrial levels by wire wound resistors or electronic loads. Additionally, electronic loads were connected in parallel with the anodes to increase the degree of parallel elements. Gas analysis equipment, both mass spectrometers and Fourier transform infrared spectrometers were used to detect when PFC gases were evolved from the anodes.

Some of the first experiments had two anodes in parallel with a resistor added to each parallel circuit to elevate the cell potential to industrial levels (Chapter 4). It was realised that this set-up could be improved to better mimic the industrial cell by introducing an electronic load in parallel, which could act as a series of "virtual anodes". The theory behind this and the why the approach is beneficial for the discovery of low cell-voltage PFC in the laboratory is the main focus of Chapter 5. The chapter also includes some results from initial gas measurements on the two-compartment cell.

With the electronic load as a balance and gas analysis attached experiments were conducted, but the PFCs were mostly absent from the gas analysis, save for a small peak encountered at the transition to full passivation. It was believed that the low current kept the PFC concentrations below the detection limit so anodes were exchanged for larger ones and a more powerful power supply and electronic load was also equipped. These experiments are the focus of Chapter 6.

Passivation potentials of carbon materials in cryolite-alumina melts

The passivation and reactivation of carbon materials were investigated by cyclic voltammetry, linear sweep voltammetry and potentiostatic stepping. In some of the experiments reaction gases were sampled and measured close to the anodes to determine at which potential detectable amounts of PFC were produced, and if it occurred before full passivation. Experiments that incorporated gas analysis were only conducted in 1 wt% Al_2O_3 melts, whereas voltammetric studies were performed in a few different electrolytes with alumina content ranging from 1 wt% and up to alumina saturation. The samples consisted of graphite with only vertical surface area ($\sim$50), graphite rods with both vertical and horizontal surface area ($\sim$10) and glassy carbon with only vertical surface area (2). Due to the difficulties of manufacturing vertical samples of glassy carbon they had to be reused in the different melts, manually adjusting the surface area for the already reacted carbon.

Wetting of graphite in cryolite-alumina melts

Wetting of carbon based anodes for the aluminium industry is for the most part performed by the sessile drop method in which a droplet is placed on a solid surface and the contact angle can be measured visually, or with a camera and image software, and a static contact angle can be observed. In this work the wetting of graphite samples were investigated with the immersion/emersion technique. This method provides the ability to measure wetting at dynamic conditions, as well as measuring with applied polarisation. It is performed by the use of a load cell to report the weight change observed by a sample when lowering and raising it in a liquid. By correcting for the buoyancy exerted by the liquid the wetting weight of the load cell can be converted to a corresponding contact angle. Different angles will be observed from the immersion and emersion part of the experiment, making up the contact angle hysteresis. Samples may also approach an equilibrium angle. With the ability to apply polarisation, it becomes possible to determine how this affects the contact angle, and what happens to the contact angle when anode effect and PFC production is approached. The experiments were conducted in a variety of different melt compositions with alumina content ranging from 1 wt% to 12 wt% (supersaturated) and in total about 20 inverted cup samples and 10 vertical samples were used.

2.2 The electrochemical cell

The study of any electrochemical reaction requires a few key ingredients such as electrodes, an electrolyte and a cell container. For production of aluminium by reduction of alumina material selection is of particular importance as the current production reaction takes place at high temperature and all materials should be able to sustain a temperature of at least 1000 °C. The electrolyte is in most cases based on a variant of cryolite (Na_3AlF_6) with some weight percent additions of the alumina (Al_2O_3), the raw material for the reaction, and possibly other elements to alter the physical and chemical properties of the melt. As the alumina is consumed in the process it is sometimes necessary to replenish it and this is done through a tube that is inserted through the lid and down to about 3 cm above the molten electrolyte. When the theoretical alumina content is quoted in later chapters this expresses the difference between initial value and that consumed by the passing current (generally assuming CO_2 as the anode product).

The cathode, the negative electrode, is where the aluminium metal is produced. In high-temperature molten salts experiments in the laboratory the cathode is often combined with the cell container. With such a combination it is paramount that the container can act as a conductor at the working temperature. Graphite is most often used and it is an excellent conductor with high inertness to most chemical attacks.

The anode, the positive electrode, is where the gas reaction products are produced. The current production process demands an anode made out of carbon as it is consumed. Industrially this is a blend of different cokes with a binder like coal tar pitch, however, the laboratory offers the possibility to work with other carbon materials like graphite or vitreous carbon (glassy carbon, GC). Such materials are much more homogeneous and, even though they will never replace the coke blend industrially, can still provide good information about how carbon behaves under different perturbations. It is also possible to play with size and shape to alter e.g. bubble flow and investigate its influence on the process.

Many electrochemical cells also incorporate what is known as a reference electrode. While it is not technically necessary for the system to work, it can provide valuable information regarding the different anode and cathode reactions (potentials) and not just the system as a whole. The reference electrode does not take part in the reaction and can be regarded as an observer. In water electrochemistry there are many good references with well defined and stable potentials, but the list is less populated in high-temperature molten salts. In molten fluorides the aluminium pseudo-reference is commonly used. It does not have well defined potential and one has to rely on empirical data.

This small section just provides some general thoughts on what is common practice at NTNU of cell and material set-up in aluminium electrowinning from high-temperature molten salts. It is referred to the specific chapters for other details.

2.3 Gas analysis

2.3.1 Fourier transform infrared spectroscopy

Fourier transform infrared spectroscopy (FTIR) is a technique that can tell what molecules are present in a sample and their concentrations. When light (electromagnetic radiation) passes through matter it may be absorbed and the degree of absorption will vary with both matter and wavelength/frequency. The first infrared (IR) measurement was conducted in 1881 and some 20 years later the first infrared spectrometer was constructed [52]. Michelson [53] published a paper describing the two-beam interferometer already in 1891, however, the computing power to perform the Fourier transform and other technical difficulties had to be overcome. The first commercial FTIR were pioneered by Digilab (now part of Agilent/Keysight) in 1969 [54]. Being able to measure absorptions at all wavelengths simultaneously (as opposed to sequentially at each wavelength) had huge advantages like reduced measurement time and better signal-to-noise ratio [55].

Properties of light

An important property of light is the wavelength which describes the distance travelled per cycle. Different types of light waves come at different wavelengths. Visible light have wavelengths of about 400 nm to 700 nm, while infrared extends from the red edge of visible light (700 nm) all the way up to 1 000 000 nm. When working with several types of electromagnetic radiation it is common to use the wavenumber (which is reciprocal to wavelength) measured in inverse centimeters (cm^{-1}) as this property is proportional to energy according to the Planck–Einstein relation:

$$E = h\nu = h\frac{c}{\lambda} = hcW \tag{2.1}$$

where E denotes energy, h is Planck's constant (6.63×10^{-34} Js), ν is the light frequency, c is the velocity of light ($\sim 3 \times 10^{10}\,\mathrm{cm\,s^{-1}}$), λ is the wavelength and W the wavenumber.

When light is passed through a sample some it its radiant power may be absorbed and what is transmitted through can be expressed as:

$$T = \frac{P}{P_0} \tag{2.2}$$

$$\%T = T \cdot 100\% \tag{2.3}$$

where T is the transmittance, $\%T$ is the percent transmittance, P_0 is the incident radiant power and P is the radiant power leaving the sample. Even though transmittance is what is actually measured by the equipment it is the absorbance that has the closest link to physical concepts as will be shown below. The absorbance, A, is related to the transmittance by the following relations:

$$A = \log_{10}\frac{1}{T} = \log_{10}\frac{P_0}{P} \tag{2.4}$$

$$A = \log_{10}\frac{100}{\%T} = 2 - \log_{10}\%T \tag{2.5}$$

The absorbance is also proportional to concentration according to the Beer–Lambert law:

$$A = \epsilon l c \tag{2.6}$$

where ϵ is the absorptivity of species, l is the beam path-length through the species and c is the concentration of the species. The infrared spectrum recorded for a certain sample is unique and can be regarded as a “fingerprint” for that sample. This property can be used to identify unknown species [56]. Calibration with references of known concentration makes it possible to extract quantitative data of the measured samples. Even though the Beer-Lambert law states the relationship between concentration and absorbance to be linear it is in practice subjected to certain deviations. At higher concentrations absorbing species tend to interact with each other and the refractive index of the medium can be altered. This tends to attenuate the absorbance producing a lower absorbance than expected from the concentration. At very high absorbances (> 2) the signal becomes saturated because the equipment detector is unable to detect the differences in light transmittance, as shown in Table 2.1. Often shoulders of peaks, smaller peaks and harmonics needs to be considered to obtain an accurate concentration from the absorbance of such a sample. Additionally, if the sample contains species with overlapping or partially overlapping absorbance bands this will need to be considered as well. A list of some infrared gas reference spectra that can be encountered during aluminium electrolysis is provided in Appendix A.

Table 2.1: Absorbance and its corresponding transmittance.

Absorbance (optical density)	Percent light transmittance
0	100
1	10
2	1
3	0.1
4	0.01
5	0.001

Many newer instruments have algorithms built in that uses a large set of reference data for different compounds at different concentrations that provides an estimate of the concentrations of the specie(s) in the sample, and not just the infrared absorbance spectrum. In many cases this can give quick and accurate results for common compounds such as CO_2 and H_2O, but will often fail at detecting and quantifying exotic compounds like CF_4 or COF_2.

Gas response time

A established way to measure the response time of a gas is with the T_{90}-response method. This is the time it takes for a known amount of a sample gas to travel from its source to being detected at 90 % of its peak value at the detector. This time will be dependant upon parameters such as travel length, gas flow, instrument volume and beam path length. This value of the T_{90}-response can be quite different from the time it takes until a sample is just "detected".

FTIR equipment

Table 2.2 lists the different FTIRs that has been used in the investigations carried out during this work. The Bomem MB–154 was used during the industrial meausurements of Chapter 3. It has a very long beam path which makes it able to detect very low concentrations. This is beneficial when measuring on trains of industrial cells with heavy gas dilution. The IR measurement cell also has a large volume that decreases gas dynamics.

The Gasmet CR 4000 has been used in the work of Chapters 5 and 6. The resolution is a bit low and that can make it difficult to use if the samples contain species that absorb in the same region. The ProtIR 204M was often not available and is just present in the work of Chapter 6. It has a nice resolution and broad spectral range, but has a longer response time and fall-off time due to the larger volume.

In the present experiments (especially the industrial) water can be a "contaminant" to the IR spectrum. It can for the most part be filtered out with a desiccant such as Drierite® which is employed in the gas pathway. Similarly HF can be filtered by introducing activated alumina in the pathway and particle filters may also be employed. One should be aware that filters might also catch other constituents than the intended.

Table 2.2: Properties of the different FTIRs.

Parameter		Bomem MB–154	Gasmet CR 4000	ProtIR 204M
Cell volume	/ l	11[1]	0.4	2.7
Path length	/ m	35[1]	5	6.4
Spectral range	/ cm^{-1}	500 – 12000[2]	600 – 4200	400 – 8000
Resolution	/ cm^{-1}	1 to 64 (2X)	8	1
Absorbance		0 – 3	0 – 3	–2 – 4
Detector		DTGS/MCT–LN2	MCT–LN2	MCT–Peltier

[1] With infrared sample cell 35-V-FXD-H.

[2] Range depends on detector and optics.

2.3.2 Mass spectrometry

Mass spectrometry (MS) is a powerful technique for the study of molecular structures and the identification of unknown substances [57]. Some applications of MS include determining steroids in athletes and metals and other impurities in water and foods. Other applications include atomic physics, inorganic chemical analysis, determination of thermodynamic parameters and many others.

Principles

The basis of MS is the generation of of gas-phase analyte ions, the separation of these according to their mass-to-charge ratio (m/z)[1] and subsequently the detection of these ions [58]. It is essentially a special technique for the “weighing” of molecules.

There is typically five steps to an MS experiment: (i) sample introduction, (ii) analyte ionisation, (iii) mass analysis, (iv) ion detection and (v) data processing and interpretation of the results. A high vacuum (pressure $\leq 10^{-5}$ mbar) is required for mass analysis and ion detection, whereas analyte ionisation may take place at either hight vacuum or at atmospheric pressure. The latter option does, however, require a vacuum interface to transfer the ions into the high-vacuum mass analyser part of the equipment.

In its basic operation samples are introduced into the instrument, often on-line as a continuous flow. Neutral molecules are further ionised and accelerated into the mass analyser. The mass analyser is the heart of the mass spectrometer, which separates ions in either space or time according to their mass-to-charge ratio. After the masses are separated they are detected and the signal is passed on to the data system for analysis. Data are often collected in one of two different ways. In a *total-ion chromatogram* (TIC), the sum of the ion counts in the individual mass spectra is plotted as a function of time. A slice of this data matrix represents a *mass spectrum* of a particular selected period of time and such a spectrum of CF_4 can be viewed in Figure 2.1. In an *extracted-ion chromatogram* (XIC) only the counts for specifically selected m/z are recorded. In instruments providing unit-mass resolution the selection window is in most cases $\pm 0.5\,m/z$ units (u), whereas with high-resolution instruments it can be very much less. Also important for the signal detection is the time delta the detector spends on one m/z value (usually ≤ 1 s). This is especially important if different time deltas have been selected for the different m/z values under study, as this will change the proportions between the signals.

---

[1] By convention m is the numerical value of the mass of the ion and z is the numerical value of the ion charge. The unified atomic mass (u), and the elementary charge (e) are used for these values. The unified atomic mass unit is equal to 1/12 of the mass of an atom of the nuclide ^{12}C (In many texts the non-SI unit (amu) is still used). The unit z describes the number of elementary charges lost (or gained).

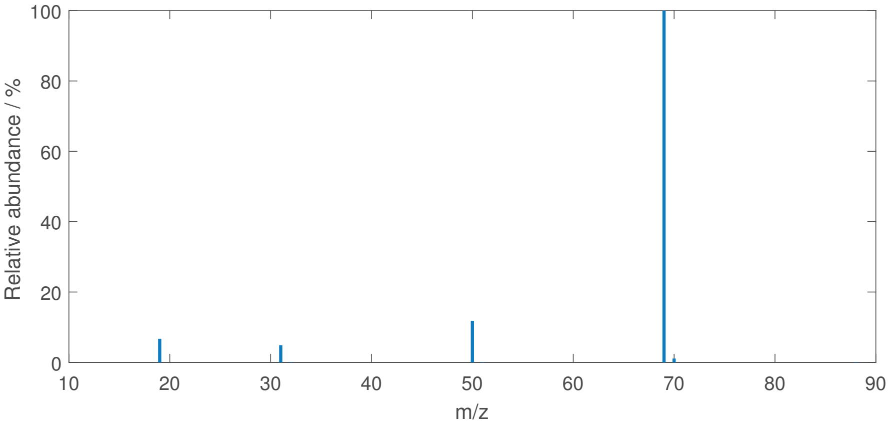

Figure 2.1: Mass spectrum of CF_4. The main peak occurs at m/z 69, which is fragment ${CF_3}^+$. Fragments ${CF_2}^+$, CF^+ and F^+ are visible at m/z values 50, 31 and 19, respectively. Data adapted from NIST [59].

Resolution

Most people in the MS community define resolution as $m/\Delta m$, where m is the mass of the ion (and should be read as m/z) and Δm can be either the peak width usually measured as full width at half-maximum (FWHM), or the spacing between two peaks of equal intesity with a valley of for example 10 % [60]. This definition of resolution is however mostly interesting for high-resolution instruments as the FWHM is virtually constant over the entire mass range for unit-mass-resolution instruments.

Mass calculation

There are different ways to calculate the mass of a molecule, an atom or an ion. For stoichiometric calculations in general chemistry the weighted average of the atomic masses of the different elements that make up the molecule, atom or ion is used. In mass spectrometry the nominal mass of the monoisotopic mass is often used. This mass is calculated using the mass of the most predominant isotope of the different elements, then rounded to the nearest integer value. The exact masses of isotopes are not exact whole numbers and differ weakly from the summed mass values of protons, neutrons and electrons, due to the binding energy that holds the particle together. Thus, every isotope has a characteristic and unique “mass defect”. The monoisotopic mass accounts for these mass defects as it is calculated by by the use of the exact mass of the most predominant isotopes of the constituent elements [61]. In general, the monoisoptic mass is used when it is experimentally possible to distinguish the isotopes, whereas the average mass is used when they are not distinguishable. The use of the nominal mass is usully not recommended for anything but low-mass compounds containing only C, H, N, O and S [61].

Fragmentation

When a molecule is bombarded with electrons the molecule tends to fragment into a cation and a radical. Smaller molecules tend to obtain just a single charge, however, higher charge values can be obtained with larger molecules. Molecule fragmentation depends on particle density, electron emission current, electron ionisation energy, material and filament temperature and cross-section and path-length for molecule ionisation [62]. Hence, even though the possible fragmentations of a molecule is specific for that molecule the relative intensities of the fragmented ions will vary with instrument and work-parameters and needs to be treated with caution [63, 64]. An example of a fragmentation pattern for CF_4 is presented in Figure 2.1. The nature of the fragmentation of molecules in MS can introduce many detection interferences of compounds, especially with unit-mass-resolution instruments. The gases CF_4 and C_2F_6 e.g. both have their base peak at m/z 69. Fragmentation data of some relevant compounds to aluminium production is provided in Appendix B.

Instruments

Historically the sector instrument was at the basis of all MS developments [58]. Ions with mass m and charge z are accelerated with a voltage V into a magnetic field of flux B. The ions are deflected to a path with radius curvature r. The following equation can be derived for the relationship between the parameters:

$$m/z = B^2 r^2 e/2V \tag{2.7}$$

The equation indicates that the separation of ions with different m/z can be achieved in a few different ways. With constant V and B, ions of different m/z will produce different curvature r and be separated in space, while varying either V or B ions of different m/z are separated in time. The latter case gives the possibility to detect ions one after another from a single-point detector at a fixed position behind a slit [61]. Better resolution of the sector instrument is facilitated by combining the magnetic sector with an electrostatic analyser. The quadrupole analyser is a device which uses the stability of the trajectories in oscillating electric fields to separate ions according to their m/z ratios. It consists of four hyperbolic- or circular-shaped rods that is placed perfectly parallel in a radial array. Rods opposite to each other are charged by either a positive or negative direct potential (DP) with a superimposed radio frequency (RF) potential. At a given DP/RF combination only the ions of a particular m/z show a stable trajectory through the quadrupole towards the detector. Other ions will hit the quadrupole rods and be eliminated. The quadrupole can resolve m/z up to about 3000 u, although many instruments are limited to 100/200/300 u. Table 2.3 list the specifications of the quadrupole instrument used in Chapters 5 and 7.

To protect the instrument it is common to introduce filters for particles and certain gases. In the present experiments particle filters were employed when the MS was engaged. Due to the fairly dry nature of the experiments the MS took part in, and the low gas throughput, H_2O and HF filters were omitted.

Table 2.3: Properties of the mass spectrometer used in the work.

Parameter		Pfeiffer QMS 200 (Prisma ^{TM})
Mass range	/ u	1 – 200
Detector type		Channeltron / Faraday
Detection limit	/ mbar	$< 10^{-14}$ / $< 10^{-11}$
Unit resolution	/ u	0.5 – 2.5
Operating pressure	/ mbar	10^{-4}
Filament		Thoriated iridium
Gas pump speed	/ ml min^{-1}	20

2.4 Electrochemical measurement techniques

The different electrochemical measurement techniques used in this work are described in the following. The techniques are well established and used in many different fields. The measurements have been performed by either a linear rectifier (power supply unit, PSU), working in constant current mode, or with a potentiostat. In the first case the system has sometimes been modified by the addition of an electronic load in the circuit. Data logging has been conducted by an external unit, or in the case when a potentiostat has been used it has performed its own logging. All electrochemical techniques work by controlling the potential and recording the current response, or vice versa. It is very convenient that the both the system perturbation and the response are electrical signals and this is the basis for the high speed and accuracy of the readings [65].

Chronopotentiometry

Chronopotentiometry (CP) is a technique were the current is controlled and the potential response is measured over a set duration. This method can easily be expanded to include two or more current steps and is then often denoted as double step or multi step chronopotentiometry. For work where the duration of an experiment is of secondary or little importance it is not uncommon to say that the work is being conducted under constant current (CC) conditions. This is often the case when a rectifier is being used as the current source. An example of the most basic CP technique is provided in Figure 2.2.

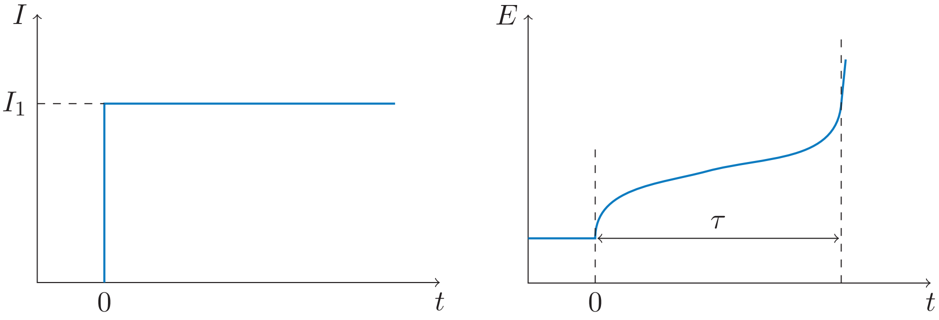

(a) Current step (b) Resulting potential response

Figure 2.2: Example of a single step chronopotentiometry. (a) The current is stepped to I_1 and kept at this value. (b) The reaction set forth by the current creates a potential response. As time passes the potential increases to keep up with the current and the diminishing number of reactants at the electrode surface. Eventually, when the flux of reactant is insufficient the potential will shift to higher values, possibly initiating another reaction to keep the current flowing. The transition time, τ is a characteristic parameter and denotes the time until this shift occurs.

Cyclic voltammetry

Cyclic voltammetry (CV) is a technique where the potential is swept at a fixed rate (sweep rate / scan rate) between two potential limits (vertex potentials) for a given number of cycles. The start and end potential does not necessarily have to be the endpoints, but can be freely selected within the cycle range. The potential scan speed usually range from the lower mV/s and up to about 1000 V/s, albeit sweep rates up to 10^6 V/s is not uncommon on ultra-microelectrodes [66]. The current is recorded and is normally plotted against the potential, producing a voltammogram, as in Figure 2.3. CV is a fast method where the system may easily be qualitatively interpreted from the plot [67]. Linear sweep voltammetry

(LSV) is a subgroup of CV, describes a potential sweep in just one direction.

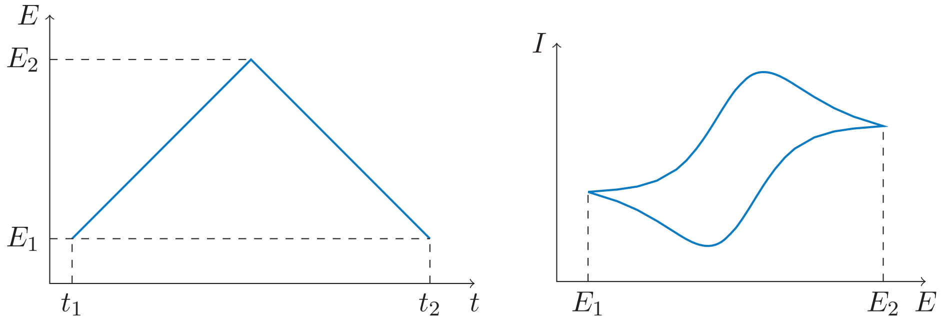

(a) Cyclic potential sweep (b) Resulting cyclic voltammogram

Figure 2.3: Example of a potential sweep (a) and its resulting cyclic voltammogram (b) for a reversible electron transfer process. During the sweep from potential E_1 to E_2 the current passes through an anodic peak current (maximum) and on the return scan through a cathodic peak current (minimum). The duration of one cycle is the difference between t_2 and t_1.

Chronoamperometry

Chronoamperometry (CA) is a potential step technique were the potential is the controlled variable and the current is measured versus time. The potential can be changed (stepped) and the number of steps, the step direction and magnitude, and the duration of each step plateau can be varied and even tailored for the experiment under study. A common routine is to begin with a potential in a region where no net reaction is taking place, before stepping into potentials of interest while recording the observations. Constant voltage (CV) is a form of chronoamperometry where the current source keeps the voltage of a system constant. The naming is commonly used for larger power sources such as rectifiers. A typical CA experiment is illustrated in Figure 2.4.

Electrochemical impedance spectroscopy

Electrical impedance is the measure of the opposition of a system to a current when a voltage is applied. It is the AC (alternating current) equivalent to the resistance of a DC (direct current) circuit, but in addition to DC resistance it has to take into account the additional opposition from the inductance and capacitance of the oscillating signal.

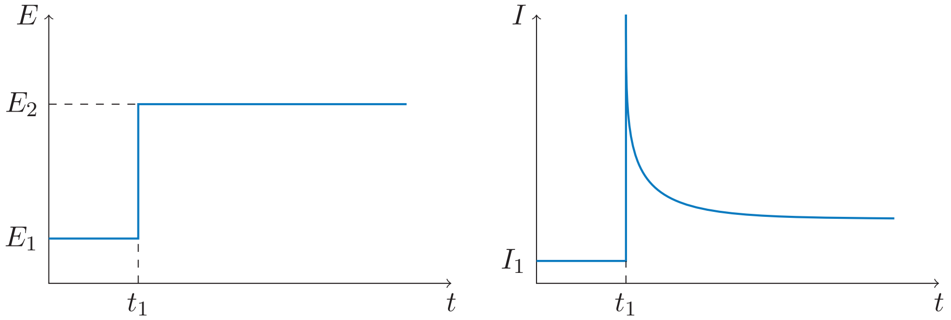

(a) Potential step

(b) Resulting current response

Figure 2.4: An example of a typical CA experiment. (a) The potential is stepped from the systems initial value E_1 to E_2 at time t_1. (b) The current has initially the arbitrary value I_1 which changes when the potential is stepped at time t_1. Initially there is a huge current spike before it relaxes towards a more stable diffusion controlled current.

In electrochemical impedance spectroscopy (EIS) a sinusoidal signal of a given frequency is superimposed on a constant electrical signal. The most common method is to superimpose an alternating potential onto a constant potential and reading the current response, however, the opposite is also possible. Some instruments even provide the ability to mix the perturbing signal and e.g. superimpose an alternating current to a direct potential producing a pseudo-EIS. The EIS is usually performed at a range of different frequencies spanning several decades (often 1 Hz to 100 kHz, but can be expanded in both directions) and also at different bias (the constant part of the perturbing signal). The amplitude of the alternating perturbations should be small enough that the systems behaves approximately linearly, but naturally still large enough to produce a signal response (normally $< 20\,\mathrm{mV}$ [67]).

The impedance is defined as the ratio between the time-dependant potential to the time-dependant current.

$$Z = \frac{U(t)}{I(t)} \tag{2.8}$$

The excitation signal, expressed as a function of time has the form $U(t) = U_0 \sin(\omega t)$, where ω is the angular frequency. The current response is on an analogous form containing a possible phase shift ϕ, that is $I(t) = I_0 \sin(\omega t + \phi)$. Inserted into Equation (2.8) and using complex notation ($j = \sqrt{-1}$) the impedance becomes

$$Z = \frac{U_0 \exp(j\omega t)}{I_0 \exp(j\omega t - \phi)} = Z_0(\cos\phi + j\sin\phi) \tag{2.9}$$

where $Z_0 = U_0/I_0$. The real and complex part of Equation (2.9) ca be extracted as the separate parts $Z_{\mathrm{Re}} = Z_0 \cos\phi$ and $Z_{\mathrm{Im}} = Z_0 j \sin\phi$. Plotting the imaginary part against the real part yields a "Nyquist plot" of which an example can be found in Figure 2.5a. A shortcoming of the Nyquist plot is that it does not convey frequency information. Another popular presentation method is the "Bode plot" where the logarithm of the absolute value of the impedance ($\log|Z|$) and the phase (ϕ) are plotted against the logarithm of the frequency. Unlike the Nyquist plot, the Bode plot shows frequency information explicitly. An example is provided in Figure 2.5b.

Some general electric components and their characteristic impedances are presented in Table 2.4. By modelling electrochemical cells as passive electric circuit elements and comparing it with experimental data, it is possible to extract information about the different processes like double layer capacitance, electron transfer resistance, uncompensated electrolyte resistance and the likes.

Table 2.4: Impedance of some general circuit elements.

Component	Representation	Defining relation	Impedance
Resistor		$U = R \times I$	$Z_{\mathrm{R}} = R$
Capacitor		$I = C\frac{dU}{dt}$	$Z_{\mathrm{C}} = \frac{1}{j\omega C} = -\frac{j}{\omega C}$
Inductor		$U = L\frac{dI}{dt}$	$Z_{\mathrm{L}} = j\omega L$
CPE[1]			$Z_{\mathrm{CPE}} = \frac{1}{T(j\omega)^{\phi}}$ [68]
Warburg[2]			$Z_{\mathrm{W}} = \sigma\omega^{-1/2}(1-j)$ [69]

[1] Constant phase element (CPE) is a general element used to model "imperfect" capacitors. CPE's normally exhibit a 80–90° phase shift. T is a constant and ϕ is related to the angle of rotation.

[2] Warburg (infinite) is a general impedance which represents a resistance to mass transfer, i.e., diffusion control. A Warburg typically exhibits a 45° phase shift. The process is assumed DC reversible where σ is the Warburg constant, a mass transfer coefficient.

EIS in this work

Electrochemical impedance spectroscopy has a lot of potential, but has in the following mostly been used to detect the ohmic drop (IR) at open circuit potential (OCP) between the anode and the reference electrode, and to determine if the anode is assembled properly (meaning the ohmic drop is far within an order of magnitude of its counterparts). The first is simply done by extracting the real impedance when the imaginary impedance is zero (this is about 0.22 Ω found at about 50 kHz in the example from Figure 2.5). All constant current electrolysis

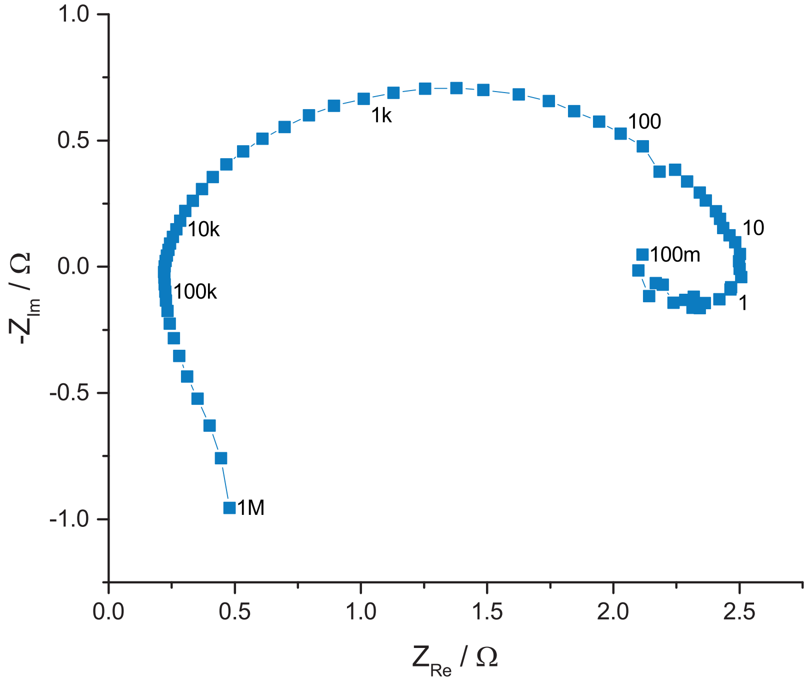

(a) Nyquist plot

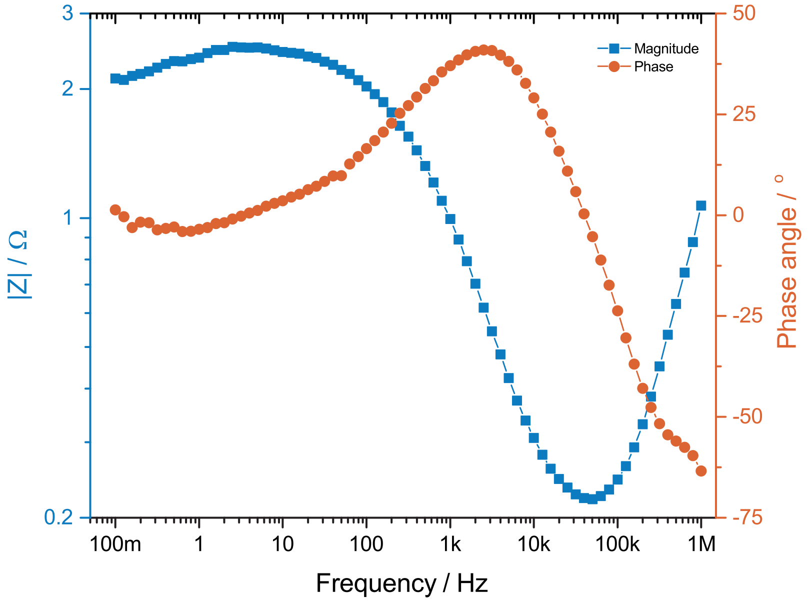

(b) Bode plot

Figure 2.5: Nyquist (a) and Bode (b) plots of a vertical graphite electrode polarised anodically with a bias of 1.2 V and a sinusiodal signal with amplitude of 10 mV against the aluminium reference electrode in a cryolite melt. Frequency was scanned from high to low on a Solartron 1287 + 1260 combo.

experiments have had their anode potential corrected with this ohmic drop post experiment. It should be mentioned that the ohmic drop might vary somewhat with both applied current/potential and duration. The current interrupt method could have been an alternative and possibly better suited method to finding the voltage drop in the electrolysis experiments, but it was not available with the present set-up. Advances over the EIS method is that it gives feedback when the cell is loaded, as well as being an on-line method, accounting for changes in the system. On the negative side it is known for introducing some artefacts, but this is more of a concern during fast transient techniques.

Ideally the ohmic drop should be accounted for in transient techniques such as CV as well, and usually this is done by performing an EIS measurement and applying a positive IR feedback so the equipment accounts for this extra resistance when the measurement is performed. Generally it is also not possible to achieve 100 % compensation, but one has to settle for 70 – 90 % to get stable readings. Otherwise ringing [70] might develop, which is false oscillations not originating from the system, but incorrect use of the equipment. Scanning over a large potential region covering several possible electrochemical reactions can further complicate matters as the real IR drop can vary over the range, especially with the passivation that occurs on the anode at high anodic potentials in aluminium production systems. Even at very low compensation rates lots of ringing and even cathodic currents were observed at anodic potentials. Performing "corrections" post-experiment is not completely possible when dealing with potential sweep techniques as this changes the sweep rate, often to a non-constant value, although it can be argued to be incorrect even before such a post-correction as well. For the above reasons no IR corrections were performed on the potential sweep techniques.

2.5 Thermodynamics

In electrochemistry one often rely on the Nernst equation to describe the potential for the rate of reaction. If a system is nernstian it is considered thermodynamically or electrochemically reversible (or also practically reversible) [66]. For the electrode process:

$$\mathrm{O}^{n+} + n\,\mathrm{e}^- = \mathrm{R} \tag{2.10}$$

the corresponding Nernst equation would be:

$$E = E^0 - \frac{RT}{nF} \ln \frac{c_\mathrm{R}}{c_\mathrm{O}} \tag{2.11}$$

where E is the resulting potential, E^0 the standard reduction potential for the reaction, R and T are the universal gas constant and the absolute temperature, respectively, n is the number of electrons transferred, F is the Faraday constant and $c_{\mathrm{R}}/c_{\mathrm{O}}$ is the fraction of the concentration of reduced to oxidised species.

The energy changes related to any reaction can be divided into three thermodynamic terms. ΔG^0, which is the standard necessary work for reaction at reversible conditions, ΔH^0, which describes the total energy required for the reaction to proceed at adiabatic and isothermal conditions, and $T\Delta S^0$, which describes heat that results from changes in entropy. They are related by:

$$\Delta H^0 = \Delta G^0 + T\Delta S^0 \tag{2.12}$$

and by dividing through with $-nF$ ($\Delta G^0 = -nFE^0$, definition of E^0) the following equation is realised:

$$E^{iso} = E^0 - \frac{T\Delta S^0}{nF} \tag{2.13}$$

where E^{iso} is the isothermal voltage. For CO_2 production the corresponding numbers for E^{iso}, E^0 and $-T\Delta S^0/3F$ at 1000 °C would be -1.90, -1.17 and -0.73 volts. The entropy term leads to a cooling effect of -0.73 V of which energy has to be added for the cell to perform at adiabatic and isothermal conditions. Thermodynamic data for reactions related to aluminium production is provided in Appendix C.

Chapter 3

Monitoring of Continuous PFC Formation in Small to Moderate Size Aluminium Electrolysis Cells

HENRIK ÅSHEIM[a], THOR A. AARHAUG[b], ALAIN FERBER[c], OLE S. KJOS[b] and GEIR M. HAARBERG[a]

[a] *Department of Materials Science and Engineering, NTNU; Sem Saelands vei 2, N–7491 Trondheim, Norway*
[b] *SINTEF Materials and Chemistry, SINTEF; Strindveien 4, N–7465 Trondheim, Norway*
[c] *SINTEF Information and Communication Technology, SINTEF; Forskningsveien 1, N - 0373, Oslo, Norway*

This paper has been published in TMS Light Metals 2014 [1]. However, note that some minor corrections have been made to this paper post-publication for spelling/typos and to improve clarity.

Abstract

The existence of continuous or non-anode effect formed perfluorocarbons (PFC) has been documented for larger size aluminium electrolysis cells. It has been proposed that less uniformity in dissolved alumina for larger cells may elevate individual anode overvoltage sufficiently to produce PFC. Continuous PFC was monitored after the dry scrubber on a train of 28 cells at a Norwegian smelter. For this work a fourier-transform infrared spectrometer was used. Equipped with a mercury cadmium telluride detector and retrofitted with a 35 m / 11 L

measurement cell it was possible to get the detection limit down in the low ppb range needed for this study.

It was discovered that also small cells could emit PFC that was not directly related to the full anode effect. Continuous formation of PFC was found to be in the form of CF_4, for the most part; however, the results indicate that C_2F_6 may also form outside the full anode effect. No numerical data for the contribution of non-anode effect emissions to the overall PFC was calculated, nonetheless, judging by the difference in intensity it will be small for this particular smelter.

Keywords: PFC, Anode effect, NAE-PFC, Aluminium electrolysis, GHG, Low voltage AE

3.1 Introduction and theory

3.1.1 Introduction

Perflourocarbons (PFCs) are potent greenhouse gases (GHG) that are emitted from the aluminium smelters. The most common gases are tetrafluoromethane (CF_4) and hexaflouroethane (C_2F_6), but others like octafluoropropane(C_3F_8) have also been reported [71]. Common for all PFCs are their long lifetimes and very high global warming potentials, and as such, a high capacity to inflict harm on the environment. Consequently, the industry has made considerable efforts to understand the mechanism behind these unwanted emissions.

PFCs have normally been linked directly to the anode effects (AEs) and over the last 20 years the industry has made a lot of advances to reduce these emissions. The International Aluminium Institute (IAI) in London reports a decrease in PFC emissions of more than 80 % from 1990 to 2010, and has set a goal to further halve this for 2020 [35].

These achievements come as a result of introduction of new technology and serious improvements in cell control and operation. This leap forward in technology and operation also brought the means to discover emissions not directly related to the full anode effect. Studies have shown that PFC gases are also produced during electrolysis at normal cell voltages (3.7 - 4.5 V). The phenomena have been termed continuous PFC formation, or so-called low-voltage anode effects, and have been reported to occur during anode change and at the end of an underfeeding period [33]. According to Chinese data it can amount to as much as 93 % of all produced PFC [32, 34], and median 70 % [35].

The motivation of this work is to investigate if non-AE PFC is also present in smaller cells with a high amperage (kA) to point-feeder ratio relative to the larger cells previously mentioned. This work has been conducted at a Norwegian smelter with pots dating from the 70s. Several changes and optimisations have naturally occurred over the years, but with a current of approximately 200 kA it is still considered small to most plants built today.

3.1.2 Background and principle

In a standard Hall-Heroult cell for aluminium electrowinning there are two principle reactions between carbon and alumina,

$$\mathrm{Al_2O_3 + 3\,C = 2\,Al + 3\,CO} \qquad E^0_{960\,^\circ\mathrm{C}} = -1.06\ \mathrm{V} \tag{3.1}$$

$$\mathrm{2\,Al_2O_3 + 3\,C = 4\,Al + 3\,CO_2} \qquad E^0_{960\,^\circ\mathrm{C}} = -1.18\ \mathrm{V} \tag{3.2}$$

Although (3.1) is preferred thermodynamically, more than 90 % of the gas evolved is CO_2 resulting from the faster reaction kinetics of (3.2). In a typical industrial cell the current densities are about 1 A/cm^2, with an anodic overvoltage of approximately 0.5 V [9]. Close to the edges of the anodes, the current density is less than within the bulk, making the CO formation from (3.1) become more important [23].

When the supply of alumina to the anode decreases the potential increases through polarisation until a level where other reactions will have to occur in order for the cell to sustain the passing current. A summary of different AE studies is given by Thonstad et al. [9]. Possible reactions include the ones commonly associated with anode effect (3.4) and (3.5), but may thermodynamically also happen by the evolution of COF_2 (3.3), a reaction that has a potential midway between that of regular electrolysis and traditional anode effect.

$$\mathrm{2\,AlF_3 + Al_2O_3 + 3\,C = 4\,Al + 3\,COF_2} \qquad E^0_{960\,^\circ\mathrm{C}} = -1.88\,\mathrm{V} \tag{3.3}$$

$$\mathrm{4\,AlF_3 + 3\,C = 4\,Al + 3\,CF_4} \qquad E^0_{960\,^\circ\mathrm{C}} = -2.58\,\mathrm{V} \tag{3.4}$$

$$\mathrm{2\,AlF_3 + 2\,C = 2\,Al + C_2F_6} \qquad E^0_{960\,^\circ\mathrm{C}} = -2.80\,\mathrm{V} \tag{3.5}$$

Although COF_2 could be produced electrochemically as described in (3.3) it is thermodynamically unstable and will decompose to CF_4 and C_2F_6 in the presence of carbon (3.6, 3.7). In the presence of water vapour it decomposes to HF and CO_2 (3.8). The gas may possibly also self-decompose to CO_2 and CF_4 (3.9). The latter reaction is very temperature dependent and its equilibrium constant will be larger than unity below 955 °C [72].

$$\mathrm{2\,COF_2 + C = 2\,CO + CF_4} \qquad K_{960\,^\circ\mathrm{C}} = 94.8 \tag{3.6}$$

$$\mathrm{3\,COF_2 + 2\,C = 3\,CO + C_2F_6} \qquad K_{960\,^\circ\mathrm{C}} = 5.1 \times 10^{-3} \tag{3.7}$$

$$\mathrm{COF_2 + H_2O = 2\,HF + CO} \qquad K_{960\,^\circ\mathrm{C}} = 2.13 \times 10^{9} \tag{3.8}$$

$$\mathrm{2\,COF_2 = CO_2 + CF_4} \qquad K_{960\,^\circ\mathrm{C}} = 9.42 \times 10^{-1} \tag{3.9}$$

There have been few reports of COF_2 having been chemically detected, although results from electrochemical experiments have suggested it to be present [21]. In an industrial cell this is not so strange since it reacts readily with the anode coal according to (3.6) or with water vapour in the off-gas stream according to (3.8). In a lab cell on the other hand there is the possibility of strict gas control and Dorreen et al. [23] has found the compound; still the presence of COF_2 is seldom reported.

In the past couple of years, measurements done with an open-path FTIR above an open industrial pot have shown convincing evidence that COF_2 can be produced industrially [24]. There is less than 0.7 V difference between (3.2) and (3.3) and with anode polarisation and bubble resistance making up approximately 0.5 V, only a small potential fluctuation is needed before COF_2 could thermodynamically be produced.

3.2 Experimental

The measuring equipment was a Hartmann and Braun Bomem MB-154 Fourier Transform Infrared (FTIR) spectrometer equipped with a mercury cadmium telluride (MCT) detector for high sensitivity at a range of scanning velocities. The instrument is equipped with the infrared analysis cell 35-V-FXD-H with total volume of 11 litres and path length spanning 35 m (see Figure 3.1). Signal to noise can be improved with number of scans averaged, with the cost of losing gas dynamics. In the lab with a low vacuum and under optimal conditions the detection limit has been estimated to be $<$ 100 ppt. A filter in the optical path had to be employed; otherwise the detector got fully saturated. GRAMS AI spectroscopy software [73] was used to record the spectra.

The apparatus was connected to the cumulative gas exhaust stream of 28 cells after it had passed through the dry scrubber. This minimises the need for any HF or particle filter and only Drierite® for H_2O removal was employed. Sample gas was taken from the duct at approximately 2 L/min and then through the Drierite® before passing the pump, and finally into the sample cell. The cell had heating elements connected that kept the temperature at 80 °C. Measurements were conducted at resolutions of 2 and 4 cm^{-1} with an acquisition speed varying from 26 – 47 samples/min, averaged over 5 seconds in the output.

3.3 Results and discussion

Figure 3.2 illustrates the part of the part of the spectrum where the PFC gases CF_4 and C_2F_6 have their most characteristic vibrational states. The spectra are

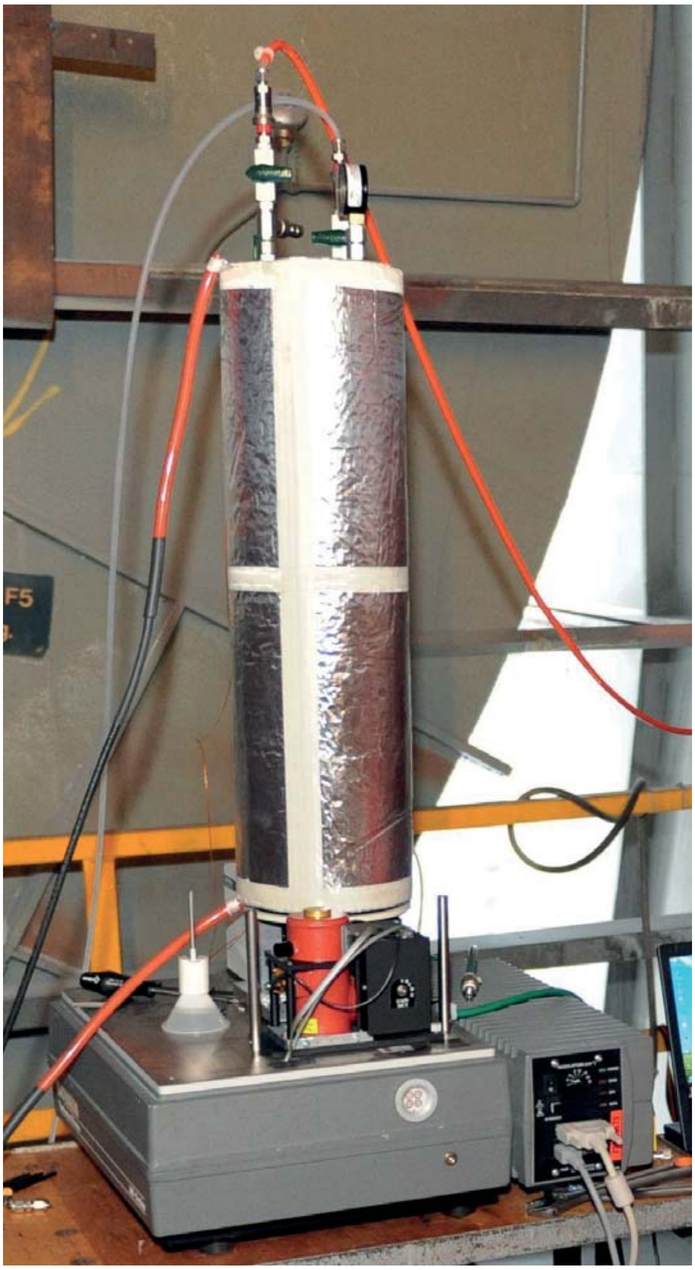

Figure 3.1: Apparatus setup with Bomem FTIR, a liquid N_2 cooled MCT detector and a large 11 L / 35 m cell. Two connected heat elements are covering the cell. Nitrogen is continuously flushed between the detector housings and the cell. (MCT detector housing detached in picture. During operation it covers the red N_2 cylinder and black detector box.)

taken 10 minutes apart, one during the anode effect and one slightly before. Two reference database spectra for the PFC gases overlay the anode effect signal well. The instrument was also calibrated with a 4.95 ppm ± 2 % CF_4 gas reference, giving a similar signal (Figure 3.3). From both the reference gas and the synthetic spectra generated by Spectral Calc [74] it was estimated that an absorbance of 0.035 equalled a concentration of 100 ± 5 ppb CF_4. Water would give an additional offset, but estimated to be much less than 5 ppb, especially at the interval the Drierite® was changed.

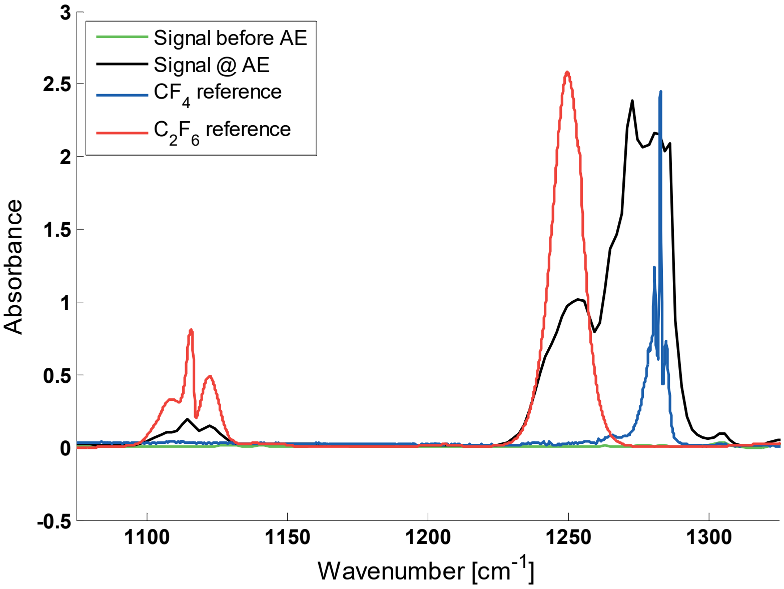

Figure 3.2: Reference signals from CF_4 and C_2F_6 overlaid spectra taken both before and during an anode effect.

Figure 3.4 shows an absorbance versus time plot for CF_4, C_2F_6, SO_2 and H_2O. Two minutes into the plot a cell is being underfed and approximately 50 minutes later it goes into full anode effect with the CF_4 and C_2F_6 signals rapidly increasing. The noise around 2000 seconds is resulting from the Drierite® being changed, and as a consequence the H_2O signal nearly drops to zero.

With dry Drierite® SO_2 passes through undisturbed. There are also some peaks of C_2F_6 close to 2000 s. They are noise from the very high water signal. If C_2F_6 had been present at such large concentrations the spacious cell volume would have showed a trail of decreasing concentration.

From about 400 – 1000 seconds there is a small, but broad CF_4 peak. Water has some spectral lines around 1281 cm^{-1}, but the peak shape is too dissimilar from the rising water at 1962 cm^{-1}. The peak might originate from PFC

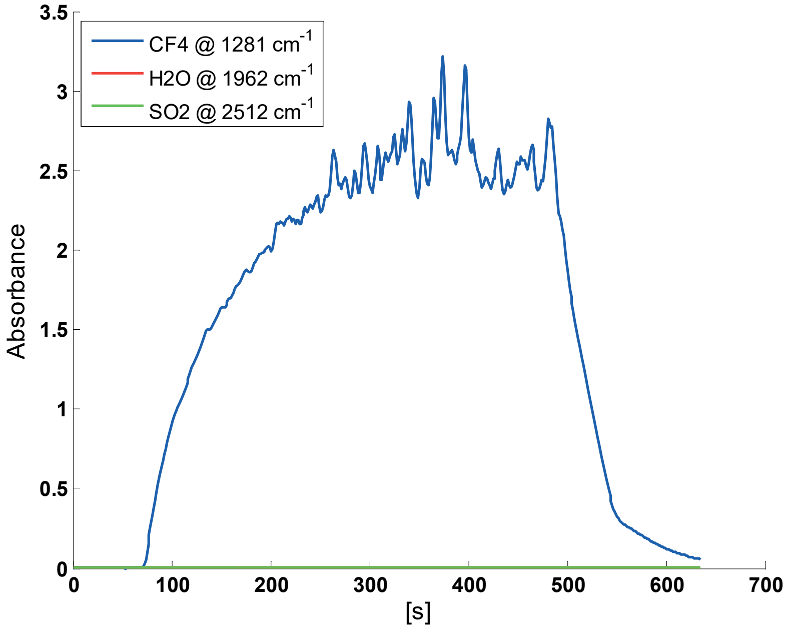

Figure 3.3: FTIR calibration curve for a 4.95 ppm ± 2 % CF_4 reference.

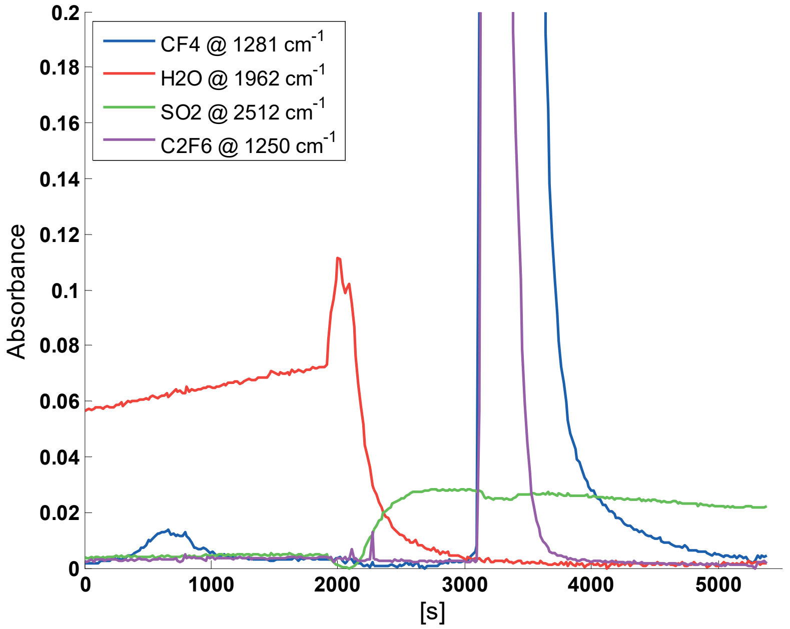

Figure 3.4: FTIR data for CF_4, C_2F_6, H_2O and SO_2 before and during an AE Water filter changed at 2000 s. The cell is on anode effect at 3100 s.

from the pot that just prior was put on underfeeding, or from any of the other 28 pots connected to the same gas duct. Interestingly, however, is that no trace of C_2F_6 is detected. During a regular anode effect the concentration of C_2F_6 is approximately 1:10 mass that of CF_4. This might stem from the fact that thermodynamically a much more negative potential is required for direct production of CF_4 and C_2F_6 through (3.4) and (3.5), than to produce COF_2 through (3.3) with a subsequent decomposition through (3.6), (3.7) or (3.9).

A similar observation was made at the event just prior to the full anode effect of the pot at 3100 s. The event is enlarged in Figure 3.5 and from the enlargement it is clear that CF_4 has been increasing steadily from about 2680 s, making it a total of 7 minutes. During this period no variation in C_2F_6 was detected. Within the control instruments of the smelter a local anode effect was reported approximately 7 minutes before the full anode effect, which coincides well with the measured change in slope for CF_4 absorbance. It is possible that the cell lies in the small electrochemical window between direct CF_4 and C_2F_6 production, however, the production of CF_4 may also go by way of the intermediary COF_2.

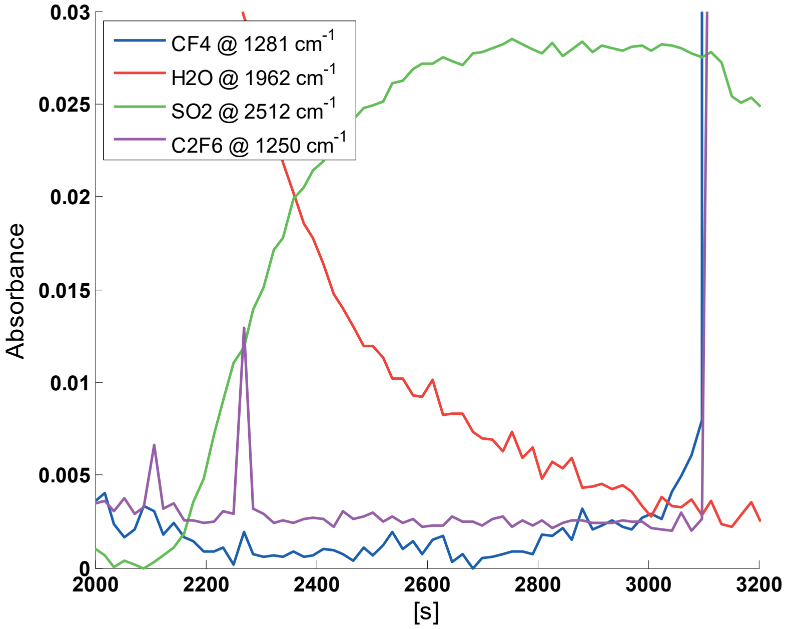

Figure 3.5: PFC signal from the anode effect and 10 minutes prior.

Evidence of CF_4 being produced before the main anode effect has also been observed in the laboratory. Figure 3.6 shows mass spectrometer data obtained from an experiment conducted under potentiostatic control. Start cell voltage was 3.0 V (anode voltage of 2.8 V vs. Al^{3+}/Al reference electrode) which was kept constant for the first 20 minutes, before being raised 0.25 V every 5 minutes.

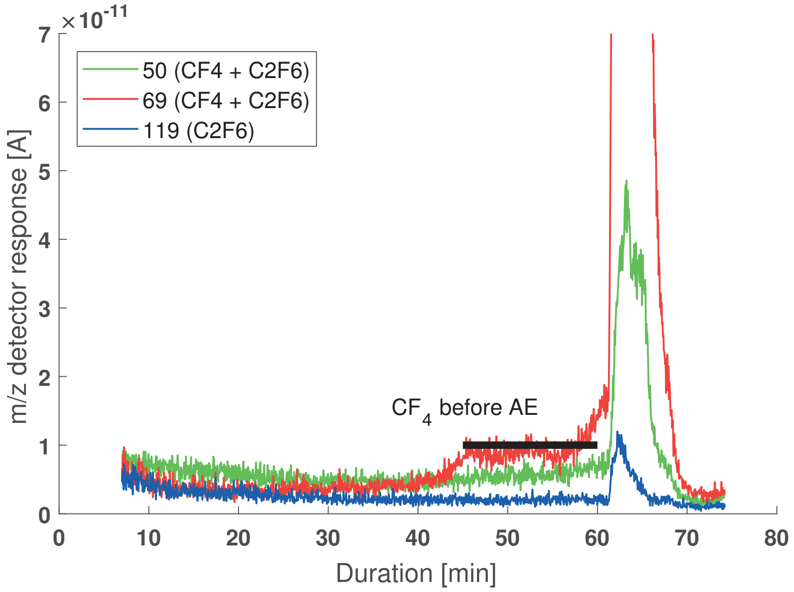

Figure 3.6: MS data for mass/charge 50 (CF_4/C_2F_6), 69 (CF_4/C_2F_6) and 119 (C_2F_6). This data is from a laboratory experiment.

At 45 minutes and 4.5 V (3.6 V vs. reference electrode) the figure shows a non-negligible jump in response for mass/charge 69 (fragment CF_3^+,CF_4/C_2F_6). This response is not shared by mass 119 and as such it is safe to assume that the signal at 69 is produced only by CF_4. Not until the major anode effect at 60 minutes and 5.25 V (4.2 V vs. reference electrode) can a change in C_2F_6 at mass 119 be observed.

Three of the industrial cells had one out of a total of two alumina point feeders turned off to disturb the oxide balance in the bath and starve it to a level where it is just on the verge of going into an anode effect. The sequence is presented in Figure 3.7.

The starving began 400 seconds into the plot and the water filter was changed at 2500 s. The slight rise in PFC level up to this point is ascribed to the many absorption lines of water and a couple of small water lines overlapping with the main peaks of CF_4 and C_2F_6. During the next 1000 s both PFC curves rise, however, they do so in a dissimilar manner. C_2F_6 doesn't follow the ups and downs of CF_4 as in a regular anode effect. There is no doubt that CF_4

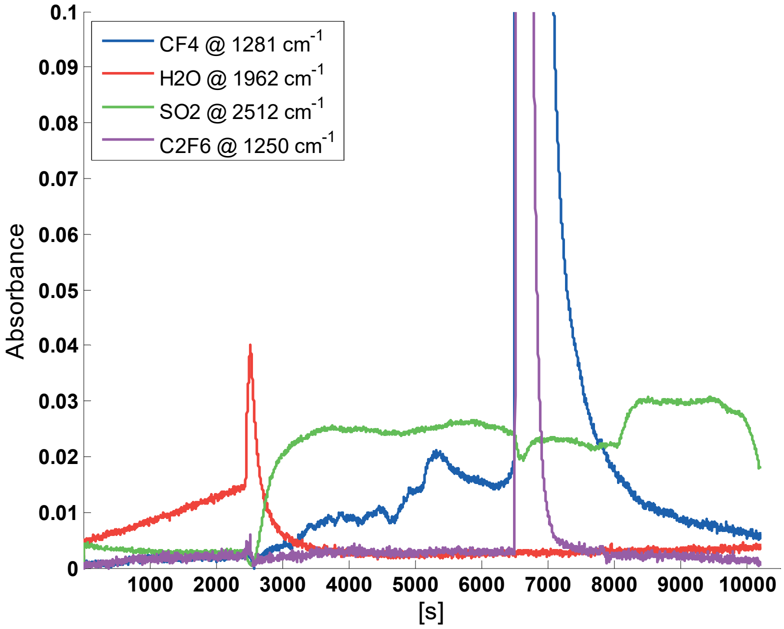

Figure 3.7: FTIR data for CF_4, C_2F_6, H_2O and SO_2 showing continuous PFC emissions for ~ 1 h before an anode effect. Water filter changed at 2500 s.

is detected, but the C_2F_6 is most likely ascribed to the filter change. On the other hand, it might also be that the rise is dampened by the falling water and that C_2F_6 is indeed produced. The amount of water would also inflict the CF_4 response, but as much more CF_4 is produced (~ 10 times during AE) any changes would be less visible. It should be clear from this that removal of water is important as it can cloud the rest of the spectra.

From 3500 s and up to 6500 s, where one of the cells went on AE, there is production of CF_4, and a mesh plot of single spectra from the region of greatest change is presented in Figure 3.8. In total it is almost an hour with continuous PFC emissions and Figure 3.8 confirms the water changes little during this time as there is no equally shaped absorbance elevation in the wavenumbers surrounding the PFC peak. It might come from any or several of the 28 cells, however, it is likely from one of the three starved of oxide, and most probable from the one that encountered the major anode effect at 6500 seconds. Interestingly the level of C_2F_6 remains entirely constant during this period, and as discussed earlier this could be the noise level; nonetheless it cannot be overlooked that the signal increased, noise or not, after the filter change, and a subsequent decrease down to the same level, is observed after the major anode effect. From one point of view it could look like there is a constant formation of C_2F_6 during this non-AE period.

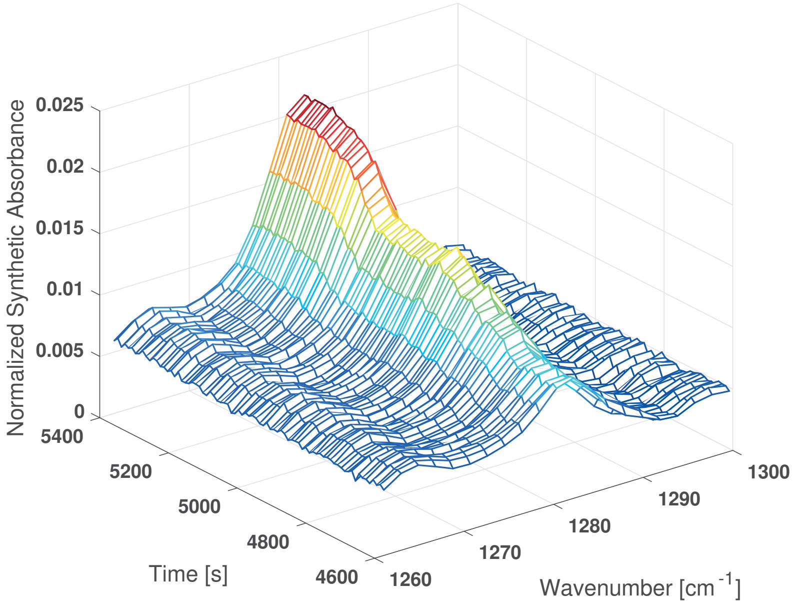

Figure 3.8: Mesh plot of single spectra the region of greatest change in non-AE PFC.

Figure 3.9 shows a plot of two cells that went on anode effect only one minute apart. It is the two remaining cells that were set to starve in Figure 3.7, yet did not end up with the full AE. Three hours after starving was initiated there was a mains decoupling to connect a new cell. As soon as the power was back up the cells went on AE only a minute apart. No long period of emissions was detected in this case, possibly as a result of the power outage; although there's no guarantee there would have been one without it either.

The change in signal happens over just 150 s, beginning around 1400 s, and is much steeper than in the previously discussed cases as well. Additionally the C_2F_6 signal changes inclination as early as CF_4, albeit to a lesser degree, which is in stark contrast to the other observed AEs where C_2F_6 only have changed abruptly just as the major AE begun. It is unclear why it looks like this. CF_4 can be argued to have a steeper slope if both cells had a relatively similar short non-AE run and the signals accumulated. C_2F_6 has previously in these results not had any stepwise increase prior to an anode effect, but the effects of tampering, both with oxide level and current, might have changed this. Possibly the oxide concentration is so badly distributed that one or more anodes are forced to an overpotential that could initiate the production of CF_4 from (3.4) and C_2F_6 from (3.5), while the rest followed regular electrolysis. Eventually

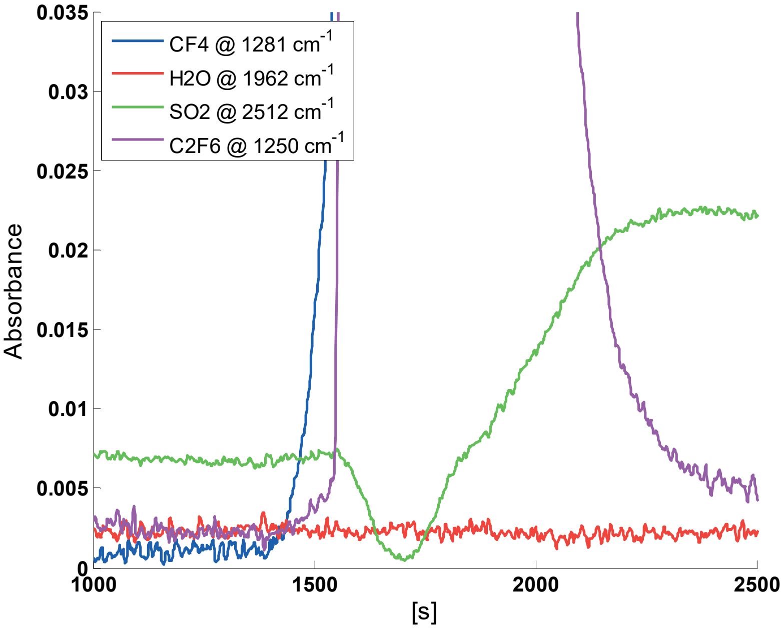

Figure 3.9: FTIR data for CF_4, C_2F_6, H_2O and SO_2 showing the PFC profile of two cells experiencing oxide starvation and current loss.

this could not be sustained and a major AE was a fact.

Figure 3.10 starts by showing the falling trend after the major two cell simultaneous AE. At the end of the spectra there are two similar shaped PFC peaks that might originate from an analogous event, albeit at a different magnitude. Interestingly the signal is much unlike the non-AE PFC discussed in both Figure 3.4 and 3.7. There is also some variation in the C_2F_6 response at these peaks. Individual spectra confirms C_2F_6 to be present for the peak around 2800 s, however the signal is too low to be significant at 3150 s. At 1700 s there is also some variation in the C_2F_6 signal, with a peak value higher than that of 2800 s. In spite of that the small trail for the larger one at 1700 s suggests it has a higher character of noise than the other.

Another property of the PFC peaks at the end of the spectra is their shape. While the previous non-AE PFC curves were broad and had a low curvature, these peaks are much sharper, and have in fact a shape comparable to that of the regular AE, despite being smaller. Although no information was received from the control unit this could be an AE on the verge of happening that was fed oxide just in time – routinely or as a consequence of pot control.

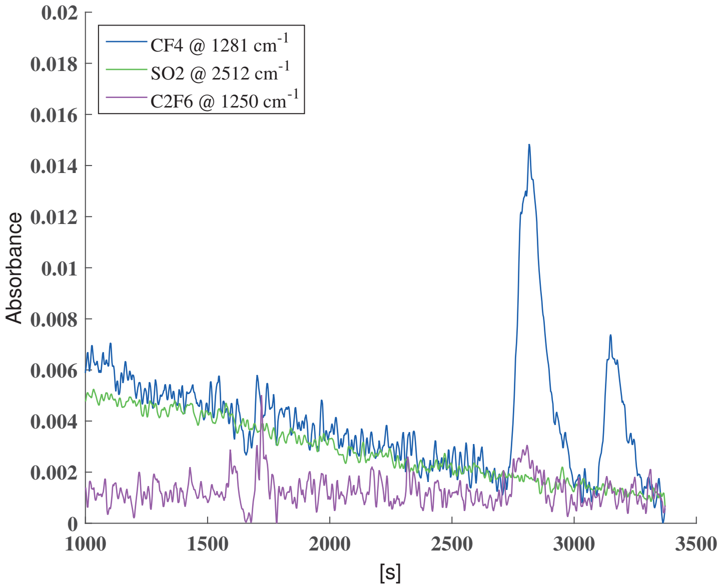

Figure 3.10: FTIR data for CF_4, C_2F_6, and SO_2 showing two non-AE PFC events and possible traces of C_2F_6.

3.4 Conclusions

Although most of the results related to continuous or non-AE PFC are from conditions artificially generated, continuous or non-AE PFC is also an attribute of smaller cells ($<$ 300 kA). More often than not just CF_4 is released, but as this article indicates C_2F_6 can also be formed during these events. Further investigation is needed to find the true mechanism.

Acknowledgements

This work has received financial support from The ROMA Project, Hydro and the Norwegian Research Council.

Chapter 4

A Laboratory Study of Partial Anode Effects During Aluminium Electrowinning

Henrik Åsheim[a], Thor A. Aarhaug[b], Espen Sandnes[a,c], Ole S. Kjos[b], Asbjørn Solheim[b], and Geir M. Haarberg[a]

[a] *Department of Materials Science and Engineering, NTNU, Trondheim, Norway*
[b] *SINTEF Materials and Chemistry, SINTEF, Trondheim, Norway*
[c] *Hydro Primary Metal Technology, Øvre Årdal, Norway*

This paper has been published in ECS Transactions 2015 [2]. However, note that some minor corrections have been made to this paper post-publication for spelling/typos and to improve clarity.

Abstract

The behaviour of graphitic anodes during electrolysis in low-alumina cryolite melts was investigated. The experimental setup consisted of two anodes in separate electrolyte compartments connected in parallel with a single combined cathode. The results show that the anodes to some extent will vary their current uptake based on their resistance towards reaction. The results also indicate that PFC production at normal industrial electrolysis potentials will give a cooling of the anode surface, even with slight elevation of the voltage as the PFC producing reactions have a much higher isothermal potential.

Keywords: GHG, PFC, NAE-PFC, Anode effect, Aluminium Electrolysis, Low voltage AE, LCV-AE

4.1 Introduction

Aluminium is industrially produced electrochemically by reduction of alumina from a melt of $Al_2O_3 + Na_3AlF_6 + AlF_3$ at approximately 960 °C. In addition to producing aluminium the carbon anode is oxidized to CO_2 with a fraction of CO. The reversible potential for the reaction is about 1.2 V, but due to overpotentials related to the electrodes, and IR drops in different parts of the cell, especially from the electrolyte, a regular industrial cell needs to operate at a much higher voltage (3.8 – 4.5 V). If the alumina content (the feed) drops too much, polarisation will increase to sustain the reaction, eventually rising so far that other anode reactions become possible. Two possible anode products are the perfluorocarbon (PFC) gases CF_4 and C_2F_6 [17, 75]. The phenomenon is termed anode effect (AE), and traditionally when this occurs the voltage can rise to levels of 20 V or higher, and the current distribution over the anodes become erratic. Standard potentials of selected possible reactions are given in Table 4.1.

PFCs are unwanted from an environmental standpoint as they possess high global warming potential and long lifetimes, making them potent greenhouse gases [39]. Additionally they impede the industrial process by passivating the anodes and increasing the total power consumption.

The existence of PFCs not related to the traditional anode effect in industrial aluminium production cells has been documented for a wide range of technologies in later years [1, 32, 34, 35]. Industrial measurements have shown that PFC production can begin at one anode during normal cell potentials and propagate to the entire cell given the right conditions [37]. In order to experience the phenomenon in the laboratory, a system with more than one anode was designed.

4.1.1 Cell and anode voltage

By treating an industrial cell as a single electrode system the overall voltage would be comprised of the anodic and cathodic potentials, as well as the IR drops over the electrolyte, through the anode, the bubble layer (bubble overvoltage) and cathode lining as described by the following equation (external IR omitted)

$$V_{Cell} = E_{An} + |E_{Cat}| + I_{tot} \cdot (R_{An} + R_{Bubble} + R_{El} + R_{Cat}) \tag{4.1}$$

Table 4.1: Thermodynamic data of reactions at 1000 °C [50].

#	Reaction	ΔH^0	ΔS^0	ΔG^0	E^0	E^{iso}
		kJ	$\mathrm{J\,K^{-1}}$	kJ	V	V
1	$\frac{1}{2}\,\mathrm{Al_2O_3} + \frac{3}{2}\,\mathrm{C\,(s)} = \mathrm{Al\,(l)} + \frac{3}{2}\,\mathrm{CO\,(g)}$	674.8	295.3	298.8	-1.03	-2.33
2	$\frac{1}{2}\,\mathrm{Al_2O_3} + \frac{3}{4}\,\mathrm{C\,(s)} = \mathrm{Al\,(l)} + \frac{3}{2}\,\mathrm{CO_2(g)}$	548.9	165.3	338.4	-1.17	-1.90
3	$\frac{1}{2}\,\mathrm{Na_3AlF_6(l)} + \frac{1}{4}\,\mathrm{Al_2O_3} + \frac{3}{4}\,\mathrm{C\,(s)} = \frac{3}{2}\,\mathrm{NaF} + \mathrm{Al\,(l)} + \frac{3}{4}\,\mathrm{COF_2(g)}$	731.4	142.4	550.1	-1.90	-2.52
4	$\frac{3}{4}\,\mathrm{COF_2} + \frac{3}{8}\,\mathrm{C\,(s)} = \frac{3}{4}\,\mathrm{CO\,(g)} + \frac{3}{8}\,\mathrm{CF_4(g)}$	34.9	51.4	-30.6		
5	$\frac{1}{2}\,\mathrm{Na_3AlF_6(l)} + \frac{1}{4}\,\mathrm{Al_2O_3} + \frac{9}{8}\,\mathrm{C\,(s)} = \frac{3}{2}\,\mathrm{NaF\,(l)} + \mathrm{Al\,(l)} + \frac{3}{4}\,\mathrm{CO\,(g)} + \frac{3}{8}\,\mathrm{CF_4(g)}$	766.3	193.9	519.5	-1.79	-2.65
6	$\mathrm{Na_3AlF_6} + \frac{3}{4}\,\mathrm{C\,(s)} = 3\,\mathrm{NaF\,(l)} + \mathrm{Al\,(l)} + \frac{3}{4}\,\mathrm{CF_4(g)}$	857.7	92.4	740.1	-2.56	-2.96
7	$\mathrm{Na_3AlF_6} + \mathrm{C\,(s)} = 3\,\mathrm{NaF\,(l)} + \mathrm{Al\,(l)} + \frac{1}{2}\,\mathrm{C_2F_6(g)}$	889.8	67.8	803.5	-2.76	-3.07
8	$\mathrm{Na_3AlF_6} = 3\,\mathrm{NaF\,(l)} + \mathrm{Al\,(l)} + \frac{3}{2}\,\mathrm{F_2(g)}$	1557	206.1	1295	-4.47	-5.38

However, an industrial cell has a number of anodes (20 – 40+) connected in parallel that needs to be exchanged at certain intervals (~ every month) since they are consumed in the process. Hence, at any instance there can be as many different anode resistances, R_{An}, as there are anodes, as discussed by Welch et al. [76]. In addition, there can be variations in alumina concentration due to the feeding system or electrolyte mixing. The anode to cathode distance (ACD) may vary due to magnetohydrodynamics (MHD) or work practices. To maintain the condition that the potential over each of the parallel circuits has to be the same, the current might develop non-uniformly over the anodes. By considering the fact that molten aluminium has very high electrical conductivity and is uniformly connected to the carbon cathode, its potential can be assumed equal for all parallel circuits. Split up on a per anode basis with partial currents the cell voltage becomes:

$$V_{Cell} = E_{An,i} + I_i \cdot (R_{An,i} + R_{Bubble,i} + R_{El,i}) + |E_{Cat}| + I_{tot} \cdot R_{Cat} \tag{4.2}$$

From this it is understood that current flow through an anode can vary with anode age, temperature, electrolyte and alumina mixing, and work practises like anode change. If there is a drop in current over one parallel circuit, that current will have to be distributed to the remaining circuits, or parts of them. The total cell voltage will rise as a consequence, but only marginally due to the parallelism of the system. However, for the parallel circuit that observed a drop in current, bigger changes might occur. As the circuit "sees" the same cell voltage a redistribution of potential will occur, since all per circuit ohmic potential drops will have decreased. This brings about a change in interfacial electrode potential that might give rise to new reactions. Approximately all of this potential will relocate to the anode, as little overpotential is associated with the cathode. Additionally, it is interconnected and maintained equal for all circuits.

4.1.2 Energy flux at electrodes

The energy changes related to any cell reaction can be divided into the three terms ΔG^0, ΔH^0, and $T\Delta S^0$. The first describes the necessary work for a reaction to proceed at reversible conditions, the second describes the total energy required for a reaction to proceed at adiabatic and isothermal conditions and the third term describes the heat that results from changes in entropy. They are connected to each other by the relation $\Delta H = \Delta G + T\Delta S$ and by dividing through with the number of exchanged electrons per mole of aluminium, of reaction (−3F in this case), it can be expressed as voltages

$$E^{iso} = E^0 - \frac{T\Delta S^0}{3F} \tag{4.3}$$

where E^{iso} and E^0 are the isothermal cell voltage and the standard cell voltage, respectively. Most of the values are listed in Table 4.1 , and for the production of CO_2 (#2, Table 4.1) the entropy term corresponds to a drop in cell voltage by −0.73 V at 1000 °C. The heat is evolved at the electrode/electrolyte interface and in the bulk electrolyte for alumina dissolution. The distribution between them is not obvious, and researchers have used different methods to predict it. Ratkje [77] used irreversible thermodynamics, while Solheim [78] used formal activity data for the system $NaF-AlF_3-Al_2O_3$ applied to separate anodic and cathodic reactions. An excerpt of the data from the latter is given in Table 4.2.

The cathodic part of the reaction is the same for all total reactions and is virtually independent of alumina content at NaF/AlF_3 molar ratios above 2. Alumina will be dissolved in the bath and consumed at the anode surface and thus, the cooling effect will vary at these positions. Direct production of CF_4 or C_2F_6 does not consume alumina so the bath term is omitted. From the values of the table it is also realised that the cooling of the anode in most circumstances is larger than the difference between E^0 and E^{iso}. This is especially true when no alumina mixing is involved.

Table 4.2: Voltages (in volts) related to entropic heating and cooling of different locations in the cell. The data is given for NaF/AlF$_3$ molar ratio of 2.2, 2.5 wt% alumina and a temperature of 960 °C [78]. The last two rows are unpublished data from the same author. Values in parentheses are estimated data with an alumina concentration of ~ 0.2 wt%. Negative values represent cooling.

#	Reaction	Cathode	Anode	Electrolyte/Bath	Total
1	CO	0.31	−1.32	−0.24	−1.25
2	CO_2	0.31 (0.31)	−0.78 (−0.60)	−0.24 (−0.42)	−0.71
6	CF_4	0.31	−0.92	0	−0.61
7	C_2F_6	0.31	−0.82	0	−0.51
5	$COF_2 \longrightarrow CF_4$	0.31 (0.31)	−0.91 (−0.82)	−0.12 (−0.21)	−0.72

4.1.3 Aim

The aim of this paper is to investigate what happens in an aluminium production cell with more than one anode when the alumina supply in a part of the cell becomes insufficient.

4.2 Experimental

The experiments were conducted in a cell that consisted of two anodes connected in parallel and a shared cathode. The cathode was machined out of a cylindrical block of graphite (Schunk-Tokai) and consisted of two separate oval compartments with a 5 mm wall in between. The separate compartments made it possible to employ different electrolytes, especially variations in alumina concentration. In each compartment a 5 mm steel plate was placed at the bottom to provide better wetting for the aluminium produced to give a flat and uniform metal pad. A sketch of the setup can be viewed in Figure 4.1. The cell was placed in an externally heated vertical tube furnace, with a temperature set point that would give ~ 1000 °C in the cell when idle.

The electrolyte consisted of cryolite (Aldrich), aluminium fluoride (industrial grade, sublimed at 1090 °C) and alumina (Aldrich). The molar ratio (NaF/AlF$_3$) was 2.3 at the beginning of the experiment, and each chamber had enough electrolyte to give a bath height of ~ 4 cm. The anodes were made from graphite (Schunk-Tokai, ultrapure) rods (⌀ 16 mm) encased in hot-pressed boron nitride (Kennametal) rods (⌀ 22 mm). The horizontal surface as well as 3 mm of the vertical surface of the graphite was unshielded from the electrolyte melt, giving an initial surface area of 3.518 cm^2. The anodes were electrically connected by a steel tube (⌀ 6 / 8 mm) and within the current collector tube a thermocouple

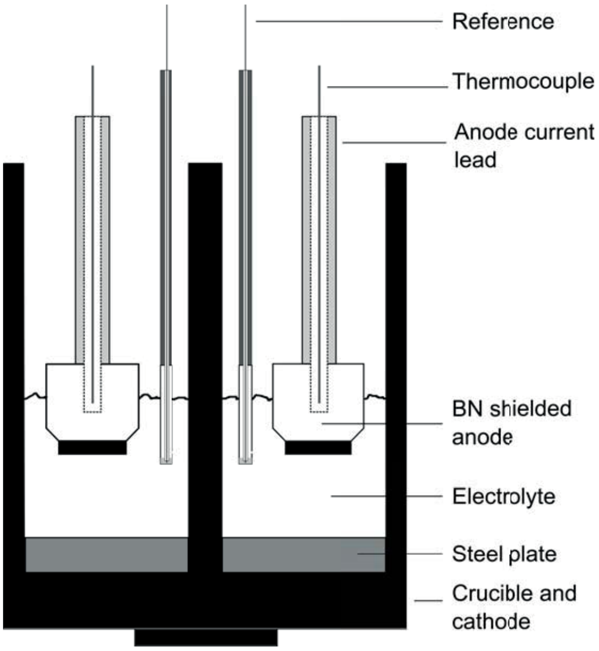

Figure 4.1: Experimental setup of two-compartment crucible. Each compartment has its own anode, reference and electrolyte.

as well as a sense wire was housed in a 5-bore alumina tube. The thermocouple and sense gave direct anode temperature and potential readings, respectively. The anodes were placed about 1 – 1.5 cm into the melt, giving an ACD of about 2.5 – 3 cm.

Aluminium reference electrodes were used. They were made from milled out BN rods with ~ 1.5 cm of aluminium inside. A small hole of approximately 2 mm in diameter was drilled through one side of the rod about 5 mm above the aluminium level. Electrical connection was made with a tungsten wire shielded in an alumina tube, except for the bottom 5 cm that would otherwise be in contact with both aluminium and electrolyte, which was shielded with a small boron nitride tube. The current was supplied to the cell by a power supply unit (PSU) (Agilent 6032A) controlled through LabView software. The positive side was split in two parallel sections and each connected through a resistor ($1\,\Omega$) before going through the anodes and being combined again at the cathode. A simplified overview of the electric circuit is given in Figure 4.2.

The added resistances are in part used to measure the individual currents, but they also provide a means to get the cell voltage up to levels seen in the industry. It provides a clear analogue to the redistribution issue that can happen at an individual anode that begins to draw less or more current. However, it might

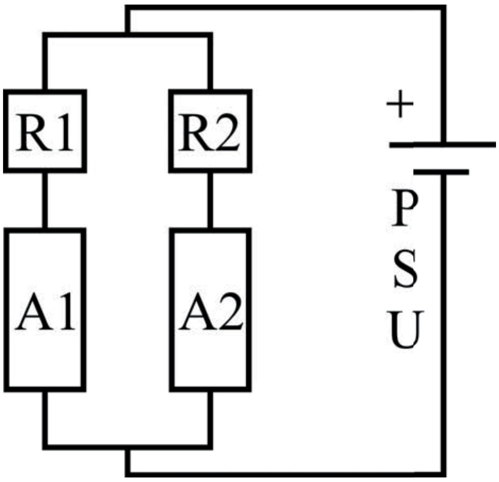

Figure 4.2: Electric circuit of the electrochemical cell. R1 and R2 are resistances of 1 Ω. The current flows from the power supply down through the resistances (across which the current is measured) and over the anodes before it combines at the cathode. (The anodes are depicted as resistances for simplicity.)

not be an apt analogue to “the rest of the cell” as the rest in this case is just one anode / parallel circuit. All data was logged with a National Instruments CompactRIO 9074 controller with analog voltage modules NI 9229 and NI 9205, as well as thermocouple module NI 9211. The equipment was controlled through LabView and data was sampled at 10 Hz, except the thermocouple module that only updates at 3 – 4 Hz.

4.3 Results and discussion

4.3.1 Onset of partial PFC production

An experiment was conducted with the alumina concentration set to 3 wt% and 1.8 wt% in chambers 1 and 2, respectively. The current was ramped in the beginning from 0.29 through 0.58, 0.86, 1.01 and up to 1.16 A/cm^2. This was to see if one parallel compartment could sustain the full current load given an anode effect with full blocking occurred on one anode at a current set point of 0.58 A/cm^2. Following the stepping, the current was kept constant at 0.58 A/cm^2 until the phenomena in Figure 4.3 were observed.

At this point (17 780 s), the theoretical concentration of alumina with a 100 % current efficiency would be 0 wt% in both chambers, and depleted 0.5 h and 2.3 h ago in chambers 1 and 2, respectively. Up until this event, the chambers

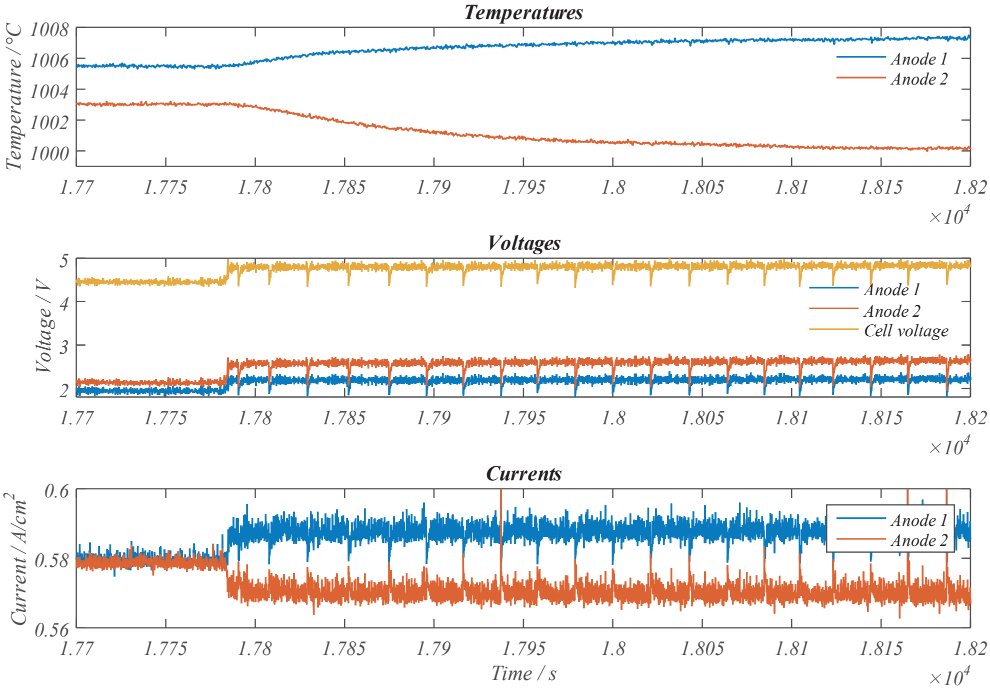

Figure 4.3: Current, voltage and temperature development over two anodes connected in parallel. The shift in current and voltage profile is believed to be a change of reaction happening on anode 2.

shared the current evenly, even though the initial amount of alumina was uneven. The voltage of anode 2 was consistently higher than that of anode 1 at all times up to the event. Even though this anode saw a lower alumina concentration, which would suggest a higher reversible potential for the reaction, it is in this case believed to be a bias between the references as a higher voltage would mean a higher equivalent resistance, which should have been observed in the distribution of current.

When the event occurred, the current decreased with $10\,\text{mA/cm}^2$ (35 mA) through anode 2 and increased with the same amount through anode 1, a change of about 1.7 % for each anode. The anodic potential increased by about 0.28 V (1.93 to 2.21) on anode 1 and about 0.47 V (2.12 to 2.59) on anode 2. The temperature of anode 1 increases, and given that there is no change in reaction (e.g. #2 of Table 4.1, which is regarded as the dominating one) this is expected with a small increase in current ($10\,\text{mA/cm}^2$) and voltage (0.28 V). However, anode 2 decreased in temperature after a small decrease in current, but a rather large increase in voltage (0.47 V). If the reaction before and after the event was the same, consuming approximately the same energy, a net surplus of energy would be expected, and consequently – an increase in temperature.

It is the authors' opinion that a change of reaction has happened, at least partly, and at least on anode 2. Anode 1 does also show similar traits as anode 2, like the downward spikes in voltage where it for a brief instance experiences the previous average potential, but it has to be taken into account that the anodes are interrelated. The current that does not go through anode 2 needs to go through anode 1. Likewise may the voltage vary to keep an equilibrium, sometimes this means lifting the voltage of an anode if the new voltage drop across a resistor does not suffice. Some possible reactions are listed in Table 4.1. They are all endothermic and the excess energy needed to keep a reaction at constant temperature is given by the difference between the enthalpy and Gibbs free energy – $T\Delta S$ as previously described. Any cooling effect will be facilitated by an electrochemical reaction that has a higher isothermal potential than the measured potential (reversible potential plus overpotentials), or by an endothermic chemical reaction. Any reaction with a lower reversible potential will still happen and provide heat energy proportional to the difference between the electrode potential and the isothermal potential, and the fraction of the current it consumes. By neglecting the electrochemical production of CO, the heat production in the system can due to the electrochemical reaction be expressed as below if we regard direct production of CF_4 as the most likely reaction (an expression for C_2F_6 will be completely analogous).

$$P = x_{\mathrm{CO_2}} \cdot \left(|E_C - E_A| + E^{iso}_{\mathrm{CO_2}}\right) \cdot I + x_{\mathrm{CF_4}} \cdot \left(|E_C - E_A| + E^{iso}_{\mathrm{CF_4}}\right) \cdot I \tag{4.4}$$

In addition to direct production of CF_4 it is thermodynamically possible to produce COF_2 (#3, Table 4.1) at elevated potentials, which has been demonstrated electrochemically by Calandra et al. [21]. This gas may then subsequently undergo a chemical reaction with carbon to produce CO and CF_4 (#4, Table 4.1). Together these reactions can be combined to a quasi-electrochemical reaction (#5, Table 4.1) with an equivalent isothermal potential accounting for the enthalpies of both reactions. Thus, an analogue expression regarding the heat production of the indirect CF_4 route can be made.

$$P = x_{\mathrm{CO_2}} \cdot \left(|E_C - E_A| + E^{iso}_{\mathrm{CO_2}}\right) \cdot I + x_{\mathrm{CF_4}} \cdot \left(|E_C - E_A| + E^{iso}_{\mathrm{COF_2 \to CF_4}}\right) \cdot I \tag{4.5}$$

The polarisation associated with the cathodic reaction is small, almost negligible. With this assumption, and taking into account that the anode and cathode have different shares of the entropic heat, the following equations describe the heat production at the anode/electrolyte interface

$$\begin{aligned} P_A &= x_{\mathrm{CO_2}} \cdot \Big(E_A + (E^{iso}_{\mathrm{CO_2}} - \Delta E^{total-anodic}_{Entropy\,\mathrm{CO_2}}) \Big) \cdot I \\ &\quad + x_{\mathrm{CF_4}} \cdot \Big(E_A + (E^{iso}_{\mathrm{CF_4}} - \Delta E^{total-anodic}_{Entropy\,\mathrm{CF_4}}) \Big) \cdot I \end{aligned} \tag{4.6}$$

$$\begin{aligned} P_A &= x_{\mathrm{CO_2}} \cdot \Big(E_A + (E^{iso}_{\mathrm{CO_2}} - \Delta E^{total-anodic}_{Entropy\,\mathrm{CO_2}}) \Big) \cdot I \\ &\quad + x_{\mathrm{CF_4}} \cdot \Big(E_A + (E^{iso}_{\mathrm{CF_4}} - \Delta E^{total-anodic}_{Entropy\,\mathrm{COF_2 \to CF_4}}) \Big) \cdot I \end{aligned} \tag{4.7}$$

where the ΔE terms relate to the difference between the total and anodic part of the entropic heat from Table 4.2.

The calculated heat production from Equations (4.6) and (4.7) for different fractions of CF_4 (as well as C_2F_6) production is shown in Figure 4.4. The value of the anodic potential is 2.59 V (taken from anode 2, Figure 4.3), the current is 2 A, the isothermal potentials were taken from Table 4.1, and the entropic voltage difference were taken from Table 4.2 (at low alumina when applicable), neglecting the fact that the numbers are produced for a slightly different electrolyte composition and temperature.

The mechanism for indirect production of CF_4 via COF_2 is unknown, but for direct production of CF_4 the actual fraction of the current would be expected to be small since this reaction tends to passivate the anode and eventually results in a blocking of the anode surface [79]. The event lasted for about 0.5 h before the current was stepped to 0.86 A/cm^2, which made both anodes go into full anode effect with soaring potentials.

4.3.2 Self-termination of partial PFC production

A similar event to that described above, but with a transition from what is believed to be partial anode effect and back to regular production was also observed. It was the same experiment as described previously, but after the full anode effect the cell was fed alumina. 1.5 g was added to compartment 1 and 3.2 g to compartment 2, making the new concentrations about 0.74 and 1.5 wt% for the respective compartments before electrolysis was continued. It was somewhat difficult to get the electrolysis started again, and especially the anode that saw the lowest alumina concentration had elevated potentials with fluctuations unlike what is common from CO/CO_2 bubble release on small graphitic anodes [80]. The fluctuations from this event have a steady linear rise for almost one second, with a plateau value of a somewhat shorter period, before dropping to the base level to repeat, while the common for bubble release on graphite is a close to linear increase with a sudden drop at the peak potential. The event is shown in Figure 4.5.

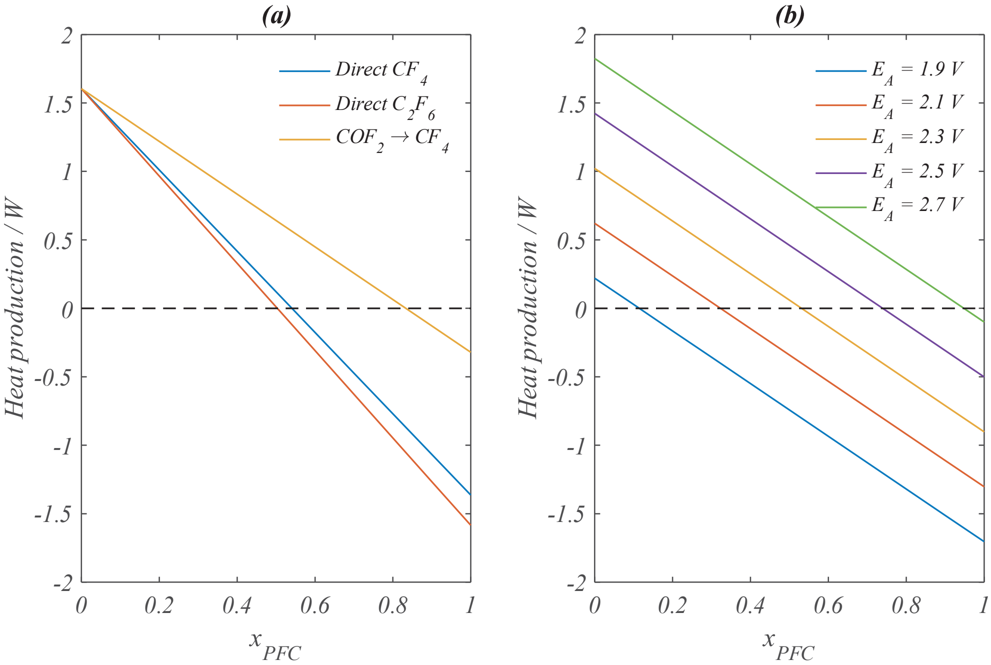

Figure 4.4: (a) Theoretical heat production at anode 2 considering both direct production of CF_4 and C_2F_6, as well as indirect production of CF_4 via COF_2. C_2F_6 production is not really possible at this anodic potential, except when very small partial pressures are considered. (b) Theoretical heat production of the indirect COF_2 route at different anodic potentials.

There is a lot of noise associated with the readings of the thermocouple from anode 1, especially before the drop in voltage. The reason for this is that corrosive electrolyte vapour has managed to enter the thermocouple chamber and started to dissolve the alumina tubing, decreasing insulation and making it react to current fluctuations. Nevertheless, the temperature trend should be clearly visible.

When the event happened the theoretical alumina concentration was 0 wt% in compartment 1, depleted 24 minutes earlier. Compartment 2 still had 0.33 wt% alumina. Anode 1 went from an average potential of 2.36 V, with peaks reaching 2.6 V, to 1.95 V, while anode 2 went from an average of 2.15 V, with peaks at 2.26 V, to 1.98 V. As discussed previously, the voltage of the non-dominating anode is probably elevated by the total system due to interconnectivity. The cell voltage seen by the PSU has in this plot been omitted for visibility, since it due to the resistors at this current has a value in the range 7.2 – 7.7 V, oscillating in the same manner as the anodes. The current at the same positions transitioned from an average of 1.29 to 1.30 A/cm^2 (0.8 % change) for anode 1

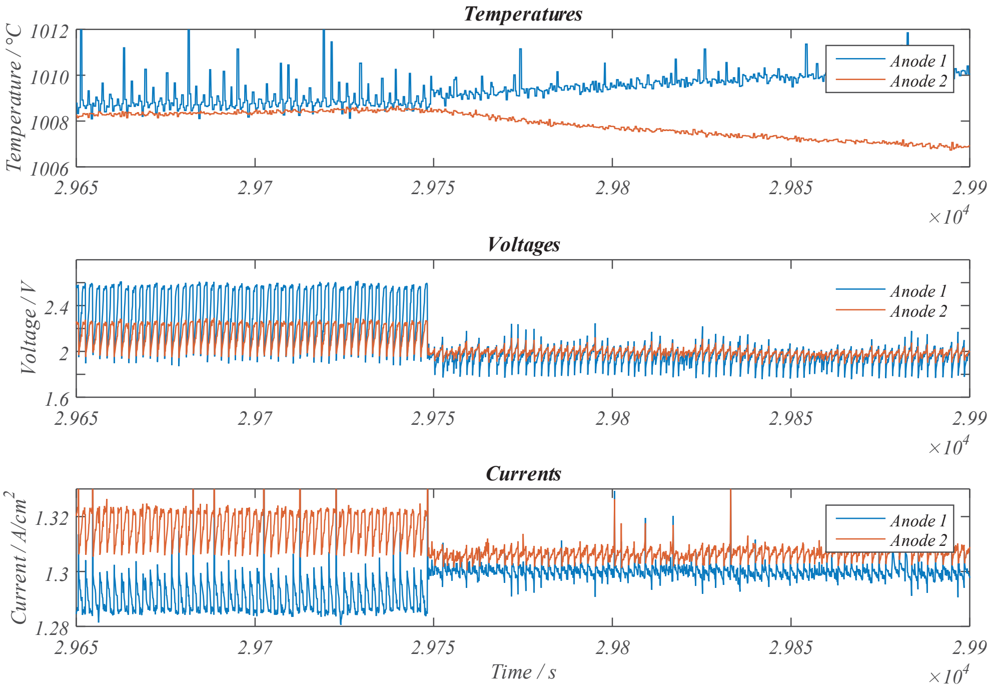

Figure 4.5: Current, voltage and temperature development over what is believed to be a change from some PFC production to regular CO/CO_2 evolution on anode 1, while anode 2 simply moves from regular production at a higher potential to a lower potential, thus decreasing heat output.

and 1.32 to 1.31 A/cm^2 (0.7 % change) for anode 2. The change that happened on anode 2 somewhat resembles that of anode 1 from Figure 4.3, albeit in an opposite manner. Previously a small increase in current and voltage gave a rise in temperature, this time a drop in the same variables produce a decrease in temperature, something that is probable if there is no change of reaction. Anode 1 observed a fair drop in voltage, especially when considering the plateaus of about 2.6 V, but a very small increase in current, clearly making the energy input before the change higher than after. The only way the increasing temperature of anode 1 can be explained is if it went from a higher energy requiring reaction to a lower one, especially since the energy input is lower after the change. Since the furnace is externally heated, any reaction will eventually find an equilibrium temperature, and hence; the new reaction does not need to have a positive heat production at the current voltage, it only needs to be less negative in order to give a positive change in temperature. It is the authors' opinion that anode 1 underwent a reaction mechanism change from partial production of PFC to what is believed to be entirely regular CO/CO_2. PFC production could have been facilitated both directly to CF_4 (#6, Table 4.1) or indirectly to CF_4 via

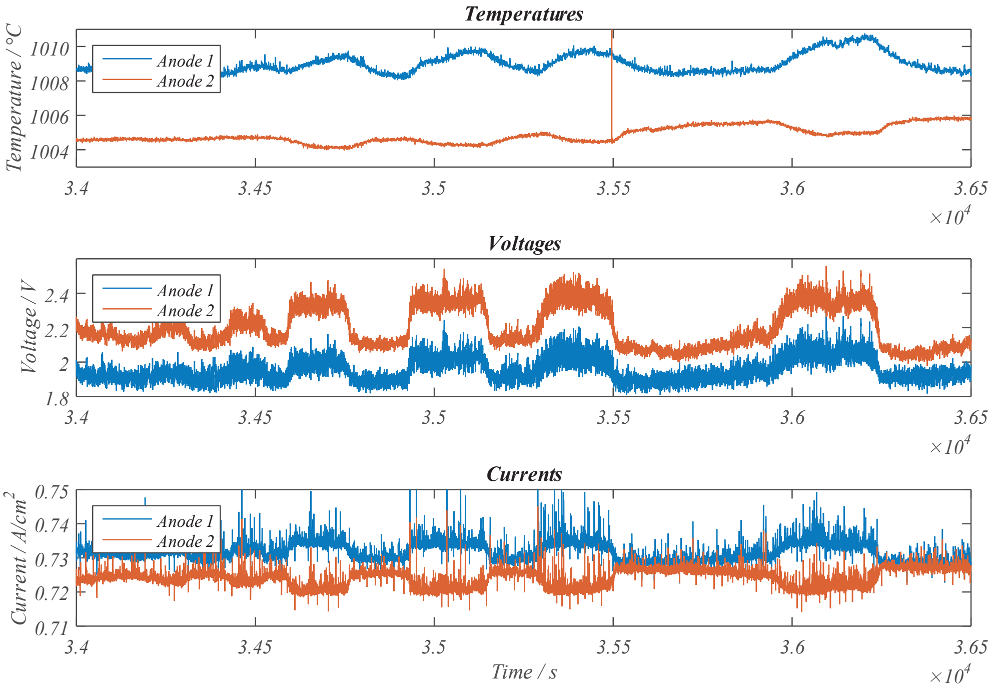

Figure 4.6: Current, voltage and temperature development for two anodes during electrowinning of aluminium. In the authors' opinion, Anode 2 changes between PFC and regular anode gas production with changes in alumina concentration close to the surface. Anode 1 is believed to just produce CO/CO_2 and any change in temperature is due to voltage (and current) fluctuations.

COF_2 (#3 – 5, Table 4.1), however, since the anode potential is so close to the reversible potential of direct CF_4 production the latter is more likely (due to the fact that some overvoltage is expected for the reactions).

4.3.3 On and off partial anode effect

Above, both the onset and self-termination of what is believed to partial anode effect has been described. Given the right circumstances, the current should decrease on an anode that experiences alumina depletion and rising voltages, provided that the other anode (or the rest) can take the extra load. And, should the supply close to the reaction interface replenish (convection/diffusion) it may be possible that the change could be reverted. An observation of such a mechanism is believed to be shown in Figure 4.6.

At this point (34 500 s), the theoretical amount of alumina was depleted 1.5 h and 0.9 h ago in compartments 1 and 2, respectively. Anode 2 is clearly struggling and is controlling the current uptake. It might have been expected that anode 1 should have shown this behaviour as it theoretically should be depleted first, but overall for the total experiment duration, compartment 2 had the least alumina. At around 34 500 s one of the first fluctuations is observed. There is an increase in voltage and a decrease in current, yet the temperature appears to be unaffected. This could be due to the fact that this is one of the shorter fluctuations (~ 100 s) and any change is too small to be noticed. However, the starvation of the cell could also be so small that only a slight elevation of voltage and decrease of current was enough to keep the reaction going. The voltage at this point could be too low to thermodynamically sustain another reaction, making a substantial change in heat output unexpected. On the other hand, the next fluctuations are longer and reach a higher potential, perhaps high enough to facilitate another reaction with a higher isothermal voltage (e.g. indirect production of CF_4 via COF_2). The fluctuations also appear to increase in duration (even though most are about 200 s), which suggest increasing depletion of alumina and a greater difficulty to return to normal production each time. In fact, both anodes entered full anode effect shortly after, as depicted by Figure 4.7.

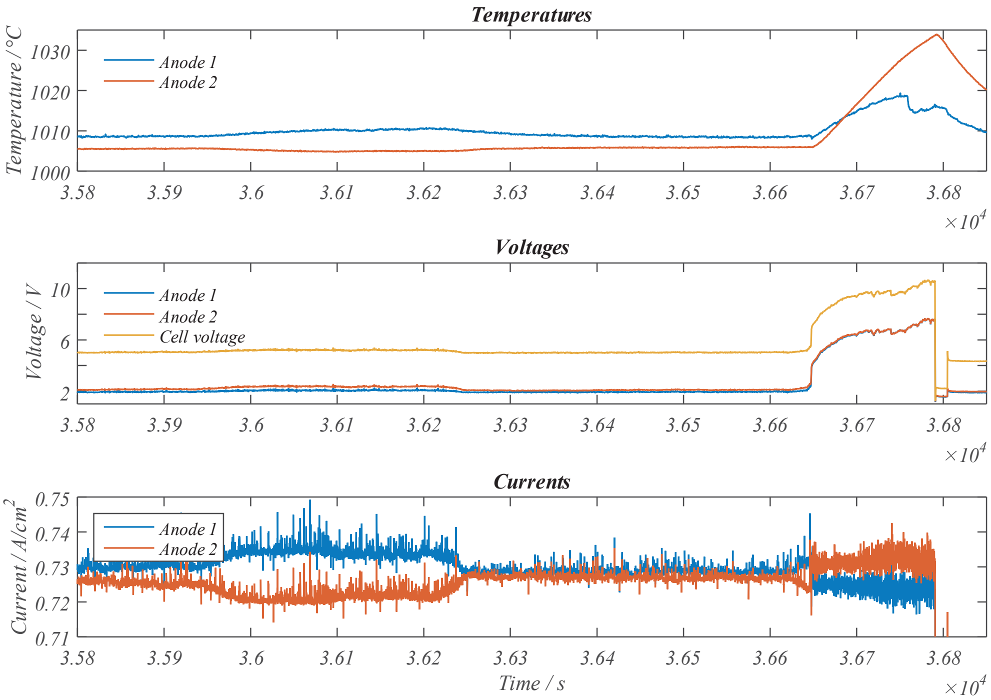

Figure 4.7: Current, voltage and temperature development for two anodes prior to onset of a full anode effect. Anode 2 struggled and let most of the current pass through anode 1, eventually anode 1 is unable to take the load and they both enter full anode effect with rising potentials.

The initiation of the full anode effect is clearly visible with the rapid increase in voltage at about 36 650 s. Just prior to that the data indicate that anode 2 wanted to continue the fluctuations in current and voltage it had executed for the previous ~ 0.5 h, however, anode 1 is not able to take the extra load this time and the voltage spikes. Such high voltages as observed will always generate a lot of heat and as a consequence the temperature will increase. To completely verify the authors' perception of the formation of PFC gases during the observed phenomena, gas analysis with high level of detection will have to be performed.

4.4 Conclusions

By using two anodes with internal thermocouples connected in parallel, it was possible to observe the current uptake when approaching alumina depletion. It was also possible to study what most likely is PFC production and the initiation of the anode effect. Normally, during an anode effect the potentials soar and so does the temperature. In the present paper, slightly elevated potentials went together with a decrease in temperature, indicative of a change to a reaction with a higher isothermal voltage, which is a property of all PFC producing reactions.

Acknowledgements

The authors would like to thank Norsk Hydro and the Norwegian Research Council for financial support.

Chapter 5

Anode Effect Initiation During Aluminium Electrolysis in a Two-Compartment Laboratory Cell

Henrik Åsheim[a], Thor A. Aarhaug[b], Espen Sandnes[a,c], Ole S. Kjos[b], Asbjørn Solheim[b], Steinar Kolås[c] and Geir M. Haarberg[a]

[a] *Department of Materials Science and Engineering, NTNU; Sem Saelands vei 2, N–7491 Trondheim, Norway*
[b] *SINTEF Materials and Chemistry, SINTEF; Strindveien 4, N–7465 Trondheim, Norway*
[c] *Hydro Primary Metal Technology, Øvre Årdal, Norway*

This paper has been published in TMS Light Metals 2016 [3]. However, note that some minor corrections have been made to this paper post-publication for spelling/typos and to improve clarity.

Abstract

Most laboratory cells used in the investigation of the alumina reduction process use a single anode. When investigating the initiation of the anode effect an approach with more than one anode might give better results, as the probability of obtaining partial anode effect is higher. Additionally, the design is closer to the industrial, where several anodes are connected in parallel. The system constructed consisted of two anodes in separate electrolyte compartments connected in parallel with a single combined cathode. The results indicate that an anode can go in and out of partial anode effect with little influence on the

current, although, kept untreated a full anode effect is likely imminent. The results also show that under certain current and alumina conditions, with only two anodes in parallel, an anode can handle approximately the whole load of a fully passivated anode for a certain time.

Keywords: PFC, Anode effect, NAE-PFC, Aluminium electrolysis, GHG, Low voltage AE

5.1 Introduction

Anode effects (AEs) have been a part of the aluminium production industry from its infancy. At some point in time a certain AE frequency was wanted as this meant the probability of having sludge in the electrolyte was limited. The big shift in working procedure came together with the invention of the transistor and the rise of the semiconductor industry in the second half of the 21^{st} century. Improved cell control and operation reduced the amount of anode effects, and by extension also the emission of perfluorocarbon (PFC) greenhouse gases CF_4 and C_2F_6. The International Aluminium Institute (IAI) in London reports a decrease in PFC emissions of more than 80 % from 1990 to 2010 [35]. Most of the improvements are the results of a decrease in the traditional AE where cell voltages would rise to levels of 8 V and above [9] with an accompanying erratic current distribution. However, the possibility of producing PFC gases is not governed by the cell voltage, but interfacial electrode potential, and recent investigations show that PFC evolution at normal cell voltages does occur and can be a substantial part of the total [1, 32, 34, 35].

5.1.1 Cell and anode voltage

Most laboratory cells for investigation of aluminium production are a simple electrochemical cell consisting of an anode and a cathode. The cell voltage of such a system would be comprised of the anodic and cathodic potentials, as well as the ohmic voltage drops (IR) over the electrolyte, through the anode, the bubble layer (bubble overvoltage) and cathode lining, as described by the following equation (external IR omitted)

$$V_{Cell} = E_A + |E_C| + I_{tot} \cdot (R_A + R_{Bubble} + R_{El.} + R_C) \tag{5.1}$$

An industrial cell, on the other hand, have a large number of anodes (20 – 40+) connected in parallel. In an ideal case all the parallel segments would be the same with the current shared evenly among them. However, in a real cell there will be as many different systems as there are segments, as discussed by Welch [81]. The anodes are consumed and their resistance will change throughout their lifetime and the number and size of anode slots will influence the bubble resistance. In addition, alumina concentration gradients can develop due to electrolyte mixing or poor feeding. The anode to cathode distance (ACD) may vary due to magnetohydrodynamics (MHD) or work practices.

To maintain the condition that the voltage over each of the parallel circuits is equal, the current can develop non-uniformly over the anodes. By considering the fact that molten aluminium is uniform and has very high electrical conductivity, its potential can be assumed equal for all parallel circuits. Split up on a per anode basis with partial currents the cell voltage becomes:

$$V_{Cell} = E_{A,i} + I_i \cdot (R_{A,i} + R_{Bubble,i} + R_{El.,i}) + |E_C| + I_{tot} \cdot R_C \tag{5.2}$$

From this it is understood that current-flow through an anode can vary with anode age, temperature, electrolyte and alumina mixing, and work practises like anode change. Any change of current through one segment will introduce an equal, but opposite change that will be divided over the rest of the segments, or parts of them. The cell voltage, on the other hand, will increase, but only marginally (up to a certain redistribution limit where the critical current density is reached). From this it is evident that a segment carrying low current will have an elevated interfacial electrode potential that can give rise to new reactions. Approximately all of this potential will be located on the anode, as little overpotential is associated with the cathode. In addition the cathode is interconnected by a highly conducting aluminium metal pad and the potential maintained equal for all parallel segments. If the anodic potential rise is of sufficient magnitude co-evolution of fluoride containing gases like CF_4 is possible. This again could give an increased interfacial resistance bringing forth an even larger drop in current and larger redistribution to other segments. Untreated, such an initiation of PFC evolution on one anode can propagate to a full cell anode effect [37].

In this work a two-compartment cell has been constructed in order to extract some of the properties of the parallel circuitry of the large industrial cell.

5.2 Parallel circuitry

5.2.1 Properties of parallel anodes

Consider a laboratory cell with a single anode running under constant current conditions. The cell will be described by Equation (5.1), and given it is properly fed by alumina the interelectrode potential will be of such a magnitude that only production of CO/CO_2 is thermodynamically possible. If the current is decreased, the voltage drop across the different resistances will decrease and the cell voltage will be lowered. This is quite contrary to an industrial cell where the cell voltage only changes marginally with current decrease on a single anode, and in fact to a higher value. Consequently, in an industrial cell this will introduce a redistribution of potential that will mostly be taken up by the anode that saw a lowering of current, perhaps making co-evolution of fluoride containing gases thermodynamically achievable. The laboratory cell circuit, on the other hand, will see little change. The lowering of current will lower the anodic potential slightly, but with just one segment the overall cell voltage will be lowered as the circuit is connected in series and voltage redistribution (to the anode) is not possible.

Another important difference between the single and multi-anode system is the pathway towards an anode effect. In the laboratory cell, when the alumina starts to be depleted, polarization will increase the possibility for other reactions. Evolution of PFC gases will begin to passivate the electrode. The set current has to pass through a smaller and smaller active area, beginning a transition that ultimately ends up in a full anode effect. In the industrial case, when polarisation increases due to limited alumina there will be a corresponding increase in equivalent resistance of that parallel segment, redirecting current elsewhere. Should the alumina concentration improve (as it might with less current) the cell can return to normal. In the meantime, it is likely that the affected anode will produce some PFC.

From the above reasoning, it is understood that normal cell voltage PFC production cannot easily be achieved on a single electrode system. For any redistribution of current to be possible a minimum of two parallel circuits are required. Additionally, the potential needs to be at a level where it is thermodynamically possible to produce PFC. Industrially this is accomplished through the sheer parallelism of all the different resistances in the cell. In the laboratory, this is perhaps easier realised by introducing resistances in series with the anodes, as shown in Figure 5.1.

The shunts are just precise resistances used to measure the current through each of the anodes. The electronic loads (ELs) depict the added resistances that are used to take the cell potential to industrial levels. Regular resistances can be used; however, ELs present better options for control.

All ELs provide a certain resistance to the system, but the way they do so depends on the control mode they are set to. In constant resistance (CR) mode the resistance is set directly. A redistribution of current will give a redistribution of voltage as the voltage drop over the resistance changes. In constant current (CC) mode the maximum current allowed through a segment is set. In this

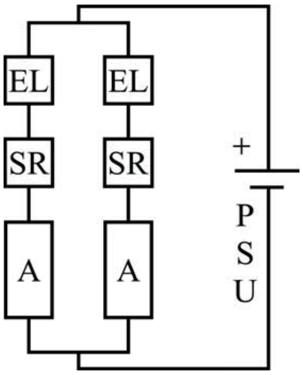

Figure 5.1: Electric circuit representation of the electrochemical cell. The shunt resistances (SR, $0.05\,\Omega$) are used to measure the current of each parallel circuit and the electronic loads (EL) are used to bring the total cell voltage to industrial levels. The anodes (A) are depicted as resistances for simplicity.

mode the resistance is as low as possible when the current is below its set-point, while it will increase to any possible resistance to keep this current set-point. This makes the mode unfit for anything other than setting a specific current and forcing the rest through the remaining parallel circuit(s).

Constant voltage (CV) mode works by setting a voltage drop, and the load will vary the resistance with the segment current to maintain this voltage drop. In this mode current can to some extent be easily diverted by changing the voltage, however, there will be no automatic redistribution of voltage, from load to anode, with an approaching AE within a segment. With loads of equal magnitude, the setup is no different from just connecting two anodes in parallel, except that the cell voltage will be higher, and more energy dissipated as heat. The extra voltage of the load will not be able to redistribute to the anode, making observation of PFC during normal cell voltages less likely. The CV mode can be improved by constructing a program that changes the set-point from certain system inputs. A possible method would be to have the load change to always keep the total cell voltage at a specific value, making voltage redistribution possible within a segment. This will additionally require very fast response for satisfactory results.

5.2.2 Virtual anodes

A future extension to the system is to increase the parallelism by adding purely electrical elements. When a large industrial cell runs ideally each segment will have an equivalent resistance. Similarly, the series combination of resistance, shunt and anode in the laboratory cell, will also have an equivalent resistance, that will henceforth be denoted the ideal segment resistance, R_S. Each of these electrical segments will act as a virtual anode. Consider a cell having n number of segments, where m of these segments are real live anodes. An equivalent resistance for all the virtual anodes can be created as shown in the following relation:

$$\frac{1}{R_{eq}} = \frac{1}{R_{S,1}} + \frac{1}{R_{S,2}} + \frac{1}{R_{S,3}} + \cdots + \frac{1}{R_{S,n-m}} \tag{5.3}$$

With an increasing number of virtual anodes the equivalent resistance will decrease rapidly, making it necessary with a very stable and precise resistor like an electronic load of good quality. Still, the system will be limited by the short circuit resistance of such a load, but also by the current capabilities of the power supply, since the amperage scales linearly with the number of segments. An example of a circuit diagram with two real anodes and a number of virtual anodes is depicted in Figure 5.2.

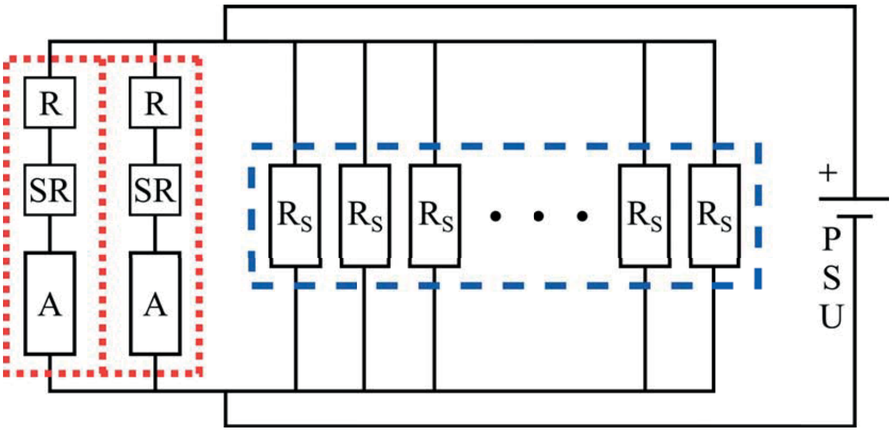

Figure 5.2: Circuit diagram of two real and a number of virtual anodes connected in parallel. R depicts resistances to bring the cell voltage up to industrial levels, SR are shunt resistances to measure the current going through the segment, and A are the anodes. $\mathrm{R_S}$ is the virtual segment resistance.

The system should work in the same manner as the two-segment one described earlier, however it is less likely to go straight to full anode effect when a real segment struggles, since there is a larger number of parallel circuits to redistribute the current across. The virtual anodes will naturally behave ideally at all times and cannot enter a full anode effect. In fact, the likelihood of very high potentials on the real anodes will also decrease with increasing number of virtual anodes, still slightly elevated industrial levels is more than enough to produce PFC.

5.3 Methods and equipment

5.3.1 Experimental cell and electrodes

The experiments were conducted in a regular laboratory furnace with closed atmosphere. The cathode was machined out of a cylindrical block of graphite (Schunk-Tokai). The block had a diameter of 90 mm and an inner height of 110 mm. The two electrolyte compartments were separated by a 5 mm wall. Two steel plates of the same shape (1 mm smaller on all sides) and 5 mm thickness was added to the base of the crucible to improve the cathode aluminium wetting and give a flat and uniform metal pad. A picture of the cathode and electrolyte container is given in Figure 5.3. Two purely round compartments could have made it possible to easily shield the sides from conducting any current; however, this concept was dropped as it would have made the electrolyte compartments too small to employ reference electrodes or gas collecting tubes.

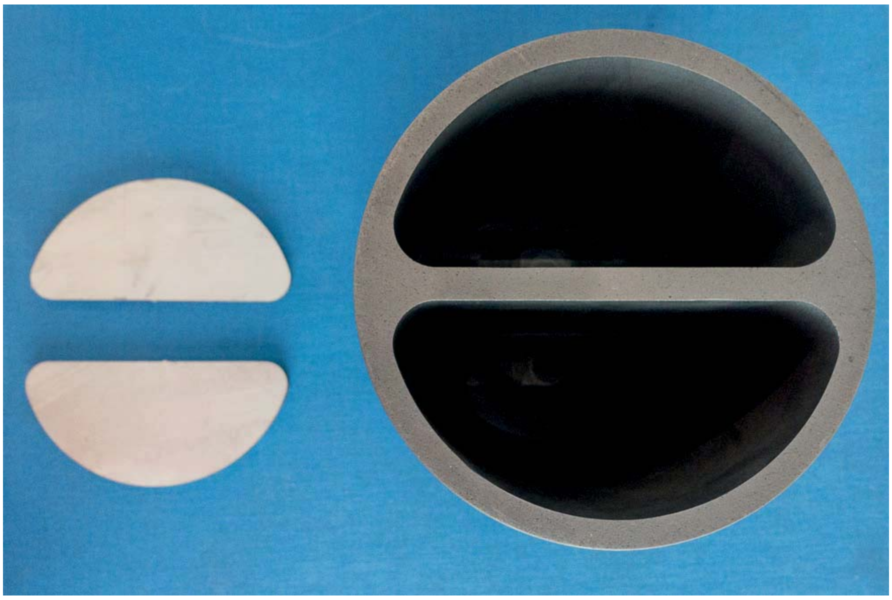

Figure 5.3: Graphite two-compartment crucible (cathode) and steel bottom plates.

The electrolyte consisted of cryolite (Aldrich), aluminium fluoride (industrial grade, sublimed at 1090 °C) and alumina (Aldrich). The cryolite ratio (CR, NaF/AlF_3) was set to 2.3 at the beginning of each experiment, but was slightly altered through the experiment with consumption of alumina. The amount of electrolyte in each sub-cell was about 100 cm^3 giving a bath height before electrode immersion of approximately 4 cm.

The anodes were made from graphite (Schunk-Tokai, ultrapure) rods (⌀ 16 mm) encased in hot-pressed boron nitride (Kennametal) rods (⌀ 22 mm). The BN insulation had a 45° inward slope towards the bottom of the anodes, making 3 mm of the vertical graphite surface accessible by the electrolyte, as can be seen from Figure 4. In total the initial active surface area was 3.5 cm^2. The sloping was added to better facilitate gas removal, as purely horizontal surface would create a BN gas trap after the initial graphite layers had been consumed. The anodes were connected electrically by a steel tube (⌀ 6 / 8 mm). This gave room inside for an alumina (⌀ 5 mm) 5-bore rod encasing both a thermocouple, and a sense wire that connected to a hole in the top of the anode carbon, giving potential and temperature readings as close to the reaction interface as possible. In some experiments, after ~ 5 h of run time electrolyte fumes were observed to penetrate the steel–graphite–BN coupling, dissolving the open-end alumina tube such that the thermocouple shorted with the anode, giving rise to incorrect readings. This has partially been solved by either using a closed end alumina tube or a BN shield. Unfortunately, in the latter case, there is no room for a sense wire so it has to be connected to the current lead, later subtracting the ohmic drop found by impedance measurement.

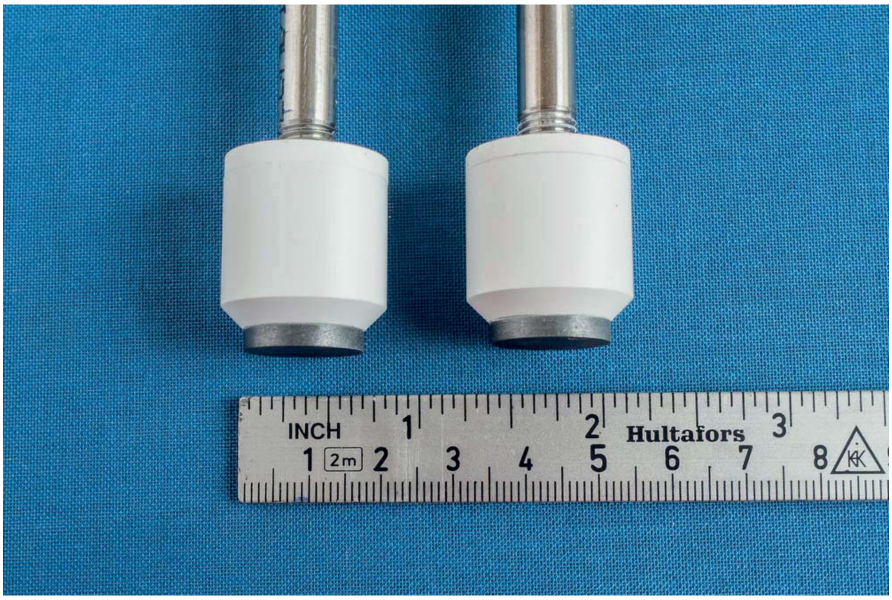

Figure 5.4: Anode made out of a graphite rod (⌀ 16 mm, active height 3 mm) shielded with a 3 mm wall of BN, 5 mm on top. The current is supplied by a hollow steel tube that can be fitted with a sense electrode and/or a thermocouple.

Two aluminium references were used, one for each electrolyte chamber. They were constructed from a milled out BN rod (⌀ 5 / 10 mm) of length 10 cm that was threaded onto a steel tube. Aluminium was placed inside, enough to make a pad of ~ 1.5 cm in height and a hole was drilled through the BN rod about 5 mm above the aluminium level. Electrical connection was provided with a tungsten wire (⌀ 1 mm) shielded in an alumina tube (⌀ 1.5 / 3 mm), except for the bottom 5 cm that would otherwise be in contact with electrolyte and aluminium, which had to be shielded with a BN tube of similar diameter. When doing experiments in alumina saturated melts, the outer BN and steel tube can be exchanged with an alumina tube for simplicity. A sketch of the complete electrode setup can be viewed in Figure 5.5.

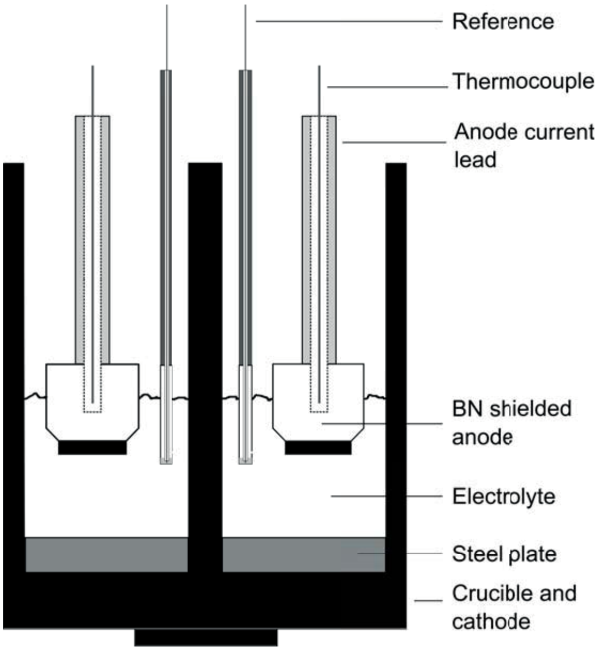

Figure 5.5: Experimental setup of two-compartment crucible. Each compartment has its own anode, reference and electrolyte.

5.3.2 Electrical equipment and data loggers

The current was supplied to the cell by a power supply (Agilent 6032A) controlled through LabView software. The positive side was split in two parallel sections, each connected through an electronic load (Agilent N3302A in Agilent N3301A chassis) and a shunt resistor (0.05 Ω) before passing through the anode, as showed in Figure 5.1. All data was logged with a National Instruments CompactRIO 9074 controller with analog voltage modules NI 9229 and NI 9205, as well as thermocouple module NI 9211. The equipment was controlled through

LabView and data was sampled at 10 Hz, except the thermocouple module that only updates at 3 – 4 Hz.

5.3.3 Gas analysis

Current voltage characteristics can provide valuable information about cell performance; nonetheless, in order to improve certainty about the reactions occurring at the electrode interface, gas analysis has to be performed to evaluate the gases produced at the anode. Two different mass spectrometers (MS), an FTIR and a CO/CO_2 logger were used in these experiments.

Gas samples were taken from ~ 2 cm above the anode to get reasonable response time (< 1 min) and sensitivity. In the case of the MS that sampled gas at ~ 20 ml/min rate, a thin alumina tube (⌀ 2 / 4 mm) was used. The tube would clog from evaporating electrolyte in 1 – 2 hours, requiring it to be cleaned or changed. The FTIR and CO/CO_2 logger were set to sample at ~ 80 ml/min and a wider alumina tube (⌀ 4 / 6 mm) was used to extract the gas. The furnace was purged with ~ 100 – 150 ml/min of argon, which was always kept higher than the combined sampling rate of the attached gas equipment, with surplus gas exiting the main exhaust. The main exhaust port could also have been used for gas analysis, which would have eliminated the clogging problem. However, the response time would have been severely decreased and it would have been difficult to distinguish from which anode gas evolution originated from.

5.4 Results and discussion

The network of parallel virtual anodes was discussed as a concept above, however, the data is not yet ready and the following section will only present results from the scenario with just two real anodes connected in parallel.

Figure 5.6 shows an event observed on a two-compartment cell with a shunt and an electronic load in series with each anode. The load was running in CV mode, the one previously argued to less likely give partial AE, with a potential of 1.4 V. The power supply ran under constant current conditions with a throughput of 6 A, enough to give a current density of 0.85 A/cm^2 on each anode (relative to initial geometric area). The voltage limit of the power supply was set to 10 V. The temperature set-point was ~ 1000 °C at idle.

At 28 730 s anode 2 was abruptly passivated and reduced to carrying less than 10 % of its initial load. On the other hand, anode 1 increased its current load by almost 90 %, and in most cases such a big change at this current density would tend to result in another fully blocked anode. The theoretical

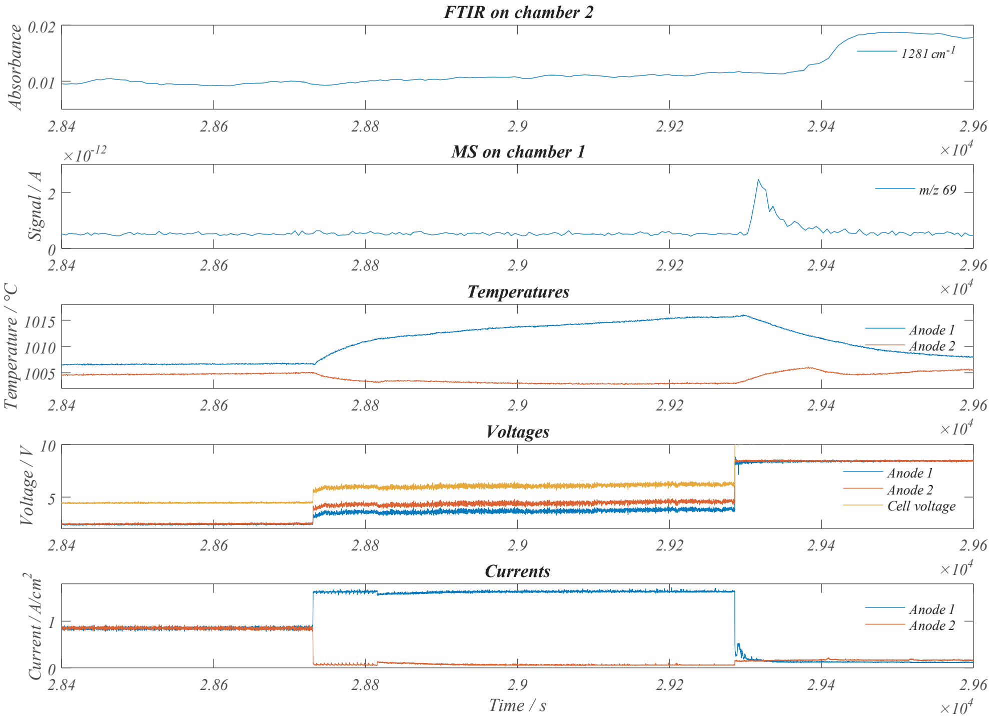

Figure 5.6: Development of current, voltage, temperature and PFC gas signals, as two anodes make the transition to AE and complete passivation. The cell voltage of the system maxed out at 10 V with the second transition to AE, thus limiting the current.

alumina concentration at this point was 1.6 wt% and 0 wt% for anodes 1 and 2, respectively, the latter theoretically depleted 50 minutes prior. The FTIR shows the gas analysis on anode 2 with 1281 cm^{-1} being the wavenumber of the strongest absorption line for CF_4. No significant change is visible in the absorbance, possibly because the gas tube was clogging up at about this time. The tube was eventually quickly exchanged just before 29 400 s, as can be seen from the cooling of anode 2 at this instance. With the new tube a shift in absorbance is observed; still, it is small and it can just be a new baseline stemming from disturbances introduced by the change.

Anode 1 carried almost the full load of the power supply for ~ 9 minutes before it eventually went on full AE. At this point no further redistribution of current was possible since anode 2 already was fully passivated. The MS shows gas analysis on anode 1 and mass to charge (m/z) ratio 69 is the strongest signal for CF_4/C_2F_6. The signal is not strong, but there is a significant shift just as anode 1 is passivated. After the initial passivation the current stabilized at about 0.12 A/cm^2 and the anode potential increased to approximately 8.5 V, while the PFC signal has dropped to below the noise level.

In another experiment the electronic load and shunt was replaced with a 1 Ohm resistor. The current was set to ~ 0.73 A/cm^2 per anode and the temperature set-point was 1000 °C at idle. An event believed to show an anode going in and out of partial anode effect is shown in Figure 5.7.

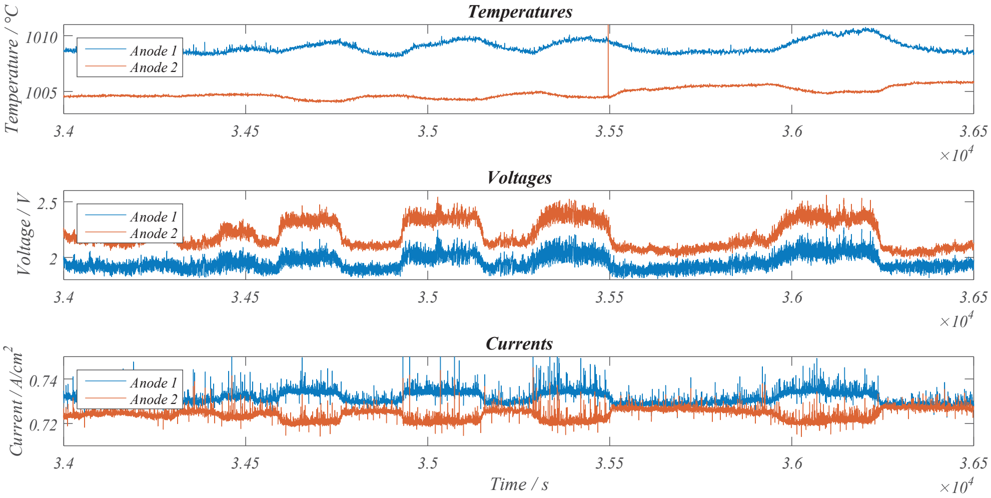

Figure 5.7: Development of current, voltage and temperature at two anodes connected in parallel. Anode 2 is believed to go in and out of partial anode effect.

At time point of 34 500 s the theoretical alumina concentration was depleted in chambers 1 and 2 approximately 1.5 h and 0.9 h ago prior to the onset of initial AE. Anode 2 is believed to be under intermittent anode effect in the areas where the observed current is lowered. The current shift is only a mere 10 mA/cm^2, however it is believed that this change is sufficient for alumina concentration to restore and the anode effect to be extinguished, at least temporarily. The voltage drop related to the extra load on the parallel circuits will in this case fluctuate completely as the current does, giving a slightly decreased voltage drop with decrease of current and a corresponding increased voltage drop with increase of current. Thus, by considering segment 1 a slightly higher voltage drop over the load is expected; additionally, the potential of anode 1 is expected to increase with increased current, albeit just marginally. Nonetheless, the potential over anode 1 increased by ~ 100 mV, which is more than what is expected from a small increase in current. The extra shift can be due to degree of parallelism of the system as the total cell voltage is shifted by anode 2's reach for new reactions by increased polarisation. It is expected that a larger degree of parallel circuitry would influence the voltage of non-AE anodes less.

The cell went on full anode effect on both anodes about 150 s after the events shown. Unfortunately gas analysis data are not available to confirm the onset of anode effect.

5.5 Conclusions

By employing a laboratory cell with more than one anode it is possible to study how an anode effect on one anode (either partial or full) affects the rest of the system. Gas analysis can be used to verify the reactions accompanying certain events. Robust laboratory equipment and a well-designed system are needed to observe gas constituents at low concentrations in a relatively low-amperage laboratory cell.

Acknowledgements

The authors acknowledge the financial support received from Norsk Hydro and the Norwegian Research Council.

Chapter 6

Partial Anode Effect in a Two-Compartment Laboratory Alumina Reduction Cell

Henrik Åsheim[a], Thor A. Aarhaug[b], Wojciech Gębarowski[a], Espen Sandnes[a], Asbjørn Solheim[b] and Geir M. Haarberg[a]

[a] *Department of Materials Science and Engineering, Norwegian University of Science and Technology, N–7491 Trondheim, Norway*
[b] *SINTEF Materials and Chemistry, SINTEF, N–7465 Trondheim, Norway*

This paper has been published in TMS Light Metals 2017 [4]. However, note that some minor corrections have been made to this paper post-acceptance for spelling/typos and to improve clarity.

Abstract

Most laboratory systems investigating the aluminium production process utilize a single anode set-up. When approaching alumina depletion under constant current conditions in such a system, the potential will increase to high levels ($>$ 10 V) and initiate an anode effect and perfluorocarbon generation. However, it has been discovered by industrial measurements that perfluorocarbon generation may also occur at normal cell voltages. With the use of a two-anode setup in parallel with an electronic load this phenomena was investigated in the laboratory. The results indicate that as long as the rest of the cell can acquire the extra load, partial passivation of one or more anodes is possible and can be accompanied by small amounts of PFC evolution (0 – 3 ppm mol CF_4).

Individual anode potentials can be highly elevated, albeit the changes get buried in the total cell voltage. Only when the total load becomes too large the voltage rises abruptly and substantial amounts of PFC can be produced ($\gg$ 1000 ppm mol CF_4).

Keywords: PFC, Partial Anode Effect, Non-AE PFC, Low Cell Voltage PFC, Aluminium Electrolysis

6.1 Introduction

Aluminium is produced industrially by reduction of alumina from a melt based on $Na_3AlF_6-AlF_3-Al_2O_3$, often together with several wt% CaF_2 and/or MgF_2 at about 960 °C [6]. Under normal conditions aluminium metal is produced at the cathode and CO_2 with a fraction of CO is formed at the anode [82, 83]. The reversible potential for the reaction producing CO_2 (6.1) at the anode is about 1.2 V. Due to a rather large anodic activation overpotential [84] and several ohmic drops through the electrolyte and cell, the total cell voltage is usually about 3.8 – 4.5 V.

$$2\,Al_2O_3 + 3\,C = 4\,Al + 3\,CO_2 \quad E^0_{1000\,^\circ C} = -1.17 \text{ V} \tag{6.1}$$

Should the alumina content drop too much, polarisation will increase to sustain the reaction, eventually extending so far that other reactions become possible. Feasible combinations include the two main anode effect reactions producing the perflurocarbons (PFCs) CF_4 (6.2) and C_2F_6 (6.3) [17, 75], although, before the potential reaches such levels the anodic production of COF_2 (6.4) is thermodynamically also possible [21]; a gas that readily reacts with water, carbon, or even self decomposes at working temperatures.

$$\begin{aligned} Na_3AlF_6 + \frac{3}{4}\,C &= 3\,NaF + Al + \frac{3}{4}\,CF_4 \\ E^0_{1000\,^\circ C} &= -2.56 \text{ V} && (6.2) \\ Na_3AlF_6 + C &= 3\,NaF + Al + \frac{1}{2}\,C_2F_6 \\ E^0_{1000\,^\circ C} &= -2.76 \text{ V} && (6.3) \\ \frac{1}{2}\,Na_3AlF_6 + \frac{1}{4}\,Al_2O_3 + \frac{3}{4}\,C &= \frac{3}{2}\,NaF + Al + \frac{3}{4}\,COF_2 \\ E^0_{1000\,^\circ C} &= -1.90 \text{ V} && (6.4) \end{aligned}$$

PFCs have gained much focus from governments and environmentalists in later years due to their high global warming potentials and long atmospheric lifetimes, making them potent greenhouse gases [39]. The existence of PFCs not related to the conventional anode effect with voltages of 8 volts and above, combined with an erratic current distribution, has been documented for a variety of different technologies [1, 33–35]. Industrial measurements have shown that PFC production may begin on one anode and under the right conditions propagate to the entire cell [37].

6.1.1 Components of the cell voltage

Consider a laboratory cell with one anode and a cathode. The total cell voltage of that system would be composed of the anodic and cathodic electrode potentials, together with ohmic drops (IR) over the electrolyte, the bubble layer, through the anode carbon and cathode lining, as well as any other external current carrying parts (omitted in this representation). It can be described by the following relation

$$V_{Cell} = E_A + |E_C| + I_{tot} \cdot (R_A + R_{Bubble} + R_{El.} + R_C) \tag{6.5}$$

An industrial cell, however, has a large number of anodes ($20 - 40+$) connected in parallel. In the ideal case all the parallel segments are the same and share an equal part of the total current. Nevertheless, reality is that there are as many different cases as there are anodes [3, 76]. Anodes are being consumed and their resistance, R_A, will vary throughout their lifetime, wear of anode slots will vary and this will influence bubble overvoltage, and the anode to cathode distance (ACD) might vary with magnetohydrodynamics (MHD). Alumina concentration gradients can also develop due to poor mixing, blocked feeder holes or work practices. Keeping in mind that the voltage over the segments has to be equal, it is clear that the current can develop unbalanced over the anodes. Inasmuch as the molten aluminium is uniform and inhabits high electrical conductivity, its potential can be assumed equal for all parallel circuits. Hence, on a per anode basis the cell voltage becomes:

$$\begin{aligned} V_{Cell} = {} & E_{A,i} + I_i \cdot (R_{A,i} + R_{Bubble,i} + R_{El.,i}) \\ & + |E_C| + I_{tot} \cdot R_C \end{aligned} \tag{6.6}$$

Thus it can be inferred that the current-flow through an anode will vary with several factors like age, temperature, electrolyte mixing and work practices like anode change. Any change in current of one segment will induce an equal and opposite change that will be distributed over the other segments, or parts of them. Any current redistribution will produce an increase in cell voltage, an increase that diminishes as the number of segments increases, as modelled by Wong et al. [85] for two theoretical smelters. It is hence evident that a segment carrying low current will have an elevated interfacial electrode potential, and since little overpotential is associated with the cathode it will display as heightened anodic potential. If the anodic potential rise is of sufficient magnitude co-evolution of fluorine containing gases like CF_4 becomes possible.

6.2 Methods and equipment

6.2.1 Cell and electrodes

The experiments were conducted in an electrically heated vertical laboratory furnace with a mullite inner tube and alumina heat radiation shields. A cylindrical block (⌀ 90 mm) of graphite (Schunk-Tokai) was used as cathode material. From this block two equally shaped electrolyte compartments were machined, with a depth of 110 mm and separated by a 5 mm wall. Two matching steel plates (~ 1 mm smaller than electrolyte compartment, 5 mm height) were added to the crucible base to improve cathode/aluminium wetting and give a flatter and more uniform metal pad. The non-circular shape of the electrolyte compartments makes it difficult to shield the sides from stray currents, however, it was necessary to include space for reference electrodes and gas sampling tubes.

The electrolyte was made up of cryolite (Na_3AlF_6, Aldrich), aluminium fluoride (AlF_3, industrial grade, sublimed at 1090 °C) and alumina (Al_2O_3, Merck / Aldrich). The alumina concentration in the different compartments was often selected as 5 wt% and 1 wt% at the beginning of an experiment, with occasional additions after heavy anode passivations. The cryolite ratio (CR, NaF/AlF_3) was adjusted to 2.3, being somewhat altered throughout due to consumption of alumina and evaporation of electrolyte constituents [10]. All electrolyte components were dried at 200 °C prior to the experiments.

The anodes were made from graphite (Schunk-Tokai) cylinders (⌀ 22 mm, height 40 mm) that were electrically connected by a steel tube (⌀ 6 / 8 mm). The anodes were submerged 10 mm, giving an approximate surface area of 10.7 cm^2. Within the steel tube and 10 mm into the anode carbon thermocouples were placed to read the anode temperature. Additionally, a short piece of alumina tube (50 mm, ⌀ $>$ 8 mm) was placed around the steel current carrier just above the anode carbon to protect it from corrosion due to electrolyte splashing or condensation.

Two aluminium reference electrodes were used, one for each electrolyte compartment. The bottom exterior was produced from a milled out BN rod (⌀ 5 / 10 mm) of length 70 mm that was threaded on to a steel tube (⌀ 8 / 10 mm). Aluminium to cover 15 mm of inner height when molten was placed inside the BN rod and a hole (⌀ 2 mm) was drilled 5 mm above the aluminium level.

Electrical connection was provided with a tungsten wire (⌀ 1 mm) shielded by an alumina tube (⌀ 1.5 / 3 mm), except for the bottom 5 cm that would otherwise be in contact with electrolyte and aluminium, which was shielded with a BN tube of similar diameter. A sketch of the complete electrode set-up can be viewed in Figure 6.1.

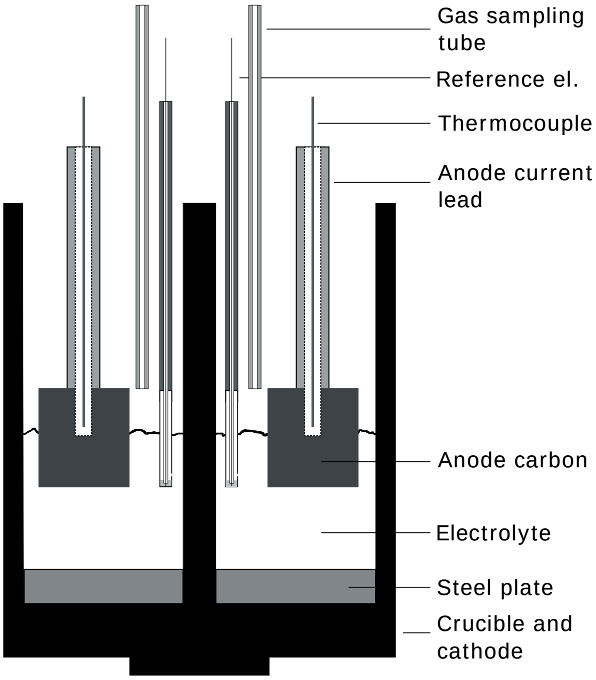

Figure 6.1: Experimental setup of two-compartment crucible. Each compartment has its own anode, reference electrode and electrolyte. (Reference and gas sampling tube placed beside anode for clarity, in reality they are in front and behind.)

6.2.2 Electrical equipment and data loggers

The current was supplied with a system power supply (Agilent 6682A, 240 A). The positive terminal was split in three parts; the two real anodes and load balancing with “virtual anodes” by a high amperage electronic load (Chroma 63201, 300 A). Electronic loads (Agilent N3302A in Agilent N3301A chassis) were also added in series with the real anodes to add an ohmic drop so the total cell voltage was elevated to industrial levels. All loads were set to operate in constant resistance mode. A diagram of the electric circuit is presented in Figure 6.2.

Data were logged with National Instruments CompactRIO 9074 with modules

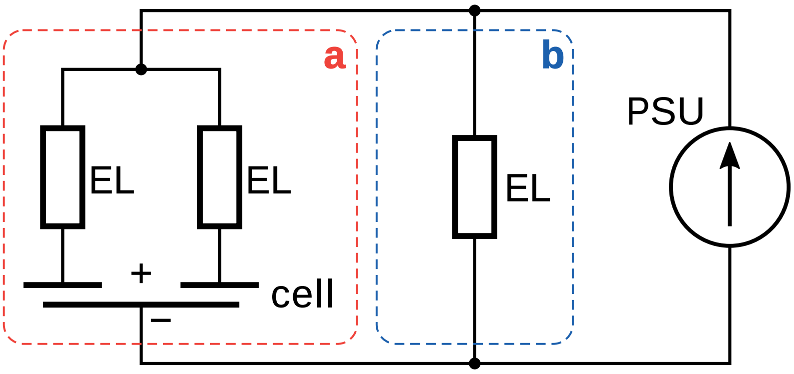

Figure 6.2: Electric circuit representation of the electrochemical cell. EL – electronic load, PSU – power supply; a) two electrodes under test, b) simulation of anodes in parallel.

NI 9229 and NI 9205 for voltage logging, as well as thermocouple module NI 9211. The currents flowing through the different segments were captured from the current monitor outputs on the loads. The Chroma load output was passed through a polynomial function to correct for the slightly non-linear output. Data were sampled at 10 Hz (thermocouple data limited to 3.5 Hz) through LabView software.

6.2.3 Gas analysis

Two FT-IRs were used in these experiments, one for each anode chamber. They are somewhat dissimilar as two equal instruments were not available. Details on the equipment are given in Table 6.1. Gas samples were taken from about 3 cm above the electrolyte surface, approximately 0.5 cm off the side of the anodes.

Table 6.1: Specifications of the two different FT-IRs.

Parameter		Gasmet CR 4000	ProtIR 204M
Cell volume	/ l	0.4	2.7
Path length	/ m	5	6.4
Spectral range	/ cm^{-1}	600 – 4200	400 – 8000
Resolution	/ cm^{-1}	8	1
Absorbance		0 – 3	−2 – 4
Detector		MCT–LN2	MCT–Peltier

The furnace was continuously being served argon at a small overpressure. This pressure produced a flow of ~ 300 Nml min^{-1} through the ProtIR connected to chamber 1 (ch. 1), and a flow of ~ 150 Nml min^{-1} through the Gasmet of chamber 2 (ch. 2). No other exhaust ports were being used. The gas to each instrument passed through two 15 µm particle filters connected in parallel, a Drierite® filter for water removal, and an active alumina filter for HF removal. The flow rate through the instruments were approximately the same during electrolysis. Gas production during electrolysis at 10 A was approximately 35 Nml min^{-1} when considering CO_2 and CF_4, and twice that with CO as the only anode product. An Environics 4000 gas mixer was employed for calibration purposes together with a 5 ppm mol CF_4 reference gas cylinder.

6.3 Results and discussion

The response and dynamics of the gas analysis equipment is given in Figure 6.3 for the Gasmet FT-IR. It shows the absorbance of a 5 ppm mol CF_4 reference gas cylinder that was diluted to concentrations 1 through 5 ppm mol with an Environics 4000 mixer. Gas was input at the anode position of the furnace at ambient temperature. T_{90}-response for the Gasmet and ProtIR is estimated to be 248 s and 300 s, respectively, with first visible change occurring from 106 s and 50 s.

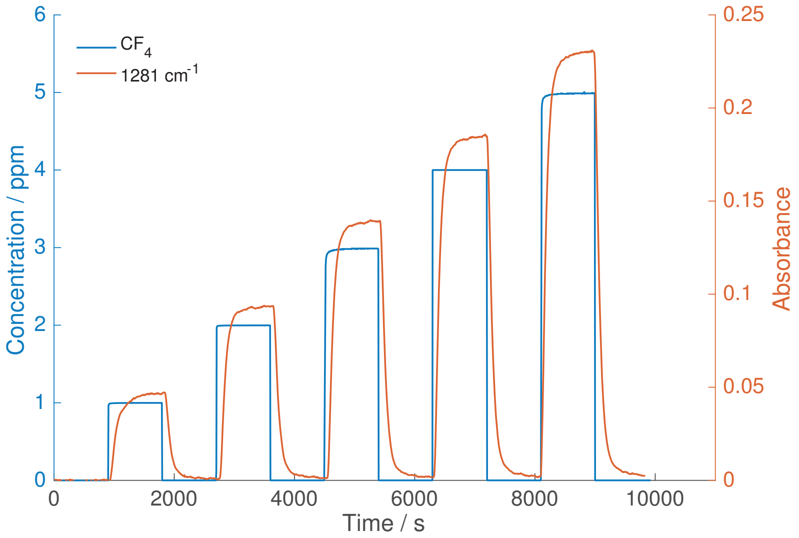

Figure 6.3: Response of Gasmet FT-IR when applying 5 ppm mol CF_4 reference gas diluted through Environics 4000 gas mixer to different concentrations. T_{90}-response of about 248 s.

The most prominent absorption line for CF_4, 1281 cm^{-1}, is plotted for both

Gasmet and ProtIR in Figure 6.4. The lower concentrations (1 ppm to 5 ppm) for Gasmet are data produced with the gas mixer, all the others points (Gasmet and ProtIR) are OEM reference calibration data. Beyond the concentrations presented the absorbance data quickly become increasingly non-linear and for higher concentrations other absorption lines have to be considered.

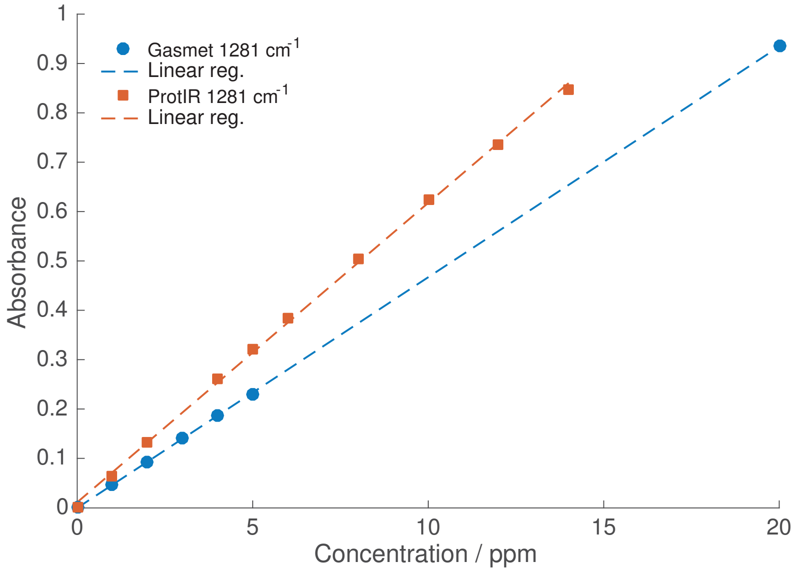

Figure 6.4: Absorbance response of CF_4 at wavenumber 1281 cm^{-1} for different FT-IRs. Beyond these concentrations the absorbances at this wavelength became increasingly non-linear.

The same mixing procedure as that of Figure 6.3 was conducted in-between electrolysis with the furnace heated to 1000 °C, and no CF_4 response was visible on either FT-IR. Since the anode positions were now occupied by anodes, the pathway between inlet and detector became longer, as it passed from the bottom of the furnace, past heat radiation shields and around the crucible before it finally left through the sampling tubes by the anodes. Response times can thus not be directly compared, but the main goal was to see if PFC was detected from a defined source. The CF_4 might decompose over solid substrates like tungsten and steel as discussed by Rogers et al. [46], or over SiO_2 according to Siegemund et al. [86], and decomposition over activated alumina has been shown by Thonstad et al. [48]. Øygard et al. [87] extracted gas both directly from the anodes and from the gas duct and found that a large part of the PFC decomposed on its way out of the cell. Thermal decomposition has also been found to begin at about 800 °C [86]. In the furnace the radiation shields were composed of alumina and the tube was made from mullite, a mineral of alumina and silica. From an environmental point of view it is good that the PFCs get broken down, however, it also makes it difficult to investigate conditions with low concentration PFC production. High temperature residence time is a key parameter that needs to be kept low in order to detect the lower concentrations.

Figure 6.5 shows an IR spectrum recorded directly after 5 g alumina (undried, ~ 1 wt% H_2O, whereas “dry” alumina has been dried at 200 °C) was fed to the cell as it was starving. Overlaid is a plot of a 1000 ppm mol CH_4 reference that shows a clear match. Several methanation routes are possible e.g. $H_2O + C = CO + H_2$ and subsequently $H_2 + C = CH_4$ as discussed by Walker et al. [88]. Before alumina addition the corresponding anode had previously run into AE and was on a “passivation” current of 3.1 A (29 % of initial) with an anode potential of 4.6 V. The abrupt initial partial passivation produced a peak of 1.5 ppm mol CF_4 while it thereafter hovered around 0.2 ppm mol for ~ 1 h. During feeding of (wet) alumina there is a small peak at 1281 cm^{-1} not well accounted for in the methane reference spectrum. Inasmuch as water is not visible in the spectrum, the added absorption is considered to be due to presence of CF_4. Multiplying the reference spectra with 1.25 to make a better overlap and then taking the difference in absorbance, gave a coarse estimate of 3.3 ppm mol CF_4 released during feeding. Current and voltage changed to 4.9 A and 4.1 V for that particular anode. No PFC was found to be released when feeding dry alumina.

Figure 6.6 shows an event from the two-compartment set-up where at 9800 s the external electronic load has its resistance doubled in a two step manner (too low voltage set-point for PSU gave short downward bump in load current before treated). In practice this halved the number of “virtual anodes” (from 20:2 to 10:2) and approximately doubled the pressure on the real elements. Before this step the two anodes had been partially passivated for 22 min (Anode 1) and 32 min (Anode 2), both passing about 1.7 A (16 % of initial). The cell voltage rose from 5.4 to 10.7 V and initiated a rocking motion of both current and voltage for Anode 2, not unlike the oscillations seen by Åsheim et al. [2] previously, albeit at less elevated potential. Anode 1, on the other hand, just noticeably increased to between 2 and 3 A.

Anode 2 is clearly producing a lot of PFC, the CF_4 absorbance detected is well beyond the 0 – 20 ppm linear calibration for CF_4 at 1281 cm^{-1}. Absorption at 1536 cm^{-1} was used (using linear regression of OEM absorption data from 20 and 100 ppm mol CF_4 references) to estimate the concentration to upwards of 1400 ppm mol at an absorbance of about 0.2. The absorbance also markedly increased for CO, which is not uncommon [89], while CO_2 appeared to be produced to a lesser extent. At Anode 1 there is only marked change in CO and to some extent CO_2, no visible PFC detection. In an industrial cell Anode

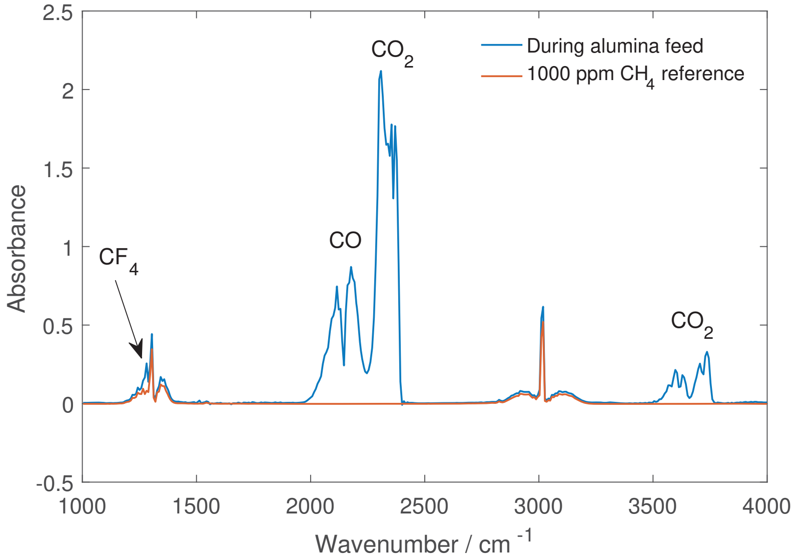

Figure 6.5: IR spectrum from Gasmet during feeding of (wet) alumina with an overlaid 1000 ppm mol CH_4 reference. There is a clear overlap in the CH_4 absorption region around 1300 and 3000 cm^{-1}, and multiplying the reference spectra with 1.25 provides an even better overlap. The rest of the spectra is CO/CO_2 with a small CF_4 peak at 1281 cm^{-1}.

1 would have been influenced by mixing from the oscillating gas production at Anode 2, but with completely separated chambers this is not possible here. The discrepancy at 10 850 s is because the large EL was overloaded when trying to return to the former 20:2 anode setting in one go, and it instead had to be stepped to not trigger over-current protection.

Figure 6.7 shows an anode going from partial passivation to regular production and back to partial passivation again with a 20:2 ratio between virtual elements and real anodes. Entering the plot both anodes had previously been passivated and subsequently fed more alumina, with the theoretical concentration being 4.5 wt% and 3.7 wt% for ch. 1 and ch. 2, respectively. Throughout, compartment 1 was theoretically depleted at 21 800 s while compartment two had a theoretical concentration of 1.6 wt% at the right end of the plot. While Anode 2 looks steadily passivated with a current of about 2.3 A, Anode 1 was initially wobbling between 7.5 and 10 A before it observed about 50 % partial passivation and a much higher noise. At the same time there was a marked drop in CO and a very tiny increase of PFC spectral lines. In this experiment only the Gasmet FT-IR was employed, and placed in ch. 2; even so, it is evident from the gas analysis that without the second FT-IR much of the gas produced in ch. 1 also flow to the FT-IR on ch. 2. It is believed that some CF_4 was formed under

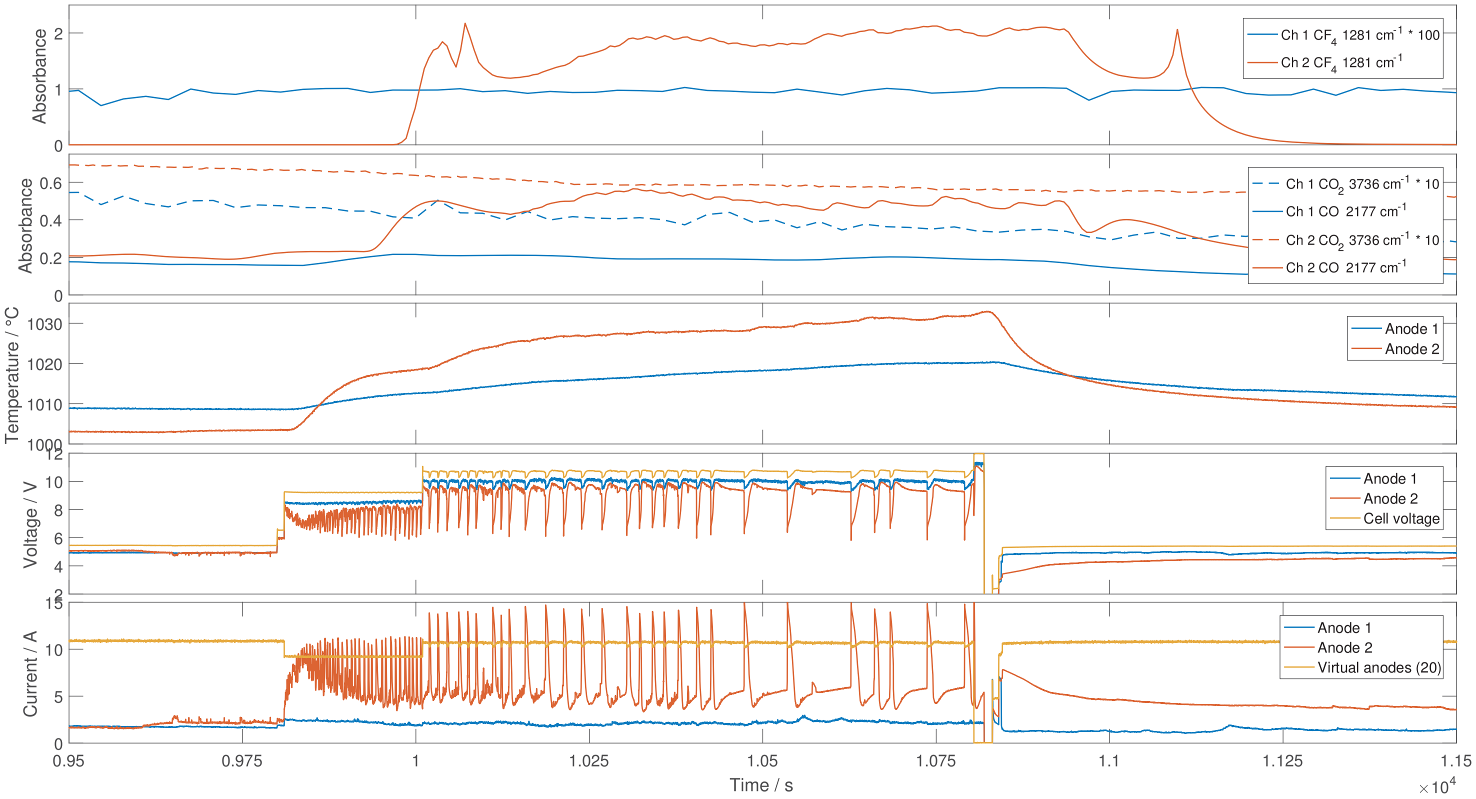

Figure 6.6: Two anodes that already were partially passivated have their degree of parallel elements decreased by almost half. Anode 2 started to oscillate in current and voltage and produced upwards of 1400 ppm mol CF$_4$. Anode 1 showed no detectable change in CF$_4$ level. Note the multiplier on some of the absorbance traces and that the “Virtual anodes (20)” current represent 1/20 of the total current passing through the electronic load connected in parallel with the real anodes.

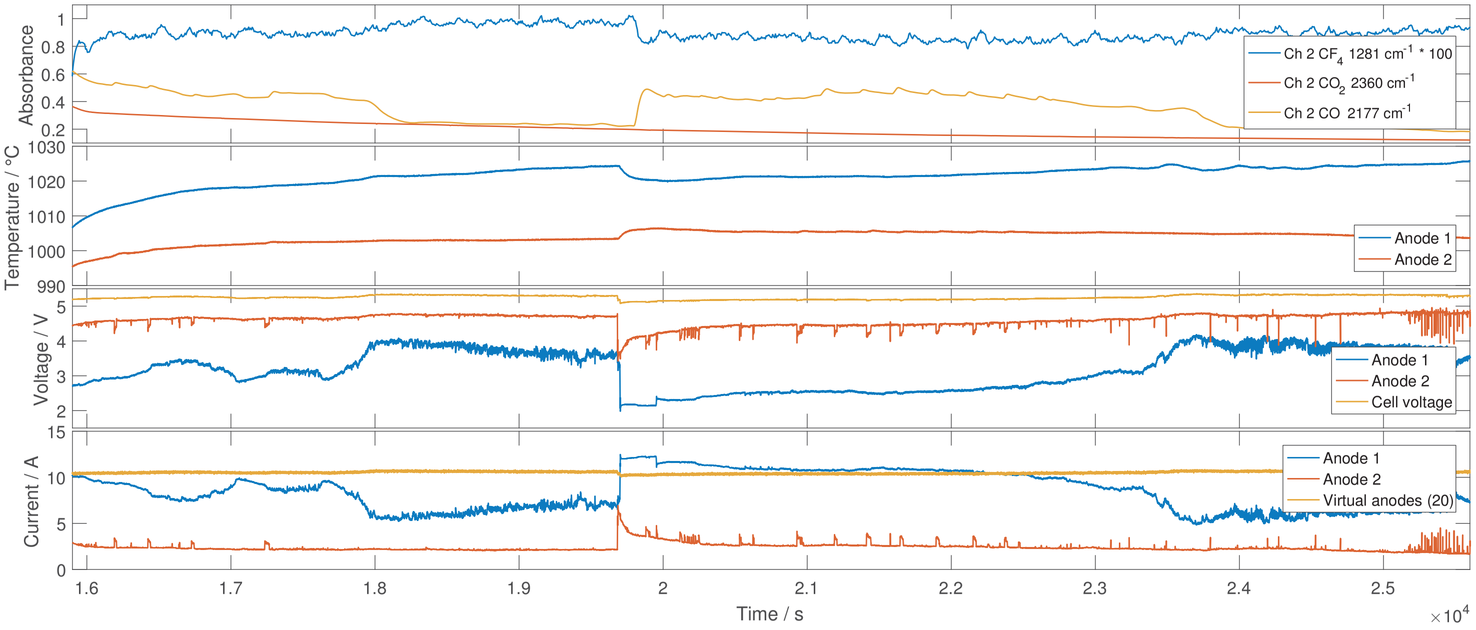

Figure 6.7: Current, voltage, gas and temperature profiles of two anodes. Anode 1 experienced a change from regular production, through partial passivation, back to regular production before ending up at partial passivation again. Absorbance of CF_4 is very slightly elevated. Anode 2 was passivated to about 20 % of the initial current throughout the plot with just a few current humps that get visualised as small hills in CO absorbance. Note the multiplier on one of the absorbance traces.

these conditions, and mostly at Anode 1 with the higher current. However, the added gas path and residence time are not beneficial for detection, as discussed above.

Sometime before 20 000 s there is a big change in the system that occured without any personnel intervention and Anode 1 spiked back to regular production with much less noise. The increased production most likely gave an initial pressure effect that is visible in the FT-IR data. Anode 2 also peaked in current, albeit quickly crept back to its former value with only some distant spikes that are visualised as humps in the CO gas data. After a while Anode 1 was depleted of alumina and turned back to partial passivation with a throughput of 5 – 7 A, again coupled with a very slight increase in CF_4 absorbance. Due to the degree of parallel elements of the system, the cell voltage merely varied between 5.09 and 5.34 V during these events.

Clearly, as long as “the rest” of the cell is able to acquire the electrical current, several anodes can be partially, or even fully passivated. A full conventional anode effect will not be initiated until the critical current density has been reached on a large number of anodes, producing a large upswing in voltage. Such a condition cannot be reached in the present set-up with a high degree of parallel segments with electrical elements (20 : 2). The virtual anodes can easily accompany the extra current of the real anodes with a relatively small increase in voltage (~ 0.5 V). Only when approximately halving the number of “electrical segments” (10 : 2) is something resembling the conventional industrial anode effect visible, with high cell voltage ($>$ 10 V), considerable production of CF_4 and an erratic current distribution. Even still, for one of the anodes this potential drive was not enough to break away from low current constant passivation.

6.4 Conclusions

By increasing the degree of parallel segments of a laboratory cell with additional anodes and/or electric elements it is possible to investigate the phenomena of partial anode effect in the laboratory. The results indicate that as long as the rest of the cell (real and/or virtual anodes) is able to pass most of the current, only small amounts of PFC are produced (0 – 3 ppm mol CF_4), even with one or more anodes completely passivated. Individual anode potentials of a small number of anodes can be elevated far into the PFC territory, but the changes get buried when looking at the total cell voltage. However, when the total resistive load for the cell is too high and the voltage increases by a large margin substantial amounts of PFC can be produced ($\gg$ 1000 ppm mol CF_4).

The anodic production of PFC is likely somewhat higher than what is released to the environment as at high temperature it may decompose on several substrate materials used in the production of aluminium, both in the laboratory and presumably also on industrial scale.

Chapter 7

Anodic Passivation of Carbon Materials in Cryolite-Alumina Melts

Henrik Åsheim[a], Thor A. Aarhaug[b], Espen Sandnes[a], Asbjørn Solheim[b] and Geir M. Haarberg[a]

[a] *Department of Materials Science and Engineering, Norwegian University of Science and Technology, N–7491 Trondheim, Norway*
[b] *SINTEF Materials and Chemistry, SINTEF, N–7465 Trondheim, Norway*

Abstract

The anode passivation and recovery potentials were measured on graphite and glassy carbon in electrolytes containing 1 to 11 wt% Al_2O_3. Passivation was found to be very dependent on alumina concentration, with higher alumina melts becoming passivated at a higher anodic potentials. Recovery potentials were less influenced by the alumina concentration, although recovery began at a higher potential in electrolytes with high alumina content, especially at lower sweep rates. Electrodes instantly recovered when the potential was lower than the thermodynamic potential for PFC generation.

Assessing at which potential PFC gases are evolved from the anode is tricky as they in small amounts can decompose, however, the voltage/current signal indicates a change at about $(3.0 \pm 0.5)\,\mathrm{V}$ anodic and CF_4 was found to be present from at least 2.8 V in a 1 wt% alumina melt. On a vertical anode with good electrolyte convection PFC was not discovered until the anodic potential reached 5.2 V. In higher alumina melts regular CO_2 production overshadows the PFC generation and the results indicate that anodic potentials can be higher before detectable amounts of PFC are released.

Keywords: PFC, anode effect, cyclic voltammetry, anode passivation

7.1 Introduction

Primary aluminium is produced industrially by reduction of alumina dissolved in a cryolite melt at about 960 °C. The cathode generally consists of graphite blocks covered by a molten aluminium pad, and the cathodic reaction producing aluminium from its ions occurs at this metal/electrolyte interface. The anode is produced from carbon. Graphite can be used, but industrially a calcined blend of different cokes together with coal tar pitch is employed. Depending on polarization the anodic reaction can vary and has been a matter of discussion [17, 26, 79, 82, 90, 91]. It is generally accepted that CO_2 (7.2) and CO (7.1) are the two main off-gases of the anodic process [82, 83], with only minor amounts of CO being found in carefully performed experiments [6].

$$\frac{1}{2}\,\mathrm{Al_2O_3} + \frac{3}{2}\,\mathrm{C} = \mathrm{Al} + \frac{3}{2}\,\mathrm{CO} \qquad E^0_{1000\,^\circ\mathrm{C}} = -1.03\ \mathrm{V} \tag{7.1}$$

$$\frac{1}{2}\,\mathrm{Al_2O_3} + \frac{3}{4}\,\mathrm{C} = \mathrm{Al} + \frac{3}{4}\,\mathrm{CO_2} \qquad E^0_{1000\,^\circ\mathrm{C}} = -1.17\ \mathrm{V} \tag{7.2}$$

The ratio of CO_2 to CO is not only influenced by what is produced on the anode. Much of the CO formed during regular electrolysis originates from the reoxidation reaction

$$\mathrm{Al} + \frac{3}{2}\,\mathrm{CO_2} = \frac{1}{2}\,\mathrm{Al_2O_3} + \frac{3}{2}\,\mathrm{CO} \qquad K_{1000\,^\circ\mathrm{C}} = 1.05 \times 10^{31} \tag{7.3}$$

which is also the main reason for the loss in cathodic current efficiency [9, 48]. Additionally, some CO will be formed by the Boudouard reaction

$$\mathrm{CO_2} + \mathrm{C} = 2\,\mathrm{CO} \qquad K_{1000\,^\circ\mathrm{C}} = 1.47 \times 10^{2} \tag{7.4}$$

When the electrolyte becomes depleted of alumina and oxygen-containing ions polarisation increases and co-discharge of fluoro-ions takes place. The formation of anode effect species CF_4 and C_2F_6 can be represented by the following relations

$$\mathrm{Na_3AlF_6} + \frac{3}{4}\,\mathrm{C} = 3\,\mathrm{NaF} + \mathrm{Al} + \frac{3}{4}\,\mathrm{CF_4} \qquad E^0_{1000\,^\circ\mathrm{C}} = -2.56\ \mathrm{V} \tag{7.5}$$

$$\mathrm{Na_3AlF_6} + \mathrm{C} = 3\,\mathrm{NaF} + \mathrm{Al} + \frac{1}{2}\,\mathrm{C_2F_6} \qquad E^0_{1000\,^\circ\mathrm{C}} = -2.76\ \mathrm{V} \tag{7.6}$$

Another possible fluoro-containing gas is the compound COF_2 that can be formed by a reaction of cryolite and alumina over carbon as described by the following reaction

$$\frac{1}{2}\,\mathrm{Na_3AlF_6} + \frac{1}{4}\,\mathrm{Al_2O_3} + \frac{3}{4}\,\mathrm{C} = \frac{3}{2}\,\mathrm{NaF} + \mathrm{Al} + \frac{3}{4}\,\mathrm{COF_2} \qquad E^0_{1000\,^\circ\mathrm{C}} = -1.90\ \mathrm{V} \tag{7.7}$$

Whereas the presence of CF_4 and C_2F_6 in the anode gas is well established [28, 92], the presence of COF_2 is seldom documented. Calandra et al. [21] observed a voltammetric peak that was assigned to the compound and Aarhaug et al. [24] used an open path FT-IR above an open industrial cell during anode effect to detect the compound. It has also been detected in laboratory investigations as reported by Dorreen et al. [23]. If formed, COF_2 may decompose in the presence of carbon or moisture, and it might also self-decompose according to the following reactions.

$$2\,\mathrm{COF_2} + \mathrm{C} = 2\,\mathrm{CO} + \mathrm{CF_4} \qquad K_{1000\,^\circ\mathrm{C}} = 2.23 \times 10^{3} \tag{7.8}$$

$$3\,\mathrm{COF_2} + 2\,\mathrm{C} = 3\,\mathrm{CO} + \mathrm{C_2F_6} \qquad K_{1000\,^\circ\mathrm{C}} = 6.61 \times 10^{-1} \tag{7.9}$$

$$\mathrm{COF_2} + \mathrm{H_2O} = 2\,\mathrm{HF} + \mathrm{CO} \qquad K_{1000\,^\circ\mathrm{C}} = 1.78 \times 10^{9} \tag{7.10}$$

$$2\,\mathrm{COF_2} = \mathrm{CO_2} + \mathrm{CF_4} \qquad K_{1000\,^\circ\mathrm{C}} = 1.51 \times 10^{1} \tag{7.11}$$

Even though CF_4 and other PFCs are comparatively inert compounds investigations have shown that they are not so thermodynamically stable, and might decompose in the presence of catalysts, even at fairly low temperatures. Modica et al. [45] observed that CF_4 and CF_4 diluted with argon decomposed to CF_3, CF_2 and F at temperatures above 1900 °C. Rogers et al. [46] observed a reaction between CF_4 and steel and tungsten at 1000 °C and White et al. [47] demonstrated the reaction of C_2F_6 with silica even down to 600 °C. Thonstad et al. [48] have shown that conversion of CF_4 over activated alumina begins at about 500 °C and Castellano et al. [49] found that 26 % of CF_4 was transformed into CO_2 when passing through a cryolite melt enriched with 2 wt% Al_2O_3.

7.2 Experimental

All experiments were conducted in an electrically heated vertical tube laboratory furnace. The inner tube was made of mullite and kept in place by two brass lids with greased O-rings for a tight seal. A graphite (Schunk-Tokai) crucible (⌀ 80 / 90 mm) with an inner depth of 110 mm was used as cathode in the experiments. It was positioned in the middle of the furnace on a graphite support block that was further connected by a steel rod (⌀ 10 mm) through the bottom lid, shielded with PTFE where necessary.

The electrolyte was made up of cryolite (Na_3AlF_6, Aldrich), aluminium fluoride (AlF_3, industrial grade, sublimed at 1090 °C) and alumina (Al_2O_3, Merck /

Aldrich). The alumina concentration was varied from 1 to 11 wt% (saturated) between experiments, while the cryolite ratio (CR, NaF/AlF_3 molar ratio) was kept constant. An overview of the different electrolyte compositions employed is given in Table 7.1. A height of about 4 cm of molten electrolyte was employed in each experiment.

Table 7.1: Electrolyte composition and molar cryolite ratio of experiments.

Na_3AlF_6 wt%	Excess AlF_3 wt%	Al_2O_3 wt%	CR
88.2	10.8	1	2.3
86.5	10.5	3	2.3
84.7	10.3	5	2.3
79.3	9.7	11	2.3

Anodes were made from ultrapure graphite (Schunk-Tokai) rods (⌀ 10 mm) and glassy carbon (GC, vitreous carbon, Schunk-Tokai) rods (⌀ 10 mm). Three different anodes were used and they were vertical graphite, vertical GC and a graphite rod with both horizontal and vertical surface area. Purely vertical anodes were achieved by placing boron nitride (BN) of similar diameter both below and on top of a carbon disc (height 5 mm), connected in the interior with an M3-threaded graphite rod. Such vertical design produces a well known geometric surface area of 1.57 cm^2 where it is also easier to estimate and correct for changes in area during anode consumption. Additionally it removes most bubble induced voltage oscillations. For the graphite rod the active surface area had to be estimated from the immersion depth, later measured by visual inspection of the immersed part post experiment.

An aluminium reference electrode was employed. The part in contact with aluminium was produced of a milled out BN rod (⌀ 5 / 10 mm) of length 70 mm. This was threaded on a steel tube (⌀ 8 / 10 mm). Aluminium metal (0.7 g) placed inside the BN rod and a hole (⌀ 2 mm) was drilled 5 mm above the molten aluminium level. Electrical connection was provided with a tungsten wire (⌀ 1 mm) shielded in an alumina tube (⌀ 1.5 / 3 mm), except for the bottom 5 cm, which was shielded with a BN tube of similar diameter. A sketch of the crucible set-up with electrodes can be viewed in Figure 7.1.

7.2.1 Electrical equipment

A few different potentiostats were used during the experiments. IviumStat XRi (10 A, 10 V) has been used for most of the work with 1 and 3 wt% Al_2O_3 melts and a PARSTAT 4000+ (4 A, 10 V) in combination with a Kepco BOP20-20M

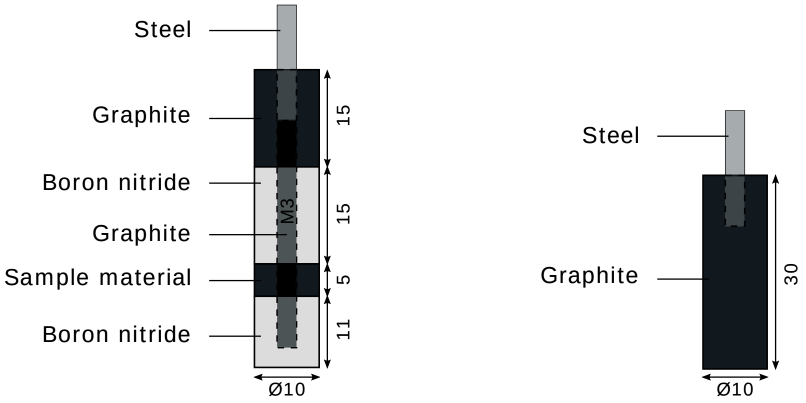
Steel
Graphite
Boron nitride
Graphite
Sample material
Boron nitride
M3
15
15
5
11
Ø10
Steel
Graphite
30
Ø10

(a) Vertical electrode

(b) Rod electrode

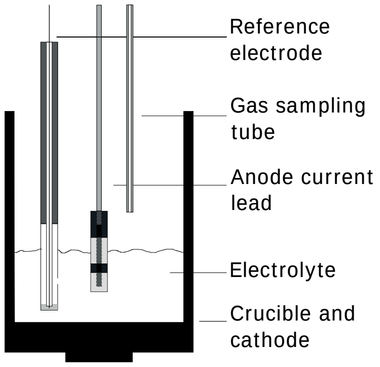
Reference electrode
Gas sampling tube
Anode current lead
Electrolyte
Crucible and cathode

(c) Crucible and electrodes

Figure 7.1: Sketches of electrodes and crucible. (a) Electrode with only vertical active surface. Sample material either ultrapure graphite or glassy carbon. (b) Graphite rod electrode with vertical and horisontal active surface area. (c) Sketch of set-up with cathode, anode, reference electrode and gas sampling tube. Gas sampling was only carried out in some experiments. All measures in mm.

(20 A, 10 V) bi-polar DC power supply was mostly used for the work with 5 and 11 wt% Al_2O_3. Initial impedance measurements at or close to open circuit potential (OCP) were performed with Solartron 1287 electrochemical interface (2 A, 12 V) in combination with Solartron 1260 frequency response analyser, due to its 2 A limit. Impedance measurements at higher currents were conducted by the PARSTAT combo. Solartron was controlled with Schribners CorrWare and ZPlot software while the IviumStat and PARSTAT were controlled with their own software, IviumSoft and VersaStudio.

In this work the potential was scanned over a broad range from OCP to anode passivation. Throughout this range the resistance towards reaction changes significantly. Current interrupt as an IR compensation technique was with the equipment not available for all procedures, additionally it is not well suited for high speed, and might introduce minor artefacts [70]. Positive IR feedback is not limited by speed, but has the drawback that it needs to be set manually on a per sample basis. Generally it is also not possible to achieve 100 % compensation, but one has to settle for 70 – 90 % to get stable readings without ringing or oscillation. However, with the scan range set in this survey positive feedback was impossible to employ. Lots of ringing with cathodic currents during anodic potential sweeps were observed, even at very low compensation rates. Positive feedback also assumes the uncompensated resistance to be constant. Any variation and the applied correction becomes incorrect. Impedance at OCP was used to find the uncompensated resistance that for most samples had the relatively low value of 0.02 Ω or less. However, this value was not used as positive feedback for the reasons stated above, although it was used to filter out bad samples that showed poor conductivity, likely due to poor assembly, worn-out machine threads etc.

7.2.2 Gas analysis

A mass spectrometer (MS, Pfeiffer QMS 200) was used in some experiments in order to investigate at which potential co-evolution of PFC occurs. The MS has its own pump that samples at a rate of ~ 20 ml/min. Due to the low sampling rate tubes with low inner volume have to be employed to minimise gas delay, both to lessen gas mixing and make it easier to compare with the electrical signal, in addition to reduce the probability of PFC decomposition. An alumina tube (⌀ 2 / 4 mm) placed approximately 3 cm above the anode/melt interface was used to bring the gas out of the furnace, before it subsequently passed through a 15 µm particle filter and into the analyser.

7.2.3 Experimental procedures

Cyclic voltammetry (CV) was performed on vertical graphite, vertical glassy carbon and some graphite rods in the different melts mentioned in Table 7.1. The scans were performed from OCP and until passivation occured, and in most cases a bit further if the equipment allowed for it, before returning to the starting point. This meant a voltage range from about 0.8 V to 6/8/10 V, depending for the most part on the amount of alumina in the electrolyte. The scans were performed at a range of different sweep rates ranging from $20\,\mathrm{mV\,s^{-1}}$ to $12\,500\,\mathrm{mV\,s^{-1}}$ (20, 100, 500, 2500 and 10 000/12 500 depending on equipment capabilities) to see how it influenced the current/voltage characteristics. The graphite rod was included to observe the difference between horizontal/vertical surfaces. Only vertical surfaces can be useful to study fundamentals as the voltage oscillations originating from bubble release is very much reduced, however the horizontal part is very much present in the industrial production process. Linear sweep voltammetry (LSV) was performed in an analogue fashion, except only scanning in the forward direction (anodic direction).

Chronoamperometric stepping and was combined with gas analysis to investigate if PFCs evolved before full passivation. The anodic voltage was elevated in steps of 0.2 V from 1 to 5/6 V relative to the reference electrode. Dwell time on each step was 25, 50, 100 or 200 s; longer in potential ranges were it was beforehand most expected that partial passivation would occur, as this would enhance the visual interpretation of the gas signal. About 10–15 samples in total of vertical graphite and graphite rod were tested.

7.3 Results and discussion

7.3.1 Cyclic voltammetry and passivating potentials

The current voltage relationship prior to AE with high levels of passivation was studied by the potential sweep technique. Scanning by cyclic voltammetry (CV) in both directions it is possible to discover differences between the onset of AE and the return to regular production.

Figure 7.2 shows the behaviour of GC and graphite at different sweep rates with an alumina concentration of 1 wt%. From the voltammograms on GC a large positive shift in slope can be observed at about 3.5 V anodically vs. the aluminium reference. This is frequently visible for low sweep rates, and in the present diagram very visible also at higher sweep rates. Moreover, the transition brings forth a change in noise, which is visually much larger past 3.5 V in the forward scan. For the graphite anode a less pronounced change occurs at about the same voltage. Interestingly, this time a negative change of slope is observed, again combined with an increase in voltage noise. It is at this point believed that other reactions are taking place, like the ones described above. However, being thermodynamically possible does not necessarily mean fast kinetics, and any other reaction will place itself in parallel with the ones already feasible, possibly seizing just a fraction of the current.

While the reactions producing CO (7.1) and CO_2 (7.2) are limited by the oxide concentration, PFC producing reactions (7.5) and (7.6) are only limited by the bulk electrolyte. With the former reactions reaching their limiting current, the PFC producing reactions will have to pick up the additional current. The full mechanism is not completely understood, but the end result is that with an

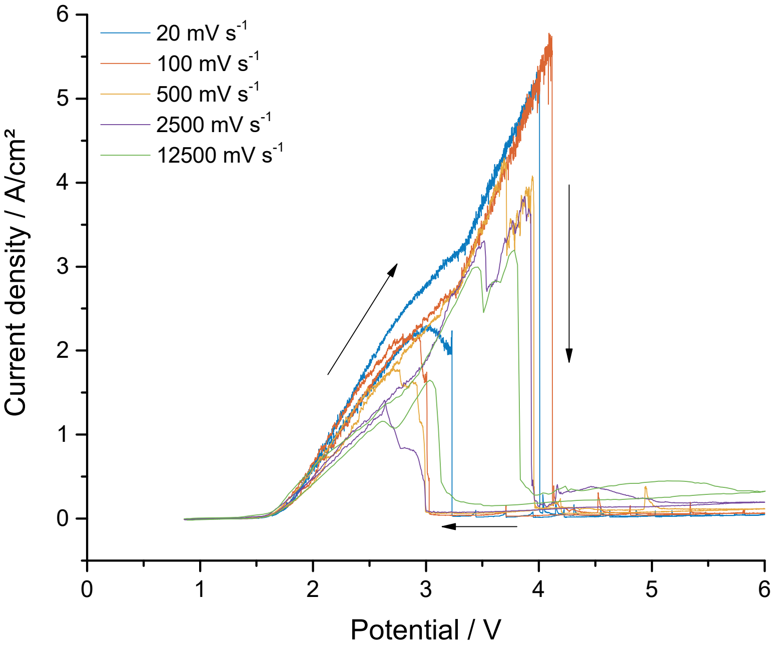

(a) Voltammetric sweeps on GC

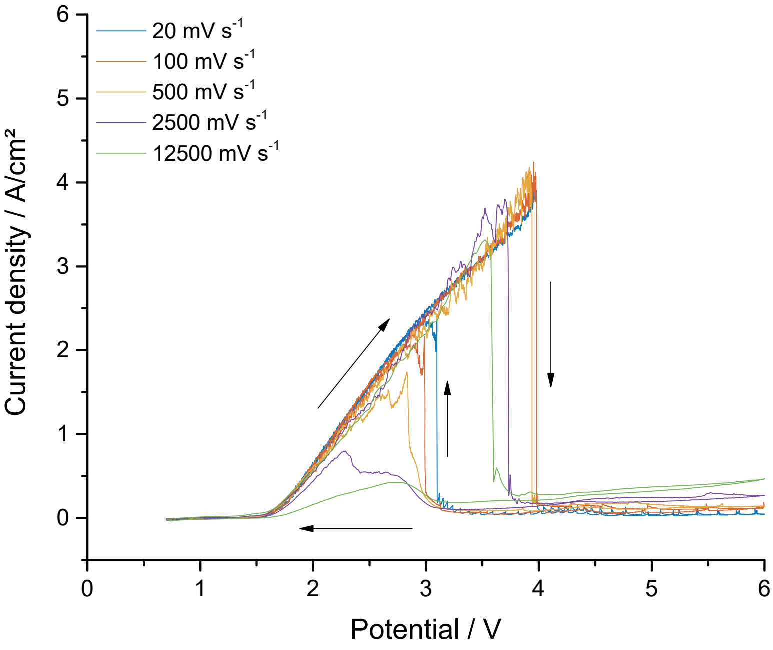

(b) Voltammetric sweeps on graphite

Figure 7.2: Current voltage relations of GC and graphite at different sweep rates. $C_{\mathrm{Al_2O_3}} = 1$ wt%.

increased PFC partial current density (cd) more of the surface get blocked by what is most likely a C-F film. This creates a domino effect that decreases the active surface, thus increaing the real current density, and within milliseconds an anode can be fully passivated. C-F bonds have been positively identified with EXAFS by Haverkamp [93] on anodes that had undergone long (1 h) anode effect, and Haverkamp et al. [94] also showed that the same bonds to a smaller extent may appear on anodes that has not observed full passivation.

There is no clear difference between the passivation voltages of different sweep rates at the same alumina concentration, although slower scans most often reach the higher potentials. This might be due to convection from gas production that is considerably higher at lower sweep rates. Complete passivation is observed at a moderately higher potential than the initial change of slope. Similar curves were seen by Zhu et al. [95] on tubular graphite surface in a 1.56 wt% Al_2O_3 melt, although passivation was observed between 6 and 8 V vs. the aluminium reference. The proposed reason for the late passivation was large IR drop in the high current system. In the present study the IR drop is also a likely contributing factor, nonetheless the flow regime set up by the vertical electrode arrangement and the total oxide concentration is presumably the bigger contributing factor.

Reactivation on the reverse scan begins at about the same potential as the slope change in the forward sweep. For lower alumina melts there seems to be little difference in the reactivation potential, although slower sweeps have a tendency to resume gas production earlier and at a higher voltage. The slower scans have more “time” at an activating potential. Slow scans approximately overlap its current voltage slope after reactivation, while faster scans sees a lower current. Likely for the same reason that “time” is insufficient for full reactivation of the surface. This is especially visible for the graphite (Figure 7.2b), in all likelihood due to the rougher surface than GC. The figures also indicate that there is a lower potential limit to maintaining passivation as everything activates when the reverse scan reaches about 3 V, not too dissimilar from what was observed by Zhu et al. [95].

Figure 7.3 shows how the current voltage characteristics of vertical GC develops with increasing amounts of alumina in the electrolyte. The passivation potential increases with increasing alumina concentration, albeit not in a perfectly linear manner. The change in slope described earlier is quite visible for concentrations 1 and 3 wt%, however imperceptible for 5 and 11 wt%. Presumably the regular reactions producing CO (7.1) and CO_2 (7.2) dominate the plot due to increased critical current density (ccd) and overshadow any contribution from PFC producing reactions. There is a somewhat odd relationship between cd and alumina content. Some is due to the fact that the vertical GC parts are difficult to machine, giving a variation in surface area, while some can be ascribed the unreliable nature of AE and when passivation occurs. From the figure it is evident that the activation potentials on the reverse scan vary broadly with alumina and rising with increasing alumina content, which is probably one of the reasons why adding quite a bit of alumina is so efficient in quenching industrial AEs. At 11 wt% only a partial passivation is observed at first, accompanied by a noise elevation and ambiguous current/voltage characteristics. Full passivation occurs at 9 V vs. Al reference and a similar, albeit opposite two-step activation develops on the reverse sweep.

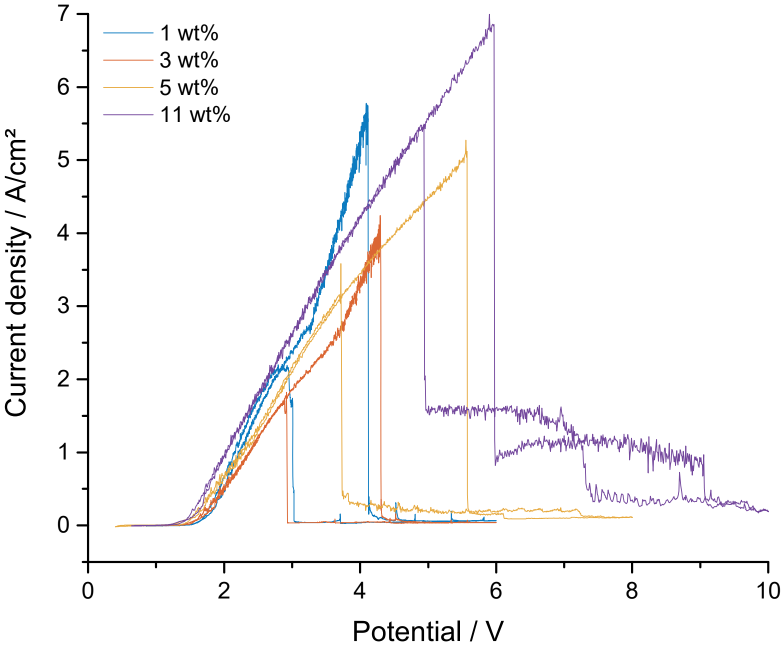

Figure 7.3: Cyclic voltammetry on GC at different concentrations of Al_2O_3. Sweep rate kept at 100 $mV\,s^{-1}$.

The same procedure on graphite is presented in Figure 7.4. Again the critical passivation potential scales with alumina content and in this case the current scales in a similar manner. The curves all show a clean one-step passivation, however, saturated melts sometimes show similar behaviour as the GC at 11 wt% (Figure 7.3). At higher concentrations all passivation potentials are well past the potential where PFC co-evolution is thermodynamically possible, suggesting the kinetics of CO and CO_2 production to be favourable. Reactivation potential on reverse scan is anew elevated for higher alumina content. In the saturated case it slowly begins to regain current from 5.5 V vs. Al and instantly fully reactivates at about 4 V. This slow reactivation is too a function of sweep rate, occurring more frequent at lower rates.

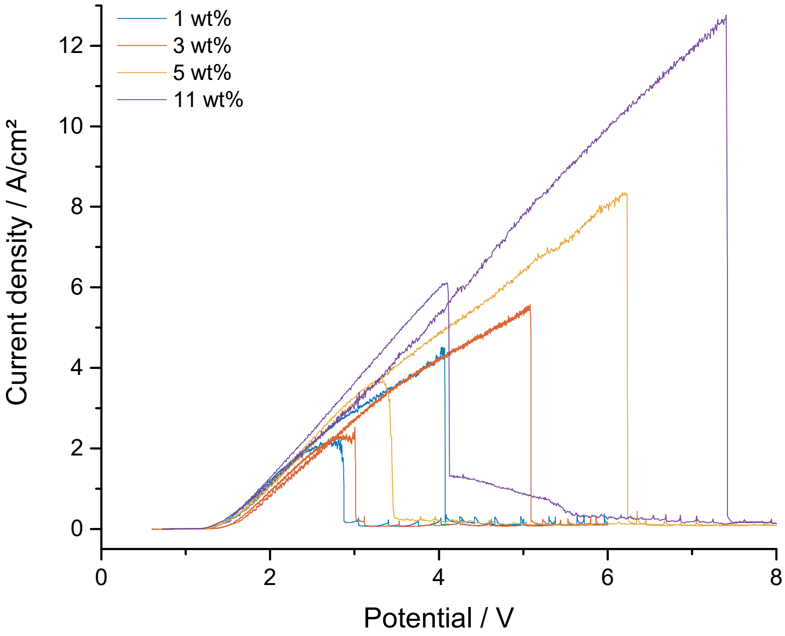

Figure 7.4: Cyclic voltammetry on vertical graphite at different concentrations of Al_2O_3. Sweep rate kept at 100 $mV\,s^{-1}$.

Figure 7.5 shows voltammograms on a graphite rod at different sweep rates, the alumina concentration being 5 wt%. Geometrical area in this case is somewhat uncertain, depending on the wetting of the electrode as well as splashes and motion due to bubbles. The aim was to achieve similar area for the vertical electrodes and approximately equal parts shared by the horizontal and vertical components, giving an estimated immersion of 2.5 mm. Visual inspection puts the immersion depth to about 3 mm, providing an estimated 45/55 ratio between horizontal/vertical surface area. This number is however not without uncertainty, both from the visual inspection, but also from the fact that the meniscus arguably has moved throughout the experiments due to changing wetting conditions.

At low scan rate voltage oscillations stemming from gas release originating at the horizontal part of the electrode are clearly visible, and has been described in the literature [80, 96, 97]. With increasing sweep rate less current is passed and fewer bubble drop-off peaks are visible, ultimately ending in sweep rates passing less current than needed for a single bubble detachment. The latter case approaches that of a purely vertical electrode, still, any product, however small can escape the vertical surface, while buoyancy will spread it out on a horizontal one. A feature not very visible in the curves from the vertical electrodes is the slope change of the current voltage relation in melts with more than 3 wt% alumina. For the rod at 5 wt% alumina this is clearly present once the sweep rate is high enough to omit the bubble oscillations. Additionally, there is a very clear straight line up to 3 V with another rougher linear slope continuing until passivation, certainly suggesting something is happening at the electrode surface.

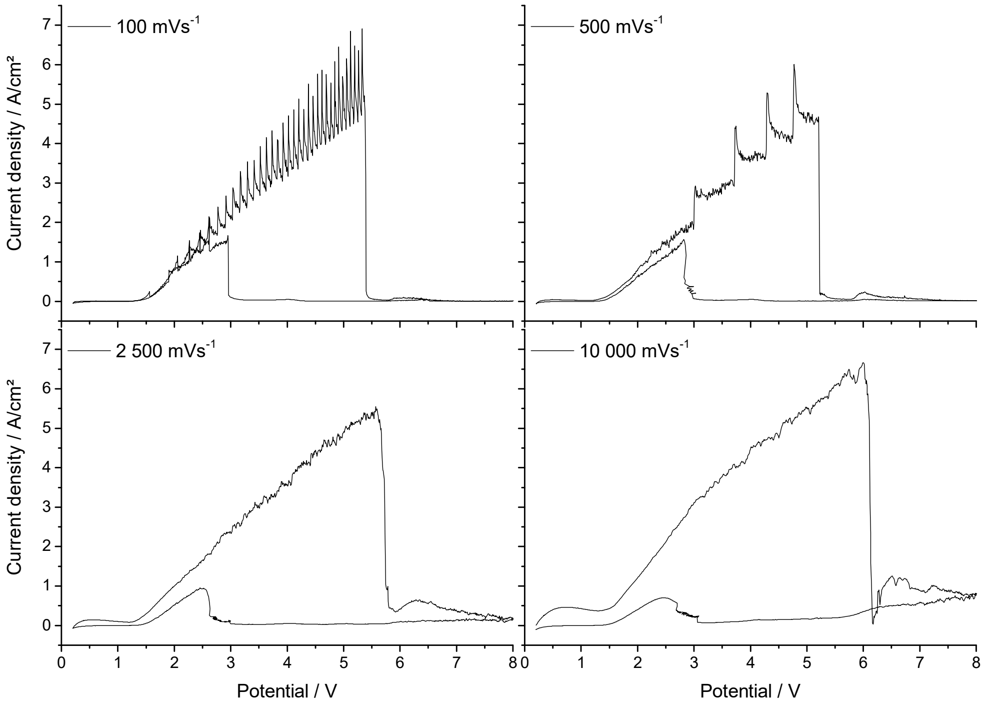

Figure 7.5: Cyclic voltammetry on graphite rod at different sweep rates. $C_{Al_2O_3}$ = 5 wt%.

The passivation current densities of all forward sweeps from cyclic and linear sweep voltammetry (LSV) are plotted against alumina concentration in Figure 7.6. Any variation in oxide concentration is invisible, nonetheless attempted kept constant by adding alumina according to theoretical consumption with 100 % current efficiency (CE) and 4F (CO_2/CF_4). Both graphite and GC produced a linear least squares fit that placed itself inside 1 SD at the different measurement points, with an R–squared value of 0.98 and 0.91, respectively.

Figure 7.7 shows the critical current density of passivation against anodic potential. Passivation data from both CVs and LSVs at all sweep rates were included,

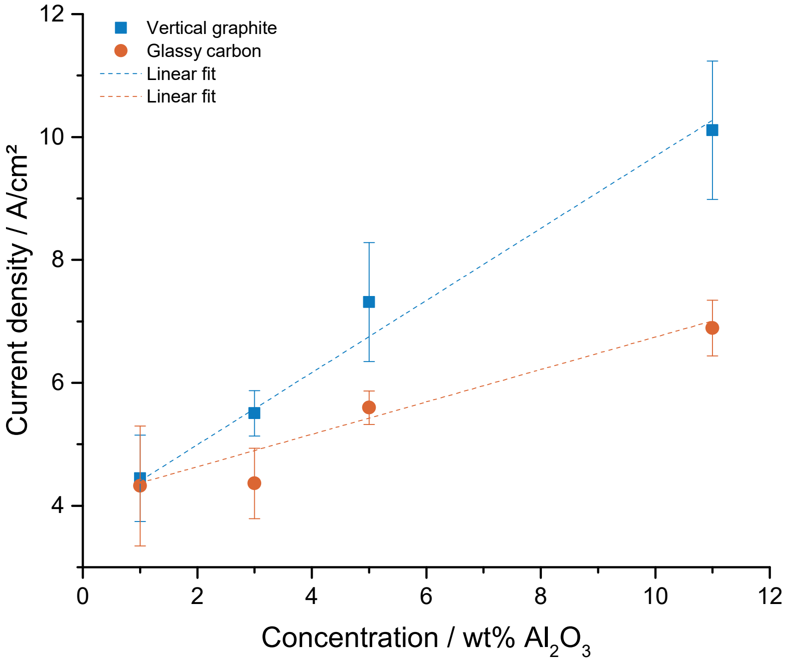

Figure 7.6: Passivation potentials of vertical graphite and GC vs. Al_2O_3 content.

with the only differentiating variable being the alumina concentration in the electrolyte. Glassy carbon shows a modest linear trend, whereas the graphite shows a very linear trend. For GC, part of the deviation might stem from the difficulty in producing samples with accurate geometric surface. With proper surface control this plot should give a good trend regardless of the real oxide concentration behind the data, save for the colour and shape of the scatter. Nevertheless, the concentrations are creating groups with occasional overlaps. The graphite scatter stretches out much further, especially when saturated with alumina.

Figure 7.8 describes the opposite procedure, the reactivation of the anode. LSVs were not run in the reverse direction so only reverse CV data are included. Contradictory to the passivation where the differences in oxide concentration produce a linear current/voltage trend most data are here situated much closer. Higher concentrations and lower sweep rates are located towards the upper right, while lower concentrations and faster sweep rates gravitate towards the lower left. Still, most points are located around (3.0 ± 0.5) V. Below approximately this voltage direct production of PFCs from (7.5) and (7.6) cannot occur. It is natural that everything underneath this level has recovered, given there is oxide in the melt. The very low recovery currents on graphite (Figure 7.8b) are

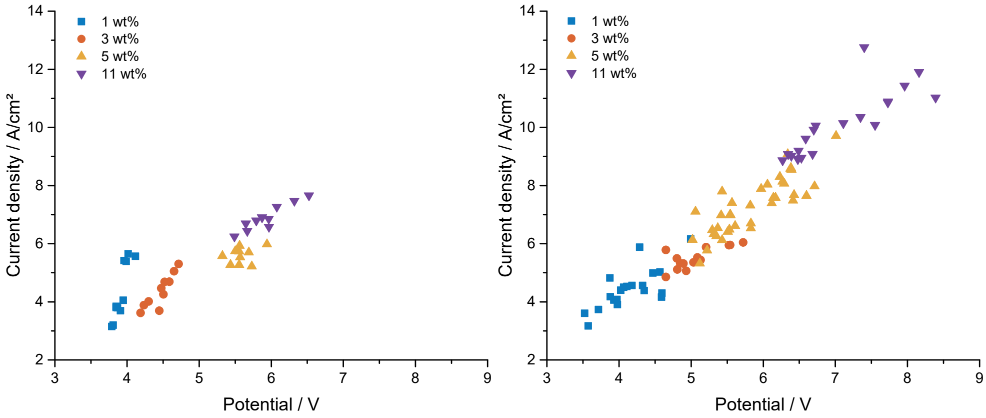

(a) Passivation on GC

(b) Passivation on graphite

Figure 7.7: Critical current densities for passivation on vertical electrodes of GC and graphite during forward sweeps. Passivations from both LSVs and CVs at all sweep rates are included and separated on a concentration basis.

from the higher sweep rates of 2500 mV s^{-1} and 10 000/12 500 mV s^{-1}. It is not visible for GC and as discussed before, being probably a feature of the different micro-structure on the surface.

7.3.2 Voltammetry and gas analysis

Gas analysis by MS was conducted on anodes of different shape (vertical and rod) and with different electrochemical techniques (chronoamperometric (CA) step and LSV) to investigate at which anodic potential PFC co-evolution is introduced. Detection of first traces of PFC is troublesome because the gas may decompose before it reaches the detector. It is likely that co-evolution of C-F gases often commences before it is detected by gas analysis equipment. With the MS mass/charge (m/z) ratio 69 was monitored for detection of PFC. m/z 69 is fragment $CF_3{}^+$ which is the main fraction for both CF_4 and C_2F_6. The latter can be individually identified at at m/z 119 (fragment $C_2F_5{}^+$). In the present work no signal was observed at m/z 119 so it can be assumed that m/z 69 is only contributed to by CF_4.

In most cases an elevation of the CF_4 signal was only visible just beyond full passivation, probably because it for a very short time was forced an appreciable amount of current through the insulating layer. Nothing was observed before full passivation, either because no PFC was produced, the production was below detection level (LOD) or because it was broken down before reaching the detector.

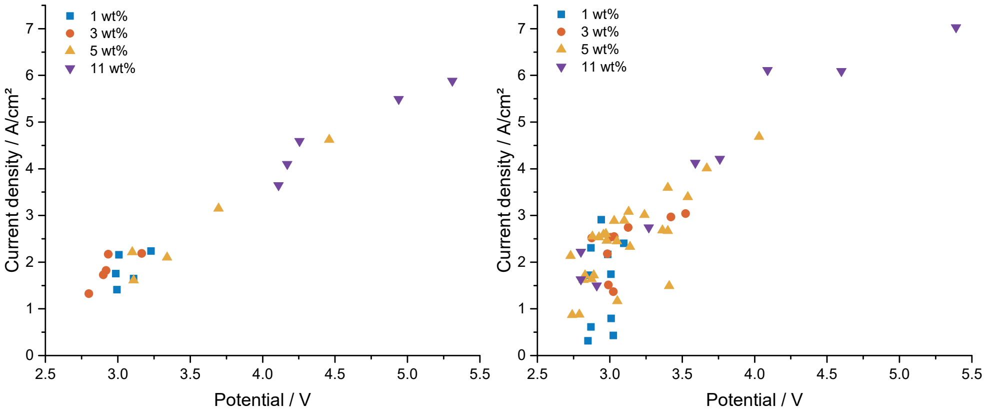

(a) Recovery on GC (b) Recovery on graphite

Figure 7.8: Scatter showing recovery from passivation on reverse sweep. Data includes all sweep rates, only separated by alumina concentration. Potential is the reactivation potential while the current is the highest observed succeding recovery.

Figures 7.9, 7.10 and 7.11 shows PFC production that is detected before complete passivation. They are all run with the same electrical parameters except that the latter two continue to the potential stepping all the way to 6 V vs. Al. The first two describes the development on a graphite rod with both horizontal and vertical surface, while the latter is a purely vertical graphite surface. The broad current trace is a function of the bubble release, enlarged it follows the saw-tooth behaviour described by Thorne et al. [98]. At potentials from 2.6 – 2.8 V vs. Al the periodic consistency begins to deteriorate. Likely contributors are the rounding of the electrode edge and the fact that direct PFC producing reactions are becoming available.

Partial passivation is observed on the rod of Figure 7.9 at 3.2 V vs. Al. Average current is reduced by ~ 1/3 and current oscillations severely decreased, indicating that large parts of the horizontal surface is passivated. Partial passivation is accompanied by a small, albeit significant release of CF_4. Some PFC might even be released at 3.0 V, however, it is at a level around LOD and therefore cannot be confirmed. With full passivation at 3.4 V CF_4 returns to base level, possibly being produced in small undetectable amounts. Partial passivation on these electrodes is often not observed when working on a one electrode system as the current load on the rest of the surface is much increased, causing an instant passivation of that part of surface as well.

The electrode of Figure 7.10 begins partial passivation already at 2.8 V, accompanied by a rapid shift in CF_4 level. Current oscillations are still quite prominent at this time and a large part of the horizontal surface is likely still ac-

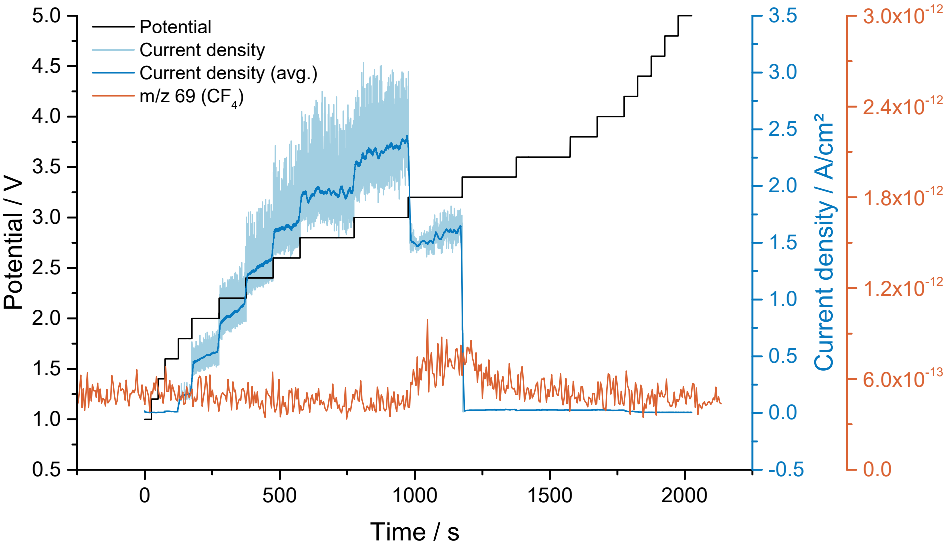

Figure 7.9: Current and CF_4 gas response of a graphite rod under voltage stepping. CF_4 production is initiated before complete passivation. $C_{\mathrm{Al_2O_3}} = 1$ wt%.

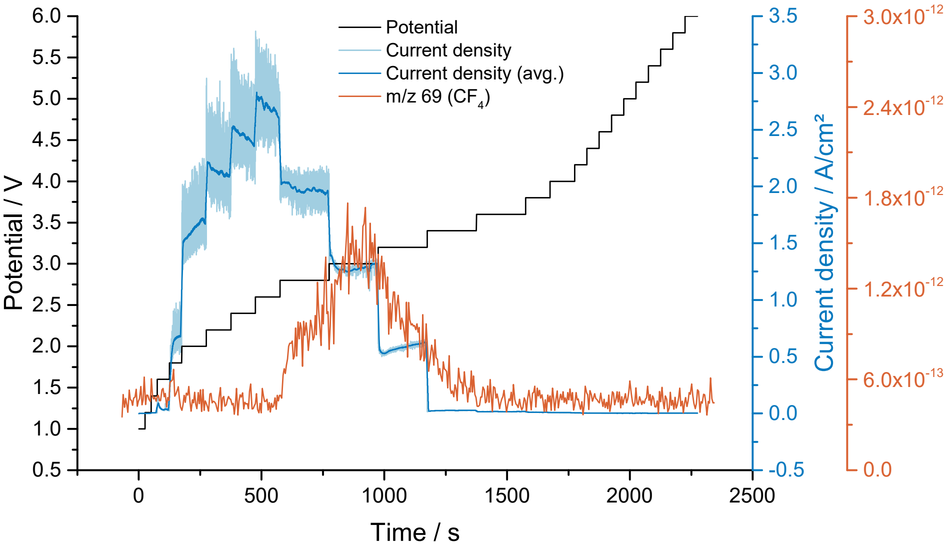

Figure 7.10: Current and CF_4 gas response of a graphite rod under voltage stepping. Passivation occurs in several steps with different levels of CF_4 production. $C_{\mathrm{Al_2O_3}} = 1$ wt%.

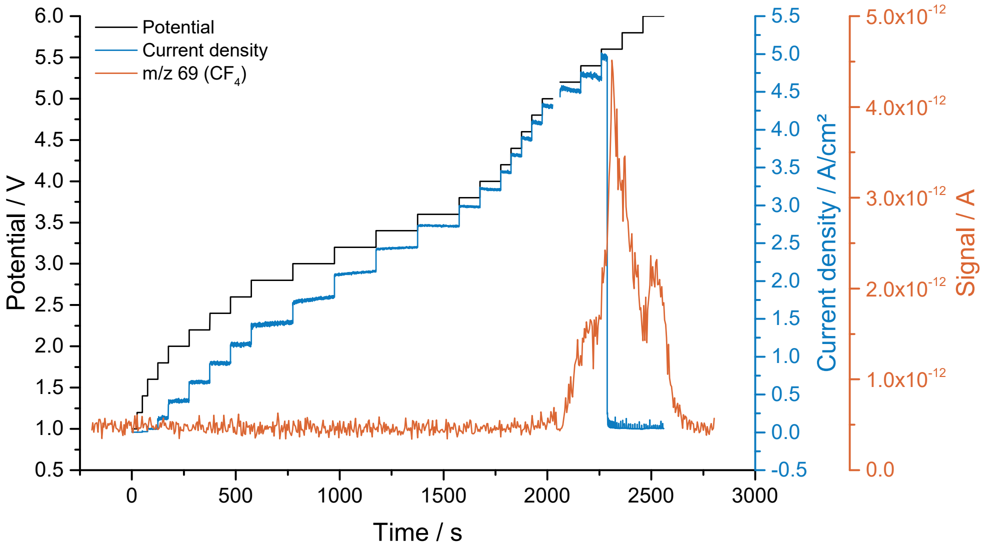

Figure 7.11: Current and gas response of vertical graphite during potential stepping. CF_4 is detected before it abruptly passivates. $C_{Al_2O_3} = 1$ wt%.

tive. With the next potential step (3.0 V) the oscillations are quenched followed by another increase in PFC. With the next potential step CF_4 decreases and full blocking is again reached at 3.4 V. Throughout all the partial passivation steps the current decreased, although the real current density of active area likely increased. PFC evolution sees a maximum in-between the partial passivations. It is proposed that the fraction of PFC increases with increasing potential; meanwhile, the total current drops with increasing passivation. Somewhere in the middle maximum PFC evolution will be realised.

On a purely vertical electrode (Figure 7.11) the flow regime is somewhat different and it is able to pass much higher currents before passivating. The vertical electrode is submerged fully and observes little liquid surface/edge effects while the traditional rod has active surface in contact with the liquid electrolyte level. The potential is stepped in a similar manner as with the rods. The current noise is naturally much lower overall with the somewhat strange feature that it is extra "silent" from about 3 to 3.8 V. There is no visible drop in current from partial passivation, before full blockage initiates after 27 s at 5.6 V. Nonetheless, co-evolution of CF_4 clearly takes place from about 5.2 V and increases with increasing potential. The largest PFC release can here be ascribed the transition to full passivation and this selection can be viewed in Figure 7.12. Fully passivated vertical electrodes exhibit almost equidistant time based current spikes (can also be viewed on CVs at lower sweep rates) that at these potentials are accompanied by PFC release. With such high CF_4 levels at the tiny currents observed the fraction of PFC production must be large.

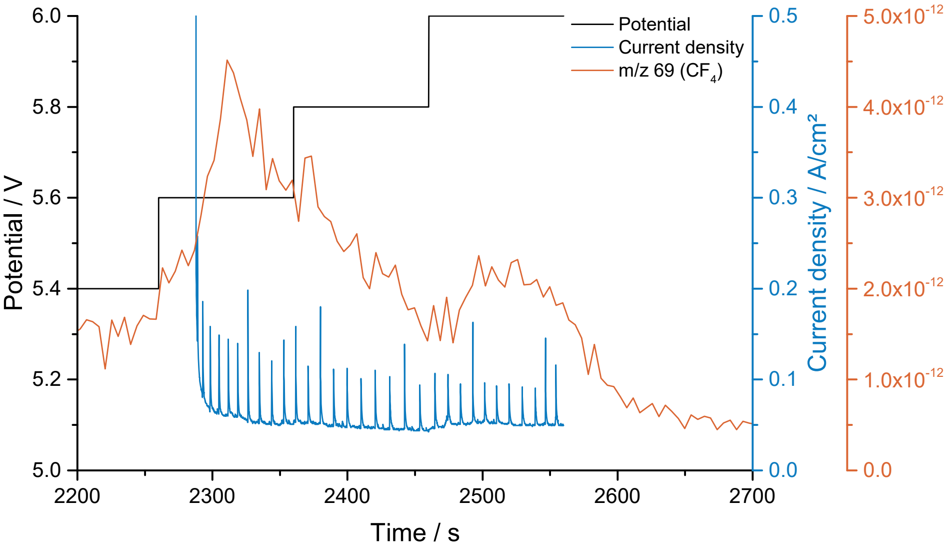

Figure 7.12: Current and gas response of vertical graphite during passivation at high voltage. Excerpt from Figure 7.11.

Overall the voltammetric sweeps show many of the same features as reported previously in the literature and glassy carbon and vertical graphite behaves mostly the same. The lower degree of pores and roughness of the glassy carbon electrode makes for an earlier passivation than its graphite counterpart. Even though the sample number of GC is low, the sample variability both seem less dispersed and is expected to be this way due to its consistent microstructure. When recovery occurs on the reverse scan in cathodic direction glassy carbon most often also see the quickest transition back to normal electrolysis, again likely due to less rough and more consistent microstructure. The graphite rod observes a somewhat different electrolyte flow regime due to it having a larger part of the active surface in near proximity, or in contact with the electrolyte surface, making for a less vivid flow in that volume, thus making it more likely to passivate at a lower potential. The rod design is closer to the anode situation within the aluminium industry, although an anode sample resembling the vertical graphite with the lower BN shield removed would compare better to its vertical counterparts in this study. Additionally it would provide a more precise geometric surface area, something that is prone to some uncertainty with manual anode setting, bubble induced electrolyte oscillations and meniscus variability with wetting on a simple anode rod. In this work the potential was the controlled variable, however, the current oscillations observed on samples with horizontal surface area do tell that the potential oscillations originating from gas bubbles under current-control are non-negligible. This is important as the bubble overvoltage will add to the total cell voltage of a multi-anode cell, increasing the total potential that can be allocated to a single anode that is low on current (because the IR drop is less on other parts of the cell segment with low current throughput), possibly ending in (partial) PFC production. Industrially this is countered by introducing one or more slots in the anodes to facilitate bubble release although towards the anode end-of-life these slots are burned off and the bubble overvoltage is increased.

7.4 Conclusions

Passivation of graphite and glassy carbon electrodes are very dependent on the alumina concentration in the electrolyte. Anodes in elevated alumina melts can sustain much higher anodic potentials. The recovery potential is not affected to the same degree, but they too get shifted to higher values in high alumina melts.

Assessing at which potential PFC gases are evolved from the anode is tricky as they in small amounts can decompose, however, the voltage/current signal indicates a change at about $(3.0 \pm 0.5)\,\mathrm{V}$ anodic and CF_4 was found to be present from at least 2.8 V in a 1 wt% alumina melt. With high electrolyte convection on a vertical electrode PFC was not discovered before the anode potential reached 5.2 V. In higher alumina melts the current/voltage relation is less influenced by the fact that PFC can thermodynamically be produced and the results indicate that the anodic potential can be somewhat higher before detectable amounts of PFC are released.

Chapter 8

The Influence of Polarisation on the Wetting of Graphite in Cryolite-Alumina Melts

Henrik Åsheim[a], Ingrid A. Eidsvaag[a], Espen Sandnes[a], Asbjørn Solheim[b], Henrik Gudbrandsen[b] and Geir M. Haarberg[a]

[a] *Department of Materials Science and Engineering, Norwegian University of Science and Technology, N–7491 Trondheim, Norway*
[b] *SINTEF Materials and Chemistry, SINTEF, N–7465 Trondheim, Norway*

Abstract

The wetting properties of graphite were measured with the immersion/emersion technique in a high temperature reduction cell. The wetting was measured at untreated, polarised and anode effect polarised samples. Most measurements were made in melts with 1 wt% alumina, although some experiments at higher alumina melts were also performed.

Polarisation was found to improve wetting as long as anode effect was not induced, with stronger improvements reached at the higher polarisations. Polarisation also decreased the hysteresis between advancing and receding contact angles compared to that of untreated graphite. Anodes polarised to anode effect exhibited consistently very poor wetting with large contact angles in both the advancing and receding direction and the smallest wetting hysteresis. Most of the negative wetting from anode effect took place during the first few seconds, being fully de-wetted from about 60 s. Increased alumina content improved bubble detachment, presumably from improvement in graphite/electrolyte wettability, notably from 6 wt% Al_2O_3.

Keywords: Wetting, graphite, cryolite, alumina, polarisation, anode effect

8.1 Introduction

Many industrial processes take place at interfaces and it is therefore important to understand how they are affected by different phenomena. Within high temperature processes common phenomena include Marangoni flow, wettability (contact angle), emulsification, foam formation jets, and surface waves, according to Mills et al. [99].

Several processes associated with the production of aluminium from alumina take place at interfaces. The reduction of aluminium containing ions to aluminium metal takes place at the metal/bath interface and the oxidation of carbon takes place at the anode/bath interface. Other processes include the formation and dissolution of sideledge and wear of the carbon cathode [100]. The wetting between the anode and bath is important as it contributes in the determination of anode gas coverage, and bubble size. The fractional gas coverage and its thickness adds additional “bubble overpotential” to the cell, increasing energy consumption. Additionally, flow induced by bubbles is the main contributor to convection in the cell, thus partially responsible for the distribution of alumina [101]. The anode effect is joined by de-wetting and researchers have suggested that deterioration of wetting properties of the anode/electrolyte could advance the onset of the anode effect [102, 103].

A handful of parameters influence the wetting of carbon anode by liquid electrolyte. It is heavily dependent on melt composition, physical properties of the carbon substrate (mainly structure), temperature and composition of gas phase [6, 104]. Matiašovský et al. [105] reported an angle of wetting for both graphite and amorphous carbon towards cryolite to be between 120° and 130°, with almost no change with increasing AlF_3 content and decreasing with increasing temperature. The contact angle was found to decrease with increasing alumina content, approaching $(110 \pm 5)°$ at saturation. Wetting has been found to improve with current, attain a maximum, and then decrease with diminishing surface active ions combined with a transition of anode gas from one that only contains CO and CO_2, to one that also contains CF_4 [6, 106].

8.2 Theory

8.2.1 Surface tension and wetting angles

Surface tension can be regarded as the tendency of a fluid to occupy the lowest surface area possible. It is what makes it possible for small insects to walk on water. In the bulk of a fluid cohesive forces between molecules are completely balanced by neighbouring molecules, while it towards the surface observes an increasing influence from adhesive forced from the gas-phase. This creates a net inward force for surface molecules making it contract to minimize area [107]. The interfacial tension depends on the chemical nature of the phases and is distinct for a specific system. Chemically similar media require less energy to form an interface between them. Adding surfactants can greatly lower interfacial tension and improve mixing/wetting between phases.

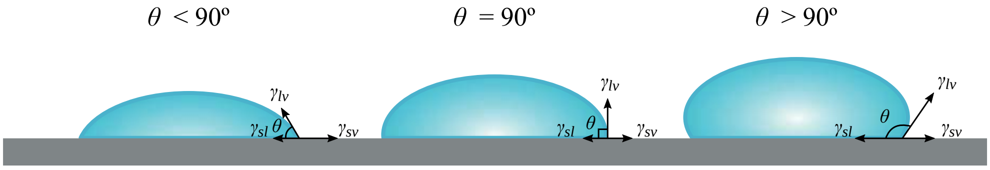

Figure 8.1: Contact angles and surface tensions of liquids on a flat homogeneous surface. The droplets represent wetting, non-wetting and de-wetting examples from left to right.

Contact angle is the inclination observed at a three-phase boundary between a liquid, a vapour and a solid. It is conventionally measured through the liquid and the angle provides information about the wettability of the system. A low contact angle ($< 90°$) describes a system with favourable wetting and a drop of liquid on a solid surface will spread out over a large area. On the other hand a large angle ($> 90°$) represents a system with unfavourable wetting and the liquid will minimize its contact area and form droplets on the surface [107], as illustrated in Figure 8.1. The balance between the contact angle and the three interfacial tensions is described by Young's equation [108, 109],

$$\gamma_{lv} \cos\theta = \gamma_{sv} - \gamma_{sl} \tag{8.1}$$

where γ_{lv}, γ_{sv} and γ_{sl} represent the liquid-vapour, solid-vapour and solid-liquid interfacial tensions, respectively, and θ, is the contact angle. Young's equation assumes a completely homogeneous and smooth surface and its equilibrium angle is often not obtained, even after long equilibration time. Most surfaces have some surface curvature and the liquid will move to expose its fresh surface and to wet the fresh surface of the solid in turn, which will give rise to a static hysteresis of contact angles [110]. A series of metastable contact angles can be obtained, ranging from a maximum denoted the advancing contact angle, θ_a, to a minimum referred to as the receding contact angle, θ_r. The concept of advancing and receding angles can be understood by imagining a droplet of liquid on on a solid surface with an equilibrium contact angle. Introducing more liquid into the droplet will increase its size and contact angle, but the contact point will not change before its advancing contact angle is reached. Similarly, liquid can be removed from the droplet without changing the contact point until the receding angle is obtained. This effect can be quite large, e.g. water droplets on a smooth homogeneous glass surface can have θ_a in the range of 40° – 60° with θ_r of approximately 0° – 5° [110].

There are several methods used for measuring contact angles and in most cases it either involves direct visual inspection of the angle, or indirect measurement of the force acting upon a solid sample. The present paper only considers a method from the latter group.

8.2.2 The immersion-emersion technique

The immersion-emersion technique is a method for measuring the contact angle through indirect measurement of force acting upon a solid substrate being pushed and pulled into and out of a liquid liquid. It can be considered a dynamic variant of the Wilhelmy balance method [111, 112] which has been extensively used to determine surface tension of liquids. The detected force change on the balance is a combination of buoyancy from the displaced liquid combined with that of wetting and is given by the following relation,

$$F = \gamma_{lv} p \cos\theta - V \Delta\rho g \tag{8.2}$$

where the first term comes from weight changes due to wetting and the second stems from buoyancy. In this equation γ_{lv} is the surface tension of the liquid, p is the perimeter of the solid being dipped into the liquid, θ is the contact angle, V is the volume of displaced liquid, $\Delta\rho$ is the difference in density between the liquid and the gas, and g is the gravitational constant [107]. The force observed in Equation (8.2) is also affected by viscosity but it can be neglected when the capillary number $Ca \ll 1$ [113, 114],

$$Ca = \frac{\mu\nu}{\gamma_{lv}} \tag{8.3}$$

where μ is the viscosity of the liquid ($\mathrm{kg\,m^{-1}\,s^{-1}}$) and ν the characteristic velocity ($\mathrm{m\,s^{-1}}$), which in this case corresponds to the immersion-emersion cycling speed. Cycling velocity was typically set to $0.2\,\mathrm{mm\,s^{-1}}$ with occasional tests at $1\,\mathrm{mm\,s^{-1}}$. With viscosity $\mu = 2.07 \times 10^{-3}\,\mathrm{kg\,m^{-1}\,s^{-1}}$ [115] and surface tension $\gamma_{lv} = 110\,\mathrm{mN\,m^{-1}}$ [116] the capillary number becomes $Ca \approx 10^{-5}$ at its highest.

8.3 Experimental

8.3.1 Apparatus and equipment

The apparatus used for measurements of anode wetting was a slightly modified version of what has been used previously by Solheim et al. [100] and Martinez et al. [101], with the largest difference being that the load sensor had been moved outside of the furnace as it sometimes experienced effects of thermal related issues.

It consisted of a water-cooled vertical tube furnace with a replaceable mullite inner tube, and sealed on each side by water-cooled steel lids with O-rings, all mounted on a free-standing aluminium structure. A stepper motor (ROBO Cylinder RCP2W-RA4C-I-42-P-5-150-P1-M-B) was fixed below the base of the furnace with an attached shaft penetrating the bottom lid. This allowed the crucible containing the melt to be moved in the vertical direction. The anode was suspended by a steel rod hanging from a load cell (FUTEK LSB200 (FSH02665)). Electrical connection was provided by a heavily stranded wire to reduce stress on the load cell. It was connected directly to the steel rod and an alumina ring was used to isolate it from the load cell. Additional weights was added upon the anode to improve stability and ensure that it stayed level. Temperature was measured at the base of the crucible from a thermocouple that was placed inside the shaft. It was also possible to record temperature beside the anode from a thermocouple passing through the upper lid, however, it added noise to the force measured by the load cell. All free wires and cables were fastened to the supporting structure to reduce noise.

Electric current was supplied with a system power supply (HP 6032A, 50 A/60 V). Current was measured over a shunt resistor ($0.01\,\Omega$), whereas cell voltage was measured on the the wire and shaft, as close to the anode and cathode as possible. To be able to reach voltages of about 30 V without saturation of the logging equipment a voltage divider was added in parallel with the system. With a total resistance of $\approx 30\,\mathrm{k\Omega}$ a negligible error of 1 mA may at worst be realised from this change.

All equipment was controlled and logged through LabView. The signal from the load cell was converted through an ADC micro-controller (FUTEK IMP650), while current and and voltage were logged with an NI cDAQ 9174 data acquisition unit with an NI 9205 module. Thermocouple data was recorded with the NI 9211 module. All data were sampled at 5 Hz, although the thermocouple data being up-sampled from 3.5 Hz.

8.3.2 Materials

The crucibles were made from graphite (Schunk-Tokai, ⌀ 76.5/90 mm) with an inner height of 110 mm. An inner shield of Si_3N_4 (⌀ 65/74 mm, height 80 mm) was employed with anodes that had some horizontal surface area. Two different anode shapes were used, both made from graphite (Schunk-Tokai). The first being an inverted cup (⌀ 26/30 mm, height 45/55 mm). The top part of the anode includes two ⌀ 3 mm “breathing” holes and M8x1 threads for connection to the steel current collector. The second type has only vertical surface area that is sandwiched between two boron nitride (hot-pressed, Kennametal) cylinders, all with a diameter of 16 mm. The carbon disc measured 10 or 30 mm in height. A sketch of the different anodes can be viewed in Figure 8.2. The inverted cup anode provides a long perimeter for the meniscus, which minimises the error in the readings from the load cell. Additionally, when insulating the sidewalls of the crucible with e.g. Si_3N_4 or Al_2O_3 most of the current passing the anode is distributed to the bottom horizontal part, which is similar to the industrial anodes [117]. The bubble noise observed during polarisation depends on the wall thickness, which should be kept low if the aim is to minimise it, however, machining very thin anodes can be difficult, especially when using the industrial coke/pitch blend. The vertical anode sample reduces the bubble noise and can make it possible to extract useful wetting data also from the polarisation period. Furthermore, when the meniscus is placed on the upper boron nitride (BN) part of the vertical sample, the electrode has a very well defined active geometric surface area.

The electrolyte was prepared by mixing cryolite (Na_3AlF_6, Aldrich), aluminium fluoride (AlF_3, industrial grade, sublimed at 1090 °C) and alumina (Al_2O_3, Merck / Aldrich). The alumina concentration was in most cases set to 1 wt% as the power supply is not powerful enough to completely passivate the anode at higher concentrations, at least without reducing the surface area significantly. Nonetheless a few experiments were conducted at 3, 5 and 11 wt% (saturated) and one experiment saw the variation from 1 – “12 wt%” (supersaturated) in 1 wt% increments. All melts were prepared with a cryolite ratio (CR, $n_{\mathrm{NaF}}/n_{\mathrm{AlF_3}}$) of 2.3.

Calculated wetting weights is shown as a function of wetting angle in Figure 8.3. The plot is based on the γ_{lv} surface tension data by Fernandez et al. [116]

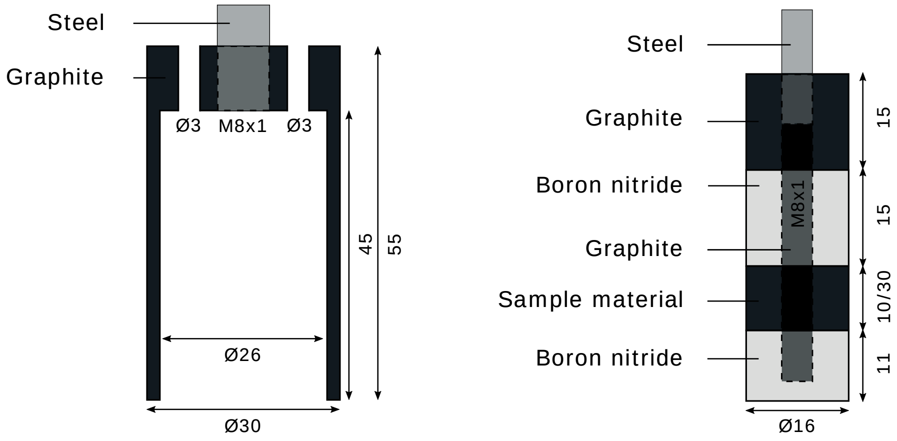

(a) Cup anode.

(b) Vertical anode.

Figure 8.2: The two main types of anodes used in the present work. The sample material of (b) was graphite with vertical dimensions of 10 or 30 mm. All units in millimeters.

which covers melt compositions very similar to the ones used in the present work. Wetting weights over perimeter were plotted as it is a more universal quantity when working with samples of different dimensions. Positive weight change describes positive wetting while negative weight change refers to de-wetting/non-wetting.

8.3.3 Measuring sequence

An example of an immersion/emersion cycle can be viewed in Figure 8.4 for a weight against time plot and in Figure 8.5 for a weight against position plot. A typical immersion/emersion cycle begins 10 mm above the melt and reverse direction 10 mm into the melt. The contact point of anode/electrolyte surface can be determined from both a change in force observed by the load cell, but also by a change in voltage from 0 V when separated to open circuit potential (OCP) when in contact. The two methods were never more than 0.2 mm apart. The anode is in contact with the surface in point (a), and until point (b) the meniscus is pinned at this position. During this time the contact angle θ is changing towards the advancing contact angle θ_a which is reached at point (b). As this is the limiting angle that may be reached during immersion it has to be kept and all changes in force from further immersion is due to buoyancy (save for sample inhomogeneity and smoothness) so the angle is the same from (b) to (c). From (c) to (d) there is a 15 s dwell time that in some systems might show a move towards an equilibrium contact angle, not visible here. Often with

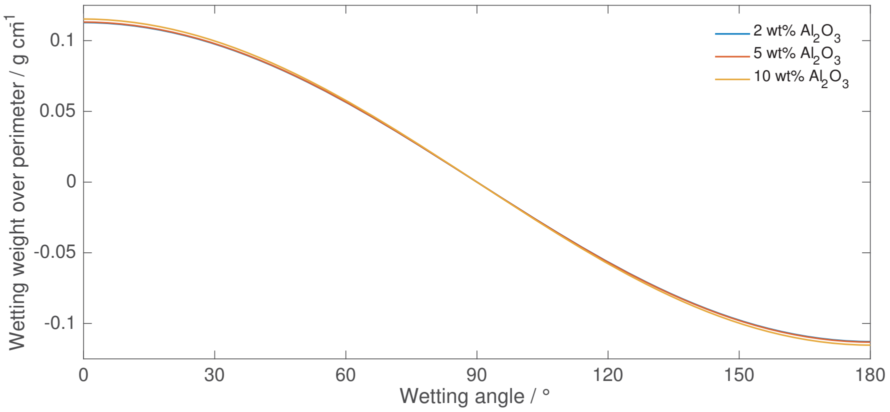

Figure 8.3: Wetting weights as a function of wetting angle for different bath compositions at 1000 °C according to the liquid surface tension data provided by Fernandez et al. [116]. 2, 5 and 10 wt% Al_2O_3 corresponds to γ_{lv} = 110.7, 111.0 and 113.1 mN m^{-1}, respectively.

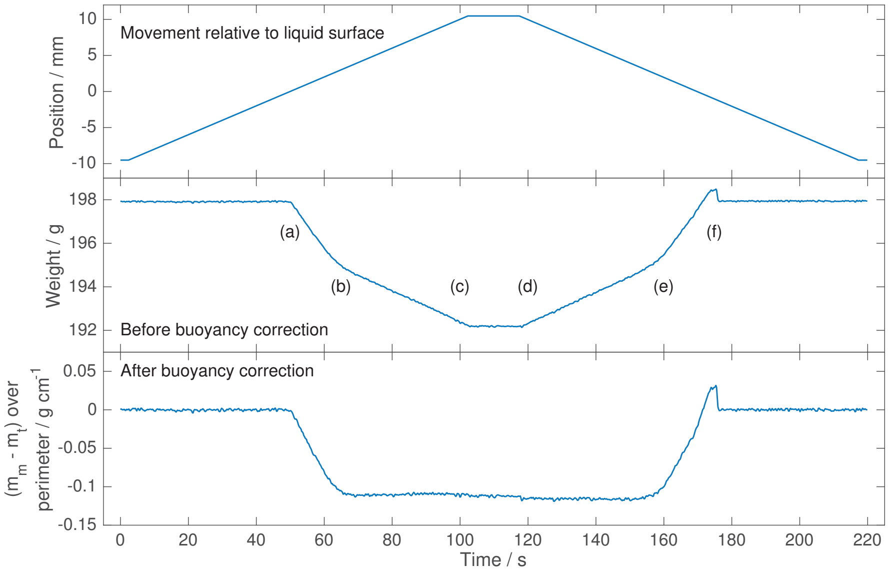

Figure 8.4: Example of an immersion/emersion vs. time procedure without polarisation on an inverted cup anode. The sample was immersed to 10 mm at 0.2 mm s^{-1}. (Upper) Movement of electrode vs. time (position positive when immersed). (Middle) Raw weight data. (Lower) Net weight data with buoyancy correction and divided by sample perimeter.

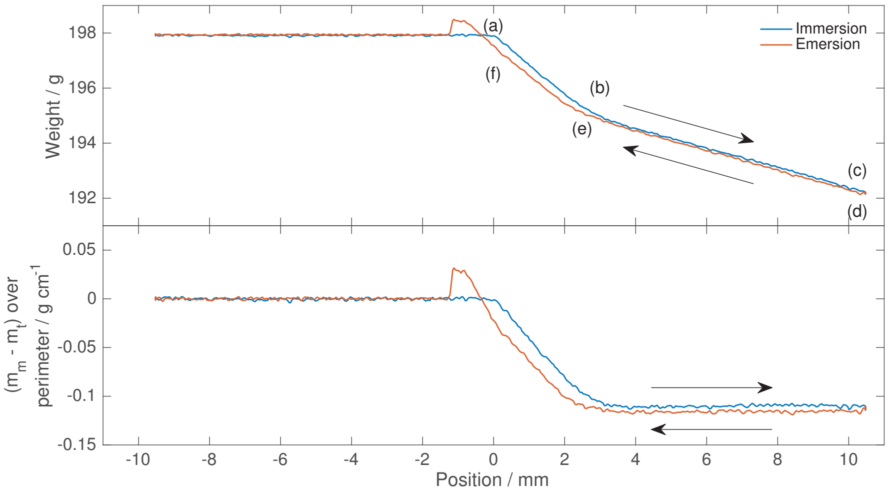

Figure 8.5: Example of immersion/emersion vs. position procedure with no polarisation on an inverted cup anode. (Upper) Raw weight data during immersion to 10 mm at 0.2 mm s^{-1}. (Lower) Net weight data with buoyancy correction divided by sample perimeter.

the transition from immersion to emersion there is a gradual change from θ_a to θ_r and during this time the liquid is pinned at the same point on the solid anode. Figure 8.5 shows little hysteresis between (c) and (d) and the advancing and receding contact angles are in this case very similar, with the odd case that $\theta_r > \theta_a$. Once the contact angle reaches the receding angle (d) the contact line again depins and the resulting force varies linearly between (d) and (e). When the contact line reaches (e) it is again pinned to the surface and from (e) to (f) the meniscus curvature decreases until the sample is completely extracted from the melt.

By correcting for buoyancy (measured mass, m_m, minus theoretical mass, m_t) the advancing and receding wetting weights can be observed as straight horisontal lines (given a homogeneous and smooth surface).

Increased polarisation

A typical measurement with polarisation is presented in Figure 8.6. The anode sample is first retracted before it is submerged into the melt at a speed of 0.2 mm s^{-1} all the way down to 10 mm below the bulk electrolyte surface. This point is designated "After reimmersion" and it refers to the previous measurement. Because some bubbles from polarisation may stick to the surface it is necessary to retract and submerge it again to "clean" it from unaccounted buoyancy. The sample dwells in this position for 120 s. After the reimmersion step the sample is polarised for 60 s at one specific voltage. 1 V for the first measurement and in steps of 1 V up to 10 V for subsequent measurements. After polarisation it dwells for 180 s before being emersed at 0.2 mm s^{-1} to −10 mm relative to electrolyte level. The whole procedure is then repeated with the next polarisation voltage.

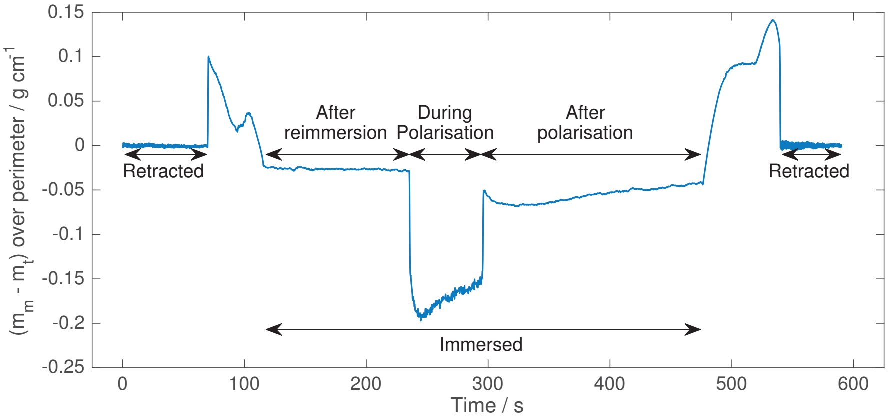

Figure 8.6: Typical buoyancy corrected immersion/emersion procedure with polarisation of sample. The arrows indicate where the different wetting weights are collected.

Increased passivation time

The effect of how increased time at passivating potentials affected wettability was conducted on a vertical anode with a graphite sample section of 30 mm. The electrode was first immersed to 21 mm (10 mm onto carbon phase) and held in that position for 60 s, before it was immersed an additional 5 mm onto carbon where it was held for another 60 s. It was then polarised before again being kept at the same position for another 60 s, subsequently retracted from the electrolyte. The wetting weight is the average recorded over the two 60 s periods that follow after the sample immersion and subsequent reimmersions.

The electrode was first polarised for 60 s at both 3 and 4 V to give good wetting. Later polarisations took place at the anode effect inducing potential of 20 V. The polarisation time started with 1 s and increased incrementally, ending with an accumulated time of 1 hour.

Increased alumina content

An inverted cup anode was used to investigate the change of wettability by alumina content. The sample was polarised with an anode effect inducing voltage of 20 V for 10 min with the sample immersed 20 mm into the electrolyte. Furthermore the surface up to an immersion depth of 10 mm was re-activated with a 3 V polarisation for 5 min. All the pretreatment took place in a 1 wt% Al_2O_3 melt. This created a surface with a lower part that was well wetted, and an upper part that was severely de-wetting.

After retraction wetting was first measured as a 300 s average immersed at 5 mm (middle of well wetted part), before it was immersed to 15 mm (middle of de-wetting part) and held for 300 s. Between the measurements, when the anode was retracted an equivalent of 1 wt% Al_2O_3 was added to the system through a tube inserted in the upper furnace lid. The procedure was repeated until the melt was theoretically supersaturated with 12 wt% Al_2O_3.

Equilibrium wetting angle

Wetting angles were observed for longer time on an inverted cup electrode to see if they approached an equilibrium value. The advancing angle was observed by immersing the sample to 10 mm and subsequently tracking the wetting weight over the next 600 s. From the receding side it was conducted by first immersing the electrode to 15 mm, before retracting it back to 10 mm, afterwards tracking the wetting weight for 600 s. The procedure was conducted on a completely untreated electrode, one that had been polarised with a cell voltage of 3 V for 300 s, and finally one that had been polarised at an anode effect inducing voltage of 25 V for 600 s.

8.4 Results and discussion

8.4.1 Wetting behaviour of polarised carbon samples

Polarisations at both normal electrolysis potentials and anode effect inducing potentials were carried out on both inverted cup anodes and purely vertical anodes. Figures 8.7a and 8.7b illustrate the general weight change behaviour for normal electrolysis (upper plots) and anode effects (lower plots) in a melt with 1 wt% Al_2O_3 at 1000 °C. In both cases the anode had previously been polarised at normal electrolysis potentials. The immersion depths are somewhat lower than 10 mm since some of the electrolyte has evaporated or splashed onto the crucible walls by agitation from the gas produced by the series of polarisations.

The immersion part of the figures is similar as expected with an analogous pretreatment and the same characteristics over the surfaces. However, from the polarization step and onwards they differ.

The upper plots with regular electrolysis show a large drop in weight stemming from gas production. The drop slowly levels off with time, likely because of increased circulation in the melt from the produced gas. The drag force observed by the bubbles is initially small, and bubbles get to grow large before detaching. With increasing convection the drag force is larger and bubbles will detach at an earlier growth stage.

Immediately after the current is turned off the wetting weight is increased. This "after polarisation" regime has some variance due to the fact that bubbles might still be attached to the anode, which strongly influences the recorded weight. The current trace shows an "after polarisation" weight that is more strongly wetting than the previous "after reimmersion" trace (4 V), which is uncommon (see Figure 8.6 for another example).

With the sample that got polarised to anode effect voltages (lower part of Figures 8.7a and 8.7b) the wetting behaviour is completely different. The weight drop during polarisation is much smaller than in the case of regular electrolysis, and from the fact that the wetting weight after polarisation (and also after next reimmersion) is almost the same it can be assumed that the anode surface has changed characteristics and the interfacial tension between solid and liquid, γ_{sl}, has changed and accounts for most of the change in weight. The current during anode effect is small, in the present case dropping from 6 to 0.5 A over the polarisation timespan. For regular electrolysis low current density is associated with the slow growth of large bubbles [80], however, large bubbles are not visualized in the weight trace.

Figures 8.8a and 8.8b show similar treatment on a purely vertical anode (see Figure 8.2b). Polarisation was applied with the meniscus at the upper boron nitride cylinder. Since the anode consists of several layers of different materials the weight against time and position traces differ from one made solely out of carbon and will vary with the wettability of the material. To further complicate matters the wettability of carbon is influenced by polarisation. During immersion the anode was first passed through the lower BN-phase, then past the carbon-phase before it was immersed 7 mm up on the second BN-phase, which is were the meniscus was held during polarization.

Boron nitride is well wetted by the electrolyte while carbon is poorly wetted in the upper plot (electrolysis) and very poorly wetted in the lower plot (anode effect). When the electrolyte surface is touched by the anode there is an abrupt rise in weight stemming from the positive wetting between the electrolyte and BN. The meniscus is at this position elevated compared to the bulk electrolyte.

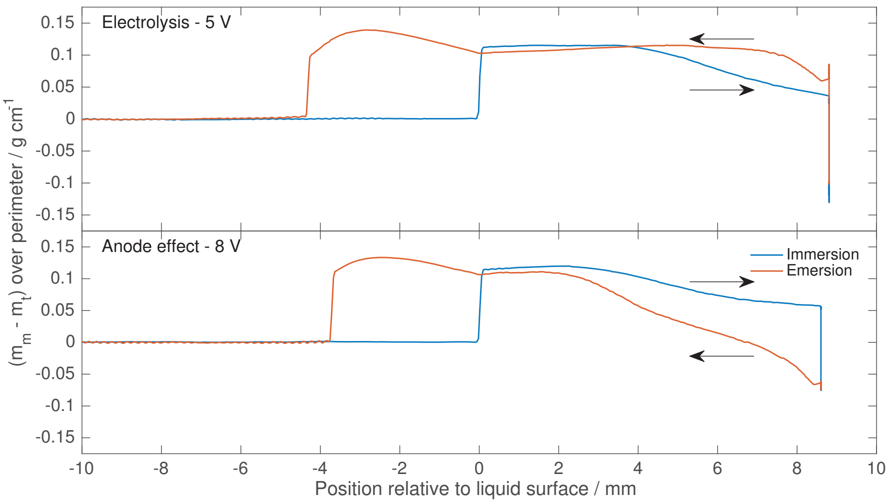

(a) Buoyancy corrected weight vs. position.

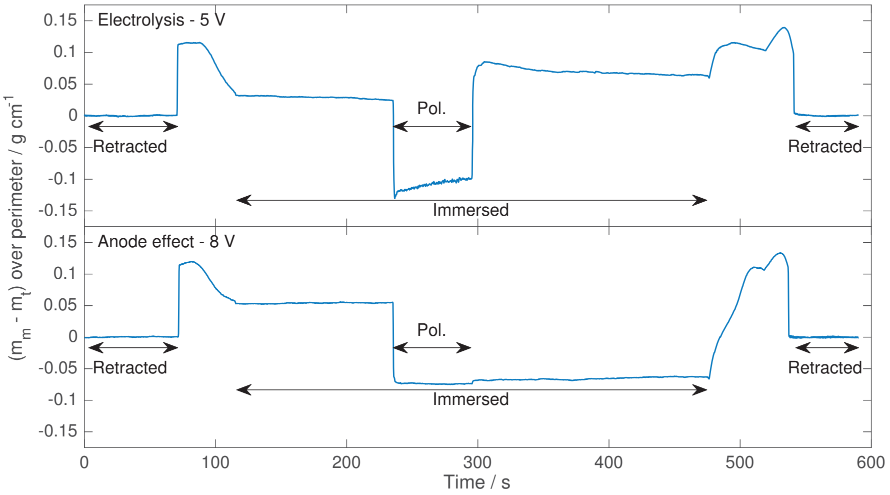

(b) Buoyancy corrected weight vs. time.

Figure 8.7: Buoyancy corrected weight vs. position and time on inverted cup anode in a melt containing 1 wt% Al_2O_3. The upper plots show regular polarisation at 5 V, while the lower plots present anode effect polarisation at 8 V. Both samples were previously treated with polarisations at non-AE inducing voltages.

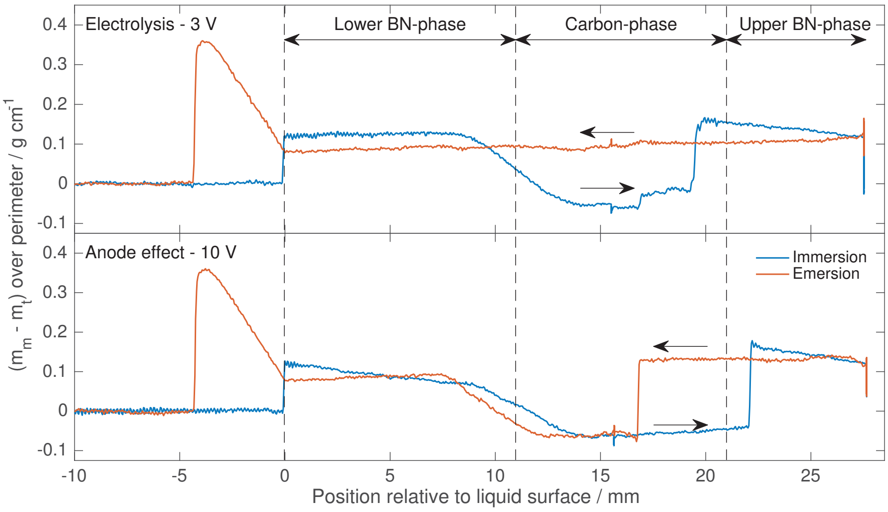

(a) Buoyancy corrected weight vs. position.

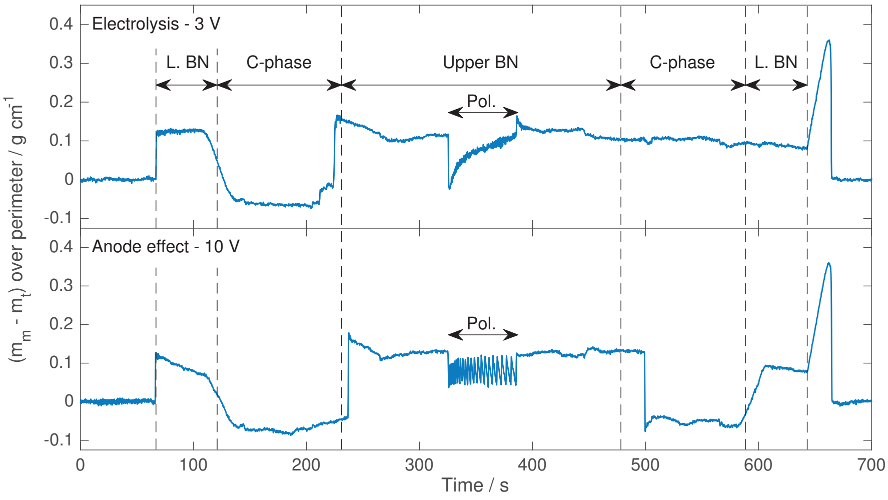

(b) Buoyancy corrected weight vs. time.

Figure 8.8: Buoyancy corrected weight vs. position and time on a vertical anode in a melt containing 1 wt% Al_2O_3. The upper plots show regular polarisation at 3 V, while the lower plots present anode effect polarisation at 10 V. The upper and lower samples were previously treated with polarisations at 2 V and 9 V, respectively. The samples were polarised with the meniscus on the BN-phase.

When approaching the carbon phase, which is negatively wetted, the elevation of the meniscus will decrease and pass through a zero in the transition region between the phases. Continuing on carbon the meniscus is lowered compared to the bulk electrolyte. When the second BN-phase is approached the very negatively wetted sample that had undergone anode effect polarisation does not “see” the BN until it is below bulk electrolyte level as is evidenced in the lower trace of Figure 8.8a. The upper trace with the less negatively wetted carbon could also be expected to touch the BN-phase at a position lower than the bulk electrolyte, yet, it is realised before as could be expected from a positively wetted material. The reason for the discrepancy is unknown, however, it may stem from previous immersions leaving a thin electrolyte layer connecting the two phases, or be related to the wetting hysteresis, which show an appreciably wetting receding contact angle (θ_r) for normally polarised carbon. More on the latter is given in a later section.

Polarisation at regular voltages produced a weight trace not unlike the the one observed on the cup anode. At first there is a large drop due to initial bubble production with little convection, however, with increasing convection the bubble buoyancy is almost cancelled (upper plot of Figure 8.8b). At anode effect voltages a regular cyclic weight trace is produced during polarisation. It is very similar to gas production and release on a horizontal surface during normal polarisation, although this sample exhibits a purely vertical surface. It is believed that gas is very slowly produced, sticking to the surface and gets entrapped between carbon and the upper BN-phase. Once enough gas has coalesced the buoyancy is large enough to detach the gas from the anode sample. The current reaches peak values with the low points of the weight trace, further suggesting small bubbles to be released revealing area to be re-passivated. The average polarization current decays from 2 A to 0.5 A, which largely explains the decreasing gas release frequency.

After polarisation the wetting weight is largely the same as before, which is expected with the meniscus on BN. Removal of bubbles is also better facilitated at a completely vertical surface. During emersion there is little change in the wetting weight for the normally polarised sample (Figure 8.8a), even difficult to detect when the meniscus passes between the different surfaces. Carbon is not generally expected to have the same wetting properties as BN, however, the receding wetting angle might approach the same values. The emersion cycle of the sample polarised to anode effect show that the meniscus is hanging on to the well wetted BN far past it has been emersed above the liquid level. When the meniscus has been passed across the BN/C junction it is rapidly dropping below the liquid surface due to the badly wetted carbon.

Polarisation was also conducted with the meniscus on the carbon layer of the vertical samples and this is presented in Figures 8.9a and 8.9b with wetting weight against immersed position and wetting weight against time, respectively. Both samples had previously undergone regular electrolysis at a cell voltage of 3 V. Initially the melt contained 1 wt% Al_2O_3, however the the anode effect appeared at a later time with a somewhat decreased alumina content. The wetting behaviour observed during immersion is similar to that of the vertical sample with polarisation on BN. The first BN-phase is well wetted by the electrolyte while carbon is somewhat less wetted. Normal polarisation produced an equal weight behaviour to that of carbon. The more positive weight after polarisation relative that before can be attributed to the higher polarisation voltage, which improves wetting as long as passivation is avoided. The anode effect polarisation instantly gave a passivated surface. The liquid level was placed in the middle of the carbon-phase creating a smaller active surface. Additionally, the meniscus is lowered from the de-wetting anode effect producing an even smaller surface area. This is also evidenced by the current which only averaged 0.1 A during the polarisation time. Any gas produced during polarisation is expected to release freely and not make much impact on the weight trace. No change in wetting weight was observed from the polarisation/OCP transition.

8.4.2 Wetting during polarisation

Wetting was observed on cup anodes with large perimeter over polarisations ranging from $U_{\text{cell}} = 1$ to 10 V and the results are presented in Figure 8.10. Two voltage rampings were carried out consecutively in a 1 wt% Al_2O_3 melt. The wetting weight during polarisation is lowered as bubbles with high buoyancy are produced. The curve has a high standard deviation due to the gas formation. The “after polarisation” data show a much improved wetting and it increased with polarisation until full passivation and anode effect was encountered. The measured wetting was further improved after reimmersion, likely because some bubbles were still attached to the surface before it was emersed and reimmersed. All polarisations improved the wetting, although positive wetting was only observed for the highest polarisations that do not end up with an anode effect. With only 1 wt% Al_2O_3 polarisations with 7 V cell voltage or higher instantly passivated the sample. The second voltage ramping is very similar to the first, however one sample was passivated already with a cell voltage of 6 V. This is both evidenced by the moderately lower wetting weight at 6 V as well as the big shift in current at this voltage. The improved wetting from polarisation can likely be related to the electrical double layer which will vary with electrification [118]. Impedance measurements were not conducted in the present work, however, literature data indicate that the capacitance of the electrified interface decreases

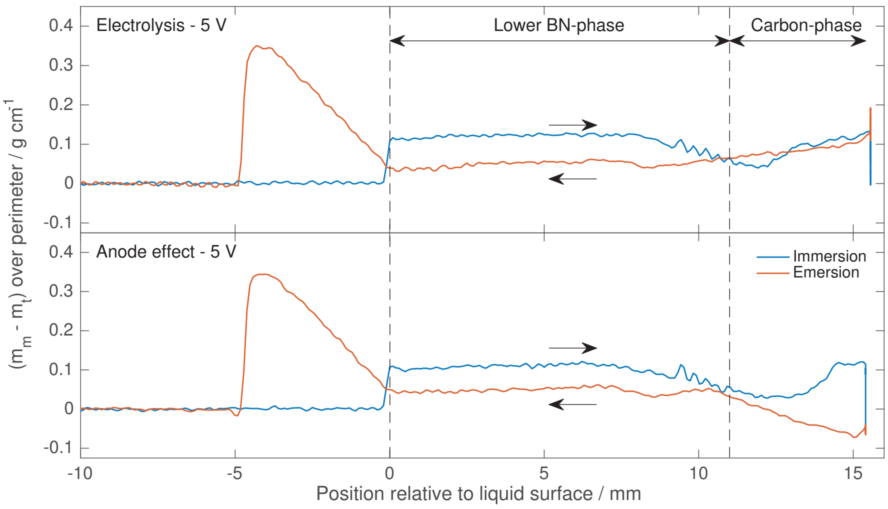

(a) Buoyancy corrected weight vs. position.

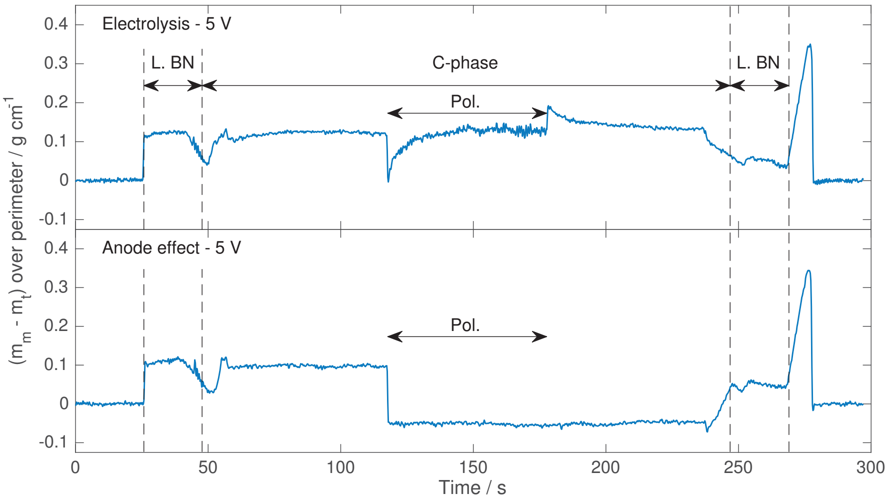

(b) Buoyancy corrected weight vs. time.

Figure 8.9: Buoyancy corrected weight vs. position and time on a vertical anode in a melt containing ~ 1 wt% Al_2O_3. The upper plots show regular polarisation at 5 V, while the lower plots present anode effect polarisation also at 5 V, albeit at a later time. Both samples were previously treated with regular polarisations at 3 V. The samples were polarised with the meniscus on the C-phase.

with potential and current density, sometimes passing through a minimum value before slightly increasing again [119–121]. This new electrified interface was “permanent” over a time frame of several minutes, only changing when another potential was applied to the cell.

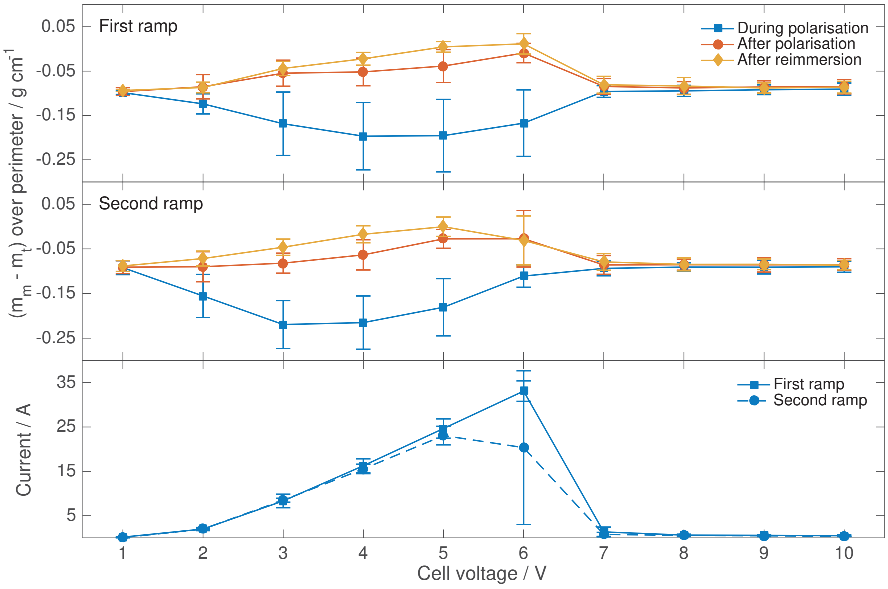

Figure 8.10: Wetting weight of polarisations at different voltages in a 1 wt% Al_2O_3 melt. The upper and middle graph show the wetting weight of the first and second polarisation ramp, while the lower plot presents the current passed during the polarisation step.

Data for wetting at Al_2O_3 concentrations 1, 3, 5 and 11 wt% is presented in Figure 8.11. Only the lowest alumina melt became passivated during the measurements. 3 wt% Al_2O_3 saturated the PSUs current capabilities at U_{cell} = 10 V while 5 wt% and 11 wt% were limited by current already at 8.2 and 9.2 V, respectively. The latter result is a bit odd as it would have been expected that the melt saturated in alumina reached the PSUs current capabilities at an even lower voltage. Sample surface area could likely have been reduced to decrease critical total current of passivation, however, that would have reduced immersion/emersion which is already quite short, considering the meniscus height which can be several millimetres at full wetting/de-wetting.

Weight drop observed during polarisation was higher for melts lower in alumina, even though the current passed is quite similar. A change in the bubble release process was likely facilitated by the different wetting properties of the melt, which increases with alumina. The data after polarisation was, for the most part, similar between the different melt compositions and rose with increasing polarisation, however the saturated melt deviated from this and showed an almost similar weight throughout the different polarisations. The wetting weight of the 1 wt% Al_2O_3 melt naturally dropped on the 7 V polarisation as it was passivated. The wetting weight after reimmersion increased similarly for all but the saturated melt. The wetting of the melt containing 1 wt% naturally stayed low after it was passivated, while the wetting of the other two melts continued to improve with increased polarisation. The saturated melt again showed strange and unexpected behaviour, not following or surpassing the wetting of the rest, even though some improvement in wetting weight is observed with increasing polarisation. One possible reason for the odd behaviour could be a very slight supersaturation of alumina, creating a heterogeneous melt with undissolved alumina particles.

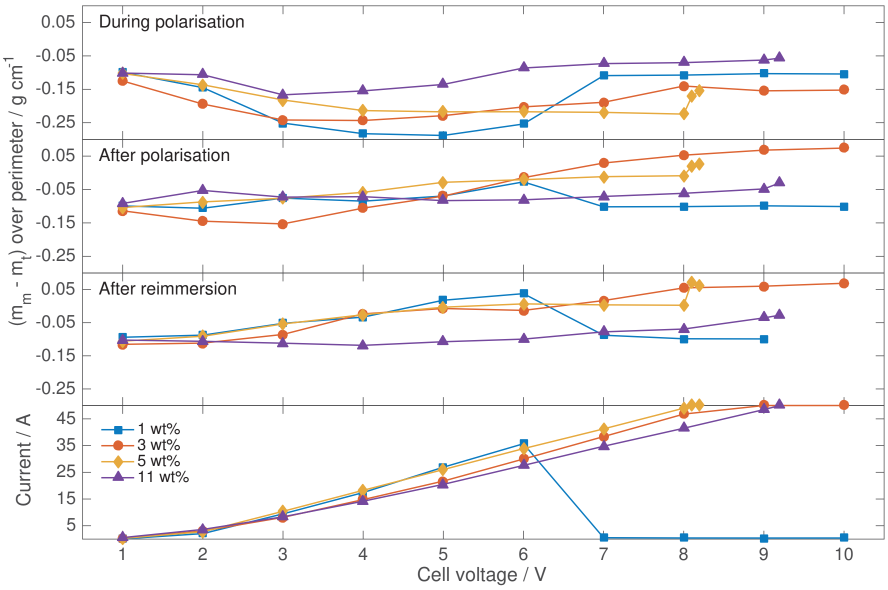

Figure 8.11: Wetting weight of polarisations at different voltages in melts with 1, 3, 5 and 11 wt% Al_2O_3. Only the lowest alumina melt reach passivation.

8.4.3 Increased passivation time

Figure 8.12 shows the development of the wetting weight with increased time at anode effect inducing potentials in a 1 wt% Al_2O_3 melt.

The two points on the lower left describe the immersion wetting of an untreated sample, which is equivalent to a very large wetting angle. After the sample was pretreated with 60 s polarisations at 3 and 4 V huge improvements in wetting were obtained (upper points at left side). Wetting after pretreatment at 10 mm has a much lower contact angle than observed at 15 mm, which can likely be ascribed to the local current density at the different planes. The upper plane was in line with the meniscus during polarisation and convection being lower than at 10 mm. The current density observed at 10 mm is likely higher and more preferred from a wetting perspective. Qiu et al. [122] also found wetting to improve with anodic current density up to about 1 A cm^{-2} at which point it started to decrease again. For anode effect polarisations the cell potential was set to 20 V. The wetting was severely decreased already after the first few seconds of anode effect, and after about 60 s no added reduction in wettability was observed. The current during passivation ranged from 0 to 1 A. The data shows that de-wetting is not necessarily linked too strongly to the surface polish that takes place during long anode effects [123]. However, surface polish may still affect the effort needed to convert an anode effect back to regular electrolysis as a smooth and polished surface has a low surface area.

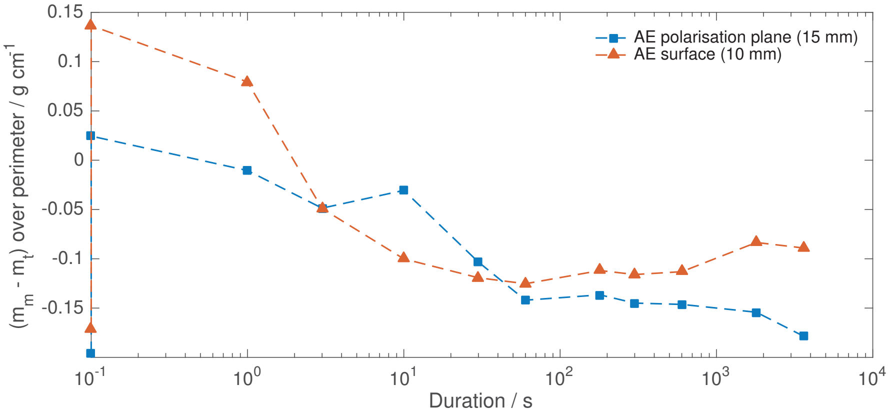

Figure 8.12: Wetting weight of inverted graphite cup electrode with increasing anode effect time. Lower points on left y-axis represent wetting weight of untreated electrode, while the upper points represent wetting weight of graphite pretreated with 60 s polarisations at 3 and 4 V.

8.4.4 Increased alumina content

In the literature there is general agreement that the contact angle of wetting is improved by alumina [6, 100, 105]. Previous measurements has for the most part been conducted on unpolarised samples, often using the "Sessile drop method". In this work wetting was observed on a polarised sample, with one part poorly wetting from anode effect, and another part well wetted from regular electrolysis at 3 to 4 V cell voltage. The results obtained by successively increasing alumina concentration are presented in Figure 8.13. At 1 wt% the observed wetting weights were according to pretreatment, positive for the electrolysis surface and negative for the anode effect surface. After the first addition of alumina both wetting weights decreased to severely de-wetting values and continued on the same path for several additions. From 6 wt% alumina an improvement in wetting was observed at the electrolysis surface, while the anode effect surface continued to be very de-wetted. Alumina was with the present melt composition at 1000 °C theoretically soluble up to a concentration of approximately 11 wt%; hence it is not unlikely that the irregular behaviour from 11 wt% Al_2O_3 is caused by a supersaturated melt with undissolved alumina particles. A similar change in anode/electrolyte wetting was observed by Solheim et al. [100].

Why the wetting weight of both electrolysis and anode effect surfaces drop when alumina was added is peculiar and not fully understood. Alumina was given about 10 min to mix, which should be ample time with stirring [124, 125], but perhaps a little short when no stirring was employed. On the other hand the added alumina contained about 1 wt% of water, which is known to induce stirring combined with the production of HF and CH_4 gas in contact with electrolyte and carbon. The produced gases or air that was possibly leaked in during the alumina additions may also have altered the electrolyte surface causing the bad wetting. A third possibility is that the polarisation effect is cancelled when the electrode is treated with a new electrolyte composition.

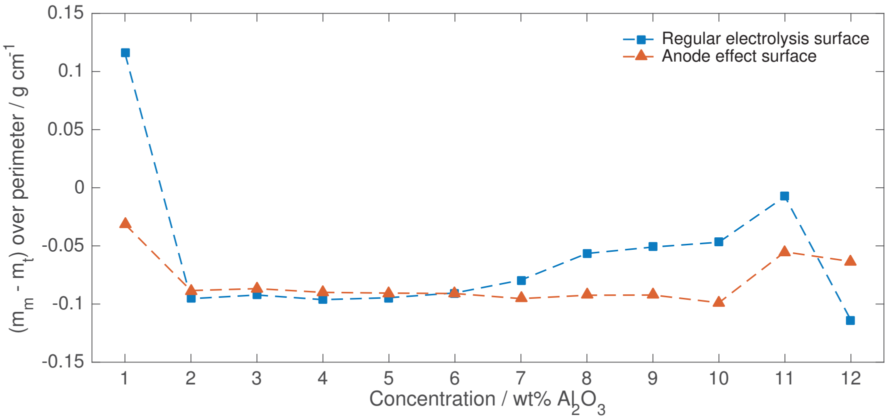

Figure 8.13: Wetting weight of inverted graphite cup with increasing alumina content. Alumina was added in 1 wt% increments. Saturation concentration expected at about 11 wt%.

It should be noted that the the wetting weight of different melts are comprised of both surface tension and wetting angle, thus cannot be directly compared. However, according to investigations by Fernandez et al. [116] the surface tension was shown to vary little with alumina (see Figure 8.3). Hence, comparing wetting weights should give good indication of how the wetting properties vary.

8.4.5 Equilibrium wetting angle

The wetting contact angle may vary between the limits of the advancing and the receding angle and should approach an equilibrium value when not exposed to external influences. However, the time frame of this movement towards equilibrium contact angle can be substantial. Wetting weight for the different samples versus time is presented in Figure 8.14 and the average angles logged over the time frame is given in Table 8.1.

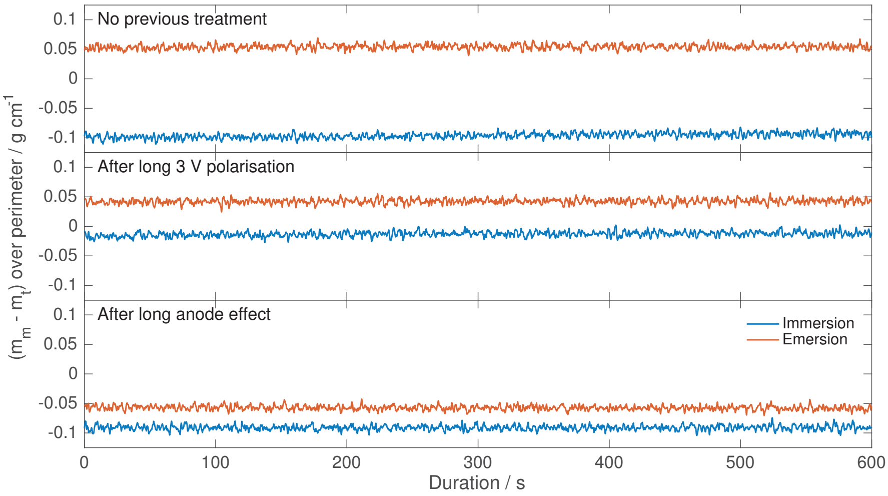

Figure 8.14: Measured weight change of untreated, normally polarised and AE polarised inverted graphite cup samples. Advancing data logged for 10 min after the sample was immersed to 10 mm. Receding data logged for 10 min after the sample was emersed from 15 to 10 mm.

The wettability observed during immersion for the three different samples always showed a larger contact angle than that found during emersion. This is the expected behaviour, however some of the above results indicate that the opposite is also possible. The trend of the immersion data is comparable to that observed above with the wettability being low before any polarisation has taken place and after anode effect, while it is somewhat higher after normal polarisation. From emersion both the untreated and normally polarised sample show quite positive wetting, while the AE sample show quite negative wetting. Little visible evidence is provided of an approach to an equilibrium value during the measurement interval, from both directions. This is unsettling as it would imply the results obtained from wetting is strongly influenced by the experimental conditions.

Hysteresis was very much decreased from an untreated sample to a polarised sample. Additionally the average between advancing and receding angles was shifted far into the wetted region. Similarly anode effect polarisation saw an even smaller hysteresis with the average shifted far into the de-wetting region.

The advancing contact angle is expected to be the most reproducible and might be a good approximation of an equilibrium value in the absence of one [107, 126]. The reproducibility of the receding angle is often lowered due to liquid sorption and swelling [127]. Previously reported values of the wetting on an untreated sample was between 120 and 130 degrees [105], which correspond best with the advancing angle of the present data. Qiu et al. [122] reported contact angles in the range of 40 to 60° at a current density of 0.6 A cm^{-2} and an alumina content of 5.5 wt%. The experimental conditions were not identical, still the receding angle correspond best at this instance.

Table 8.1: Calculated advancing and receding angles of wetting for untreated, polarised and AE polarised anodes. $\gamma_{lv} = 110.7\,\mathrm{mN\,m^{-1}}$ [116].

Type	Advancing angle θ_a / °	Receeding angle θ_r / °	Hysteresis $\Delta\theta$ / °
Untreated	148	61	87
Electrolysis (3 V)	97	68	29
Anode effect (25 V)	144	121	23

Outside of the laboratory the different angles themselves are not that interesting. In an industrial cell there are so much flow from bubbles and metal that any intersection is never stagnant, or moving perfectly in one direction. Even the meniscus around the anodes will fluctuate a fair bit from metal waves and bubble release. Therefore, it makes more sense to talk about a wetting distribution, which then includes everything in between the advancing and receding angles. Polarisation is therefore beneficial for the distributed wetting of the process, even though the maximum wetting was found to occur on an untreated sample. Passivation and anode effect is on the other hand very bad for the process as it shows a consistently bad distributed wetting. When it occurs in one place on an anode it will lock that region from producing much bubbles – reducing mixing, and this can quickly propagate to cover the whole anode where it initiated if the conditions are appropriate. Untreated it may disturb the cell so much that a full anode effect eventually develops over the entire cell.

8.5 Conclusions

Untreated graphite mostly show poor wettability by the cryolite-alumina electrolyte. Small receding contact angles were produced, however, the advancing angles were very large and poorly wetting and the larger part of the contact angle hysteresis lie in the poorly wetting region. Polarisation improved the wettability significantly and the contact angle decreased with increased polarisation as long as passivation (AE) was not initiated. Positive advancing (immersion) contact angles was exhibited only at the highest polarisations and longest polarisation duration, although all polarisations were shifted in the positive direction when compared to untreated graphite. The contact angle hysteresis was smaller than for untreated graphite with a positive average wetting ($\theta < 90°$). Anodes polarised to anode effect showed a consistent de-wetting behaviour. The hysteresis was the smallest observed and even the receding contact angle was found to be quite de-wetting. The de-wetting during anode effect was mostly established during the first ten seconds and after 60 s no additional decline in wetting was observed.

Higher amounts of alumina promoted bubble detachment from the anodes, likely by improvement of graphite wettability by the electrolyte, especially from about 6 wt%. High alumina melts can also reach better wetting than low alumina melts as it can be polarised further without inducing an anode effect.

Bad wetting is observed on anode effect treated samples after they have been extracted and reimmersed into the melt, suggesting that there is no covering gas film, but rather a changed anode surface that is the cause of an anode effect.

Chapter 9

Discussion

It is argued throughout the work that PFC production during a full anode effect follows the same basic mechanism as PFC production during what is seemingly normal cell voltages, and not something specific to a certain cell technology. In the industrial measurements of Chapter 3 it is shown that PFCs can evolve outside of the conventional AE from small cells with about 20 anodes running at approximately 200 kA, something that at the time was really only known to take place at much larger cells. It is true that the cells were provoked to yield results during the limited on-site measurement campaign; nonetheless, all of the interventions performed do also occur naturally from time to time.

Discussing how one could experience this phenomena of PFC production during normal electrolysis potentials in the laboratory, it was soon realised that having only one anode under constant current conditions could become difficult. With the partial passivation of electrode area the current density through the remaining healthy area would increase, likely invoking a domino effect that would end up with a full anode effect. Additionally, the literature data seemed to agree with this, with researchers merely seeing a shoulder of PFC production before full anode effect occurred with much elevated voltages. Having two real anodes was found to be the inflection point between “needing more than one” and “two or more is a hassle”. Also considered was a segmented larger anode, not unlike how the industrial anode is segmented by its slots, but it was abandoned because of the difficulty of controlling the electrolyte composition without physically separating compartments. Another key difference between an industrial cell and most laboratory cells is the cell voltage, which is much higher for the industrial cell. With uneven current distribution over the anodes this voltage can and will redistribute within one or more cell segments, and the anode itself is most prone to adopt this redistributed voltage. This is argued throughout the text and particularly in Chapter 5. Extra resistors (or electronic loads) were added in series with the anode(s) in order to simulate this higher industrial cell voltage.

For the same reasons that constant current power delivery was expected to propagate quickly to full AE with one anode, this was also expected to happen in a two-anode set-up if one anode went directly to full AE and the other had to incorporate the full current load. For this reason the initial plan was to perform the experiment under constant voltage conditions; after all, the anodes of the industrial cell are working under relatively constant potentials. Under constant voltage the current only flowed through the anodes initially, quickly dampening and approaching zero current throughput long before the alumina could have been depleted. Current throughput was generally low, showing a sharp peak immediately after bubble release, but spending most of the time at very low currents slowly building the bubbles. With this behaviour it also spent most time at very high potentials as the ohmic drop across the resistor was small, likely slowly building a passivating layer developing one bubble release at a time. Eventually there was almost no current throughput and just a maintaining passivating potential on a “dead” cell, much like the behaviour observed from the voltammetry experiments of Chapter 7 with elevated potentials in melts low in alumina.

Changing the power delivery to constant current made the system work and let current be easily passed through the cell. The distribution between the anodes was most of the time approximately uniform, even though one compartment could have an alumina concentration of 5 wt% and the other 3 wt%. As expected some experiments ended with a quick domino effect to full anode effect on both anodes, but it also provided us with the results of Chapter 4, which goes some way in verifying that the PFC producing reactions provides a larger cooling of the anode than regular CO_2 production, as predicted by thermodynamics. Normally during an anode effect large heating is observed, and that has also been observed here, but this is mainly caused by the much elevated voltage, introducing a lot of energy into the cell. Unfortunately no gas analysis machinery was equipped that could verify the production of any PFC, however, even with gas analysis equipment negative detection would not necessarily rule out the existence of PFCs, as it may decompose in the electrolyte and over refractories (Chapter 6). This effect was only seen in one experiment, but on three separate occasions and with a full anode effect and an alumina feeding in-between. Some cryolite fumes had possibly penetrated through the assembly on the one anode, creating the noisy temperature signal towards the end of the experiment, even so that cannot explain the behaviour of the other thermocouple or the observations in the earlier part of the experiment. Taking into account that the likelihood of observing low cell-voltage PFC on a system with few anodes it is perhaps not that strange it was not observed again.

It was further realised that the electronic load could be used not only as a potential elevator or a single anode, but could be used to simulate many anodes, further approximating some of the properties of the industrial cell like current sharing and the possibility for redistribution. An added effect of attaching a large load and having many "virtual anodes" is that a real full (industrial like) anode effect becomes impossible, simply because the load will absorb all the current before the voltage reaches really high values. With this set-up the initial anodes had a current of about 3.5 A at $1\,\mathrm{A/cm^2}$, but still it was difficult to observe any PFC evolution except when the anode transitioned to "complete" passivation. At the time the low gas production from low amperage was blamed as the cause for the low PFC signal and a change to larger anodes was invoked, only later to realise that a likely culprit could also be PFC gas decomposition/consumption. It was switched to larger anodes running with about 10 A an $1\,\mathrm{A/cm^2}$ with a large electronic load in parallel, able to simulate more than 20 similar sized virtual anodes. This was expected to increase the probability of again observing an anode lingering between regular production and anode effect, now with the additional gas analysis. The electrochemical response of such a phenomena was observed, however, the PFC concentration found with gas analysis was very low and possibly not significant. This could again be because lower PFC concentrations are difficult to detect due to their decomposition problem.

By varying the number of virtual elements the real anodes can be steered towards either full anode effect or a region were partial anode effect is more likely. By having 10 virtual and two real anodes it was observed that full industrial like anode effect with substantial PFC production initiated on one anode. It is difficult to address why the other real anode did not observe the same effect, but possibly the added "drive" was not enough for this particular sample, or maybe something in its previous history disallowed full anode effect under the specific conditions. The number of virtual anodes may also be increased. In the extreme case with very many virtual anodes (compared to real anodes) the electronic load will have no problem carrying all the current with minimal increase of cell voltage. It will in fact approach constant voltage conditions and the passivation outcome with almost no current throughput described above is likely (in the laboratory). Naturally, the anodes of an industrial cell does not behave as ideal electrical elements and their resistance is not constant, and neither are the anodes completely isolated as they share cell and electrolyte. Industrially, the full current will pass through the cell in one way or another, whereas that is not necessary in the present laboratory set-up, it may (almost) all pass through the electronic load. Nevertheless, in between the extremes of zero and infinite virtual elements the set-up seems to go a long way in representing the industrial cell. It also provides evidence that the discussed anode effect events likely have the same origin, but develops differently due to different local and global cell properties.

Quite often when carbon is passivated, PFCs are not detected by the gas analysis equipment. In some of the cases where the passivation current is very low the detection level of the analysis equipment could be insufficient. This was the initial reason why larger anodes were selected for the work of Chapter 6, even though this would decrease the sidewall distance from 11.75 mm (albeit mostly shielded) to 8.75 mm (completely unshielded) at the nearest point. This naturally has some downsides like increased stray currents, dissolved alumina and electronic conductivity; nonetheless considered acceptable as the work is mostly qualitative. However, even with passivation currents of a few amperes PFCs were often not detected. The most likely reason is that the gases decomposed before they reached the detector, either chemically over compounds such as Al_2O_3 or just thermally. It was shown that no detactable traces of a 5 ppm CF_4 reference gas remained after passing through the furnace, separately not detected by two different FTIRs. Part of the reason can also stem from the increased electronic conductivity. To discover lower amounts of the gases it seems crucial to extract them quickly away from high temperatures and catalyst materials and to utilise a well thought-out experimental set-up. Nevertheless, really small concentrations will likely decompose over alumina already before leaving the electrolyte. Environmentally this is a good thing even though we will not get to measure it.

A curious effect observed is the extreme dusting in these low alumina “approaching anode effect” experiments. After 8 plus hours of experiment time (not all electrolysis) it is almost impossible to get the anodes on anode effect (particularly the large anodes), likely due to a crude short circuit between the anodes and the side wall. The larger anodes were likely more prone to this due to a shorter anode/wall distance and that they were unshielded. The smaller anodes had their BN shield, but the design or material choice could have been improved as they often cracked towards the end of an experiment.

The voltammetry experiments with gas analysis additionally showed that partial passivation can occur on just one anode, even though most experiments showed a direct drop to full passivation. Still, the biggest takeaway from those experiments is likely the fact that in order to recover a passivated anode it is necessary to lower the anode voltage, or temporary manipulate the recovery potential by e.g. adding alumina, a method frequently used industrially. Once the anode has recovered the anode voltage will be kept low as the restored current throughput will be accompanied by an ohmic drop.

Even though the experimental data are scarce, the wetting experiments also suggest higher alumina content in the melt improves wetting, especially from about 6 wt% Al_2O_3, which again partly explains why it helps dumping large amounts of alumina in the bath of an industrial cell when quenching an anode effect. Industrially, on the other hand, it is beneficial to keep the alumina concentration quite low as this improves current efficiency and lessens the amount of sludge build-up below the metal pad. The incipience of bad wetting was observed almost instantly when polarised at anode effect voltages, being completely de-wetted after only about 60 s. Since the anode had the same wetting after being emersed/reimmersed it is unlikely that the bad wetting and reason for an anode effect is the production of a gas film covering the entire surface, but rather an anode surface "film" including many C−F bonds. Still, from the experiments on fully submerged vertical samples under polarisation a weight oscillation is observed, that may originate from slow release of fluorocarbons or carbon oxyfluorides. C−F bonds have been found to be present on anode effect treated samples [93], but has also been shown to be present to a smaller extent on normally polarised samples [94]. In the low alumina melts the buoyancy suggests that more gas is generally located under the anode, and the anode surface covered by said gas is likely higher than in higher alumina melts. The aim of the industry should be to find an an alumina content that is a good compromise between anode gas coverage and the proximity to anode effect at the low-alumina end, and the proximity to sludge production and low current efficiency at the high-alumina end.

The gas COF_2, a possible intermediary to CF_4 was not discovered in any of the experiments. Nor was it always looked for as it was difficult enough to produce relevant data that included CF_4. It is known to be quite unstable and seldom reported to be detected in the literature. On the mass spectrometer it would also either reduce detector time for others gases, or reduce sample rate. Taking into account that it has an interference at its base peak ($m/z = 47$) with SiF_4, a gas that can be encountered in these experiments, also necessitates the use of additional peaks for verification.

It seems unlikely that PFC production will be completely eliminated as long as aluminium is produced in cryolite with oxidation of carbon at the anode. To keep the production low it is important that the industry continue the good work on improving alumina distribution and lowering the cell voltage. A lower cell voltage will provide a smaller voltage window that can redistribute to the anode.

Chapter 10

Conclusions

The results show that low cell-voltage PFC evolution can occur on industrial cells in the 200 kA range and therefore is likely not specific to any cell size or technology, but can presumably take place for all aluminium production that is conducted in a cryolite based melt with carbon anodes. The frequency and likelihood of observing a low cell voltage anode effect is on the other hand quite related cell properties such as the number of anodes and the electrolyte/alumina mixing. There is less room for current redistribution in a smaller cell with few anodes and thus less likely with smaller bursts of low cell voltage PFC evolution from one or a few anodes. Instead such a cell has a higher probability of going straight to a conventional anode effect. This is also the main reason why little other than a PFC shoulder is visible before the conventional high voltage anode effect in most laboratory studies with one anode.

Low cell voltage anode effect with partial passivation and some PFC evolution was also found in a laboratory set-up with two anodes and an electronic load simulating additional elements connected in parallel. The evidence clearly indicates that the mechanism behind traditional and low voltage anode effect are the same, with other system parameters dictating how much the voltage needs to be elevated to pass the current.

The passivation potential of the anode was found to be very dependant on the amount of alumina, and increased with increasing content. Some PFC was observed before full passivation occurred, and at the lowest from about 2.8 V anodic versus the aluminium pseudo-reference electrode. Increased convection elevated the potential from which PFC was observed, either suggesting that the kinetics of regular production is faster than anode effect production, or that the increased alumina flux is able to neutralise much of the produced PFC. Since it has been shown that PFCs get decomposed by the electrolyte and refractories it is also likely that small amounts are produced at lower potentials, closer to the thermodynamically theoretical potential, than what has been detected by the gas analysis equipment. This may happen either through the direct CF_4/C_2F_6-route or even the indirect COF_2-route, although no efforts to verify the latter have been attempted in this work.

The wetting of graphite towards the electrolyte was improved by increased polarisation, well past the potential where PFCs could thermodynamically be produced. Only when the anode gets passivated is de-wetting observed. De-wetting thus maintains passivation and anode effect, however, bad wetting is likely not the cause of an anode effect.

Chapter 11

Suggestions for Further Work

With the realisation that cell segments can to some extent be simulated by the inclusion of an electronic load it could in many ways be beneficial to work with only one real anode as this is much easier to set up and control, especially with the use of gas analysis equipment. Naturally this limits the number of elements that can realise anode effect. Several improvements can also be made to the two-compartment design and especially to the gas analysis design. It would be advantageous with two equal analysers and enough flow controllers to account for all inputs and outputs so that the two output flow can be selected identical and that the input inert carrier gas provides a very small overpressure, the latter to reduce the evaporation of electrolyte, and by extension the clogging of gas sampling tubes (can also be applied with one real anode). This should eliminate any possibility of gas crossover when output flows are selected much higher than the total possible gas flow from electrolysis. The larger anodes used at the end were equipped to be able to increase the current and not part of the original design. The distance to the side wall is arguably on the narrow side with these anodes and substantial fraction of the current likely passed through to the side wall, which likely has provided increased electronic conductivity and back reaction. Further such experiments could be conducted with purely vertical anodes to cancel out most of the “bubble noise”.

Beneficial for all experiments where individual electrode voltages are of interest is a stable and long lasting reference electrode. Initial testing during this work showed that the used reference electrodes approached a fairly stable value (measured against to a graphite rod as pseudo-reference electrode as well as the cathode crucible) after about two hours of equilibration time, and began to deteriorate after 24 – 48 h. The use of thin BN was also prone to cracking. It would be interesting to look into a few additional reference electrode types and play with the design to improve them.

It could be interesting to combine the wetting analysis with gas analysis to determine what type of gas evolution is related to the anode/electrolyte wetting. Gas analysis equipment can be connected at the gas exhaust with some improvements to system design to make it sealed properly (as it mow relies on considerable gas flow to keep an inert system). Better yet the gas could be sampled close by the anode to reduce gas response time and lower the the probability of gas constituent decomposition. As of now the biggest problem with this method is that the introduction of a gas sampling tube, or any other long vertical rod, introduces so much vibrational noise that it renders the output from the load cell unusable and this needs to be remedied.

Use the wetting apparatus to investigate bubble development on horizontal anodes and combine this with visual verification from experiments in a see-through cell. Some work on the former was conducted, however not presented in this thesis and only to a smaller extent in Eidsvaag [123]. Such work could give valuable information about the bubble coverage and bubble release at different current densities, both during regular electrolysis and anode effect.

Bad wettability was shown to occur just after a few seconds of anode effect. It could also be interesting to se how fast a system recovers after different durations on anode effect. This could for instance be measured as the time it takes to reach a certain wettability, in addition to a measure of the maximum attainable wetting weight post anode effect.

Bibliography

[1] H. Åsheim, T. A. Aarhaug, A. Ferber, O. S. Kjos, and G. M. Haarberg. “Monitoring of Continuous PFC Formation in Small to Moderate Size Aluminium Electrolysis Cells.” In: *Light Metals 2014*. John Wiley & Sons, Inc., 2014. 535–539. doi: 10.1002/9781118888438.ch91. (see pp. iii, 7, 35, 50, 66, 81, 173)

[2] H. Åsheim, T. Aarhaug, E. Sandnes, O. S. Kjos, A. Solheim, and G. M. Haarberg. A Laboratory Study of Partial Anode Effects during Aluminium Electrowinning. *ECS Transactions* **69**(15): 1–12, 2015. doi: 10.1149/06915.0001ecst (see pp. iii, 49, 87, 173)

[3] H. Åsheim, T. A. Aarhaug, E. Sandnes, O. S. Kjos, A. Solheim, S. Kolås, and G. M. Haarberg. “Anode Effect Initiation During Aluminium Electrolysis in A Two Compartment Laboratory Cell.” In: *Light Metals 2016*. John Wiley & Sons, Inc., 2016. 551–556. doi: 10.1002/9781119274780.ch92. (see pp. iii, 65, 81, 173)

[4] H. Åsheim, T. A. Aarhaug, W. Gębarowski, E. Sandnes, A. Solheim, and G. M. Haarberg. Partial Anode Effect in a Two-Compartment Laboratory Alumina Reduction Cell. In: *Light Metals 2017*. Ed. by A. P. Ratvik. Springer International Publishing, 2017, 525–532. doi: 10.1007/978-3-319-51541-0_66 (see pp. iv, 79, 173)

[5] K. Grjotheim and H. Kvande, eds. *Introduction to Aluminium Electrolysis: Understanding the Hall-Heroult Process*. 2nd ed. Düsseldorf: Aluminium-Verlag, 1993. I–260. (see pp. 1, 5)

[6] K. Grjotheim, C. Krohn, M. Malinovský, K. Matiašovský, and J. Thonstad. *Aluminium Electrolysis: Fundamentals of the Hall-Héroult Process*. 2nd ed. Düsseldorf: Aluminium-Verlag, 1982. (see pp. 1, 80, 94, 114, 132)

[7] N. C. Craig. “Charles Martin Hall The Young Man, His Mentor, and His Metal.” In: *Hall-Heroult Centennial: First Century of Aluminum Process Technology, 1886 – 1986*. Ed. by W. S. Peterson and R. E. Miller. Warrendale, PA: The Metallurgical Society, Inc., 1986. 96–101. (see p. 2)

[8] W. Haupin. “History of Electrical Energy Consumption by Hall-Héroult Cells.” In: *Hall-Heroult Centennial: First Century of Aluminum Process Technology, 1886 – 1986*. Ed. by W. S. Peterson and R. E. Miller. Warrendale, PA: The Metallurgical Society, Inc., 1986. 106–113. (see p. 2)

[9] J. Thonstad, P. Fellner, G. M. Haarberg, J. Híves, H. Kvande, and Å. Sterten. *Aluminium Electrolysis / Fundamentals of the Hall-Héroult Process*. 3rd ed. Düsseldorf: Aluminium-Verlag, 2001. XI, 359 s. (see pp. 3–6, 37, 66, 94)

[10] E. H. Howard. Some Physical and Chemical Properties of a New Sodium Aluminum Fluoride. *Journal of the American Chemical Society* **76**(8): 2041–2042, 1954. doi: `10.1021/ja01637a003` (see pp. 3, 82)

[11] H. Pulker and C. Zaminer. Composition and Structure of Vapour-Deposited Cryolite Films. *Thin Solid Films* **5**(5–6): 421–428, 1970. doi: `10.1016/0040-6090(70)90113-6` (see p. 3)

[12] F. Habashi and Q. City. Bayer’s Process for Alumina Production: A Historical Perspective. *Bulletin for the History of Chemistry* **18**: 15–19, 1995 (see p. 4)

[13] F. Habashi. A Short History of Hydrometallurgy. *Hydrometallurgy* **79**(1–2): 15–22, 2005. doi: `10.1016/j.hydromet.2004.01.008` (see p. 4)

[14] L. P. Lossius, I. Holden, and H. Linga. “The Equivalent Temperature Method for Measuring the Baking Level of Anodes.” In: *Light Metals 2006*. Warrendale, PA, USA: The Minerals, Metals and Materials Society, 2006. 609–613. (see p. 5)

[15] R. J. Thorne, C. Sommerseth, A. P. Ratvik, S. Rørvik, E. Sandnes, L. P. Lossius, H. Linga, and A. M. Svensson. Correlation between Coke Type, Microstructure and Anodic Reaction Overpotential in Aluminium Electrolysis. *Journal of The Electrochemical Society* **162**(12): E296–E306, 2015. doi: `10.1149/2.0461512jes` (see p. 5)

[16] M. Sørlie and H. A. Øye. *Cathodes in Aluminium Electrolysis.* 2nd ed. Düsseldorf: Aluminium-Verlag, 1994. I–408 s. (see p. 5)

[17] J. Thonstad, F. Nordmo, and K. Vee. On the Anode Effect in Cryolite-Alumina Melts—I. *Electrochimica Acta* **18**(1): 27–32, 1973. doi: `10.1016/0013-4686(73)87006-9` (see pp. 6, 50, 80, 94)

[18] F. Nordmo and J. Thonstad. On the Anode Effect in Cryolite-Alumina Melts—III. Current—Voltage Behaviour during Anode Effect. *Electrochimica Acta* **29**(9): 1257–1262, 1984. doi: `10.1016/0013-4686(84)87188-1` (see p. 6)

[19] H. Vogel and B. Friedrich. "Development and Research Trends of the Neodymium Electrolysis – A Literature Review." In: *Proceedings of EMC 2015.* Düsseldorf, Germany, 2015. 689–701. (see p. 6)

[20] H. H. Kellogg. Anode Effect in Aqueous Electrolysis. *Journal of The Electrochemical Society* **97**(4): 133, 1950. doi: `10.1149/1.2777980` (see p. 6)

[21] A. Calandra, C. Castellano, and C. Ferro. The Electrochemical Behaviour of Different Graphite/Cryolite Alumina Melt Interfaces Under Potentiodynamic Perturbations. *Electrochimica Acta* **24**(4): 425–437, 1979. doi: `10.1016/0013-4686(79)87031-0` (see pp. 6, 38, 57, 80, 95)

[22] Z. Qiu and M. Zhang. Studies on Anode Effect in Molten Salts Electrolysis. *Electrochimica Acta* **32**(4): 607–613, 1987. doi: `10.1016/0013-4686(87)87049-4` (see p. 6)

[23] M. M. R. Dorreen, D. L. Chin, J. K. C. Lee, M. M. Hyland, and B. J. Welch. "Sulfur and Fluorine Containing Anode Gases Produced during Normal Electrolysis and Approaching an Anode Effect." In: *Light Metals 1998.* Warrendale, PA, USA: The Minerals, Metals and Materials Society, 1998. 311–316. (see pp. 7, 37, 38, 95)

[24] T. A. Aarhaug, H. Gaertner, A. Ferber, A. P. Ratvik, A. Solheim, and E. Skybakmoen. "Mapping of Primary Aluminium Raw Gas Composition by Online Fourier Transform Infrared Spectroscopy." In: *10th Australasian Smelting Technology Conference.* Hobart, Tasmania, Australia, 2011. (see pp. 7, 38, 95)

[25] H. Kvande and W. Haupin. Cell Voltage in Aluminum Electrolysis: A Practical Approach. *JOM* **52**(2): 31–37, 2000. doi: `10.1007/s11837-000-0044-x` (see p. 7)

[26] J. Thonstad and E. Hove. On The Anodic Overvoltage in Aluminium Electrolysis. *Canadian Journal of Chemistry* **42**(7): 1542–1550, 1964. doi: `10.1139/v64-237` (see pp. 7, 94)

[27] F. Nordmo and J. Thonstad. On the Anode Effect in Cryolite-Alumina Melts—IV. Gas Composition and Faradaic Efficiency. *Electrochimica Acta* **30**(6): 741–745, 1985. doi: `10.1016/0013-4686(85)80121-3` (see p. 7)

[28] R. A. Roberts and P. J. Ramsey. "Evaluation of Fluorocarbon Emission from the Aluminum Smelting Process." In: *Light Metals 1994*. Warrendale, PA, USA: Minerals, Metals and Materials Society, 1994. 381–388. (see pp. 7, 95)

[29] P. Fraser, B. Dunse, P. Steele, P. Krummel, and N. Derek. "Perfluorocarbon (PFC) Emissions from Australian Aluminium Smelters." In: *10th Australasian Aluminium Smelting Technology Conference*. Launceston, Australia, 2011. (see p. 7)

[30] International Aluminium Institute. *Results of the 2015 Anode Effect Survey*. Tech. rep. International Aluminium Institute, London, 2016, 1–17 (see p. 7)

[31] J. Kim, P. J. Fraser, S. Li, J. Mühle, A. L. Ganesan, P. B. Krummel, L. P. Steele, S. Park, S. K. Kim, M. K. Park, T. Arnold, C. M. Harth, P. K. Salameh, R. G. Prinn, R. F. Weiss, and K. R. Kim. Quantifying Aluminum and Semiconductor Industry Perfluorocarbon Emissions from Atmospheric Measurements. *Geophysical Research Letters* **41**(13): 4787–4794, 2014. doi: `10.1002/2014GL059783` (see pp. 7, 8)

[32] W. Li, Q. Zhao, S. Qiu, S. Zhang, and X. Chen. "PFC Survey in Some Smelters of China." In: *Light Metals 2011*. John Wiley & Sons, Inc., 2011. 357–360. doi: `10.1002/9781118061992.ch64`. (see pp. 7, 36, 50, 66)

[33] A. A. Zarouni and A. A. Zarouni. "DUBAL's Experience of Low Voltage PFC Emissions." In: *10th Australasian Smelting Technology Conference*. Hobart, Tasmania, Australia, 2011. 1–7. (see pp. 7, 36, 81)

[34] L. Wangxing, C. Xiping, Y. Jianhong, H. Changping, L. Yonggang, L. Defeng, and G. Huifang. “Latest Results from PFC Investigation in China.” In: *Light Metals 2012.* Hoboken, NJ, USA: John Wiley & Sons, Inc., 2012. 617–622. doi: `10.1002/9781118359259.ch105`. (see pp. 7, 36, 50, 66, 81)

[35] J. Marks and C. Bayliss. “GHG Measurement and Inventory for Aluminum Production.” In: *Light Metals 2012.* Hoboken, NJ, USA: John Wiley & Sons, Inc., 2012. 803–808. doi: `10.1002/9781118359259.ch139`. (see pp. 7, 36, 50, 66, 81)

[36] D. S. Wong, A. Tabereaux, P. Lavoie, and J. Marks. “PFCs from Low Voltage Propagating AEs & Non-Propagating AEs.” In: *11th AustralAsian Aluminium Smelting Technology Conference.* 2014. 1–20. (see p. 7)

[37] S. Kolås, P. McIntosh, and A. Solheim. “High Frequency Measurements of Current through Individual Anodes: Some Results from Measurement Campaigns at Hydro.” In: *Light Metals 2015.* John Wiley & Sons, Inc., 2015. 729–734. doi: `10.1002/9781119093435.ch123`. (see pp. 7, 16, 50, 67, 81)

[38] R. E. Weston. Possible Greenhouse Effects of Tetrafluoromethane and Carbon Dioxide Emitted from Aluminum Production. *Atmospheric Environment* **30**(16): 2901–2910, 1996. doi: `10.1016/1352-2310(95)00499-8` (see p. 7)

[39] IPCC. *Climate Change 2014: Mitigation of Climate Change. Contribution of Working Group III to the Fifth Assessment Report of the Intergovernmental Panel on Climate Change.* Ed. by O. Edenhofer, R. Pichs-Madruga, Y. Sokona, E. Farahani, S. Kadner, K. Seyboth, A. Adler, I. Baum, S. Brunner, P. Eickemeier, B. Kriemann, J. Savolainen, S. Schlömer, C. von Stechow, T. Zwickel, and J. Minx. Cambridge, United Kingdom and New York, NY, USA: Cambridge University Press, 2014. (see pp. 7, 50, 80)

[40] C. M. Trudinger, P. J. Fraser, D. M. Etheridge, W. T. Sturges, M. K. Vollmer, M. Rigby, P. Martinerie, J. Mühle, D. R. Worton, P. B. Krummel, L. P. Steele, B. R. Miller, J. Laube, F. Mani, P. J. Rayner, C. M. Harth, E. Witrant, T. Blunier, J. Schwander, S. O’Doherty, and M. Battle. Atmospheric Abundance and Global Emissions of Perfluorocarbons CF_4, C_2F_6 and C_3F_8 since 1900 Inferred from Ice Core, Firn, Air

Archive and In Situ Measurements. *Atmospheric Chemistry and Physics Discussions* **4**(June): 1–34, 2016. DOI: 10.5194/acp-2016-423 (see pp. 7, 8)

[41] A. Goldman, D. G. Murcray, F. J. Murcray, G. R. Cook, J. W. Van Allen, F. S. Bonomo, and R. D. Blatherwick. Identification of the v_3 Vibration-Rotation Band of CF_4 in Balloon-Borne Infrared Solar Spectra. *Geophysical Research Letters* **6**(7): 609–612, 1979. DOI: 10.1029/GL006i007p00609 (see p. 7)

[42] H. Vogel, B. Flerus, F. Stoffner, and B. Friedrich. Reducing Greenhouse Gas Emission from the Neodymium Oxide Electrolysis. Part I: Analysis of the Anodic Gas Formation. *Journal of Sustainable Metallurgy*: 1–9, 2016. DOI: 10.1007/s40831-016-0086-0 (see p. 8)

[43] International Aluminium Institute. *Statistics.* 2016. URL: http://www.world-aluminium.org/statistics/ (visited on 12/09/2016) (see p. 8)

[44] International Aluminium Institute. *Results of the 2014 Anode Effect Survey.* Tech. rep. London, 2015, 1–12 (see p. 8)

[45] A. P. Modica and S. J. Sillers. Experimental and Theoretical Kinetics of High-Temperature Fluorocarbon Chemistry. *The Journal of Chemical Physics* **48**(7): 3283–3289, 1968. DOI: 10.1063/1.1669605 (see pp. 9, 95)

[46] G. C. Rogers and G. H. Cady. Pyrolysis of Perfluoro-n-pentane. *Journal of the American Chemical Society* **73**(7): 3523–3524, 1951. DOI: 10.1021/ja01151a527 (see pp. 9, 86, 95)

[47] L. White and O. K. Rice. The Thermal Reaction of Hexafluoroethane with Quartz. *Journal of the American Chemical Society* **69**(2): 267–270, 1947. DOI: 10.1021/ja01194a030 (see pp. 9, 95)

[48] J. Thonstad, A. Øygård, and Q. B. Diep. "On the Formation and Decomposition of C-F Gases in Aluminium Cells." In: *International Primary Aluminium Institute (IPAI) PFC Workshop.* London, 1994. 1–13. (see pp. 9, 86, 94, 95)

[49] C. E. Castellano and A. J. Calandra. The Reaction Occurring Between Gaseous CF_4 and Oxides Dissolved in Different Molten Fluorides. Some Practical Aspects. *Journal of Applied Electrochemistry* **12**(4): 411–416, 1982. DOI: 10.1007/BF00610482 (see pp. 9, 95)

[50] Outotec. *HSC Chemistry 7*. Computer Program. url: http://www.outotec.com/ (see pp. 9, 51, C-2)

[51] Z. M. El-Bahy, R. Ohnishi, and M. Ichikawa. Hydrolysis of CF_4 over Alumina-Based Binary Metal Oxide Catalysts. *Applied Catalysis B: Environmental* **40**(2): 81–91, 2003. doi: 10.1016/S0926-3373(02)00143-1 (see p. 9)

[52] P. H. Hindle. "Historical Development." In: *Handbook of Near-Infrared Analysis*. Ed. by D. A. Burns and E. W. Ciurczak. 3rd ed. Boca Raton, FL: CRC Press, 2008. 3–6. (see p. 19)

[53] A. A. Michelson. XXVIII. Visibility of Interference-Fringes in the Focus of a Telescope. *Philosophical Magazine Series 5* **31**(190): 256–259, 1891. doi: 10.1080/14786449108620101 (see p. 19)

[54] P. R. Griffiths and J. A. de Haseth. *Fourier Transform Infrared Spectrometry*. Hoboken, NJ, USA: John Wiley & Sons, Inc., 2007. doi: 10.1002/047010631X. (see p. 19)

[55] W. J. Mccarthy and G. J. Kemeny. "Fourier Transform Spectrophotometers in the Near-Infrared." In: *Handbook of Near-Infrared Analysis*. Ed. by D. A. Burns and E. W. Ciurczak. 3rd ed. Boca Raton, FL: CRC Press, 2008. 79–91. (see p. 20)

[56] B. C. Smith. *Fundamentals of Fourier Transform Infrared Spectroscopy*. 2nd ed. Boca Raton, FL: CRC Press, 2011. xiii, 182. doi: 10.1201/b10777. (see p. 21)

[57] S. E. V. Bramer. *An Introduction to Mass Spectrometry*. Tech. rep. Department of Chemistry, Widener University, Chester, PA, USA, 1998, 1–38 (see p. 22)

[58] W. M. Niessen and D. Falck. "Introduction to Mass Spectrometry, a Tutorial." In: *Analyzing Biomolecular Interactions by Mass Spectrometry*. i. Weinheim, Germany: Wiley-VCH Verlag GmbH & Co. KGaA, 2015. 1–54. doi: 10.1002/9783527673391.ch1. (see pp. 23, 25)

[59] NIST. *NIST Chemistry WebBook*. url: http://webbook.nist.gov/chemistry (visited on 01/09/2017) (see pp. 24, A-1, A-7, B-2, B-3)

[60] K. K. Murray, R. K. Boyd, M. N. Eberlin, G. J. Langley, L. Li, and Y. Naito. Definitions of Terms Relating to Mass Spectrometry (IUPAC Recommendations 2013)*. *Pure Appl. Chem* **85**(7): 1515–1609, 2013. doi: 10.1351/PAC-REC-06-04-06 (see p. 24)

[61] E. de Hoffmann and V. Stroobant. *Mass Spectrometry: Priniples and Applications*. 3rd ed. Chichester, West Sussex, England: John Wiley & Sons, Ltd, 2007. xii, 489. (see pp. 24, 25)

[62] M. M. R. Dorreen. *Cell Performance and Anodic Processes in Aluminium Smelting Studied by Product Gas Analysis*. PhD thesis. University of Auckland, 2000. (see p. 25)

[63] B. Hu, R. Wang, and S. Zhou. Fragment Ion Pattern Coefficients of Quadrupole Mass Spectrometers. *Journal of Vacuum Science and Technology* **20**(4): 1031–1033, 1982. doi: `10.1116/1.571535` (see pp. 25, B-2, B-3)

[64] F. M. Mao and J. Leck. The Quadrupole Mass Spectrometer in Practical Operation. *Vacuum* **37**(8-9): 669–675, 1987. doi: `10.1016/0042-207X(87)90053-4` (see p. 25)

[65] V. S. Bagotsky. *Fundamentals of Electrochemistry*. 2nd ed. Hoboken, NJ, USA: John Wiley & Sons, Inc., 2005. xxviii, 721. doi: `10.1002/047174199X`. (see p. 26)

[66] A. J. Bard and L. R. Faulkner. *Electrochemical Methods: Fundamentals and Applications*. 2nd ed. John Wiley & Sons, Inc., 2001. 864. (see pp. 27, 32)

[67] D. Pletcher. *A First Course in Electrode Processes*. 2nd ed. RSC Publishing, 2009. (see pp. 27, 29)

[68] A. Lasia. "Electrochemical Impedance Spectroscopy and its Applications." In: *Modern Aspects Of Electrochemistry*. Vol. 32. Springer US, 2002. 143–248. doi: `10.1007/0-306-46916-2_2`. (see p. 30)

[69] E. Barsoukov and J. R. Macdonald, eds. *Impedance Spectroscopy*. Hoboken, NJ, USA: John Wiley & Sons, Inc., 2005. xvii, 595. doi: `10.1002/0471716243`. (see p. 30)

[70] Princeton Applied Research. *PARSTAT 273A Users Manual*. Manual. 2002 (see pp. 32, 98)

[71] P. Fraser, C. Trudinger, B. Dunse, P. Krummel, P. Steele, J. Mühle, P. Salameh, R. Weiss, C. Harth, A. Ganesan, R. Prinn, B. Miller, and P. Reny. "PFC Emissions from Australian & Global Aluminium Production." In: *2009 ESRL Global Monitoring Annual Conference*. Boulder, Colorado, USA, 2009. (see p. 36)

[72] O. S. Kjos, T. A. Aarhaug, E. Skybakmoen, and A. Solheim. "Studies of Perfluorocarbon Formation on Anodes in Cryolite Melts." In: *Light Metals 2012*. John Wiley & Sons, Inc., 2012. 623–626. doi: 10.1002/9781118359259.ch106. (see p. 37)

[73] Thermo Scientific. *GRAMS AI Spectroscopy Software*. Computer Program. url: https://www.thermofisher.com/order/catalog/product/INF-15000 (see p. 38)

[74] GETS Inc. *Spectral Calc*. Online Database. url: http://www.spectralcalc.com/ (see p. 40)

[75] J. Marks, R. Roberts, and V. Bakshi. "Perfluorocarbon (PFC) Generation during Primary Aluminum Production." In: *Light Metals 2000*. Warrendale, PA, USA: The Minerals, Metals and Materials Society, 2000. 365–371. (see pp. 50, 80)

[76] B. J. Welch, A. Jassim, C.-Y. Cheung, Y. Yao, and M. Dorreen. "Challenges for Controlling Anode Reaction Products in Multielectrode Aluminium Smelting Cells." In: *10th International Conference on Molten Salt Chemistry and Technology (MS10)*. Shenyang, China, 2015. 389–400. (see pp. 51, 81)

[77] S. Kjelstrup Ratkje. Local Heat Changes during Aluminium Electrolysis. *Electrochimica Acta* **36**(3-4): 661–665, 1991. doi: 10.1016/0013-4686(91)85155-Z (see p. 52)

[78] A. Solheim. "Practical Implications of Some Interfacial Processes in Alumina Reduction Cells." In: *11th AustralAsian Aluminium Smelting Technology Conference*. 2014. 1–26. (see pp. 52, 53)

[79] J. Thonstad, F. Nordmo, and J. Rødseth. On the Anode Effect in Cryolite-Alumina Melts—II The Initiation of the Anode Effect. *Electrochimica Acta* **19**(11): 761–769, 1974. doi: 10.1016/0013-4686(74)80020-4 (see pp. 58, 94)

[80] Z. Zhao, Z. Wang, B. Gao, Y. Feng, Z. Shi, and X. Hu. "Observation of Anodic Bubble Behaviors Using Laboratory Scale Transparent Aluminium Electrolysis Cells." In: *Light Metals 2015*. Hoboken, NJ, USA: John Wiley & Sons, Inc., 2015. 801–806. doi: 10.1002/9781119093435.ch135. (see pp. 58, 103, 124)

[81] B. J. Welch. "Quantifying PFC Emissions from Smelter Cells." In: *10th Australasian Aluminium Smelting Technology Conference*. Ed. by B. Welch, G. Stephens, J. Metson, and M. Skyllas-Kazacos. Launceston, Australia, 2011. 1–12. (see p. 66)

[82] K. Grjotheim and C. Krohn. Neuere Forschungsergebnisse in der Theorie der Aluminiumelektrolyse (Recent Progress in Research on the Theory of Aluminum Electrolysis). *Chemické Zvesti* **21**(11): 762–773, 1967 (see pp. 80, 94)

[83] J. Thonstad. On the Anode Gas Reactions in Aluminum Electrolysis, II. *Journal of The Electrochemical Society* **111**(8): 959, 1964. doi: `10.1149/1.2426300` (see pp. 80, 94)

[84] H. Kvande and W. Haupin. Inert Anodes for Al Smelters: Energy Balances and Environmental Impact. *Jom* **53**(5): 29–33, 2001. doi: `10.1007/s11837-001-0205-6` (see p. 80)

[85] D. S. Wong, A. Tabereaux, and P. Lavoie. "Anode Effect Phenomena during Conventional AEs, Low Voltage Propagating AEs & Non-Propagating AEs." In: *Light Metals 2014*. Hoboken, NJ, USA: John Wiley & Sons, Inc., 2014. 529–534. doi: `10.1002/9781118888438.ch90`. (see p. 81)

[86] G. Siegemund, W. Schwertfeger, A. Feiring, B. Smart, F. Behr, H. Vogel, B. McKusick, and P. Kirsch. "Fluorine Compounds, Organic." In: *Ullmann's Encyclopedia of Industrial Chemistry*. Weinheim, Germany: Wiley-VCH Verlag GmbH & Co. KGaA, 2016. 1–56. doi: `10.1002/14356007.a11_349.pub2`. (see p. 86)

[87] A. Øygard, T. A. Halvorsen, J. Thonstad, T. Røe, and M. Bugge. "A Parameter Study of the C–F Gases during Anode Effect in Aluminium Reduction Cells." In: *Light Metals 1995*. Warrendale, PA, USA: The Minerals, Metals and Materials Society, 1995. 279–287. (see p. 86)

[88] P. L. Walker, F. Rusinko, and L. G. Austin. Gas Reactions of Carbon. *Advances in Catalysis* **11**(C): 133–221, 1959. doi: `10.1016/S0360-0564(08)60418-6` (see p. 87)

[89] T. A. Aarhaug, O. S. Kjos, H. Gudbrandsen, A. Ferber, and A. P. Ratvik. "Evaluation of Gas Composition from Laboratory Scale Electrolysis Experiments with Anodes of Different Sulphur Content." In:

Light Metals 2016. Hoboken, NJ, USA: John Wiley & Sons, Inc., 2016. 533–536. DOI: `10.1002/9781119274780.ch88`. (see p. 87)

[90] R. D. Holliday and J. L. Henry. Anode Polarization and Flurocarbon Formation in Aluminium Reduction Cells. *Industrial & Engineering Chemistry* **51**(10): 1289–1292, 1959. DOI: `10.1021/ie50598a036` (see p. 94)

[91] E. W. Dewing and E. T. van der Kouwe. Anodic Phenomena in Cryolite-Alumina Melts: I. Overpotentials at Graphite and Baked Carbon Electrodes. *Journal of The Electrochemical Society* **122**(3): 358–363, 1975. DOI: `10.1149/1.2134215` (see p. 94)

[92] J. L. Henry and R. D. Holliday. Mass Spectrometric Examination of Anode Gases from Aluminum Reduction Cells. *Journal of Metals* **9**: 1384–1385, 1957 (see p. 95)

[93] R. G. Haverkamp. An XPS Study of the Fluorination of Carbon Anodes in Molten $NaF-AlF_3-CaF_2$. *Journal of Materials Science* **47**(3): 1262–1267, 2012. DOI: `10.1007/s10853-011-5772-5` (see pp. 101, 141)

[94] R. G. Haverkamp and B. C. C. Cowie. C K-Edge NEXAFS Study of Fluorocarbon Formation on Carbon Anodes in Molten $NaF-AlF_3-CaF_2$. *Surface and Interface Analysis* **45**(13): 1854–1858, 2013. DOI: `10.1002/sia.5332` (see pp. 101, 141)

[95] H. Zhu and J. Thonstad. “Anode Reaction in Aluminium Electrolysis Prior to and during Anode Effect.” In: *Light Metals 2003.* Warrendale, PA, USA: The Minerals, Metals and Materials Society, 2003. 343–349. (see p. 101)

[96] J. Xue and H. A. Øye. “Bubble Behaviour – Cell Voltage Oscillation during Aluminium Electrolysis and the Effects of Sound and Ultrasound.” In: *Light Metals 1995.* Warrendale, PA, USA: The Minerals, Metals and Materials Society, 1995. 265–271. (see p. 103)

[97] L. Cassayre, T. A. Utigard, and S. Bouvet. Visualizing Gas Evolution on Graphite and Oxygen-Evolving Anodes. *JOM* **54**(5): 41–45, 2002. DOI: `10.1007/BF02701696` (see p. 103)

[98] R. J. Thorne, C. Sommerseth, A. P. Ratvik, S. Rorvik, E. Sandnes, L. P. Lossius, H. Linga, and A. M. Svensson. Bubble Evolution and Anode Surface Properties in Aluminium Electrolysis. *Journal of the Electrochemical Society* **162**(8): E104–E114, 2015. doi: `10.1149/2.0321508jes` (see p. 107)

[99] K. C. Mills, E. D. Hondros, and Z. Li. Interfacial Phenomena in High Temperature Processes. *Journal of Materials Science* **40**(9-10): 2403–2409, 2005. doi: `10.1007/s10853-005-1966-z` (see p. 114)

[100] A. Solheim, H. Gudbrandsen, A. M. Martinez, K. E. Einarsrud, and I. Eick. “Wetting between Carbon and Cryolitic Melts. Part II: Effect of Bath Properties and Polarisation.” In: *Light Metals 2015*. Hoboken, NJ, USA: John Wiley & Sons, Inc., 2015. 671–676. doi: `10.1002/9781119093435.ch113`. (see pp. 114, 117, 132, 133)

[101] A. M. Martinez, O. Paulsen, A. Solheim, H. Gudbrandsen, and I. Eick. “Wetting Between Carbon and Cryolitic Melts. Part I: Theory and Equipment.” In: *Light Metals 2015*. Hoboken, NJ, USA: John Wiley & Sons, Inc., 2015. 665–670. doi: `10.1002/9781119093435.ch112`. (see pp. 114, 117)

[102] J. B. Metson, R. G. Haverkamp, M. M. Hyland, and J. Chen. “The Anode Effect Revisited.” In: *Light Metals 2002*. Warrendale, PA, USA: The Minerals, Metals and Materials Society, 2002. 239–244. (see p. 114)

[103] H. Vogt. Effect of Alumina Concentration on the Incipience of the Anode Effect in Aluminium Electrolysis. *Journal of Applied Electrochemistry* **29**(7): 779–788, 1999. doi: `10.1023/A:1003575232103` (see p. 114)

[104] E. Laé, V. Sahajwalla, B. Welch, and M. Skyllas-Kazacos. Influence of Oxide Dopants on the Wetting of Doped Graphite by Cryolite/Alumina Melts. *Journal of Applied Electrochemistry* **35**(2): 199–206, 2005. doi: `10.1007/s10800-004-6201-0` (see p. 114)

[105] K. Matiašovský, M. Paučírová, and M. Malinovský. Zmáčanie uhlíkových materiálov kryolitovými taveninami (Wetting Carbon with Molten Cryolite). *Chemické Zvesti* **17**: 181–188, 1963 (see pp. 114, 132, 135)

[106] L. Wasilewski and L. Piszczek. Wpływ działania sił powierzchniowych na przebieg procesów elektrolizy (The Effects of Surface Forces on the Process of Electrolysis). *Zeszyty Naukowe Politechniki Ślaskiej* **24**(106): 51–55, 1964 (see p. 114)

[107] Y. Yuan and T. R. Lee. "Contact Angle and Wetting Properties." In: *Surface Science Techniques*. Ed. by G. Bracco and B. Holst. Vol. 51. Springer Series in Surface Sciences 1. Berlin, Heidelberg: Springer Berlin Heidelberg, 2013. 3–34. doi: `10.1007/978-3-642-34243-1_1`. (see pp. 115, 116, 135)

[108] T. Young. An Essay on the Cohesion of Fluids. *Philosophical Transactions of the Royal Society of London* **95**(0): 65–87, 1805. doi: `10.1098/rstl.1805.0005` (see p. 115)

[109] R. Finn, J. McCuan, and H. C. Wente. Thomas Young's Surface Tension Diagram: Its History, Legacy, and Irreconcilabilities. *Journal of Mathematical Fluid Mechanics* **14**(3): 445–453, 2012. doi: `10.1007/s00021-011-0079-5` (see p. 115)

[110] V. M. Starov, M. G. Velarde, and C. J. Radke. "Surface Forces and the Equilibrium of Liquids on Solid Substrates." In: *Wetting and Spreading Dynamics*. CRC Press, 2007. 1–30. doi: `10.1201/9781420016178.ch1`. (see p. 116)

[111] D. Teeters, J. F. Wilson, M. A. Andersen, and D. C. Thomas. A Dynamic Wilhelmy Plate Technique used for Wettability Evaluation of Crude Oils. *Journal of Colloid And Interface Science* **126**(2): 641–644, 1988. doi: `10.1016/0021-9797(88)90167-1` (see p. 116)

[112] J. A. Kleingartner, S. Srinivasan, J. M. Mabry, R. E. Cohen, and G. H. McKinley. Utilizing Dynamic Tensiometry to Quantify Contact Angle Hysteresis and Wetting State Transitions on Nonwetting Surfaces. *Langmuir* **29**(44): 13396–13406, 2013. doi: `10.1021/la4022678` (see p. 116)

[113] F. Y. Lewandowski and D. Dupuis. Dynamic Measurements of Surface Tension of Solutions of Polyisobutylene in Mixtures of Polybutene Oil and Decalin. *Journal of Non-Newtonian Fluid Mechanics* **52**(2): 233–248, 1994. doi: `10.1016/0377-0257(94)80053-7` (see p. 116)

[114] L. Landau and B. Levich. Dragging of a Liquid by a Moving Plate. *Acta Physicochimica U.R.S.S.* **17**(1-2): 42–54, 1942 (see p. 116)

[115] W. Brockner, K. Tørklep, and H. A. Øye. Viscosity of Sodium Fluoride-Aluminium Fluoride Melt Mixtures. *Berichte der Bunsengesellschaft für physikalische Chemie* **83**(1): 12–19, 1979. doi: 10.1002/bbpc.19790830103 (see p. 117)

[116] R. Fernandez and T. Østvold. Surface Tension and Density of Molten Fluorides and Fluoride Mixtures Containing Cryolite. *Acta Chemica Scandinavica* **43**: 151–159, 1989. doi: 10.3891/acta.chem.scand.43-0151 (see pp. 117, 118, 120, 133, 135)

[117] H. Gudbrandsen, A. Solheim, and A. M. Martinez. *Wetting Measuring Device.* Tech. rep. SINTEF, Trondheim, Norway, 2014, 25 (see p. 118)

[118] J. O. Bockris and A. K. N. Reddy. *Modern Electrochemistry: An Introduction to Interdisciplinary Area, Volume 2.* New York: Plenum Press, 1970. 623–1432. (see p. 128)

[119] S. Jarek and J. Thonstad. Double-Layer Capacitance and Polarization Potential of Baked Carbon Anodes in Cryolite–Alumina Melts. *Journal of Applied Electrochemistry* **17**(6): 1203–1212, 1987. doi: 10.1007/BF01023604 (see p. 130)

[120] A. Kisza, J. Thonstad, and T. Eidet. An Impedance Study of the Kinetics and Mechanism of the Anodic Reaction on Graphite Anodes in Saturated Cryolite-Alumina Melts. *Journal of The Electrochemical Society* **143**(6): 1840–1847, 1996. doi: 10.1149/1.1836913 (see p. 130)

[121] W. Gebarowski, C. Sommerseth, A. P. Ratvik, E. Sandnes, L. P. Lossius, H. Linga, and A. M. Svensson. "Interfacial Boundary between Carbon Anodes and Molten Salt Electrolyte." In: *Light Metals 2016.* Hoboken, NJ, USA: John Wiley & Sons, Inc., 2016. 883–888. doi: 10.1002/9781119274780.ch149. (see p. 130)

[122] Z.-X. Qiu, Q.-B. Wei, and K.-T. You. "On the Wettability of Carbon Electrodes by Molten Cryolite-Alumina Electrolytes." In: *7th International Leichtmetalltagung.* Leoben-Wien, 1981. 256–257. (see pp. 132, 135)

[123] I. A. Eidsvaag. *The Influence of Polarization on the Wetting of Anodes in the Hall-Héroult Process.* MA thesis. Norwegian University of Sceince and Technology, 2016. (see pp. 132, 146)

[124] R. K. Jain, S. B. Tricklebank, and B. Welch. “Interaction of Aluminas with Aluminium Smelting Electrolytes.” In: *Light Metals 1983.* The Minerals, Metals and Materials Society, 1983. 609–621. (see p. 133)

[125] X. Wang. “Alumina Dissolution in Aluminium Smelting Electrolyte.” In: *Light Metals 2009.* Warrendale, PA, USA: The Minerals, Metals and Materials Society, 2009. 383–388. (see p. 133)

[126] A. W. Neumann. Contact Angles and their Temperature Dependence: Thermodynamic Status, Measurement, Interpretation and Application. *Advances in Colloid and Interface Science* **4**(2–3): 105–191, 1974. doi: `10.1016/0001-8686(74)85001-3` (see p. 135)

[127] R. Sedev, J. Petrov, and A. Neumann. Effect of Swelling of a Polymer Surface on Advancing and Receding Contact Angles. *Journal of Colloid and Interface Science* **180**(1): 36–42, 1996. doi: `10.1006/jcis.1996.0271` (see p. 135)

Nomenclature

Roman letters

A	Absorbance	–
B	Magnetic flux	Wb
c	Speed of light	$\mathrm{cm\,s^{-1}}$
c	Concentration	$\mathrm{mol\,dm^{-3}}$
C	Capacitance	F
Ca	Capillary number	–
e	Elementary charge	C
E	Energy	J
E	Electrochemical potential	V
E_i	Electrochemical potential i	V
E^0	Standard cell potential	V
E^{iso}	Isothermal cell potential	V
E^{iso}_{specie}	Isothermal cell potential of *specie*	V
E^{rev}	Reversible cell potential	V
E_A, E_{An}	Anode potential	V
E_C, E_{Cat}	Cathode potential	V
F	Faraday constant	$\mathrm{C\,mol^{-1}}$
F	Force	N
ΔG	Change in Gibbs free energy	$\mathrm{kJ\,mol^{-1}}$
ΔG^0	Standard change in Gibbs free energy	$\mathrm{kJ\,mol^{-1}}$
h	Planck constant	J s
ΔH	Change in enthalpy	$\mathrm{kJ\,mol^{-1}}$
ΔH^0	Standard change in enthalpy	$\mathrm{kJ\,mol^{-1}}$
ΔS	Change in entropy	$\mathrm{J\,K^{-1}\,mol^{-1}}$
ΔS^0	Standard change in entropy	$\mathrm{J\,K^{-1}\,mol^{-1}}$
i	Current density	$\mathrm{A\,cm^{-2}}$
I	Electrical current	A
I_i	Electrical current of element i	A
I_{tot}	Total electrical current	A

j	Imaginary unit ($j = \sqrt{-1}$)	–
l	Path length	m
L	Inductance	H
m	Numerical value of mass of ion in (u)	–
n	The number of moles of electrons transferred per reaction	–
n_i	The number of moles of compound i	–
P	Heat production	W
P	Radiant power	W
P_0	Incident radiant power	W
P_A	Heat production at anode/electrolyte interface	W
r	radius	m
R	Universal gas constant	$\mathrm{J\,K^{-1}\,mol^{-1}}$
R	Resistance (ohm)	Ω
R_A, R_{An}	Resistance of anode	Ω
$R_{A,i}$, $R_{An,i}$	Resistance of anode i	Ω
R_{Bubble}	Resistance due to bubble layer	Ω
$R_{Bubble,i}$	Bubble resistance of element i	Ω
R_C, R_{Cat}	Resistance of cathode	Ω
R_{eq}	Equivalent resistance	Ω
R_{El}	Resistance of electrolyte	Ω
$R_{El,i}$	Electrolyte resistance of element i	Ω
$R_{S,i}$	Segment resistance of element i	Ω
t	Time	s
t_i	Time at i	s
$\%T$	Percent transmittance	–
T	Transmittance	–
T	Absolute temperature	K
T	CPE constant	$\mathrm{F\,cm^{-2}\,s^{\phi-1}}$
V	Volume	$\mathrm{m^3}$
V	Acceleration voltage	V
V_{cell}	Cell voltage	V
W	Wavenumber	$\mathrm{cm^{-1}}$
x_{specie}	Fraction of *specie*	–
z	Numerical value of charge of ion in (e)	–
Z	Electrical impedance	Ω
Z_{Im}	Electrical impedance of imaginary part	Ω
Z_{Re}	Electrical impedance of real part	Ω

Greek letters

γ	Interfacial tension	$\mathrm{N\,m^{-1}}$

γ_{lv}	Interfacial tension liquid/vapour	$\mathrm{N\,m^{-1}}$
γ_{sl}	Interfacial tension solid/liquid	$\mathrm{N\,m^{-1}}$
γ_{sv}	Interfacial tension solid/vapour	$\mathrm{N\,m^{-1}}$
ϵ	Absorptivity	$\mathrm{M^{-1}\,cm^{-1}}$
θ	Contact angle	°
θ_a	Advancing contact angle	°
θ_r	Receding contact angle	°
σ	Warburg constant	$\Omega\,\mathrm{s^{-1/2}}$
λ	Wavelength	$\mathrm{cm\,cycle^{-1}}$
μ	Viscosity	$\mathrm{kg\,m^{-1}\,s^{-1}}$
ν	Velocity	$\mathrm{m\,s^{-1}}$
ν	Frequency	Hz
τ	Transition time	s
ϕ	Phase angle	°
ω	Angular frequency ($2\pi\nu$)	$\mathrm{rad\,s^{-1}}$

Abbreviations

AC	Alternating current
ACD	Anode to cathode distance
ADC	Analog-to-digital converter
AE	Anode effect
cd	Current density
ccd	Critical current density
CC	Constant current
CE	Current efficiency
CE	Counter electrode
CA	Chronoamperometry
CP	Chronopotentiometry
CPE	Constant phase element
CV	Cyclic voltammetry
CV	Constant voltage
DC	Direct current
diss	Dissolved
DP	Direct potential
DTGS	Deuterated triglycine sulfate (detector)
EL	Electronic load
EIS	Electrochemical impedance spectroscopy
FT-IR	Fourier Transform infrared spectroscopy
FWHM	Full width at half maximum
GC	Glassy carbon (vitreous carbon)
GTC	Gas treatment centre

GWP	Global warming potential
IR	Ohmic drop (IR-drop)
LOD	level of detection
LCV–AE	Low cell-voltage AE
LCV–PFC	Low cell-voltage PFC
LSV	Linear sweep voltammetry
MCT	Mercury cadmium telluride (detector)
MS	Mass spectrometer
NAE-PFC	Non-anode effect PFC
NTNU	Norwegian University of Science and Technology
OCP	Open circuit potential
OEM	Original equipment manufacturer
PFC	Perfluorocarbon
PSU	Power supply unit
RE	Reference electrode
RF	Radio frequency
SR	Shunt resistor
TIC	Total-ion chromatogram
WE	Working electrode
XIC	Extracted-ion chromatogram

List of Figures

1.1 Hall-Héroult prebaked aluminium production cell. 3
1.2 PFC emissions in CO_2 equivalents throughout the years. 8

2.1 Mass spectrum of CF_4. 24
2.2 Example of chronopotentionmetry. 27
2.3 Example of cyclic voltammetry. 28
2.4 Example of chronoamperometry. 29
2.5 Example of EIS Nyquist and Bode plots. 31

3.1 Apparatus setup with FTIR for industrial gas measurements. . 39
3.2 Refenrence spectra of CF_4 and C_2F_6. 40
3.3 FTIR calibration curve for a 4.95 ppm ± 2 % CF_4 reference. . 41
3.4 FTIR data before and during AE. 41
3.5 PFC signal from the anode effect and 10 minutes prior. 42
3.6 Mass spectrometer (MS) data for CF_4 and C_2F_6. 43
3.7 FTIR data showing CF_4 emission ~ 1 h before full AE. 44
3.8 Mesh plot of spectra prior to full AE. 45
3.9 FTIR data with CF_4 stemming from two cells low in alumina. . 46
3.10 Two non-AE events and possible traces of C_2F_6. 47

4.1 Experimental setup of two-compartment crucible. 54
4.2 Electric equivalent circuit of electrochemical cell. 55
4.3 Possible change from normal reaction to partial PFC. 56
4.4 Theoretical heat production of anode with different reactions. . 59
4.5 Change from partial PFC back to normal reaction. 60
4.6 On and off partial PFC. 61
4.7 From partial PFC to full AE and passivation. 62

5.1 Electrical circuit representation of two-anode cell. 69
5.2 Electrical circuit diagram with virtual anodes. 70
5.3 Graphite two-compartment crucible. 71

5.4 Anodes used in two-compartment experiments. 72
5.5 Experimental two-compartment setup. 73
5.6 Two anodes transitioning to anode effect. 75
5.7 An anode on and off partial anode effect. 76

6.1 Experimental two-compartment setup. 83
6.2 Electric circuit representation of electrochemical cell. 84
6.3 Response time of 5 ppm mol CF_4 reference. 85
6.4 Absorbance of CF_4 at $1281\,\mathrm{cm}^{-1}$ for different FT-IRs. 86
6.5 IR spectrum during feeding of "wet" alumina. 88
6.6 Passivation with low degree of parallel elements and much CF_4. 89
6.7 Partial passivation with high current and little CF_4. 90

7.1 Sketch of electrode and crucible set-up. 97
7.2 CV of GC and graphite at different sweep rates. 1 wt% Al_2O_3. 100
7.3 CV on GC. 100 $\mathrm{mV\,s}^{-1}$ for 1, 3, 5 and 11 wt% Al_2O_3. 102
7.4 CV on VG. 100 $\mathrm{mV\,s}^{-1}$ for 1, 3, 5 and 11 wt% Al_2O_3. 103
7.5 CV on graphite rod at different sweep rates. 5 wt% Al_2O_3. . . 104
7.6 Passivation potentials of graphite and GC vs. Al_2O_3 105
7.7 Passivation scatter of GC and graphite. 106
7.8 Recovery scatter of GC and graphite. 107
7.9 CF_4 before full passivation on rod. 108
7.10 Several levels of CF_4 before full passivation on rod. 108
7.11 CF_4 production before passivation during potential stepping. . 109
7.12 CF_4 production of passivation on vertical graphite. 110

8.1 Wetting angle and surface tension examples. 115
8.2 Electrodes for immersion/emersion experiments. 119
8.3 Wetting weight as a function of contact angle and alumina. . . 120
8.4 Immersion/emersion vs. time procedure. 120
8.5 Immersion/emersion vs. position procedure. 121
8.6 Description of typical im./em. procedure with polarisation. . . 122
8.7 Wetting with regular and AE polarisation on cup anode. 125
8.8 Wetting on vertical anode. Polarisation on BN-phase. 126
8.9 Wetting on vertical anode. Polarisation on C-phase. 129
8.10 Wetting weight with polarisation in 1 wt% melt. 130
8.11 Wetting weight with polarisation in 1 to 11 wt% melts. 131
8.12 Wetting weight as a function of AE polarisation time. 132
8.13 Wetting weight as a function of alumina concentration. 133
8.14 Approaching equilibrium contact angle from θ_a and θ_r. 134

A.1 CF_4 FTIR reference spectra. A-2

A.2 C_2F_6 FTIR reference spectra. A-2
A.3 COF_2 FTIR reference spectra. A-3
A.4 CO_2 FTIR reference spectra. A-3
A.5 CO FTIR reference spectra. A-4
A.6 H_2O FTIR reference spectra. A-4
A.7 COS FTIR reference spectra. A-5
A.8 SO_2 FTIR reference spectra. A-5
A.9 SF_6 FTIR reference spectra. A-6
A.10 CH_4 FTIR reference spectra. A-6
A.11 HF FTIR reference spectra. A-7
A.12 SiF_4 FTIR reference spectra. A-7

List of Tables

2.1 Absorbance and its corresponding transmittance. 21
2.2 Properties of the different FTIRs. 22
2.3 Properties of the mass spectrometer used in the work. 26
2.4 Impedance of some general circuit elements. 30

4.1 Thermodynamic data of reactions at 1000 °C. 51
4.2 Distribution of entropic heat for some reactions. 53

6.1 Specifications of the two different FT-IRs. 84

7.1 Electrolyte composition and molar cryolite ratio of experiments. 96

8.1 θ_a and θ_r of untreated, polarised and AE polarised electrodes. . 135

B.1 MS fragmentation pattern. $m/z \leq 45$. B-2
B.2 MS fragmentation pattern. $m/z \geq 46$. B-3

C.1 Thermodynamic data of (electro)chemical reactions. C-2

List of Publications

Paper 1 H. Åsheim, T. A. Aarhaug, A. Ferber, O. S. Kjos, and G. M. Haarberg. "Monitoring of Continuous PFC Formation in Small to Moderate Size Aluminium Electrolysis Cells." In: *Light Metals 2014*. John Wiley & Sons, Inc., 2014. 535–539. doi: 10.1002/9781118888438.ch91

Paper 2 H. Åsheim, T. Aarhaug, E. Sandnes, O. S. Kjos, A. Solheim, and G. M. Haarberg. A Laboratory Study of Partial Anode Effects during Aluminium Electrowinning. *ECS Transactions* **69**(15): 1–12, 2015. doi: 10.1149/06915.0001ecst

Paper 3 H. Åsheim, T. A. Aarhaug, E. Sandnes, O. S. Kjos, A. Solheim, S. Kolås, and G. M. Haarberg. "Anode Effect Initiation During Aluminium Electrolysis in A Two Compartment Laboratory Cell." In: *Light Metals 2016*. John Wiley & Sons, Inc., 2016. 551–556. doi: 10.1002/9781119274780.ch92

Paper 4 H. Åsheim, T. A. Aarhaug, W. Gębarowski, E. Sandnes, A. Solheim, and G. M. Haarberg. Partial Anode Effect in a Two-Compartment Laboratory Alumina Reduction Cell. In: *Light Metals 2017*. Ed. by A. P. Ratvik. Springer International Publishing, 2017, 525–532. doi: 10.1007/978-3-319-51541-0_66

Paper 5 Henrik Åsheim, Thor A. Aarhaug, Espen Sandnes, Asbjørn Solheim and Geir M. Haarberg, Anodic Passivation of Carbon Materials in Cryolite-Alumina Melts. *Manuscript.*

Paper 6 Henrik Åsheim, Ingrid A. Eidsvaag, Espen Sandnes, Asbjørn Solheim, Henrik Gudbrandsen and Geir M. Haarberg, The Influence of Polarisation on the Wetting of Graphite in Cryolite-Alumina Melts. *Manuscript.*

Appendices

Appendix A

FTIR Reference Spectra

Quite a few different gas species can be encountered evolving from an aluminium production cell. Some, like CO_2 and CO are part of the main production reaction while others become available due to unwanted side reactions and material impurities. The present chapter presents FTIR reference spectra of some of these gases at a couple of different concentrations. The spectra have been recorded by the ProtIR original equipment manufacturer (OEM), except the HF spectra which is taken from the Gasmet OEM library and the SiF_4 spectra which was obtained from NIST [59]. Reference spectra of CF_4, C_2F_6 and COF_2 are provided in Figures A.1, A.2 and A.3, respectively. Figure A.4 presents the IR spectra of CO_2 and CO is presented in Figure A.5. Figures A.7 to A.9 presents spectra of the sulphur containing species COS, SO_2 and SF_6. Figure A.10 shows the spectra of CH_4 and lastly, the FTIR spectra of HF and SiF_4 is provided in Figures A.11 and A.12.

The spectra from ProtIR has the higher resolution of $1\,\mathrm{cm}^{-1}$, while the Gasmet spectra has been recorded at $4\,\mathrm{cm}^{-1}$. The nature of the presenting format might give the illusion that it is the other way around. The spectral range of the figures have been limited to wavenumbers ranging from $750\,\mathrm{cm}^{-1}$ to $4250\,\mathrm{cm}^{-1}$. Both due to the fact that the Gasmet only operates in this range, but also because it is the region of interest for most of the gases. At higher concentrations gases like H_2O and CH_4 also show quite a bit of activity towards $8000\,\mathrm{cm}^{-1}$.

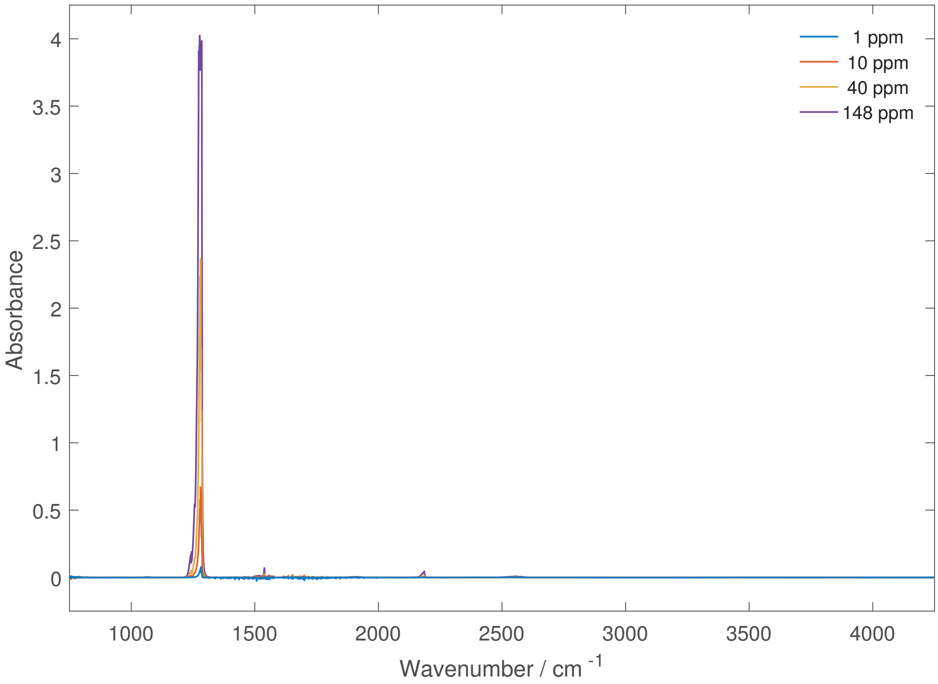

Figure A.1: CF_4 FTIR reference spectra.

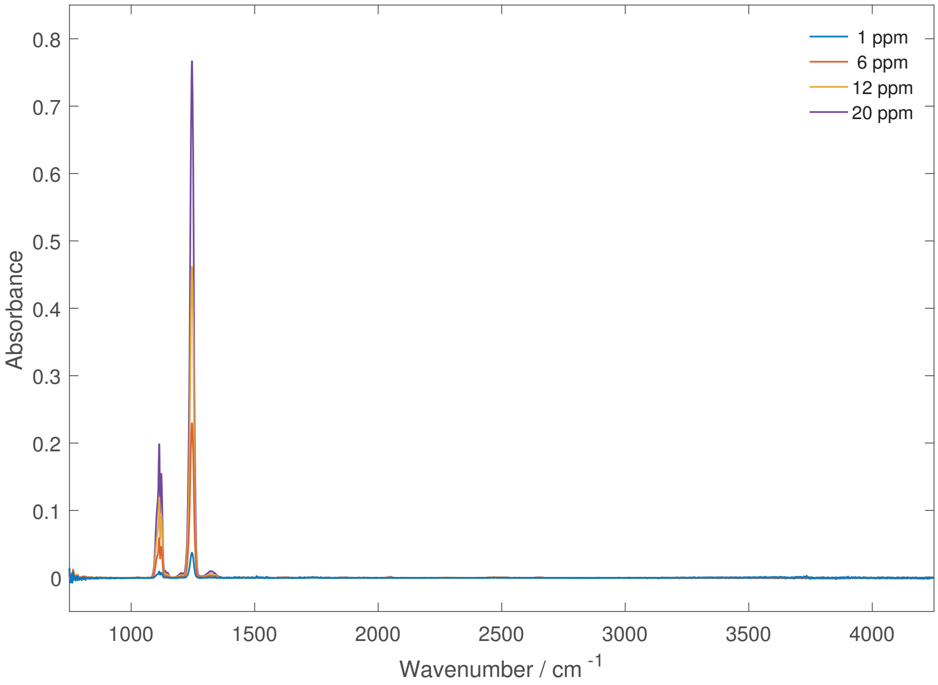

Figure A.2: C_2F_6 FTIR reference spectra.

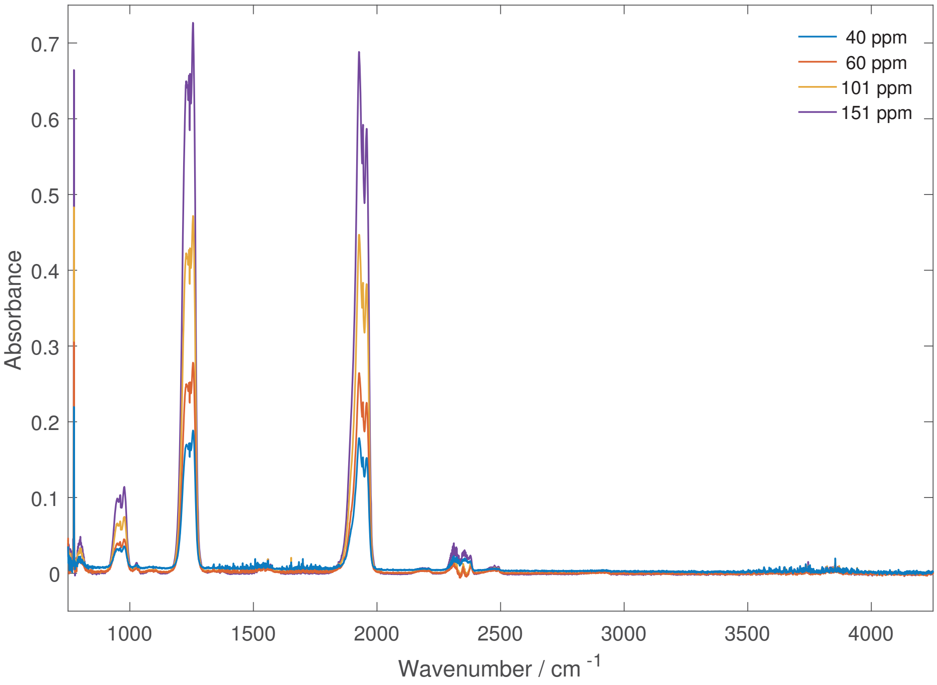

Figure A.3: COF_2 FTIR reference spectra.

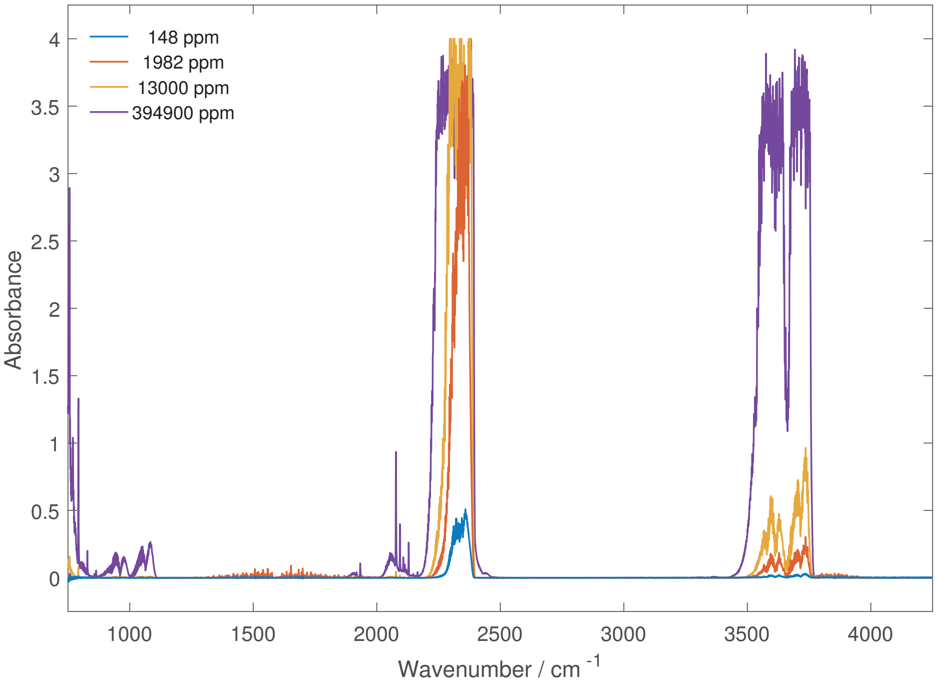

Figure A.4: CO_2 FTIR reference spectra.

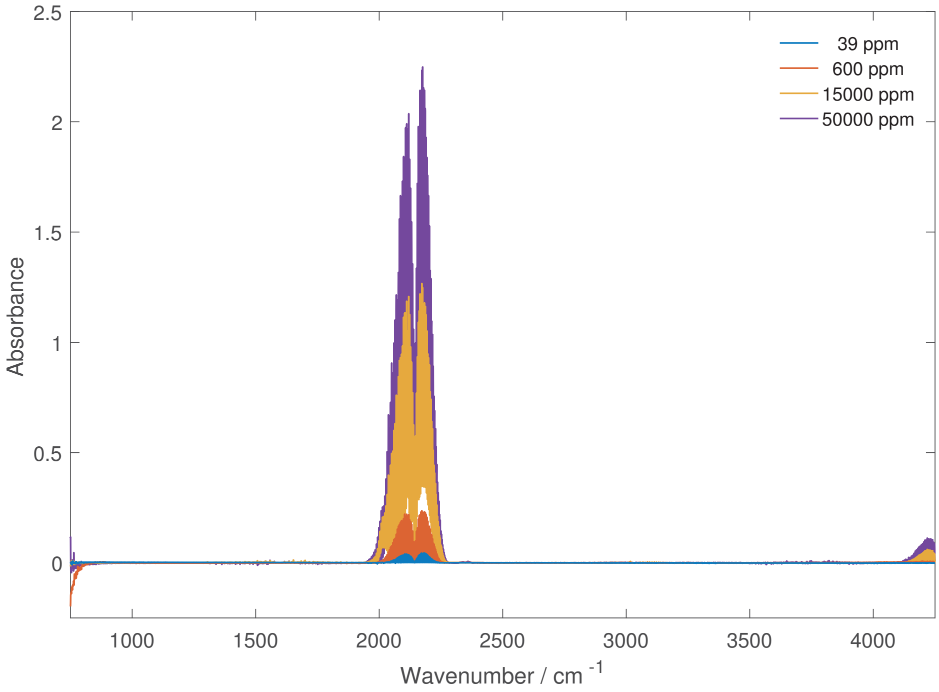

Figure A.5: CO FTIR reference spectra.

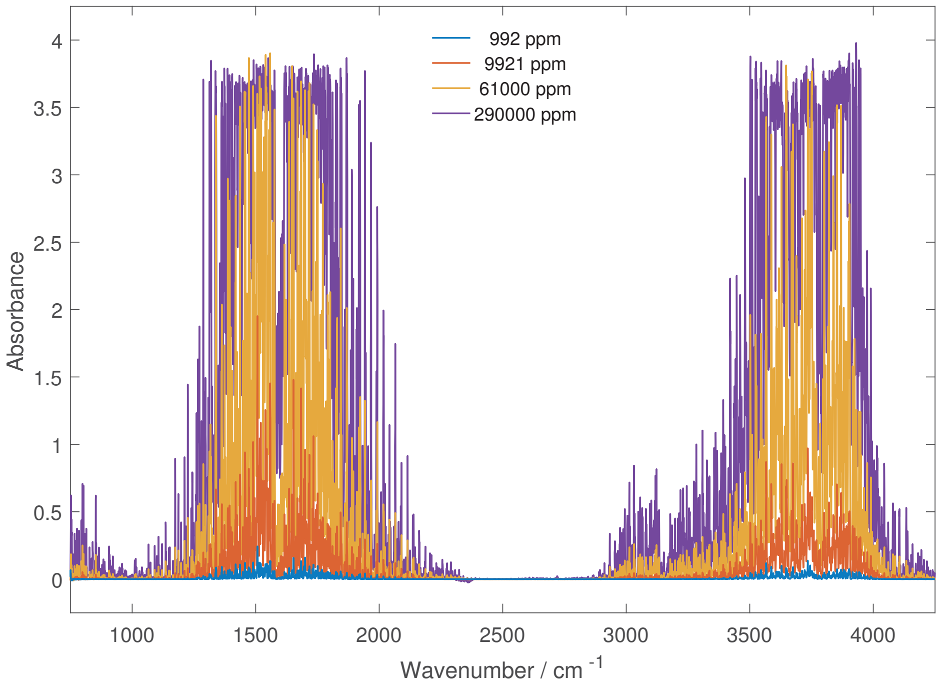

Figure A.6: H_2O FTIR reference spectra.

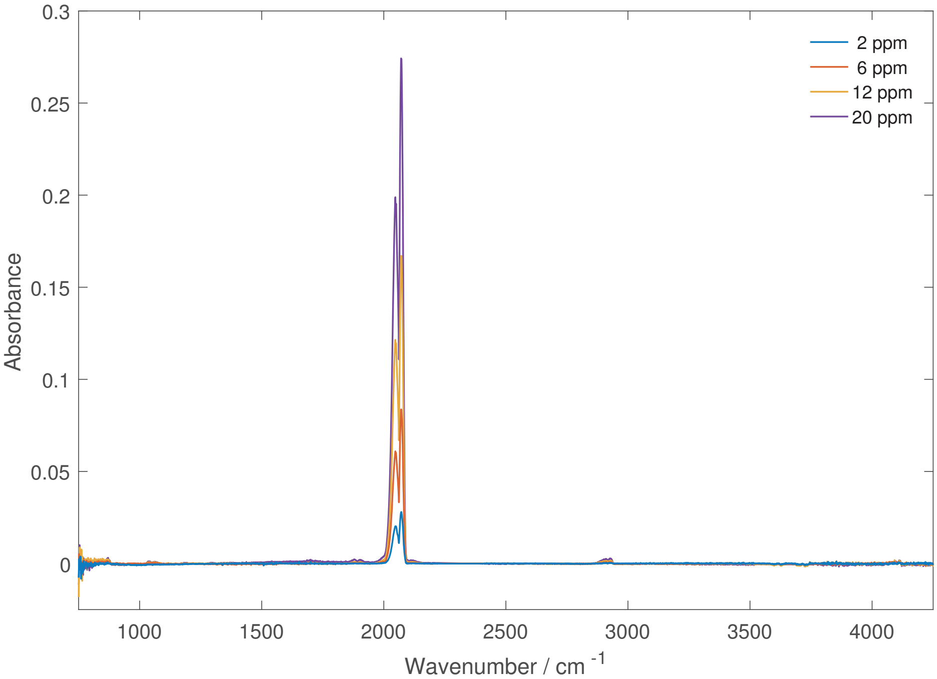

Figure A.7: COS FTIR reference spectra.

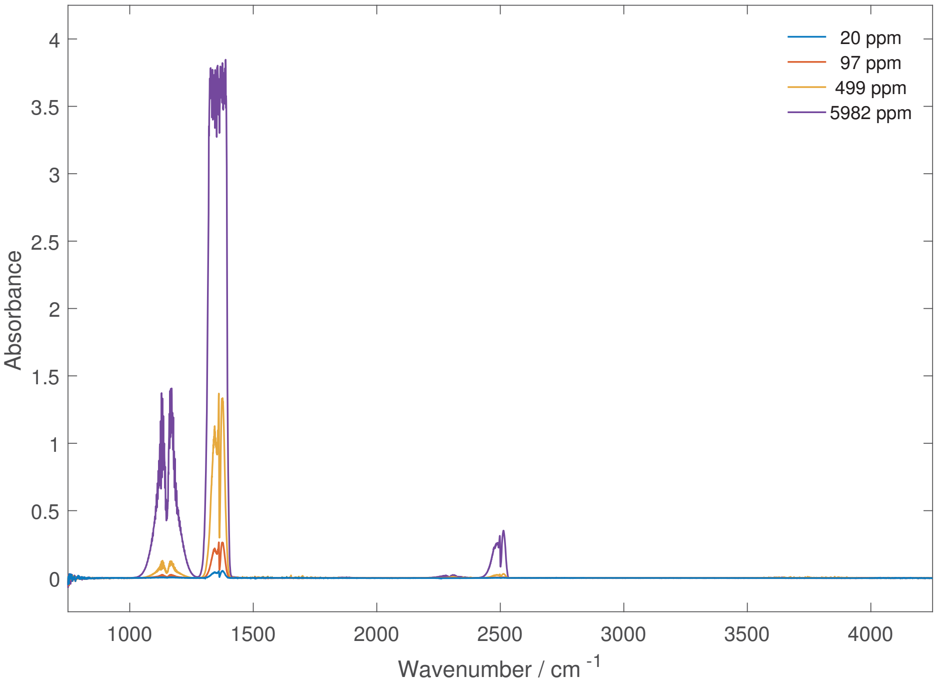

Figure A.8: SO_2 FTIR reference spectra.

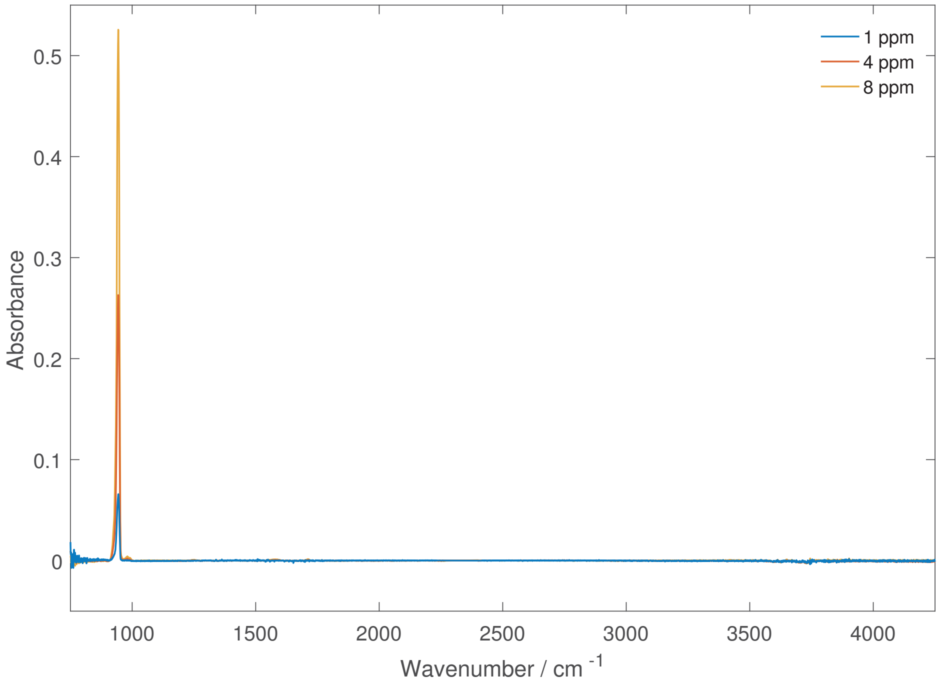

Figure A.9: SF_6 FTIR reference spectra.

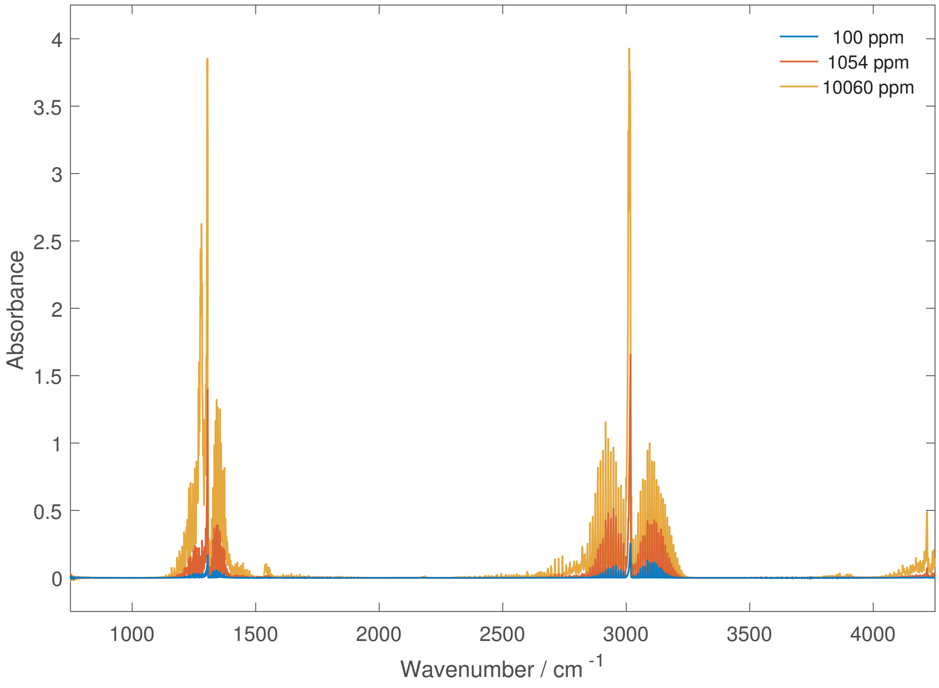

Figure A.10: CH_4 FTIR reference spectra.

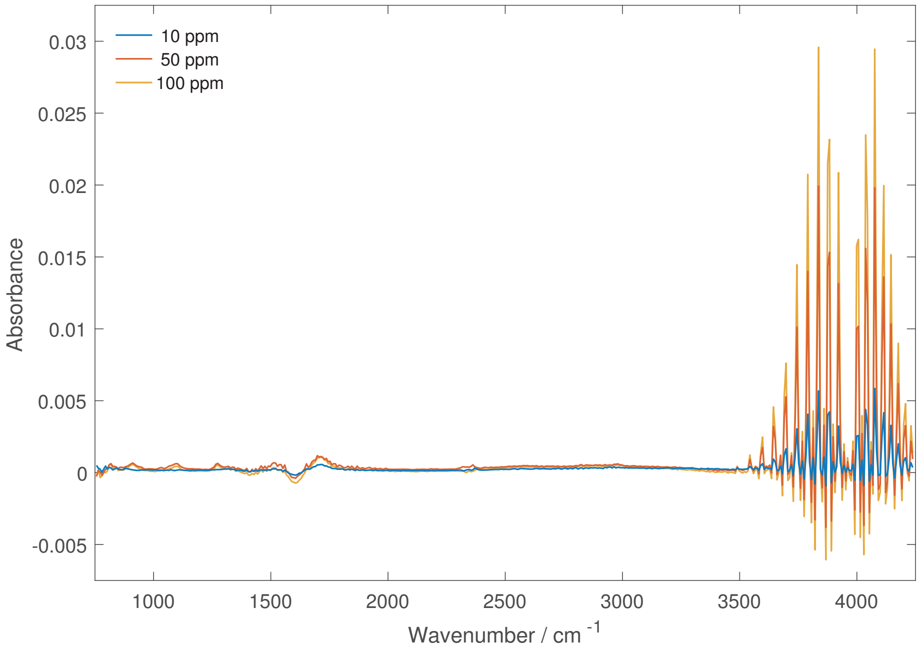

Figure A.11: HF FTIR reference spectra.

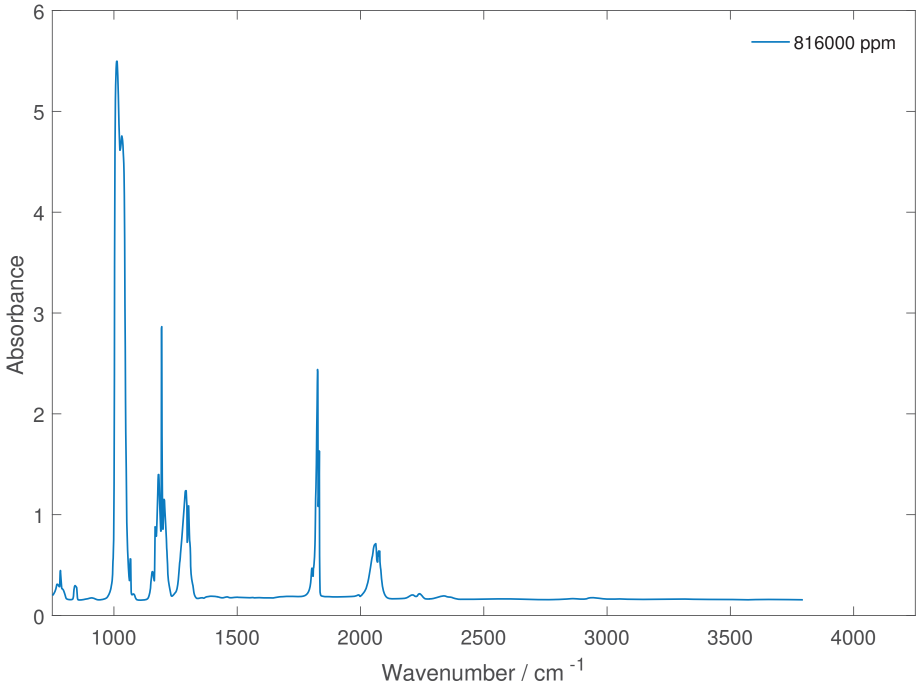

Figure A.12: SiF_4 FTIR reference spectra. Data adapted from NIST [59], digitized from a hardcopy.

Appendix B

Mass Spectrometer Fragmentation Data

Fragmentation ion pattern coefficients in quadrupole mass spectrometry is presented in Tables B.1 and B.2 for several gases that is of relevance during aluminium production in the laboratory. Notice the different intensities obtained at the m/z fragment ions from different instruments (here shown as different references).

Table B.1: Fragmentation pattern for some compounds during MS ionisation. $m/z \leq 45$

Gas	Mass	Ref	10	11	12	14	16	18	19	20	25	28	29	30	31	32	33	34	36	38	39	40	44	45
O_2	32	[63]					25.7									100								
		[59]					21.8									100								
N_2	28	[63]				13.2						100	1.00											
		[59]				13.8						100	0.74											
Ar	40	[63]								20.0									0.33	0.11		100		
		[59]								14.6									0.30	0.05		100		
CO	28	[63]			6.57	1.29	2.76					100	1.29			0.27								
		[59]			4.70		1.70					100	1.20											
CO_2	44	[63]			11.8		17.4					17.5											100	1.59
		[59]			8.71		9.61					9.81	0.10										100	1.20
Air		[63]				12.0	3.62	0.80		0.23		100	0.85			20.0						1.30	0.21	
CF_4	88	[59]							6.71						4.90	0.10								
COS	60	[59]					1.20					13.7				57.7		2.40					7.50	
COF_2	66	[59]					1.00		0.90			13.6	0.16		4.48									
CS_2	76	[59]			1.98		0.03									14.3				4.75	0.38		16.3	0.38
SO_2	64	[59]					5.20									10.4								
BF_3	68	[59]	1.50	5.40					3.20				0.30	1.10						0.01				
SiF_4	104	[59]							1.90			4.00	0.20	0.10			3.70							
C_2F_6	138	[59]			1.50				1.20						18.3	0.20								

Table B.2: Fragmentation pattern for some compounds during MS ionisation. $m/z \geq 46$.

Gas	Mass	Ref	46	47	48	49	50	60	64	66	67	68	69	70	76	78	85	86	87	88	104	119	120	138
O_2	32	[63]																						
		[59]																						
N_2	28	[63]																						
		[59]																						
Ar	40	[63]																						
		[59]																						
CO	28	[63]																						
		[59]																						
CO_2	44	[63]	0.52																					
		[59]	0.40																					
Air		[63]																						
CF_4	88	[59]					11.8						100	1.10						0.10				
COS	60	[59]						100																
COF_2	66	[59]		100	0.96		2.45			54.8	0.61													
CS_2	76	[59]	0.66												100	7.59								
SO_2	64	[59]			49.3	0.04	2.30		100	4.90														
BF_3	68	[59]			26.9	100						4.80												
SiF_4	104	[59]		3.20	0.20	0.20				0.50	0.10	0.10					100	5.20	3.40		1.50			
C_2F_6	138	[59]					10.10						100									41.3	0.90	0.20

Appendix C

Thermodynamic Data

Thermodynamic data for reactions related to the production of aluminium is provided in Table C.1. It is scaled so all data is referenced to the production of 1 mole of aluminium.

Table C.1: Thermodynamic data of (electro)chemical reactions at 1000 °C [50].

Reaction	ΔH^0 kJ	ΔS^0 $\mathrm{J\,K^{-1}}$	ΔG^0 kJ	E^0 V	E^{iso} V
$\frac{1}{2}\,\mathrm{Al_2O_3} + \frac{3}{2}\,\mathrm{C\,(s)} = \mathrm{Al\,(l)} + \frac{3}{2}\,\mathrm{CO\,(g)}$	674.8	295.3	298.8	−1.03	−2.33
$\frac{1}{2}\,\mathrm{Al_2O_3} + \frac{3}{4}\,\mathrm{C\,(s)} = \mathrm{Al\,(l)} + \frac{3}{2}\,\mathrm{CO_2(g)}$	548.9	165.3	338.4	−1.17	−1.90
$\frac{1}{2}\,\mathrm{Na_3AlF_6(l)} + \frac{1}{4}\,\mathrm{Al_2O_3} + \frac{3}{4}\,\mathrm{C\,(s)} = \frac{3}{2}\,\mathrm{NaF} + \mathrm{Al\,(l)} + \frac{3}{4}\,\mathrm{COF_2(g)}$	731.4	142.4	550.1	−1.90	−2.52
$\frac{3}{4}\,\mathrm{COF_2} + \frac{3}{8}\,\mathrm{C\,(s)} = \frac{3}{4}\,\mathrm{CO\,(g)} + \frac{3}{8}\,\mathrm{CF_4(g)}$	34.9	51.4	−30.6		
$\frac{1}{2}\,\mathrm{Na_3AlF_6(l)} + \frac{1}{4}\,\mathrm{Al_2O_3} + \frac{9}{8}\,\mathrm{C\,(s)} = \frac{3}{2}\,\mathrm{NaF\,(l)} + \mathrm{Al\,(l)} + \frac{3}{4}\,\mathrm{CO\,(g)} + \frac{3}{8}\,\mathrm{CF_4(g)}$	766.3	193.9	519.5	−1.79	−2.65
$\mathrm{Na_3AlF_6} + \frac{3}{4}\,\mathrm{C\,(s)} = 3\,\mathrm{NaF\,(l)} + \mathrm{Al\,(l)} + \frac{3}{4}\,\mathrm{CF_4(g)}$	857.7	92.4	740.1	−2.56	−2.96
$\mathrm{Na_3AlF_6} + \mathrm{C\,(s)} = 3\,\mathrm{NaF\,(l)} + \mathrm{Al\,(l)} + \frac{1}{2}\,\mathrm{C_2F_6(g)}$	889.8	67.8	803.5	−2.76	−3.07
$\mathrm{Na_3AlF_6} = 3\,\mathrm{NaF\,(l)} + \mathrm{Al\,(l)} + \frac{3}{2}\,\mathrm{F_2(g)}$	1557	206.1	1295	−4.47	−5.38